Fermilab

A Linear Collider Vision for the Future of Particle Physics

FERMILAB-PUB-25-0216-CSAID-TD

arXiv:2503.19983

This manuscript has been authored by Fermi Forward Discovery Group, LLC
under Contract No. 89243024CSC000002 with the U.S. Department of Energy,
Office of Science, Office of High Energy Physics.

Linear Collider Vision

A Linear Collider Vision for the Future of Particle Physics

In this paper we review the physics opportunities at linear e^+e^- colliders with a special focus on high centre-of-mass energies and beam polarisation, take a fresh look at the various accelerator technologies available or under development and, for the first time, discuss how a facility first equipped with a technology that is mature today could be upgraded with technologies of tomorrow to reach much higher energies and/or luminosities. In addition, we discuss detectors, alternative collider modes, as well as opportunities for beyond-collider experiments and R&D facilities as part of a linear collider facility (LCF). The material of this paper supports all plans for e^+e^- linear colliders and additional opportunities they offer, independently of technology choice or proposed site, as well as R&D for advanced accelerator technologies. This joint perspective on the physics goals, early technologies and upgrade strategies has been developed by the LCVision team based on an initial discussion at LCWS2024 in Tokyo and a follow-up at the LCVision Community Event at CERN in January 2025. It heavily builds on decades of achievements of the global linear collider community, in particular in the context of CLIC and ILC.

C. Balazs
Monash University, Melbourne 3800 Victoria, Australia

G. Taylor
University of Melbourne, Victoria 3010, Australia

W. Mitaroff
Institute of High Energy Physics, Austrian Academy of Sciences, 1050 Vienna, Austria

A.H. Hoang, S. Plätzer
University of Vienna, Faculty of Physics, 1090 Vienna, Austria

G. Durieux
Centre for Cosmology, Particle Physics and Phenomenology (CP3), Université catholique de Louvain, 1348 Louvain-la-Neuve, Belgium

M. Tytgat
Inter-University Institute for High Energies, Vrije Universiteit Brussel, 1050 Ixelles, Belgium

C. Hensel
Centro Brasileiro de Pesquisas Físicas, Rio de Janeiro 22290-180, Brazil

A.B. Bellerive
Carleton University, Ottawa, Ontario K1S5B6, Canada

F. Corriveau
Centre for High-Energy Physics, McGill University, Montreal, Quebec H3A2T8, Canada

D. Tuckler
TRIUMF, Wesbrook Mall, Vancouver, Canada

C.D. Fu, Q. Ouyang, H.R. Qi, M.Q. Ruan
Institute of High Energy Physics, Chinese Academy of Sciences, Beijing, China

I.P. Ivanov
Sun Yat-sen University, Guangzhou, Guangdong, China

M. Ouchemhou, T. Robens
Rudjer Boskovic Institute, 10000 Zagreb, Croatia

J. Cvach, J. Kvasnička, I. Polák, J. Zálešák
FZU - Institute of Physics of the Czech Academy of Sciences, 18200 Prague 8, Czechia

I.D. Gialamas, G. Hütsi, K. Kannike, A. Karam, L. Marzola, E. Nardi, J. Pata, M. Raidal
National Institute of Chemical Physics and Biophysics, 10143 Tallinn, Estonia

F. Djurabekova, K. Österberg
Helsinki Institute of Physics, University of Helsinki, 00014 Helsinki, Finland

E. Nagy, C. Vallee
Centre de Physique des Particules de Marseille, CNRS/IN2P3, Aix Marseille Université, Marseille, France

A. Arbey, G. Grenier, I. Laktineh, F. Mahmoudi
IP2I Institut de Physique des 2 Infinis CNRS/IN2P3, Université Claude Bernard, Lyon, France

D. Attié, M. Besançon, E. Cenni, P. Colas, N. Fourches, S. Ganjour, Z. Sun, M. Titov, B. Tuchming
Institut de recherche sur les lois fondamentales de l'Univers, CEA Saclay, 91191 Gif sur Yvette, France

J. Baudot
Université de Strasbourg, CNRS, IPHC UMR 7178, F-67000 Strasbourg, France

F. Alharthi[0], I. Chaikovska, R. Chehab, A. Faus Golfe, H. Guler, W. Kaabi, A. Korsun, F. LeDiberder, A. Martens, V.V. Mytrochenko[1], R. Pöschl, F. Richard, Y. Wang, M. Winter, X. Xia
IJCLab, Université Paris-Saclay, CNRS/IN2P3, 91405 Orsay, France

M.M. Altakach, S. Kraml
Laboratoire de Physique Subatomique et de Cosmologie, Université Grenoble-Alpes, CNRS/IN2P3, 38026 Grenoble, France

B. Fuks
Laboratoire de Physique Théorique et Hautes Energies (LPTHE), Sorbonne Université et CNRS, 75252 Paris, France

V. Boudry, J.-C. Brient, H. Videau
Laboratoire Leprince-Ringuet (LLR), École Polytechnique, 91128 Palaiseau, France

D. Zerwas
DMLab, Deutsches Elektronen-Synchrotron DESY, CNRS/IN2P3, Hamburg, Germany

T. Behnke, M. Berggren, J. Braathen, K. Buesser, G. Eckerlin, M. Formela, F. Gaede, E. Gallo, N. Hamann, D. Käfer, K. Krüger, J. List, B. List, T. Madlener, V.I. Maslov, F. Meloni, M.T. Núñez Pardo de Vera, J. Reuter, S. Riemann, T Schörner, I. Schulthess, S. Spannagel, M. Stanitzki, J.M. Torndal, N. Walker, G. Weiglein[2], M. Wenskat, J.C. Wood
Deutsches Elektronen-Synchrotron DESY, Germany

B. Dudar
PRISMA+ Cluster of Excellence and Mainz Institute for Theoretical Physics, Johannes Gutenberg University, 55099 Mainz, Germany

U. Einhaus, G. Heinrich, M.M. Mühlleitner
Karlsruhe Institute of Technology, Karlsruhe, Germany

A. Caldwell, J. Farmer, W. Hollik
Max Planck Institute for Physics, 85748 Garching, Germany

P. Bechtle, C. Breuning, I. Brock, J. Kaminski, M. Lupberger, L. Reichenbach, M. Vellasco
University of Bonn, Physikalisches Institute, 53115 Bonn, Germany

M. Boehler, S. Dittmaier, M. Schumacher
Physikalisches Institut, Albert-Ludwigs-Universität, Freiburg, Germany

M. Berger, M.V. Garzelli, G. Moortgat-Pick, M. Trautwein, A. Vauth
University of Hamburg, Hamburg, Germany

W. Kilian, T. Tong
Universität Siegen, 57068 Siegen, Germany

W. Porod
Institute for Theoretical Physics and Astrophysics, University of Würzburg, 97074 Würzburg, Germany

A. Subba
Indian Institute of Science Education and Research Kolkata, Mohanpur, West Bengal, India

P. Poulose[3], A. Subba[4]
Indian Institute of Technology Guwahati, Assam 781039, India

N. Kumar
Shree Guru Gobind Singh Tricentenary University, Gurugram, Haryana 122505, India

J. Dutta
The Institute of Mathematical Sciences, CIT Campus, Tharamani, Chennai, Tamil Nadu, 600113, India

H. Abramowicz, Y. Benhammou, A. Levy
Tel Aviv University, Ramat Aviv 69978, Israel

S. Bilanishvili, M. Galletti, L. Verra, M. Zobov
INFN Laboratori Nazionali di Frascati, 00044 Frascati, Italy

M. Bertucci, E. Del Core, L. Monaco, R. Paparella, D. Sertore

INFN Sezione di Milano, 20133 Milano, Italy

E. Maina
Università degli Studi di Torino, Dipartimento di Fisica, 10125 Torino, Italy

C. Oleari
Università di Milano-Bicocca, 20126 Milano, Italy

A. Aryshev, S. Asai, K. Fujii, J. Fujimoto, K. Ikematsu, A. Ishikawa, D. Jeans, T. Kubo, K. Kubo, A. Kumar, M. Kurata, Y. Kurihara, S. Michizono, J. Nakajima, M. Nojiri, Y. Okada, M. Omet, T. Omori, T. Saeki, H. Sakai, Y. Sakaki, T. Shidara, H. Sugawara, T. Tauchi, N. Terunuma, E. Viklund, A. Yamamoto, Y. Yamamoto, M. Yamauchi, K. Yokoya
KEK, Tsukuba, Japan

T. Takahashi
Hiroshima University, Higashi Hiroshima, 739-8530, Japan

A. Das
Hokkaido University, Sapporo 060-0810, Japan

S. Yamashita
Iwate Prefectural University, Takizawa-city, Iwate, Japan

R. Hosokawa, K. Mawatari, S. Narita, M. Yoshioka
Iwate University, 4-3-5 Ueda, Morioka, Iwate, 020-8551, Japan

Y. Kato
Kindai University, 3-4-1 kowakae, Higashiosaka, Osaka, 577-8502, Japan

J. Maeda
Kobe University, 1-1 Rokkodai, Nada-ku, Kobe, 657-8501, Japan

T. Watanabe
Kogakuin Univeristy of Technology and Engineering, Shinjuku-ku, Tokyo 163-8677, Japan

K. Kawagoe, K. Tsumura
Kyushu University, 744 Motooka, Nishi-ku, Fukuoka, 819-0395, Japan

T. Chikamatsu
Miyagi Gakuin Women's University, Aoba-ku, Sendai, Japan

Y. Horii, S. Iguro
Nagoya University, Nagoya, Japan

H. Ono
Nippon Dental University, Chuo-ku, Niigata 951-8580, Japan

Y. Seiya[5], K. Yamamoto[5]
Osaka Metropolitan University, Department of Physics, Osaka 558-8585, Japan

Y. Iwashita, S. Kanemura, K. Yagyu
Osaka University, Department of Physics, Toyonaka, Osaka 560-0043, Japan

T. Takeshita
Shinshu University, Matsumoto, Nagano, Japan

K. Hamaguchi, Y. Iiyama[6], M. Ishino, S. Matsumoto[7], T. Mori, N. Nagata, W. Ootani, T. Suehara, J. Tian[6]
The University of Tokyo, Bunkyo-ku, Tokyo 113-0033, Japan

K. Kyoya, T. Sanuki, H. Yamamoto
Tohoku University, Aoba-ku, Sendai 980-8577, Japan

K. Hidaka
Tokyo Gakugei University, Koganei, Tokyo 184-8501, Japan

S. Hirose
University of Tsukuba, Tsukuba 305-8577, Japan

V.M. Bjelland
Norwegian University of Science and Technology, Trondheim, Norway

J. Kersten
Department of Physics and Technology, University of Bergen, 5020 Bergen, Norway

E. Adli, J.B.B. Chen, P. Drobniak, D.K Kalvik, C.A. Lindstrøm, F. Peña[8], K. Sjobak
Department of Physics, University of Oslo, 0316 Oslo, Norway

O.M. Ogreid
Western Norway University of Applied Sciences, 5020 Bergen, Norway

S.A. Khan
Dhofar University, Salalah, Oman

M. Idzik, J. Moron, A. Ukleja
AGH University of Krakow, Faculty of Physics and Applied Computer Science, 30-055 Kraków, Poland

M. Goncerz, M. Kucharczyk, T. Wojton
Henryk Niewodniczanski Institute of Nuclear Physics, Polish Academy of Sciences, Poland

Z. Was
Institute of Nuclear Physics PAN, 31342 Krakow, Poland

M. Zielinski
Faculty of Physics, Astronomy and Applied Computer Science, ul. Lojasiewicza 11, 30-348 Krakow, Poland

B. Brudnowski, J. Kalinowski, J. Klamka, K. Mekala[9], A.F. Żarnecki, K. Zembaczynski
Faculty of Physics, University of Warsaw, Warsaw, Poland

I. Bozovic, I. Smiljanic, I. Vidakovic, N. Vukasinovic
Vinča Institute of Nuclear Sciences, University of Belgrade, Belgrade, Serbia

S.C. Park
Yonsei University, Seoul 03722, South Korea

O. Arquero, M.C. Fouz
Centro de Investigaciones Energéticas, Medioambientales y Tecnológicas (CIEMAT), Madrid, Spain

M. Almanza-Soto, C. Blanch, M. Boronat, J.C. Fernandez-Ortega, J. Fuster, N. Fuster-Martínez, B. Gimeno, D. González-Iglesias, S. Huang, A. Irles, P. Martín-Luna, J.P. Márquez, D. Melini, A. Menéndez, V.A. Mitsou, M. Moreno-Llácer, E. Musumeci, C. Orero, L.K Pedraza-Motavita, G. Rodrigo, M. Villaplana, M. Vos, K. Wandall-Christensen
IFIC, CSIC-Universitat de València, Valencia, Spain

M. Fernandez, F.J. Gonzalez, R. Jaramillo, A. Lopez-Virto, D. Moya, A. Ruiz-Jimeno, I. Vila
Instituto de Física de Cantabria, IFCA, Santander 39005, Spain

T. Biekötter, S. Heinemeyer
Instituto de Física Teórica, CSIC-Universidad Autónoma de Madrid, Madrid, Spain

F.G. Celiberto
Universidad de Alcalá (UAH), Departamento de Física y Matemáticas, 28805 Alcalá de Henares, Madrid, Spain

J.L. Avila-Jimenez, J. Berenguer-Antequera, F. Cornet-Gomez
Universidad de Cordoba, Campus Universitario de Rabanales, 14071 Cordoba, Spain

D. Espriu
Universitat de Barcelona, Institut de Ciències del Cosmos, Barcelona 08028, Spain

F. Cornet, J. de Blas
Universidad de Granada, 18071 Granada, Spain

E.M. Donegani
European Spallation Source, 224 84 Lund, Sweden

J. Björklund Svensson
Department of Physics, Lund University, Lund, Sweden

M. Coman, M. Jacewicz, M. Olvegøard
Department of Physics and Astronomy, Uppsala University, Uppsala 752 37, Sweden

V. Cilento, L.R. Evans, A. Latina, J. Osborne, S. Sasikumar, S. Stapnes, R. Tomás García, M. Williams
CERN, Geneva, Switzerland

T. Nakada
High Energy Physics Laboratory, Institute of Physics, Ecole Polytechnique Fédérale de Lausanne, 1015 Lausanne, Switzerland

M. Spira
Paul Scherrer Institut, 5232 Villigen, Switzerland

M. Vicente Barreto Pinto
Département de Physique Nucléaire et Corpusculaire (DPNC), Université de Genève, Geneva, Switzerland

T.A. du Pree, P. Kluit, P. Koppenburg, J. Rojo, J. Timmermans, H. Wennlöf, S. Westhoff
Nikhef — National Institute for Subatomic Physics, Science Park 105, 1098 XG Amsterdam, The Netherlands

M. Mulder
Van Swinderen Institute, University of Groningen, Groningen, The Netherlands

H. Duran Yildiz
Institute of Accelerator Technologies, Golbasi 06830, Ankara, Türkiye

B. Bilki
Istanbul Beykent University, Istanbul, Türkiye

H. Denizli, A. Senol
Department of Physics, Bolu Abant Izzet Baysal University, 14280, Bolu, Türkiye

H. Sert
Department of Physics, Istanbul University, TR34134, Istanbul, Türkiye

E. Bulyak
National Science Center 'Kharkiv Institute of Physics and Technology', Kharkiv 61108, Ukraine

I.R. Bailey
Lancaster University, Lancaster LA1 4YW, United Kingdom

C. Damerell, S. Easo
STFC Rutherford Appleton Laboratory, Chilton, Didcot OX11 0QX, United Kingdom

D. Angal-Kalinin, P.A. McIntosh, P.H. Williams
STFC Daresbury Laboratory, Keckwick Lane, Warrington WA4 4AD, United Kingdom

M. Wing[9]
Department of Physics and Astronomy, University College London, London WC1E 6BT, United Kingdom

N.K. Watson, A. Winter
School of Physics and Astronomy, University of Birmingham, Birmingham G15 2TT, United Kingdom

J. Goldstein
University of Bristol, Bristol BS8 1TL, United Kingdom

V.A. Khoze

University of Durham, Durham DH1 3DW, United Kingdom

V.J. Martin
University of Edinburgh, Edinburgh EH9 3FD, United Kingdom

A. Doyle, D. Protopopescu, A. Robson, Y. Zhang
University of Glasgow, Glasgow G12 8QQ, United Kingdom

T. Teubner
University of Liverpool, Liverpool L69 3BX, UK

R.B. Appleby, O. Apsimon, S. Boogert, R.M. Jones, V. Miralles
University of Manchester, Manchester M13 9PL, United Kingdom

P.N. Burrows, R. D'Arcy, B. Foster[9], D. Hynds, L. Kennedy[10]
University of Oxford, Oxford OX1 3RH, United Kingdom

K. Mimasu
University of Southampton, Southampton S017 1BJ, United Kingdom

F. Salvatore
University of Sussex, Brighton BN1 9QH, United Kingdom

K. Potamianos
University of Warwick, Coventry CV4 7AL, United Kingdom

J.A. Bagger
Johns Hopkins University, Baltimore, MD 21218, USA

K.T. Matchev
The University of Alabama, Tuscaloosa, AL 35487, USA

H. Baer
University of Oklahoma, Norman, OK 73019, USA

G. Chen, C. Jing, R. Margraf-O'Neal, A. Ody, P. Piot, J.G. Power, J. Zhang
Argonne National Laboratory, Lemont, IL 60439, USA

R. Szafron, A. Tricoli
Brookhaven National Laboratory, Upton, NY 11973, USA

M. Liepe, J.R. Patterson
Cornell University, Ithaca, NY 14853, USA

A.V. Kotwal
Duke University, Durham, NC 27708, USA

S. Belomestnykh[11], L. Gray
Fermi National Accelerator Laboratory, Batavia, IL 60510, USA

R. Dermisek, R. Van Kooten
Department of Physics, Indiana University, Bloomington, IN 47405, USA

R.L. Geng, J. Grames, R.A. Rimmer, A. Seryi
Jefferson Lab, Newport News, VA 23606, USA

E. Esarey, A. Formenti, T. Luo, K. Nakamura, J. Osterhoff, S. Pagan Griso, A. Rastogi, C.B. Schroeder, S. Schroeder, D. Terzani, J. van Tilborg
Lawrence Berkeley National Laboratory, Berkeley, CA 94720, USA

X. Lu[12]
Northern Illinois University, DeKalb, IL 60115, USA

M. Demarteau, O. Hartbrich, F. Pilat
Oak Ridge National Laboratory, Oak Ridge, TN 37830, USA

S. Ampudia Castelazo, T. Barklow, A. Dhar, S. Gessner, M.J. Hogan, M. Kagan, N. Majernik, S. Morton, E.A. Nanni, D. Ntounis, M.E. Peskin, J. Rabara Bailey, A. Schwartzman, D. Storey, C. Vernieri
SLAC National Accelerator Laboratory, Menlo Park, CA 94025, USA

P. Grannis, V.N. Litvinenko
Physics and Astronomy, Stony Brook University, NY 11794, USA

S.G. Gori, H.E. Haber
University of California, Santa Cruz, CA 95064, USA

M. Litos
University of Colorado Boulder, Boulder, CO 80309, USA

D. Bourilkov
University of Florida, Gainesville, FL 32611, USA

B. Bilki, Y. Onel, J.W. Wetzel
University of Iowa, Iowa City, IA 52242, USA

K. Kong, B. Madison, J.P. Ralston, C.S. Rogan, S. Rudrabhatla, G.W. Wilson
University of Kansas, Lawrence, KS 66045, USA

J.D. Wells
Physics Dept, Ann Arbor, MI 48109, USA

J.E. Brau, C.T. Potter, J. Strube
University of Oregon, Eugene, OR 97403, USA

K. Sugizaki
University of Pennsylvania, Philadelphia, PA 19104, USA

A. Freitas
University of Pittsburgh, Pittsburgh, PA 15260, USA

A.P. White
University of Texas at Arlington, Arlington, TX 76019, USA

Y. Bai, S. Dasu
University of Wisconsin–Madison, Madison, WI 53706, USA

[0]King Abdulaziz City for Science and Technology (KACST), Riyadh, Saudi Arabia
[1]NSC KIPT National Science Center "Kharkiv Institute of Physics and Technology" of The National Academy of Sciences of Ukraine, Kharkiv, Ukraine
[2]also at University of Hamburg
[3]St. Joseph's University, Bangalore 560027, India
[4]Indian Institute of Science Education and Research Kolkata, Mohanpur, West Bengal, India
[5]Nambu Yoichiro Institute of Theoretical and Experimental Physics (NITEP)
[6]ICEPP
[7]Kavli IPMU
[8]Ludwig-Maximilians-Universität München, 85748 Garching, Germany
[9]Deutsches Elektronen-Synchrotron DESY, Germany
[10]CERN, Geneva, Switzerland
[11]Physics and Astronomy, Stony Brook University, NY 11794, USA
[12]Argonne National Laboratory, Lemont, IL 60439, USA

Contents

1 Introduction

The 2020 update of the European Strategy for Particle Physics made a firm statement about its priorities in its first line under "High-priority future initiatives": "An electron-positron Higgs factory is the highest-priority next collider." The importance of a Higgs factory was re-emphasized by the Snowmass Study and the P5 report in the US. There are good reasons for this statement.

The key insight that we have gained from the Large Hadron Collider (LHC) is that the Standard Model of particle physics gives an excellent description of the interactions of elementary particles in all of the processes that it probes. This is true throughout studies of the strong, weak, and electromagnetic interactions. The Standard Model (SM) requires the Higgs boson, and, indeed, the LHC experiments were able to discover the Higgs boson and to show that it has properties very close to those that the SM predicts.

On the other hand, the SM is manifestly incomplete. It does not include the cosmic dark matter or dark energy, and it does not address the issues of formulating a quantum theory of gravity. But it is also incomplete in its description of particle physics. For the interactions mediated by gauge bosons, it does describe a wealth of elementary processes by a minimal set of gauge theory equations of motion with only three coupling constants that must be specified. For interactions mediated by the Higgs boson, the reverse is true. Every outcome of the theory – the spectrum of quark and lepton masses, their mixings under the weak interactions, the presence of CP violation, and the masses of neutrinos – comes from a specific number put into the Higgs couplings with no underlying explanation. Even the most basic element of the Higgs field's behaviour, the fact that it has spontaneous symmetry breaking, is put in by hand.

Actual dynamical explanations for these features must come from new interactions that couple to the Higgs boson. Over the past decades, we have searched for new physics beyond the SM in every possible low-energy setting, seeking high-precision measurements and extremely rare processes. At the energy frontier, the LHC experiments have carried out extensive searches and have made great progress in measuring the properties of the Higgs boson. Still, much opportunity remains for studies of still higher precision that can reveal the influence of new physics on the Higgs boson. We must continue this search, since this is the one place where the imprint of these new interactions must be found.

An e^+e^- collider is the ideal machine for precision measurements. Because electron and positrons are elementary particles, their reactions are simple and display the structure of the underlying interactions directly. Backgrounds are dominated by electroweak processes, and these are also simple and – more importantly – precisely understood at the part-per-mil level. The low event rates relative to proton collisions allow the construction of low-material-budget, high-precision detectors and of trigger-less data taking. All of these features minimize systematic uncertainties. This makes it possible to measure small deviations from the SM with high confidence and credibility.

The choice of a linear e^+e^- collider redoubles these advantages. Electroweak physics is intrinsically chiral, with, for example, the left- and right-handed electron giving different information. Linear colliders will have high beam polarisation to take advantage of the new observables that this produces. Higgs bosons are produced in a number of different reactions that complement one another, as is well appreciated at the LHC. Because linear collider designs have luminosities that increase with the centre-of-mass energy, they can study directly not only the reaction $e^+e^- \to ZH$ that is most important at low energies but also WW fusion, reactions involving the top quark Yukawa coupling, multiple reactions with Higgs boson pair production, and at the highest energies even constrain triple-production of Higgs bosons. They can also carry out a program of precision measurements on the top quark, the quark for which consequences of non-Standard Higgs physics would be most visible. Many of these measurements see a tremendous gain in sensitivity at higher centre-of-mass energies, significantly above the $t\bar{t}$ production threshold. This applies likewise to processes with multiple electroweak gauge bosons. Linear colliders thus provide a large number of distinct observables covering the full range of interactions of the Higgs boson and its closest relatives in the SM. These observables will be crucial to discover deviations from the SM through precision measurement, and also to re-discover it in a variety of processes. This program will allow us to confirm the presence of new physics and to fully understand the pattern of the effects it has on SM particles.

The purpose of this paper is to review our knowledge of the physics opportunities at linear e^+e^- colliders with a special focus on high centre-of-mass energies and beam polarisation, to take a fresh look at the various accelerator technologies available or under development and, for the first time, discuss how a facility first equipped with a technology mature today could be upgraded with technologies of tomorrow to reach much higher energies and/or luminosities. In addition, we will discuss detectors and alternative collider modes, as well as opportunities for beyond-collider experiments and R&D facilities as part of a linear collider facility (LCF).

Substantial documentation exists already on the more mature linear collider proposals with their detectors and physics potential, including the Technical Design Report of the International Linear Collider (ILC) [1–5] and its staging report [6], the Conceptual Design Report of the Compact Linear Collider (CLIC) [7–9], its updated baseline [10] and its Project Implementation Plan [11], the ILC and CLIC reports for the previous update of the European Strategy for Particle Physics (ESPP) [12, 13], the ILC and CLIC reports to the Snowmass 2021 study in the US [14, 15] and the current update of the ESPP [16–18]. Here, we will build on those papers, provide references to the previous literature and update the conclusions from new studies wherever possible. Based on the detailed designs for ILC and CLIC, the Linear Collider Facility at CERN [19] is now being proposed as a future flagship project for CERN.

In recent years, even more proposals or concepts for linear colliders based on technologies under development today have been proposed, including for instance – but not being restricted to – C^3 [20, 21], HELEN [22, 23], HALHF [24, 25], ALEGRO [26–28], the Design Initiative for a 10 TeV pCM Wakefield Collider [29] or ReLiC [30]. We will discuss how these technologies, or a photon collider like for instance XCC [31] could boost the performance of the linear collider facility in later upgrades. From the beginning, a linear collider could also host a large variety of beyond collider experiments and R&D facilities.

The material of this paper will support all plans for e^+e^- linear colliders and additional opportunities they offer, independently of technology choice or proposed site, as well as R&D for advanced accelerator technologies.

An outline of this paper is as follows: in Section 2 we will outline potential running scenarios and the experimental environment as the foundation for the following section. Section 3 reviews the science opportunities offered by a linear collider facility, Section 4 discusses the available baseline designs and future upgrade strategies for a linear collider facility. Section 5 is dedicated to the facilities that a linear collider facility would make available for beam dump and fixed target experiments, while Section 6 will discuss linear collider detectors with their current technologies and future developments. Section 7 will present our conclusions.

2 Operating Scenarios, Experimental Environment and Algorithmic Developments

In this section we summarise the operating scenarios discussed for linear colliders as well as the experimental environment. For a comprehensive introduction to the energy and polarisation dependence of various physics processes in e^+e^- collisions, as well as the physics impact of beam polarisation and the measurement strategies for luminosity and polarisation we refer to Chapter 5 of [32] and to [33].

Quantitative studies of the physics potential of future colliders are necessarily based on some reference assumptions on the centre-of-mass energy, integrated luminosity as well as the beam polarisation (absolute values and luminosity sharing between the different sign configurations). In electron-positron collisions, different physics observables often have their own preferred centre-of-mass energy range. Therefore the overall physics performance of any e^+e^- collider depends on the choice of a full operating or running scenario, combining a set of energies with the respective luminosity and polarisation information. Different choices made in the running scenarios often reflect different choices on which part of the physics program to emphasize. In case of detailed Geant4-based detector simulations, i.e. the de-facto standard for ILC and CLIC projections, analyses in some cases have been performed on MC data sets corresponding to much lower integrated luminosities and then extrapolated to the full running scenario due to resource limitations.

Beam polarisation is an important aspect of linear collider physics, and so the beam polarisations to be used must be specified as part of the operating plan. In the following, the level of polarisation is expressed as signed fraction or percentage, where a positive value refers to a dominantly right-handed beam and a negative value to a dominantly left-handed beam. R and L denote pure chiral states. e^+e^- collisions with non-polarised beams lead to equally populated four e^+e^- helicity combinations −+, −−, ++, and +−. In the scenarios below, usually polarisations of 80% for electrons and 30% for positrons are assumed. A row of each table shows the assumed splitting among the −+, −−, ++, and +− operating modes. The luminosity sharing between the beam polarisation sign configurations can be adjusted depending on the physics needs. This is especially true for the ILC where the configurations can adjusted arbitrarily at run time.

2.1 Operating scenarios

For the ILC, a canonical straw-man running scenario has been worked out by the LCC Joint Working Group on Beam Parameters [34], based on a comprehensive physics-driven optimisation, which aimed to pick the optimal energy for each of the targeted measurements, leading to several desired operation energies below 1 TeV. Capitalising on the fact that a linear accelerator based on super-conducting radio frequency cavities (SCRF) can easily be run at lower gradients, operation at centre-of-mass energies below the maximal installed energy is almost always possible. While an extended running period at 250 GeV is optimal for measuring the total Higgsstrahlung cross-section, giving access to the Higgs boson's total width and its coupling to the Z boson, most measurements of top-quark properties benefit from a centre-of-mass energy significantly above the $t\bar{t}$ production threshold. A theoretically proper determination of the top quark mass requires a threshold scan at a centre-of-mass energy around twice the top quark mass. The experimental uncertainties become negligible compared to the theory uncertainties already with about 100 fb^{-1}. Thus, the ILC run plan foresees only a brief run at the $t\bar{t}$ production threshold.

The time ordering of the centre-of-mass energies was later adjusted to the staged machine starting at 250 GeV [35]. At the same time, the importance of the left-right asymmetry A_{LR} in the Higgs-strahlung process for disentangling certain SMEFT operators was recognized, leading to an adjustment of the luminosity sharing between the polarisation sign configurations at 250 GeV. At the $t\bar{t}$ threshold, however, the majority of the luminosity is foreseen to be taken in the (-,+) configuration. We'd like to stress, however, that the ILC design foresees fast helicity reversal for both beams, which allows the luminosity sharing between the polarisation sign configurations to be adjusted arbitrarily at run time, depending on physics needs.

Table 1 summarises the integrated luminosities envisioned at each energy stage, along with the beam polarisations. The Cool Copper Collider [20] envisions a similar scenario, adopting though 550 GeV instead of 500 GeV due to the significantly higher $t\bar{t}H$ cross-section. The real-time needed for any of the stages will depend on the assumed instantaneous luminosity as well as on the assumptions on operating efficiency and learning curves when starting to operate the collider in a new mode.

	91 GeV	250 GeV	350 GeV	500 GeV	1000 GeV
$\int \mathscr{L}$ (ab^{-1})	0.1	2	0.2	4	8
beam polarisation (e^-/e^+; %)	80/30	80/30	80/30	80/30	80/20
(−+, −−, ++, +−) (%)	(10,40,40,10)	(5,45,45,5)	(5,68,22,5)	(10,40,40,10)	(10,40,40,10)

Table 1: Centre-of-mass energy, integrated luminosity and beam polarisation of the various stages of the straw-man ILC operating scenario [34]. Running at the WW threshold is technically possible, however currently not prioritized, c.f. Sec. 3.2.2 for a discussion of the role of the threshold running for the W mass determination.

The main objective for CLIC, on the other hand, is to reach the TeV-regime as quickly as possible. Thus, the optimisation of the running scenario was conducted in a very different way by considering which single centre-of-mass energy is best suited to cover the whole physics program below 1 TeV, as detailed in [10]. This concluded that a centre-of-mass energy of 380 GeV is the optimal choice before proceeding to the TeV-regime, since it allows to perform both top-quark and Higgs boson measurements. In particular the total Higgsstrahlung cross-section measurement via the hadronic recoil benefits at this energy from a much cleaner kinematic separation from important background processes compared to 250 GeV, minimizing model-dependencies due to decay-mode-dependent selection efficiencies [36].

Building on the CLIC report to Snowmass [15], the CLIC luminosity has been updated in December 2024 [37] for all three stages: 380 GeV, 1.5 TeV and 3 TeV. For the lowest energy point two options are available differing only in the repetition rate of 50 Hz or 100 Hz, i.e., doubling the luminosity. The envisaged integrated luminosities and beam polarisations are summarised in Table 2.

	380 GeV	1500 GeV	3000 GeV
$\int \mathscr{L}$ (ab^{-1})	2.2 (4.3)	4	5
beam polarisation (e^-/e^+; %)	80/0	80/0	80/0
(-, +) (%)	(50,50)	(80,20)	(80,20)

Table 2: The updated baseline CLIC operation model (December 2024). Two options for 380 GeV running are given, with 50 Hz and 100 Hz repetition rates, respectively. Running at $\sqrt{s} = 91$ GeV is an option.

Many of the physics projections in the following section will be based on these "classic" operating scenarios for ILC and CLIC.

In the context of the LC Vision discussions, however, the physics-driven optimisation for a generic Linear Collider has been revisited, considering also that up to now there is no indication of a clear physics target beyond about a TeV, giving more emphasis to precision measurements of the Higgs boson, the top quark, and the electroweak gauge bosons, while keeping the flexibility to target energies of up to 3 TeV in the future. The design of the ILC as a linear collider based on superconducting technologies was frozen more than 10 years ago. Meanwhile there is major progress in SCRF (R&D as well as operational experience with XFELs), ultra-low emittance storage rings and other individual components (e.g. klystron efficiency). Implications will be discussed in Sec. 4, where we lay out suggestions for an updated SCRF-based linear collider and discuss the option to upgrade an initial facility constructed with today's technology with higher-gradient developments in the future. Based on a significantly higher instantaneous luminosity compared to ILC as considered in Japan, the LC Vision team proposes the run plan summarised in Table 3. Note for completeness that up to 550 GeV this plan is identical to the plan presented in the LCF proposal for CERN [19]. Thus we will refer to this operating scenario as the LCF scenario. Example upgrade scenarios and timelines for collecting these data sets will be discussed in Sec. 4.6.

	91 GeV	250 GeV	350 GeV	550 GeV	1-3 TeV
$\int \mathscr{L}$ (ab^{-1})	0.1	3	0.2	8	8
beam polarisation (e^-/e^+; %)	80/30	80/30	80/30	80/30	80/20
(−+, −−, ++, +−) (%)	(10,40,40,10)	(5,45,45,5)	(5,68,22,5)	(10,40,40,10)	(10,40,40,10)

Table 3: Centre-of-mass energy, integrated luminosity and beam polarisation of the various stages of the straw-man LC Vision scenario. Running at the WW threshold is technically possible, however currently not prioritized, c.f. Sec. 3.2.2 for a discussion of the role of the threshold running for the W mass determination.

2.2 Instantaneous luminosity and power consumption of linear colliders

The instantaneous luminosity is intimately connected to the electrical power budget of a collider. Linear collider proposals have traditionally been designed against self-imposed limits on the power consumption. For instance ILC aimed to stay around 100 MW for operation at 250 GeV, and not to exceed 300 MW for operation at 1 TeV. This has led to some misconceptions about the technical possibilities of linear colliders. In Sec. 4, we will come back to this theme and discuss in more detail the possibilities to increase the luminosity wrt. the classic linear collider proposals and their respective implications on the power consumption. Here, we give already a summary in Fig. 1(a), where LCF refers to an ILC-like collider with some of the improvements discussed in Sec. 4 applied, as proposed in [19].

2.3 Experimental environment and detector requirements

The beam structure of an ILC results in 0.73 ms long bunch trains being delivered to the interaction point with a rate of 5 Hz/10 Hz. The bunches are spaced equally every 550 ns. For CLIC the bunch separation is reduced to 0.5 ns. For C^3 the bunch separation ranges between 1.85 ns and 2.65 ns. These interaction rates are much lower than at a proton collider.

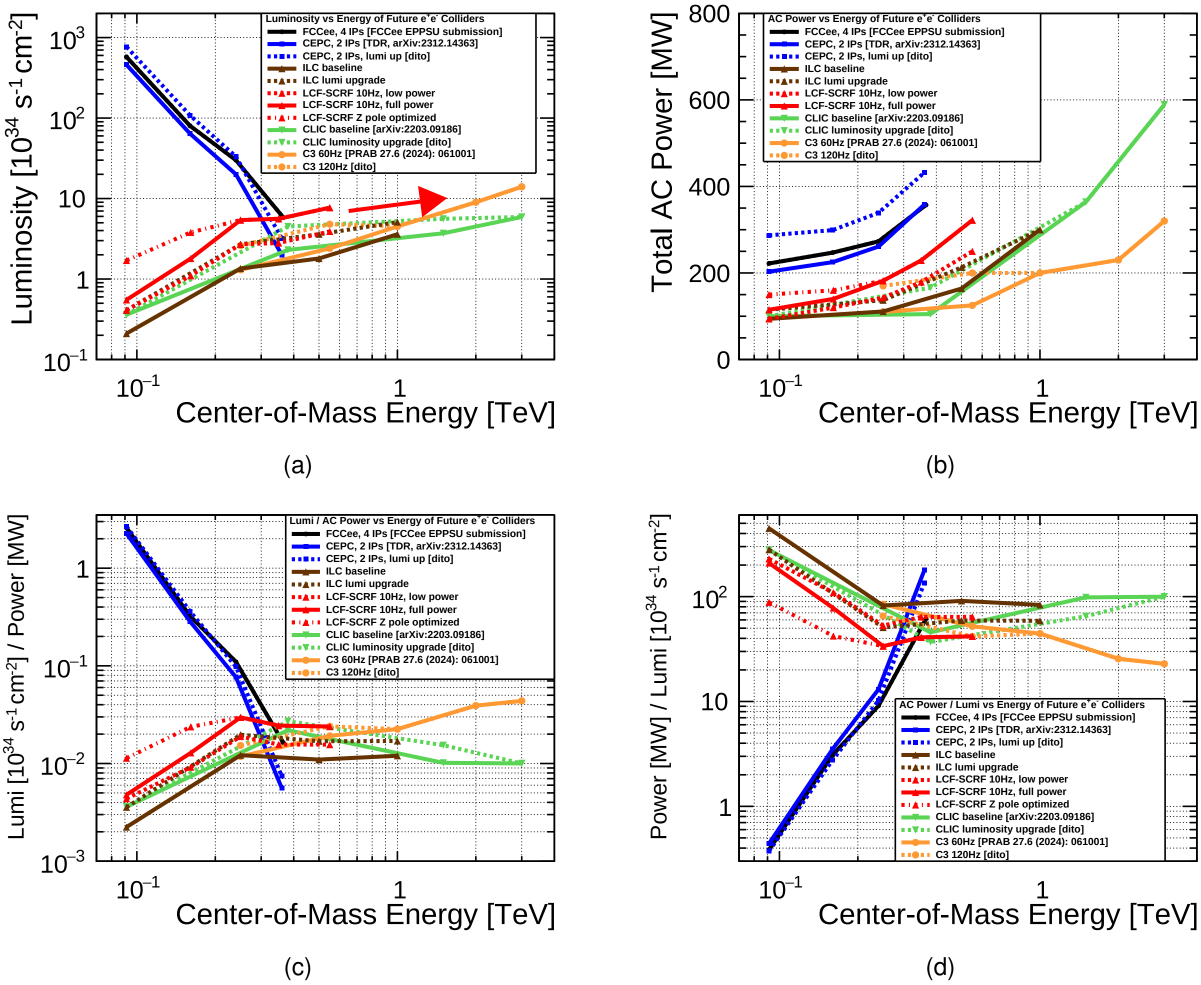

Figure 1: Instantaneous luminosity (a), total site power (b), and their ratios (c), (d) as a function of the centre-of-mass energy for various e^+e^- colliders. The LCF is drawn only up to 550 GeV, since the luminosity and power consumption of higher energies will depend on the yet-to-be-chosen technology for these energies. However, they can be expected to be similar to the high-energy stages of CLIC and C^3, as indicated by the red arrow.

The detectors at a future LC will be optimized for precision measurements of the Higgs boson, electroweak bosons, the top quark, and other particles, with requirements significantly exceeding those of hadron colliders due to the cleaner e^+e^- collision environment and lower radiation levels. The LC detectors must achieve precise tracking, exceptional jet energy resolution, and trigger-less operation, leveraging the lower complexity and rates of e^+e^- collisions. The considerations in the previous paragraphs lead to following set of requirements, for more information see e.g. [14]:

- **Impact parameter resolution:** An impact parameter resolution of $5\ \mu\text{m} \oplus 10\ \mu\text{m}/[p\ [\text{GeV}/c] \sin^{3/2}\theta]$ has been defined as a goal in order to enable efficient identification of charm-quark decays.

- **Momentum resolution:** An inverse momentum resolution of $\Delta(1/p) = 2 \times 10^{-5}$ $[(\text{GeV/c})^{-1}]$ asymptotically at high momenta should be reached in order not to limit the precision of the Higgs recoil measurement in the $Z \to \mu\mu$ channel. Maintaining excellent tracking efficiency and very good momentum resolution at lower momenta will be achieved by an aggressive design to minimise the detector's material budget.

- **Jet energy resolution:** A jet energy resolution $\Delta E/E = 3-4\%$ is required for the statistical separation of hadronically decaying W, Z, and Higgs bosons. Particle flow-based detectors and corresponding reconstruction algorithms have been show to meet this requirement.

- **Readout:** The detector readout will not use a hardware trigger, ensuring full efficiency for all possible event topologies.
- **Powering** The power of major systems will be cycled between bunch trains. This will reduce the power consumption of the detectors and minimise the amount of material in the detector. The corresponding reduced service requirements will also be beneficial for the acceptance and hermeticity of the detectors.

The detectors must also handle radiation exposure, with most regions experiencing modest doses ($\sim 10^{11}$ n/cm^2/year NIEL), except for the forward calorimeters near the beamline.

Common to all linear machines is the need for strong beam focusing resulting in beam sizes in the nanometer range at the interaction point. This causes a challenge – but also brings a benefit:

- The strong electromagnetic fields generated by the tiny beams lead to beamstrahlung and the creation of e^+e^- pair background, posing a potential challenge to the detectors. However all LC detector concepts demonstrated that the expected impact is manageable, with detector occupancies kept under control, see e.g. [5] for the ILC detector concepts. A recent example for C^3 is presented in [38]. The CLIC detector [39] has been adapted from the ILC SiD and ILD [40] designs to be compatible with 3 TeV operations, which constitutes the most challenging environment for the detectors in view of the high beam induced background levels. For this reason the inner tracking and the vertex detectors of CLICdet are deployed with a larger inner radius compared to the other LC detector concepts.
- For the identification of b- and c-jets, the tiny beam spot is a clear advantage, as the transverse size of the luminous region is negligible and does not contribute visibly to the impact parameter and vertex significance. This enables a full exploitation of the vertex detector resolution in high-level reconstruction.

More details on the LC detector concepts, the R&D supporting these designs and new ideas will be discussed in Sec. 6.

2.4 Event reconstruction - a brief overview and outlook

The physics performance of modern highly-granular particle-flow detectors decisively depends on both excellent hardware, discussed in more detail in Sec. 6, and sophisticated reconstruction algorithms. This concerns track reconstruction and particle flow as well as particle identification, jet flavour tagging and many other aspects. Linear collider physics studies have a long-standing tradition of using detailed and realistic detector simulations, based upon performance of prototypes observed in test beam campaigns. Reconstruction and analysis tools leveraging machine-learning and other advanced techniques are however only now being developed, and the vast majority of physics projections use more traditional algorithms. A deeper discussion of the state of the art in this respect can be found in e.g. the ILD Interim Design Report [40], the ILC Report to Snowmass [14] and, even more recently, in the report of the ECFA Study on Higgs / Top / Electroweak Factories [41].

Here, we focus on highlighting the recent and very dynamically ongoing developments in jet flavour tagging. Since jets (especially with heavy bosons) are contained in most of final states including Higgs and gauge bosons, the identification of the jet flavour is an essential tool to distinguish such final states to derive various coupling constants. LCFIPlus [42] is a successful software tool (released in 2013) which consists of vertex finding, jet clustering and BDT-based jet flavour tagging. Most of the current physics analyses use LCFIPlus.

More recently, jet flavour tagging based on deep-learning technologies have been rapidly advanced and significant improvement has been observed for hadron collider experiments. Among many algorithms, ParticleNet and ParticleTransformer (ParT) have been applied to linear collider studies and in particular ParT shows 5-10 times better rejection ratio for both b-tag and c-tag with (ILD) full simulation, as shown in Figs. 2(a) and 2(b). These techniques also enable tagging strange [43] and gluon jets with appropriate particle identification (PID) features implemented in detectors such as dE/dx in gaseous trackers, time-of-flight in outer detectors (calorimeters or outer trackers) or dedicated Cherenkov detectors. The PID information is provided by the new tool CPID [44] and both this and the inference part of the flavour tagger have been recently implemented in the ILD reconstruction chain. Work is ongoing to identify jet charge using a similar algorithm.

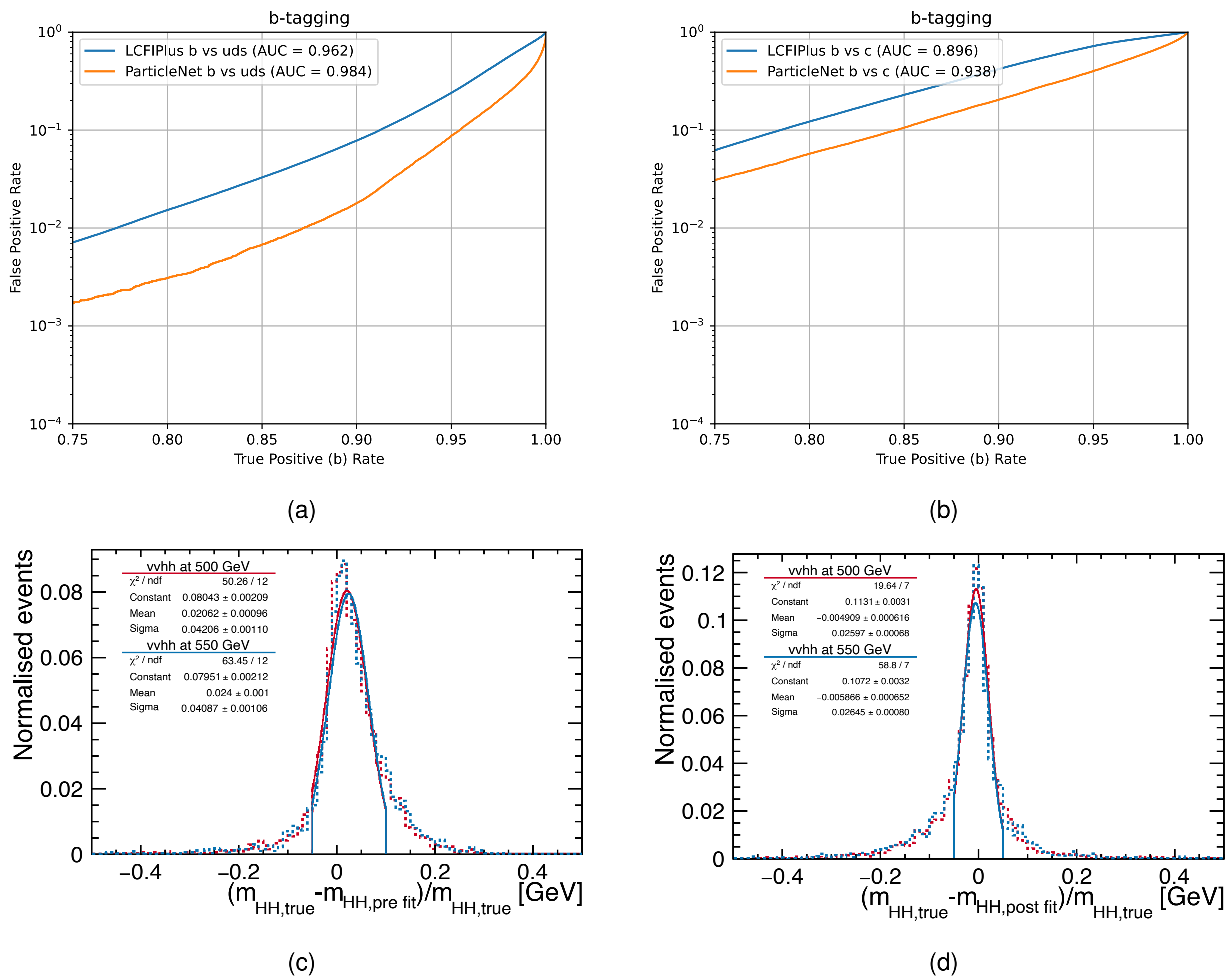

Figure 2: Reconstruction improvements considered in the updated di-Higgs analysis: (a), (b) b-tagging efficiency (true positive rate) increases by about 10% (relative) for the same background efficiency (false positive rate) at typical working points of the previous analysis (80% b-tagging efficiency with LCFIPlus) (c), (d) the resolution on the di-Higgs invariant mass improves by about a factor of two when the new semi-leptonic decay correction and kinematic fit are applied.

Beyond the tagging of jet flavour, another important development is a decay-by-decay correction for the missing four-momentum of neutrinos from semi-leptonic b-decays. The impact on the di-Higgs invariant mass reconstruction is illustrated in Figs. 2(c) and 2(d), showing about a factor of two improvement of the resolution.

The impact of these and many other ongoing improvements on physics analyses is expected to be broad. In case of the di-Higgs analysis, the impact on the analysis has recently been estimated, c.f. Sec. 3.3.1. Full analysis updates of the projections on Higgs branching fractions and on double-Higgs production are ongoing. Other studies including heavy flavour jets are about to be updated accordingly.

3 The Portal to New Physics

As we have discussed already in the introduction, precision measurements of the Higgs boson offer a unique opportunities to discover deviations from the SM that point to solutions to the many questions the SM cannot answer. In this section, we will review the many signals of new physics that could appear in the precision study of the Higgs boson and other heavy particles of the SM, as well as in direct searches for new particles.

The program requires several stages, at different e^+e^- centre-of-mass energies that are listed again here for convenience and match the stages sketched in Table 3.

- An initial stage at 250 GeV: The cross section of the Higgs-strahlung process $e^+e^- \to HZ$ is largest close to the HZ production threshold. Therefore, this energy allows for recording a large dataset for determining the Higgs branching fractions as well as the absolute normalisation of Higgs couplings and the Higgs boson mass. The clean environment of e^+e^- collisions is also an ideal situation in which to search for non-standard Higgs boson decays, including invisible ones.

This data set will also give the most precise measurements of the W boson non-linear interactions and of electroweak fermion pair production, providing further opportunities for discovery. The W boson's mass can be measured using the 250 GeV data or in an optional one-year threshold scan. Also, at this stage, one can collect a few 10^9 events on the Z pole with polarised beams, to test the SM electroweak sector with high precision. In this regard, the use of beam polarisation compensates almost three orders of magnitude in integrated luminosity with respect to unpolarised colliders.

- A second stage at 550 GeV: At this energy the WW fusion reaction $e^+e^- \to \nu\bar{\nu}H$ has become the dominant production mechanism for Higgs bosons. This will provide an independent setting for the measurement of Higgs branching fractions and searches for exotic decays. It also allows the measurement of the top-quark Yukawa coupling and the trilinear Higgs self-coupling through the processes $e^+e^- \to t\bar{t}H$ and $e^+e^- \to ZHH$, respectively.

  The top quark is the SM particle most strongly coupled to the Higgs boson and thus most likely to be affected by new Higgs interactions. This stage, well above the top-quark threshold, will also provide precision measurements of the top-quark electroweak couplings and include a short run around the top pair production threshold for a precise mass determination.

- A third stage of at least 1 TeV: Here the reaction of WW fusion to HH is the dominant Higgs pair production mechanism. This energy stage thus provides a second method to determine the trilinear Higgs self-coupling, and can put constraints on the quartic Higgs self-coupling [45]. The two Higgs pair production processes, ZHH and WW fusion, are strikingly complementary; as the self-coupling is increased from its SM value, the ZHH cross section increases while the WW fusion cross section decreases. Observing these deviations in the same experiment would give the most persuasive evidence for a non-standard value of the Higgs self-coupling.

  Anomalies in top-quark or multi-gauge-boson couplings suggested in earlier stages will be dramatically larger, proportionally to E_{CM}^2 in typical cases. The ample production of (single) Higgs bosons in WW fusion and $t\bar{t}H$ will allow us to further scrutinise the couplings of the Higgs boson to SM particles including the top quark and the W boson.

At any of these stages, but increasingly so at the higher energies, there is additional discovery potential for new particles. We also stress that in case a discovery – at the HL-LHC, at any other current experiment, or at the first stage of a linear collider itself – points to a specific energy scale, the run plan and upgrade schedule of a linear collider should be – and can be – adjusted.

3.1 Scrutinizing the Higgs boson via single-Higgs production

The precise measurement of Higgs boson properties is critical for probing effects of new physics in the electroweak sector of the Standard Model. At a Linear Collider (LC) operating at a centre-of-mass energy of 250 GeV, precision studies of the Higgs boson will focus on the dominant Higgs-strahlung process, $e^+e^- \to ZH$. At this energy there is also sensitivity to the W W fusion process, measured in the Higgs' decay to b quarks. For CLIC the first stage has a nominal centre-of-mass energy of 380 GeV, where the contribution of WW fusion processes to Higgs production increases. The physics projections, however, have been performed with Monte-Carlo samples generated at a centre-of-mass energy of 350 GeV, which is thus used as reference energy in this section.

The Higgs-strahlung production mechanism allows for model-independent measurements of Higgs boson properties by reconstructing the Higgs mass from the recoil mass spectrum of the Z boson, independent of the Higgs decay mode. The WW fusion process contributes to the determination of the Higgs boson width.

3.1.1 Impact of beam polarisation on Higgs production

An important characteristic of a linear collider is its polarised beams. In the following, the level of polarisation is expressed as signed fraction or percentage, where a positive value refers to a dominantly right-handed and a negative value a dominantly left-handed beam, whereas R and L denote pure chiral states, as explained in Sec. 2. e^+e^- collisions with unpolarised beams lead to four e^-e^+ helicity combinations −−, −+, +−, and ++ that are equally populated. Neglecting the difference between helicity and chirality, only the opposite-sign initial states couple to the Z boson, leading to Higgs-strahlung production. For WW fusion, due to the pure left-handed coupling of the W bosons, only the e^-e^+ LR initial state can produce Higgs bosons.

In the following all factors are given at leading order. Including radiative corrections will lead to changes at the level of about 5 % for processes mediated through the Z boson. The WW fusion process is not affected as there is only one diagram/one coupling involved, while for the Z boson exchange the coupling strength and therefore the choice of $\sin^2\theta_W$ affects the calculation.

For $P(e^-,e^+) = (-1,1)$ the Higgs-strahlung cross section is enhanced by a factor 2.43 and for $P(e^-,e^+) = (1,-1)$ by a factor 1.57 compared to the unpolarised cross section. The difference in the enhancement factor is due to the different couplings for L and R fermions to the Z boson.

As explained in Section 2, for all LC machines an electron polarisation of ± 0.8 is assumed to be readily achievable. In this beam, 90% of the electrons are in the favoured helicity state. For positron polarisation, ILC and C^3 are designed to provide a polarisation of ± 0.3, corresponding to 65% of the positrons in the favoured state. For Higgsstrahlung, running with $P(e^-,e^+) = (-0.8, 0.3)$ therefore leads to an effective enhancement of the cross section by a factor 1.48, whereas $P(e^-,e^+) = (0.8,-0.3)$ leads to a cross section roughly equal to the unpolarised cross section. For the like-sign polarisation combinations the factors are 0.87 and 0.65. If the positron beam is not polarised, for $P(e^-,e^+) = (-0.8, 0)$ the enhancement is reduced to 1.17 and for $P(e^-,e^+) = (0.8, 0)$ the cross section is reduced to 0.83 of the unpolarised cross section.

For WW fusion only one helicity combination, the $(e^-,e^+) = (-1,1)$ initial state leads to a signal. Running with $P(e^-,e^+) = (-0.8, 0.3)$, the effective fraction of LR increases from 25% to 58%, resulting in an effective enhancement of the cross section by a factor 2.34. Without positron polarisation, the factor is reduced to 1.8, normalized to the unpolarised cross section.

In the running scenario of Table 3, the integrated luminosity of $3\mathrm{ab}^{-1}$ is divided among the four polarisation combinations as (5%, 45%, 45%, 5%). Running of the collider with the two polarisation combinations that enhance the cross section corresponds to 90% of the total expected integrated luminosity. This leads to a sample with about 20% more Higgs bosons from both Higgsstrahlung and WW fusion than for a machine without beam polarisation delivering the same integrated luminosity. Similarly, for 550 GeV and possible 1 TeV running, the division of polarisation components is (10%, 40%, 40%, 10%). If the goal were to maximize the number of Higgs bosons, running purely in $P(e^-,e^+) = (-0.8, 0.3)$ is clearly favoured. However, the absolute number of Higgs bosons is not the only consideration. The Standard Model backgrounds to the Higgs measurements result from processes mediated through photon, Z boson and W boson exchanges. The polarisation will therefore affect the background composition, since the photon exchange is agnostic to the helicities, the Z couplings are modified as in single Z production, and the W boson pairs only contribute in the pure e^-e^+ LR state, resulting in a significant reduction of this background for the +− polarisation choice. Another important consideration is the resulting sensitivity to the EFT operators, which is discussed in Section 3.7.

The disfavoured helicity combinations provide further information for the determination of the background. These combinations provide also a significant sample of Higgs bosons, between 65% and 87% of the unpolarised cross section for the same integrated luminosity. Furthermore the $2 \times 5\%$ components of the integrated luminosity also provide data for a closure test, testing the compatibility of the measured polarisation and integrated luminosity under the assumption of the Standard Model couplings for the Higgs boson.

CLIC foresees (50%, 50%) sharing of the integrated luminosity at lower energies, therefore de facto producing the same number of Higgs boson for the total integrated luminosity as an unpolarised machine. At and above 1 TeV a (80%, 20%) sharing of $P(e^-,e^+) = (-0.8, 0)$ and $P(e^-,e^+) = (0.8, 0)$ is foreseen for the integrated luminosity, since the predominant production mode moves from Higgs-strahlung to WW fusion.

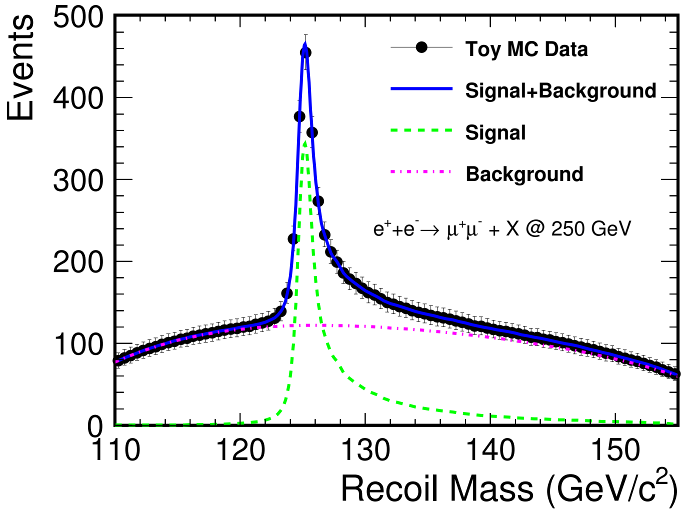

(a) Determination of the Higgs mass at the ILC [46].

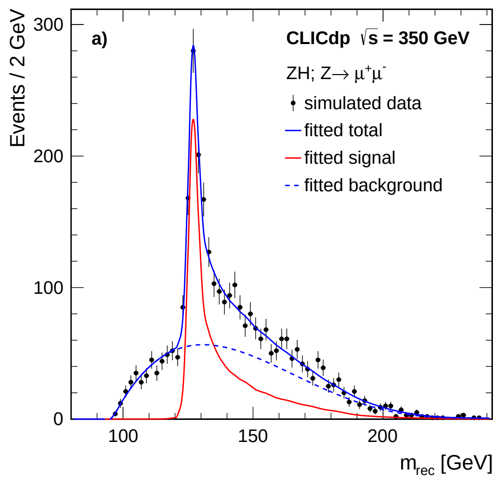

(b) Determination of the Higgs mass at CLIC [47].

3.1.2 Higgs mass and total cross section

The Higgs boson mass will be determined, as discussed in [36, 46], using the recoil mass technique at the lower energies. At these energies the combination of the high precision measurements of the leptonic decays of the Z boson is compensated by the about ten times higher statistics in the intrinsically less precise hadronic channel. At higher energies CLIC uses the WW fusion process in the decay channel with the highest statistics, i.e., $\mathrm{H} \to \mathrm{b\bar{b}}$ to reconstruct the Higgs boson mass directly.

Accelerator	LCF	CLIC	CLIC	CLIC	CLIC
$\sqrt{s}$	250 GeV	350 GeV	350 GeV	1.4 TeV	3 TeV
$\mathscr{L}$	2.7ab^{-1}	2.2ab^{-1}	4.3ab^{-1}	4ab^{-1}	5ab^{-1}
Δm_H	[MeV]	[MeV]	[MeV]	[MeV]	[MeV]
HZ Recoil	12	52	38		
$\nu_e\bar{\nu}_e\mathrm{H} \to \nu_e\bar{\nu}_e\mathrm{b\bar{b}}$				29	28

Table 4: Summary of the expected precision of the Higgs mass measurement at ILC and CLIC from [37] and scaled statistically from [48].

The determination of the Higgs boson mass is shown in Figure 3(a) for the ILC for the dominant helicity combination $P(\mathrm{e}^-,\mathrm{e}^+) = (-0.8, 0.3)$ and in Figure 3(b) for CLIC as discussed in [37, 46, 47]. The analysis has been performed with full simulation for an integrated luminosity of 250 fb^{-1} in each of the major polarisation combinations. The results, extrapolated to 2.7 ab^{-1}, the integrated luminosity for the LCF at 250 GeV of the major polarisation combinations listed in Table 3, are shown in Table 4, based on [48]. With CLIC running at 350 GeV, the expected precision is 52 MeV with 2.2 ab^{-1} and even 38 MeV with 4.3 ab^{-1}. This measurement can be further improved at 1.4 TeV and 3 TeV to about 28 MeV [37].

This precision is particularly important for accurate predictions of branching fractions to WW and ZZ, which depend strongly on the Higgs mass. The achievable precision at the ILC is sufficient to reduce the parametric error on the branching fractions to the per-mille level.

The inclusive cross section σ_{HZ} is determined in a joint fit with the Higgs boson mass. Its value in the two major polarisation combinations has been determined in full simulation with 250 fb^{-1}. Translating this estimation into a precision on the measurement with the full expected statistics, the expected error for one of the major polarisation combinations is 0.87 % as shown in Table 5, giving an error of 0.6 % for the combination of the two major polarisation combinations. This means that an error on the absolute coupling measurement g_{HZZ} of 0.3 % is reachable.

For CLIC, operating at an energy of 350 GeV, the expected precision on the cross section measurement has been discussed in [47]. Translating the numbers to the new CLIC running scenarios with increased integrated luminosity, a precision of 0.79 % or even 0.56 % can be reached as listed in Table 5, thus reaching the several permil level precision on the measurement of the absolute coupling value g_{HZZ}.

3.1.3 Branching ratio measurements

Collider	LCF	LCF	CLIC	CLIC	LCF	LCF	CLIC	CLIC
$\sqrt{s}$	250 GeV	350 GeV	350 GeV	350 GeV	500	1 TeV	1.4 TeV	3 TeV
$\mathscr{L}$	2.7ab^{-1}	0.135ab^{-1}	2.2ab^{-1}	4.3ab^{-1}	6.4ab^{-1}	6.4ab^{-1}	4ab^{-1}	5ab^{-1}
	[%]	[%]	[%]	[%]	[%]	[%]	[%]	
σ_{HZ}	0.62	2.5	0.79	0.56	0.8		2.0	4.3
$\sigma_{\mathrm{HZ}} \cdot \mathrm{BR}_{\mathrm{b\bar{b}}}$	0.41	2.1	0.41	0.29	0.5			
$\sigma_{\mathrm{HZ}} \cdot \mathrm{BR}_{\mathrm{c\bar{c}}}$	2.5	15	7	5	3.6			
$\sigma_{\mathrm{HZ}} \cdot \mathrm{BR}_{\mathrm{gg}}$	2.1	11.4	2.9	2.1	3.0			
$\sigma_{\mathrm{HZ}} \cdot \mathrm{BR}_{\tau\tau}$	0.98	5.5	3.0	2.1	1.2			
$\sigma_{\mathrm{HZ}} \cdot \mathrm{BR}_{\mathrm{ZZ}}$	5.5	34			6.9			
$\sigma_{\mathrm{HZ}} \cdot \mathrm{BR}_{\mathrm{WW}}$	1.4	7.6	2.4	1.7	1.6			
$\sigma_{\mathrm{HZ}} \cdot \mathrm{BR}_{\gamma\gamma}$	10				10			
$\sigma_{\mathrm{HZ}} \cdot \mathrm{BR}_{inv}$	0.19	1.2	0.3	0.2	0.42			
$\sigma_{\nu_e\bar{\nu}_e\mathrm{H}} \cdot \mathrm{BR}_{\mathrm{b\bar{b}}}$	2.5	2.5	0.9	0.6	0.30	0.30	0.2	0.2
$\sigma_{\nu_e\bar{\nu}_e\mathrm{H}} \cdot \mathrm{BR}_{\mathrm{c\bar{c}}}$		26	12	9	2.5	1.6	3.7	4.4
$\sigma_{\nu_e\bar{\nu}_e\mathrm{H}} \cdot \mathrm{BR}_{\mathrm{gg}}$		11	4.8	3.4	1.6	1.3	3.6	2.7
$\sigma_{\nu_e\bar{\nu}_e\mathrm{H}} \cdot \mathrm{BR}_{\tau\tau}$		22			2.8	1.5	2.6	2.8
$\sigma_{\nu_e\bar{\nu}_e\mathrm{H}} \cdot \mathrm{BR}_{\mu\mu}$					28	16	23	16
$\sigma_{\nu_e\bar{\nu}_e\mathrm{H}} \cdot \mathrm{BR}_{\mathrm{ZZ}}$		27			3.4	2.2	3.4	2.5
$\sigma_{\nu_e\bar{\nu}_e\mathrm{H}} \cdot \mathrm{BR}_{\mathrm{WW}}$		7.8			0.96	0.88	0.6	0.4
$\sigma_{\nu_e\bar{\nu}_e\mathrm{H}} \cdot \mathrm{BR}_{\gamma\gamma}$					7.6	4.6	9	6
$\sigma_{\mathrm{e^+e^-H}} \cdot \mathrm{BR}_{\mathrm{b\bar{b}}}$							1.1	1.5

Table 5: Expected measurement precision of $\sigma \cdot$ BR at different centre-of-mass energies, extrapolated from [48] for the running scenarios discussed in Section 2. For the LCF the precision is based on detailed ILC studies extrapolated to the running scenarios. The precision for the two CLIC running scenarios is based on [47] extrapolated for the increased luminosity in [37]. The precision on the total cross section is given for the subsample of events with hadronic Z boson decay. For CLIC not all of the exclusive final states have been studied. Both the CLIC and ILC are based on pairs of samples with opposite beam polarisation. See the text for details. For simplicity, in this table, the two results from each accelerator configuration are combined. In practice, the two results are used separately, to provide the maximum information to the global fits described in Sec. 3.7.

The measurement of Higgs couplings at the LC is projected to reach a precision at the per-mille level, making it highly sensitive to deviations from the Standard Model caused by new physics at the TeV scale. The cross section will be measured in all beam polarisation combinations, switching between dominantly left- and right-handed electrons and positrons. The asymmetry between these measurements in different polarisations offers an important additional input to the global understanding of Higgs couplings.

The Higgsstrahlung cross section decreases as a function of the energy. At higher energies, above 450 GeV, the WW fusion process is dominant [12] and the $\mathrm{t\bar{t}H}$ channel will open. The latter will be discussed in Sec. 3.5.2.

The expected precisions for the inclusive cross section measurements as well as the exclusive final states are listed in Table 5. The numbers are based on original work and extrapolated to the running scenarios [37, 47, 48]. For the LCF running scenarios, the measurement precisions listed for ILC in [48] have been scaled to the new running scenario presented in Sec. 2.

The ILC results are based on full simulation studies for the dominant polarisation mode $P(e^-,e^+) = (-0.8, 0.3)$. Several final states and their backgrounds have also been studied for $P(e^-,e^+) = (0.8, -0.3)$ achieving comparable precision within 20%. The lower cross sections for +– beams are approximately compensated by lower levels of background processes. Therefore similar precision is expected, independent of the final state for the Higgsstrahlung process for the major polarisation combinations. Dominated by the statistical error, the combined precision was obtained as scaling with the statistics increase from [48] and combining the two major polarisation combinations, de facto a three-fold increase in statistics for 250 GeV. According to the running scenarios in Section 2, at 350 GeV data will be taken mainly in $P(e^-,e^+) = (-0.8, 0.3)$ mode, therefore the expected precision is given for this polarisation combination as in [48]. For Higgsstrahlung, the combined error for the two major polarisation combinations at this energy is improved by about 14%. It is basically unchanged for WW fusion processes. For the highest energy of 550 GeV, the running the analyses performed at 500 GeV are listed in the table. For this energy and for 1 TeV running, the Higgsstrahlung processes are enhanced in 80% of the total integrated luminosity, and so this is the luminosity quoted in the table. For the WW fusion processes, the dominant -+ mode comprises 40% of the total integrated luminosity. The results for CLIC are quoted for unpolarised cross sections for all energies. The individual contributions of the two polarisation running modes can be calculated using the cross section scaling factors and the fraction of the integrated luminosity. The optimized running scenario for CLIC in Section 2 differs in energy by about 10% with respect to the energy at which the analyses were performed, therefore the analysis energy is quoted in Table 5.

The cross section times branching fraction for key decay modes such as the gauge bosons $H \to gg$ and $H \to WW$ will be measured with high precision. Due to the smallness of its branching fraction, the mode $H \to ZZ$ is less precisely measured.

Decays to fermions, $H \to \tau^-\tau^+$, $H \to b\bar{b}$, $H \to c\bar{c}$ will be measured at the (sub)percent level. The study of hadronic decays, particularly $H \to s\bar{s}$, presents a significant experimental challenge due to small branching fractions and large multi-jet backgrounds. Nonetheless, novel experimental techniques, including advanced K/π particle identification and dE/dx measurements, could enable the observation of this process.

Rare decays of the Higgs boson, such as $H \to \mu^-\mu^+$ and loop induced processes such as $H \to \gamma\gamma$ and $H \to Z\gamma$, will be explored as well, though less precisely than at the HL-LHC as their small branching fractions limit the achievable precision. The $H\gamma Z$ coupling can also be probed via the $e^+e^- \to \gamma H$ process, whose cross section is also maximal around 250 GeV. Upper limits at 95% on the production cross sections in the different polarisation scenarios can be set at 1.8 fb for the same beam polarisation [49]. The polarisation-dependence of this limit and the implications for limits on SMEFT parameters are discussed in [50]. In Table 5 only measurements where the expected relative precision is better than 25% are listed.

To extract the total width of the Higgs boson (Γ_H), the inclusive cross section measurement, electroweak decays to WW and ZZ and the decay to $b\bar{b}$ will play a pivotal role in constraining the total Higgs decay width. Using the inclusive cross section (at tree-level proportional to g^2_{HZZ}) and the exclusive Higgs-strahlung final state $\sigma_{HZ} \cdot BR_{ZZ}$ (proportional to g^4_{HZZ}/Γ_H) allows to extract the total width with a precision dominated by the exclusive decay channel which suffers from a low branching fraction. At 250 GeV this will result in a precision of 5-6%.

A more precise estimate can be achieved by putting together four measurements: the Higgsstrahlung exclusive final states WW (proportional to $g^2_{HZZ}g^2_{HWW}/\Gamma_H$), $b\bar{b}$ (proportional to $g^2_{HZZ}g^2_{Hb\bar{b}}/\Gamma_H$), the inclusive cross section and the WW fusion channel to $b\bar{b}$. The fusion channel divided by the product of the ratios of Higg-strahlung channel to inclusive cross section is the total width. With the precisions given in Table 5 the measurement precision is dominated by the W–fusion channel, improving the precision significantly.

The results summarized in Table 5 are based on the standard flavour tagging algorithms. The performance of the LCFIPlus package has been improved significantly using modern machine learning techniques as described Section 3.2. A task for the future is to evaluate the impact of new working points which promise improved rejection for the same efficiency or improved tagging efficiency for the same background rejection. Additionally the introduction of particle identification may open the measurement of the $H \to s\bar{s}$ final state, albeit with large uncertainties.

3.1.4 CP properties

The search for CP violation is an important research direction of future experiments in particle physics, as CP violation is required for baryogenesis and cannot be sufficiently explained with present knowledge. CP violation can be tested in interactions of the Higgs boson with either fermions or bosons, see e.g. [51] for a recent overview. At e^+e^- linear colliders, Higgs CP properties can be tested in $H \to \tau\tau$ decays [52], in ZZ fusion production [53] as well as in $t\bar{t}H$ associated production [54].

The amount of CP violation is characterized by the quantity,

$$f_{CP}^{HX} \equiv \frac{\Gamma_{H\to X}^{CP\ odd}}{\Gamma_{H\to X}^{CP\ odd} + \Gamma_{H\to X}^{CP\ even}}, \tag{1}$$

Polarisation of the colliding beams may give additional sensitivity in these measurements. Using the major polarisation mode $P(e^-, e^+) = (0.8, -0.3)$ the background cross section is decreased while the signal cross section is increased. However negative interference compensates partially this improvement. In total up to 10% improvement in the expected constraints on the f_{CP}^{HZZ} parameter [55] are expected.

Table 6: List of expected precision (at 68% C.L.) of *CP*-sensitive measurements of the parameters f_{CP}^{HX} defined in Eq. (1). The $e^+e^- \to ZH$ projections are performed with $Z \to \ell\ell$ in Appendix but scaled to a ten times larger luminosity to account for $Z \to q\bar{q}$. The table is adapted from Ref. [55]

Collider	e^+e^-	e^+e^-	e^+e^-	e^+e^-	target
E (GeV)	250	350	500	1,000	(theory)
$\mathscr{L}$ [ab^{-1}]	2.5	3.5	5.0	10.0	
HZZ/WW	$3.9 \cdot 10^{-5}$	$2.9 \cdot 10^{-5}$	$1.3 \cdot 10^{-5}$	$3.0 \cdot 10^{-6}$	$< 10^{-5}$
$Ht\bar{t}$	–	–	0.29	0.08	$< 10^{-2}$
$H\tau\tau$	0.01	0.01	0.02	0.06	$< 10^{-2}$

3.1.5 Interpretation

Once deviations of the Higgs boson couplings from the SM predictions are discovered in future experiments, we can perform "fingerprinting" of the Higgs sector and can extract the mass scale of new particles such as a second Higgs boson mass. Such analyses can generally be done by using the SMEFT approach because non-zero deviations come from the coefficients of higher-order operators, and the new mass scale typically corresponds to the cutoff parameter Λ which appears in the denominator of such an operator.

Although the SMEFT approach captures the general patterns of the deviation, we here discuss some concrete examples of renormalizable models giving rise to the coupling deviations, especially focusing on the models with extended Higgs sectors.

- In models with iso-singlet scalars, the coupling deviation only comes from the Higgs boson mixing α. In this case, all the Higgs boson couplings are universally suppressed by the factor of $\cos\alpha$, i.e., $\kappa_V = \kappa_f = \cos\alpha$.
- In the 2 Higgs doublet models (2HDMs), the Yukawa couplings ($Hf\bar{f}$) and the gauge couplings HVV ($V = W^\pm, Z$) can differently be modified from the SM predictions. The pattern of the deviations of $Hf\bar{f}$ couplings depends on the scenarios of the 2HDM. In the most general case, i.e., without imposing any additional symmetries, Yukawa couplings for H depend on an arbitrary 3×3 matrix in flavour space. Therefore, any values of $Hf\bar{f}'$ couplings (even for flavour-violating cases $f \neq f'$) can be taken in principle. This general scenario, however, introduces dangerous flavour-changing neutral currents (FCNCs) at

tree level, so that some assumptions to avoid such FCNCs are often imposed on the 2HDM. For instance, the Yukawa-alignment scenario has been proposed in [56], in which two Yukawa matrices are assumed to be proportional with each other, and then the flavour-violating Yukawa couplings for neutral Higgs bosons are forbidden. In this case, κ_f take flavour universal values, and are expressed as $\kappa_f = \kappa_V + \zeta_f\sqrt{1-\kappa_V^2}$ with ζ_f being constants (generally complex and $\zeta_u \neq \zeta_d \neq \zeta_e$). The 2HDMs with a softly-broken Z_2 symmetry correspond to the special case of the Yukawa-alignment scenario, where three ζ_f parameters are determined either $\cot\beta$ or $-\tan\beta$ depending on the four types of the Yukawa interactions (Type-I, Type-II, Type-X and Type-Y) [57–59].

- In models with higher isospin representation fields such as $SU(2)_L$ triplet Higgs field, we expect the situation that cannot be realized in the previous two examples. Namely, the HWW and HZZ couplings can differently be modified from the SM predictions, and also κ_W and κ_Z can exceed unity. The size of deviations in HVV couplings are often constrained by the electroweak ρ parameter because the deviation depends on vacuum expectation values of such exotic Higgs fields. However, one can consider models with $\rho = 1$ at tree level by imposing the custodial symmetry in the Higgs sector. The simplest example has been known as the Georgi-Machacek model [60, 61], where a real and a complex triplet Higgs fields are added to the SM.

3.2 Two and four fermion production – Z-pole and above

The programme described serves several purposes. Di-fermion production at the Z-pole allows for the measurement of electroweak precision observables to at least an order of magnitude better than this was possible at LEP/SLC (and than this is possible at the LHC). These updated electroweak precision observables are the backbone of the measurements at higher energies. Di-fermion production might also see the onset of new physics and the interpretation of the data must not be compromised by an insufficient knowledge of electroweak precision observables. W pair production leads to four-fermion final states. These are thus at the heart of the determination of the W mass and of flavour physics by the determination of CKM-Matrix elements. Multi-boson production in general, including triple and quartic gauge couplings, will be discussed in Sec. 3.4.1.

3.2.1 Z-pole

A linear e^+e^- collider designed for Higgs boson production can be run at the Z resonance. The program for this mode of operation, and the expected precision measurements of SM parameters, have been described in some detail in the Snowmass report [14] Section 9.1. That discussion envisioned a program of about 2 years to collect an event sample of 5×10^9 Z boson decays. Typical precisions on SM observables are at the 10^{-4} level. Also, since the most important electroweak observables at the Z are chiral and a linear collider will provide highly polarised beams, these observables provide highly effective tests of the SM electroweak theory. Precision theory for the Z pole observables is presented in the review [62] and in [63–65].

The strongest test of the SM available from precision electroweak interactions is the closure test

$$0 = \sin^2 2\theta_{\text{eff}} - \frac{4\pi\alpha(m_Z)}{\sqrt{2}G_F m_Z^2} \tag{2}$$

up to calculable SM electroweak radiative corrections. Using results from [14] Section 9.1, cited already above, and assuming that lattice QCD will give a precise accounting of the hadronic corrections to α, the dominant uncertainties will come from $\Delta sin^2\theta_{\text{eff}} = 2.5\times10^{-6}$ and $\Delta m_Z = 0.2$ MeV, giving an absolute uncertainty on the right-hand side of 0.9×10^{-6}. This is quite comparable with the strongest precision electroweak tests available in a TeraZ program with unpolarised beams at a circular collider. The comparison between linear and circular colliders with larger event samples is reminiscent of the comparison of SLC and LEP results for $\sin^2\theta_w$ in the 1990's. The measurement of $\sin^2\theta_w$ at a linear collider using polarised beams makes use of the polarisation asymmetry of the hadronic and leptonic[1] total cross sections, while the measurement at a circular collider requires selection of specific leptonic processes and therefore has to tacitly assume lepton universality. At the LCF, the measurement needs to control well the uncertainty from beam polarisation, this

[1] Excluding Bhabha events

will be much improved from the SLC measurement with new strategies and the use of both electron and positron polarisation [33, 66].

The higher event rates of circular colliders have the potential to reduce the advantage of linear colliders for asymmetry measurements. Polarised beams give direct access to the lepton and quark asymmetries. Naively, this compensates for a factor $(|P_{\mathrm{eff.}}|/\mathscr{A}_e)^2 \approx 36$ with $\mathscr{A}_e^2$ being the electron asymmetry and $|P_{\mathrm{eff.}}|$ the effective beam polarisation assuming $P(\pm 0.8, \mp 0.3)$. Given the large number of Z bosons it is also however reasonable to suppose that the final uncertainties may be dominated by systematic uncertainties. In this respect the knowledge of the centre-of-mass energy and the polarisation are essential elements with both being measurable in situ to high precision with the total systematic uncertainty projected to be subdominant for the flagship A_{LR} measurement with 5×10^9 Z boson decays. An important limitation for the measurement of quark asymmetries will likely be systematic uncertainties in flavour tagging. This uncertainty source is independent of the collider type. We also note that the smaller beam spot was a notable advantage for SLC over LEP. One may expect that a similar advantage, though considerably reduced, would still hold. It is important to note that the linear collider measurements do not require an exceptionally high-rate environment that would compromise the detector capabilities both at the Z and for the precision Higgs boson program at higher energy.

In fact, we expect to do even better in the precision electroweak closure test than the estimate given above, since in the intervening time there have been significant updates to the linear collider Z-pole program. These are:

1. Much higher luminosities at the Z-pole than originally envisaged for ILC [67] can be realized by accommodating higher beamstrahlung with an ILC-like accelerator. Studies reported in Sec. 4.5.1 indicate that an eight-fold increase in luminosity to 1.7×10^{34} cm^{-2}s^{-1} is potentially within reach, allowing polarised data-sets of 0.8 ab^{-1} to be collected in a reasonable time frame.

2. Results from polarised Z scans that include the statistical effects of the luminosity spectrum indicate statistical precisions with such an 800 fb^{-1} data-set with (80%/30%) beam polarisations of 14 keV, 18 keV, and 1.0×10^{-6} on m_Z, Γ_Z and $\sin^2\theta_{\mathrm{eff}}$, respectively, using simply the hadronic and leptonic polarisation-averaged lineshapes and left-right asymmetries. Higher luminosities still can be envisaged particularly if the accelerator can provide even higher bunch charges.

3. The eventual precision on observables such as A_b, R_ℓ, and σ^0_{had} depends partly on how well one can measure hadronic events, and do b-tagging at very forward angles. Current estimates for the Z-pole are based on full simulation studies at 250 GeV as presented in Sec. 3.2.3. A key part will be being able to instrument the tracking to low angles where the linear collider design and the associated backgrounds may permit tracking instrumentation down to the 40 mrad regime.

4. Measurements rely on precise knowledge of the initial-state conditions. One recent development is a new approach to precision luminosity where the process $e^+e^- \to \gamma\gamma$ is also considered [68]. The measurement techniques for precision centre-of-mass energy measurement using leptonic final states discussed in [69] have been further refined including a method for measuring statistically the energy of each colliding beam [70].

The potential for highly longitudinally polarised electron and positron beams, and the ability to instrument well the detector to very low angles are significant advantages for the linear collider approach. Polarisation adds unique observables, improves statistical precision, and allows for control of backgrounds. Forward acceptance and the freedom to design appropriate detectors may be determinative in setting the scale for realistic systematic uncertainties both absolute and relative that play a key role in measuring the Z lineshape. Figure 4 illustrates that polarised beams in the −+ and +− configurations result in a significant increase in the averaged cross section over a facility with no polarisation, while providing a simple way of simultaneously measuring A_{LR} which is proportional to $(\sigma_{-+} - \sigma_{+-})/(\sigma_{-+} + \sigma_{+-})$. By taking some data with all four polarisation sign combinations and so measuring also σ_{--} and σ_{++}, the polarisation magnitudes can be reliably reconstructed [33].

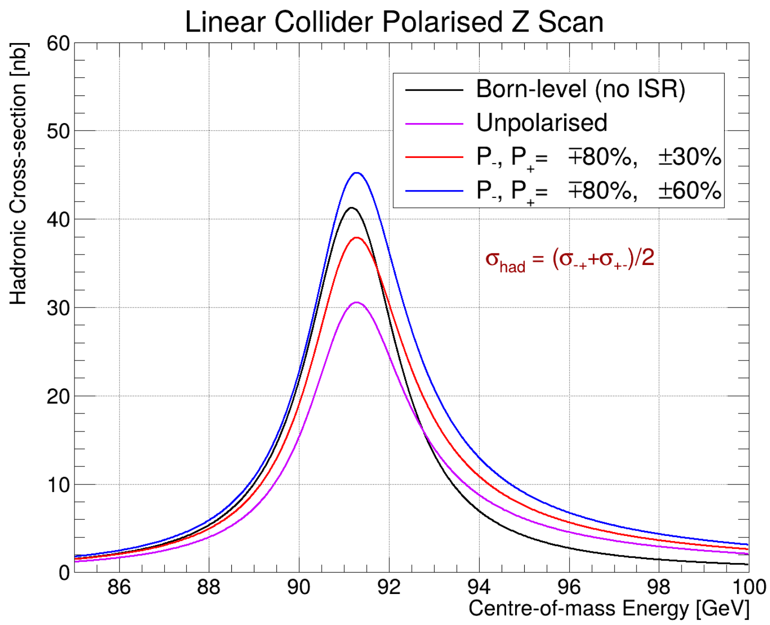

Figure 4: Z lineshape with polarised beams. The blue, red, and violet curves are the measurable averaged hadronic cross section after including ISR for various polarisation values of the electron and positron beams. The black curve is with unpolarised beams and no QED radiative corrections.

For ultimate luminosity at the Z-pole and WW threshold, while retaining the polarisation advantages inherent to a LC, luminosities in the 10^{36} cm^{-2}s^{-1} regime may be realizable in the future using energy and particle recovery technologies such as those discussed in Sec. 4.5.3.

3.2.2 W mass measurements

Any e^+e^- collider designed to explore the Higgs boson with high precision will collect hundreds of millions of W bosons and has the opportunity to make significant improvements to the measurement of the W mass. Prospects for m_W measurement with ILC are documented in some detail in [32] and references therein, based partly on earlier studies documented in [71]. The measurements are likely to be primarily systematics limited. As was done at LEP, there are four well established techniques[2] for measuring the W mass that can be utilized at a future linear collider operating at centre-of-mass energies above the ZH threshold. This would be synergistic with the envisaged overall physics programme. The techniques include:

1. kinematically-constrained reconstruction of semi-leptonic WW events (denoted K)
2. direct measurement of the hadronic mass in single-W and semi-leptonic events (H)
3. measurement of the lepton energy spectra in particular the kinematic endpoints in both fully-leptonic (FL) and semi-leptonic WW events
4. measurement of the pseudo-masses in fully-leptonic WW events with electrons and muons (FL)

The estimated uncertainty on m_W from these techniques is best for data taking at $\sqrt{s} = 250$ GeV given the higher cross section and in general somewhat smaller systematic uncertainties. Quantitatively we estimate total uncertainties of 2.2 MeV (K), 2.6 MeV (H) and 5.0 MeV (FL) for the subsets of these measurements that are most easily separable, where statistical uncertainties are 0.6 MeV, 0.6 MeV and 4.8 MeV respectively for 3.0 ab^{-1} at $\sqrt{s} = 250$ GeV. Combined, the overall uncertainty on m_W is estimated to be 1.8 MeV taking

[2] It is expected that kinematically-constrained reconstruction of fully-hadronic WW events will not be useful for a precision m_W measurement given current and projected uncertainties from colour reconnection and Bose-Einstein effects. Future e^+e^- colliders can help to model better these phenomena [72].

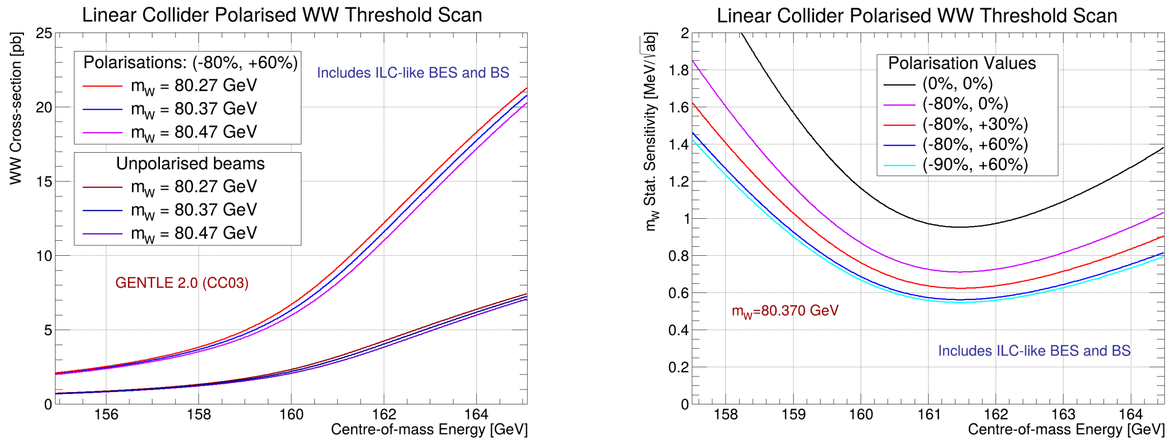

Figure 5: Left. Illustration of the centre-of-mass energy dependence of the WW cross section on m_W and the level of polarisation. Right. The intrinsic sensitivity, K, of polarised cross section measurements to m_W near threshold assuming an efficiency-purity product of unity.

into account (positive) correlations from effects such as beam energy, luminosity spectrum, and hadronisation modelling. As the dominant measurements are foreseen to be systematics limited, the additional data taken at higher centre-of-mass energies will give further cross-checks with two detectors, but is not expected to add significantly in overall precision.

A similar overall precision of 2.0 MeV could also be reached with a dedicated 0.5 ab^{-1} polarised scan[3] near the WW threshold where all WW final states contribute to the cross section measurement. Together with the baseline program discussed above the estimated combined uncertainty on m_W would be 1.3 MeV. The availability of longitudinal polarisation significantly increases the cross section near threshold when using left-handed electrons and right-handed positrons given that the t-channel ν_e exchange dominates as illustrated in Figure 5, and it is this data-set that dominates the sensitivity. This is a significant advantage over circular colliders. It is not just an increase in signal rate and consequent m_W sensitivity, but a capability of switching helicities and turning off WW production to assist in measuring directly the background at the same centre-of-mass energy. The right hand plot shows the centre-of-mass energy dependence of the basic sensitivity factor of the polarised cross section to m_W, defined as K below, including the effects of beam energy spread (BES) and beamstrahlung (BS) with beam parameters consistent with the ILC-250 baseline. The relationship [73] is

$$\Delta M_{\text{stat}} = \left|\frac{d\sigma}{dM}\right|^{-1} \Delta\sigma = \left|\frac{d\sigma}{dM}\right|^{-1} \sqrt{\frac{\sigma}{\varepsilon p \mathscr{L}}} = \frac{K}{\sqrt{Q\mathscr{L}}} \text{ with } Q \equiv \varepsilon p\,.$$

Clearly high polarisations can improve the sensitivity dramatically over the unpolarised case. Values for the quality factor, Q, vary by WW final state and polarisation assumption. With the current scan assumptions the systematic uncertainty of 1.7 MeV is dominated by the statistical uncertainty on the background measurement while the overall statistical uncertainty of the polarised data-set is 1.1 MeV equivalent to an effective $K/\sqrt{Q} = 0.77$. Further improvements in the background uncertainty can be envisaged by reducing hadronic event backgrounds for example by rejecting/de-weighting events with one or more b-tagged jets or those with hadronic W candidates consisting of two c-tagged jets. There is also potential for improving the statistical uncertainty by devoting more time to the most favorable helicity combination, namely the one illustrated in Fig. 5.

In summary, there are excellent prospects for a major advance in the m_W precision by an order of magnitude from today's PDG uncertainty of 13.3 MeV with both the data collected above the production threshold for Higgs bosons and from a dedicated run of at least 0.5 ab^{-1} with a polarised WW threshold scan. The projected precisions in the two regimes are similar but running at WW threshold precludes many other measurements of prime interest. The current accelerator designs retain accelerator compatibility with running at WW threshold with polarised beams, recognizing the complementary nature of such a measurement, but do not include

[3] For illustration these numbers use (90%, 60%) polarisation and a 6-point scan with all four helicity combinations.

such a dedicated run in the running scenarios. W W threshold running is retained as an option. Further improvements in the instantaneous luminosity near WW threshold as discussed in section 4.5.1 and potentially different future physics perspectives can lead to such running becoming part of the actual run plan whenever it becomes the most interesting thing to do.

3.2.3 Quark pair production

The physics potential of two fermion processes above the Z-pole is illustrated at the example of recent studies of quark pair production. The publications [74, 75] describe comprehensive experimental studies on viability and prospects for the measurement of electroweak observables in $e^+e^- \to b\bar{b}$ and $e^+e^- \to c\bar{c}$ processes at the International Linear Collider (ILC) operating at $\sqrt{s}$ = 250 GeV and 500 GeV of centre-of-mass energy. The studies are based on a detailed simulation of the International Large Detector (ILD) concept. The ILD design is based on the particle flow approach and excellent vertexing and tracking capabilities, including charged hadron identification thanks to the dE/dx. Polarised beams allow for inspecting in detail the four independent chirality combinations of the electroweak couplings to electrons and other fermions with an almost background-free analysis. A classical key observable is the forward-backward asymmetry A_{FB}. Figure 6(a) shows the expected statistical precision at 250 GeV and 500 GeV for integrated luminosities of 2ab^{-1} and 4ab^{-1}, respectively. It illustrates the successive improvements obtained by particle identification and an updated flavour tagging that introduced in Sec. 2.4. The results can be interpreted in the frame of so-called Grand Higgs Unification Models. In these models that include *compactified* warped extra dimensions the Higgs appears as a fluctuation mode of the Aharonov-Bohm phase θ_H and can be associated as the fifth component of the know Standard Model vector potentials. For an introduction see [76] and references therein. The model predicts massive Kaluza-Klein excitation of neutral vector bosons that influence observables like A_{FB}. A statistical analysis carried out in [75] demonstrates the discovery potential of a linear collider. The result is shown in Fig. 6(b). Different running scenarios of ILC are compared: ILC (no pol.) (hypothetical case with no beam polarisation and 2000 fb^{-1} of integrated luminosity), ILC250 (2000 fb^{-1}), ILC500 (4000 fb^{-1}), and ILC1000* (8000 fb^{-1}, not using full simulation studies but extrapolations of uncertainties from ILC500). Three different assumptions for the Z-fermion couplings uncertainties are considered [32]: C for current knowledge; R for expected knowledge after the full ILC250 program and the study of Z-fermion couplings from radiative return events, and Z for expected knowledge after a full ILC Z-pole program.

Neutral boson masses $M_{Z'}$ of up to 19.6 GeV have been tested. The results show that already at 250 GeV different GHU predictions could be distinguished from the Standard Model prediction. The separation power is amplified at higher energies as expected. At 250 GeV also polarisation increases the separation power.

3.2.4 Flavour physics with W bosons: CKM matrix elements

A Linear Collider already at its energy stages below 1 TeV typically produces a few 10^8 W bosons in a clean e^+e^- environment. The hadronic decays of these real W bosons offer an opportunity to measure CKM matrix elements in a complementary approach to B factories. In particular, there is at the moment an intriguing discrepancy at the 3σ level in the value of $|V_{cb}|$ from B decays, being at $(42.19 \pm 0.78) \times 10^{-3}$ from inclusive B decays and at $(39.10 \pm 0.50) \times 10^{-3}$ from exclusive B, B_s and Λ_b decays. While this discrepancy is difficult to solve in B decays due to inherent hadronic uncertainties, these are absent in decays of real W bosons. With the large QCD background, the LHC prospects for this measurement are only at the level of 10%.

Moreover, $|V_{cb}|$ is not the only point of interest, rather all six CKM matrix elements that do not involve the top quark can be determined via hadronic W decays in a manner complementary to B and D meson decays at corresponding factories. Table 7 summarises the branching fractions, expected number of W decays for 10^8 Ws and the following ideal determination uncertainty for these six elements.

A first study [81] considering 2-fermion processes as background, a parametrised flavour tagging inspired by the IDEA detector concept for FCC-ee and potentially limiting systematic effects showed that for $|V_{cb}|$ a control of the flavour tagging efficiency at the level of about 0.1 % would be sufficient, while $|V_{cs}|$ the efficiency would need to be controlled to better than 0.01 % in order not to limit the achievable precision. Based on this study, the report of the ECFA Higgs/Electroweak/Top Factory study [41] concluded that if the flavour tagging efficiency could be controlled to a precision of 0.1%, $|V_{cb}|$ could reach a precision of 0.15 %, and $|V_{cs}|$ of 0.05 %, to be compared to the current precisions of 3.4 % and 0.6 %, respectively.

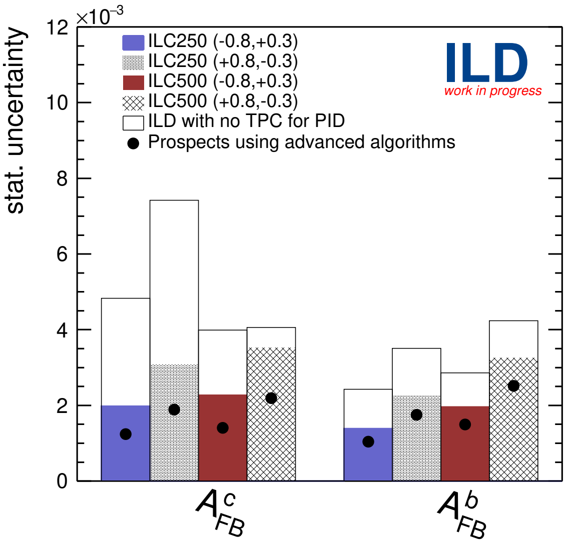

(a) Statistical precisions on A^b_{FB} and A^c_{FB} for integrated luminosities of 2ab^{-1} and 4ab^{-1}, respectively [41]. The figure also shows the improvements by particle identification and updated flavour tag

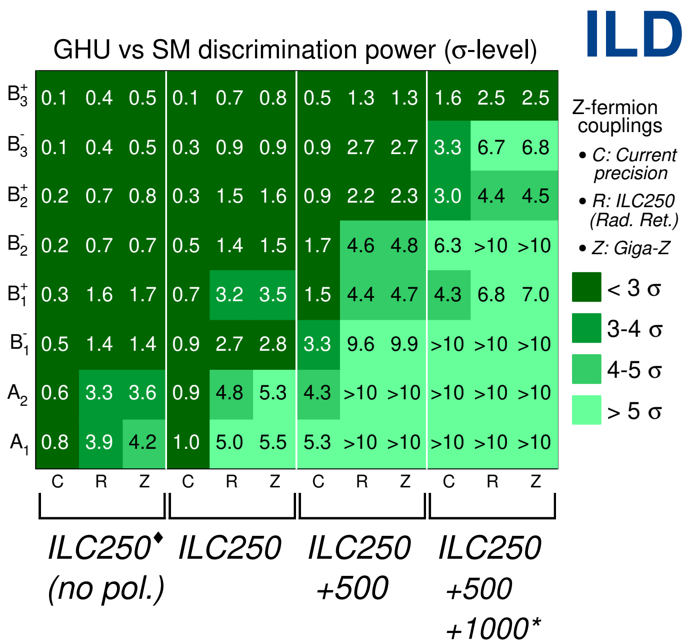

(b) Statistical discrimination power between the GHU models [77–79] and the SM. For more details see text. Figure taken from [75].

W^-	$\bar{u}d$	$\bar{u}s$	$\bar{u}b$	$\bar{c}d$	$\bar{c}s$	$\bar{c}b$
BR	31.8%	1.7%	4.5×10^{-6}	1.7%	31.7%	5.9×10^{-4}
N_{ev}	32×10^6	1.7×10^6	450	1.7×10^6	32×10^6	59×10^3
$\delta^{stat}_{V_{ij}}$	0.018%	0.077%	4.7%	0.077%	0.018%	0.41%

Table 7: W decay branching fractions in the Standard Model, corresponding occurrence for 10^8 W^- bosons and CKM matrix element determination precision assuming an efficiency-purity product of unity; adapted from [80].

A more comprehensive set of background processes and systematic uncertainties has been considered in a full-simulation study based on the ILD version for CEPC [82]. This study showed that it is not sufficient to consider only 2-fermion backgrounds, since also 4-fermion processes contribute significantly to the final selection. It also showed that systematic uncertainties should improve by about a factor 4 over LEP systematics in order not to limit the final result and that in terms of statistical precision, 5 ab^{-1} of unpolarised data give about the same result as 2 ab^{-1} of polarised data.

ILD and CLD are working towards a full analysis of all WW and single-W channels. Detailed detector simulation studies are of particular importance given the significant impact of the flavour tagging, which will be discussed in the following section. As the CEPC study showed, the statistical precision at a linear collider is expected to be comparable to those at circular collider due to the strong enhancement of W production processes from beam polarisation. The much smaller beam spot at a linear collider gives an additional advantage in flavour tagging. Z pole operation will be an important ingredient to minimising the systematic uncertainties related to flavour tagging. The final results of the ongoing studies are needed for a reliable quantitative assessment of the potential of CKM matrix element determinations from hadronic W decays at future e^+e^- colliders.

3.3 Higgs at high(est) energies

The higher energy stages are of crucial importance to a comprehensive Higgs program: they add many more produced Higgs bosons and thereby typically improve precisions on the Higgs couplings to gauge bosons and fermions by a factor two or more, but – even more importantly – the do so by opening different production modes of the Higgs boson, allowing a complementary scrutiny of any observed deviation. The impact on the Higgs couplings to fermion and gauge bosons is discussed in Secs. 3.1 and 3.7.

Here, we will focus on illuminating the Higgs potential, the origin of electroweak symmetry breaking and whether it provides the strong-first order phase transition required to explain the observed baryon-antibaryon asymmetry in the universe. We will also comment on the interplay with gravitational wave experiments and primordial black hole searches.

3.3.1 The Higgs self-coupling

Many of the open questions of particle physics are related to the Higgs sector and in particular to the Higgs potential, which for this reason is often referred to as the "holy grail" of particle physics. The Standard Model (SM) postulates a minimal form of the Higgs potential, with a single Higgs boson that is an elementary particle. However, Beyond-the-Standard-Model (BSM) theories often feature extended scalar sectors, resulting in a complicated form of the Higgs potential in the multi-dimensional field space of all contributing scalar fields. As a consequence, the Higgs potential can have a rich structure of minima, as illustrated for example in Figure 7. The Higgs potential triggers electroweak symmetry breaking (EWSB), and for this reason, obtaining information about it is crucial to understand how the electroweak phase transition (EWPT) took place in the early Universe. In turn, this is especially important when investigating the scenario of electroweak baryogenesis (EWBG) [83, 84] as a possible explanation for the observed baryon-antibaryon asymmetry in the Universe (BAU).

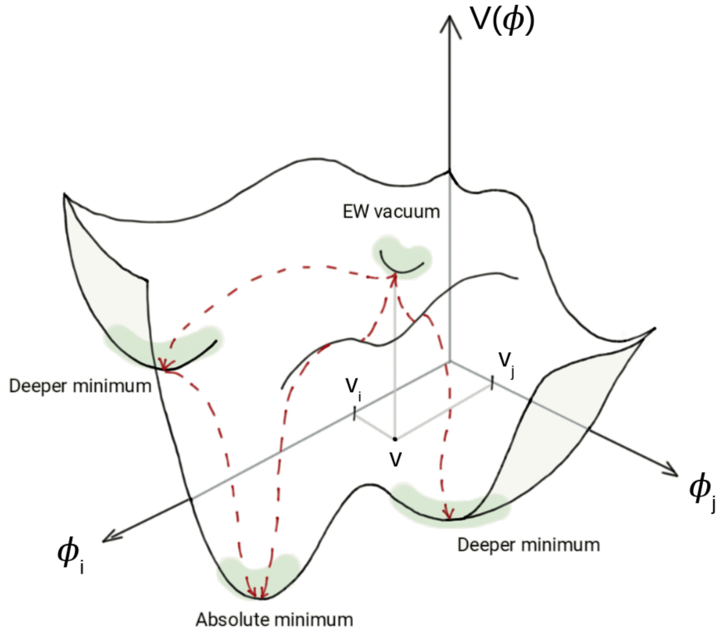

Figure 7: Simplified illustration of the form of the Higgs potential V in a two-dimensional field space (fields ϕ_i and ϕ_j) for a theory with an extended Higgs sector [85]. The electroweak vacuum and possible tunnelling directions into deeper minima are indicated.

While the Higgs discovery in 2012 has confirmed the existence of the Higgs potential, its actual form realised in Nature as well as its physical origin remain until now largely unknown. In particular, the Higgs potential receives contributions not only from the detected Higgs boson[4] H, but also from all additional BSM scalars that may be present but have escaped detection so far. While the location of the electroweak minimum and curvature of the Higgs potential around this minimum are known, the trilinear and quartic Higgs self-couplings $\lambda_{\rm HHH}$ and $\lambda_{\rm HHHH}$ — i.e. the coefficients of the $\rm H^3$ and $\rm H^4$ terms in the Higgs potential, respectively — are

[4] We continue to denote the 125-GeV Higgs boson here with H, independently of its mass ordering with other neutral, CP-even scalars in extended Higgs sectors.

only loosely constrained so far. For models with extended scalar sectors the Higgs potential comprises further terms involving the additional scalar fields that determine the shape of the Higgs potential in the different directions of field space (see Figure 7). In the present section we focus on the self-couplings of the detected Higgs boson, while Higgs self-couplings involving additional Higgs fields are discussed in Section 3.6.5.

Existing constraints on λ_{HHH} from the LHC have mainly been obtained from the searches for the Higgs pair production process. Here gluon fusion is the dominant channel, and the dependence on λ_{HHH} appears at leading order. A large destructive interference between the SM-type diagrams with and without λ_{HHH} implies that the total cross section for di-Higgs production changes very substantially – by up to two orders of magnitude – if λ_{HHH} is varied around the SM value. The current upper bound on the di-Higgs production cross section from ATLAS and CMS translates into an upper limit on λ_{HHH} that is about 7 times larger than the SM value (while a lower limit can also be set around –1), assuming SM-like values for all other Higgs couplings besides λ_{HHH} [86, 87] (this assumption can be relaxed by incorporating data from single Higgs production [88]). The current projections for the HL-LHC – using the combined integrated luminosity that is expected to be collected by both ATLAS and CMS – yield a 68% C.L. of [0.74, 1.29] for λ_{HHH} if the SM value is realised in nature ($\kappa_\lambda = 1$) [89].

At an e^+e^- linear collider with a CM energy of 500 GeV or higher, di-Higgs production can be directly measured in two processes, $e^+e^- \to \mathrm{ZHH}$ and the W fusion process $e^+e^- \to \nu\bar{\nu}\mathrm{HH}$, in a model-independent way. This is a qualitatively new feature of high-energy running of a linear collider, distinguishing its physics capabilities from those of Higgs factories at lower energies. The direct measurement of the di-Higgs production processes allows the determination of the self-coupling λ_{HHH} from its lowest-order contribution to these processes in a way that is independent of other possible BSM effects on Higgs couplings [90, 91] that affect the indirect determination of λ_{HHH} from its loop contributions to other observables at lower energies. Remarkably, the two reactions $e^+e^- \to \mathrm{ZHH}$ and $e^+e^- \to \nu\bar{\nu}\mathrm{HH}$ have opposite dependence on λ_{HHH}, so that an enhancement in ZHH can be checked by observation of a deficit in the WW fusion reaction.

With recent improvements in the full-simulation studies of HH pair production, the projected accuracy at a 550 GeV linear e^+e^- collider is now 15 % for $\kappa_\lambda = 1$ and an integrated luminosity of 4.4 ab^{-1} [41]. This value is an update (superseding the values of 20% from Ref. [92] and 27% from Ref. [93]), reflecting analysis improvements including the combination of results from the ZHH and $\nu\bar{\nu}\mathrm{HH}$ production channels as well as significant progress made on flavour tagging and jet reconstruction [41]; see also Sec. 2.4. The LCF, thanks to operating at 10 Hz, aims to collect 8 ab^{-1}, and would thus reach even a precision of 11 % for $\kappa_\lambda = 1$. The projected accuracy for $\kappa_\lambda = 1$ for CLIC operating at 3 TeV was previously obtained as [–8%, +11%] [94].

If the value of λ_{HHH} realised in nature corresponds to $\kappa_\lambda = 2$ (which would be favoured in scenarios giving rise to a strong first-order electroweak phase transition, as discussed below), the projected accuracy on λ_{HHH} at the HL-LHC stays at the level of 25%. Owing to the different interference pattern in the ZHH channel, the accuracy at the LCF at 550 GeV improves to around $\kappa_\lambda = 2 \pm 0.1$ (i.e. 5%), c.f. Fig. 8(b). It is expected that future projections for the HL-LHC will be improved over the present case, but this is also true in case of the e^+e^- projections, which by far are not yet fully exploiting the capabilities of the proposed detectors and modern data analysis techniques. Fig. 8(a) compares the current projections for the HL-LHC [89] and for an LCF, as a function of κ_λ. The improvements in accuracy from additional e^+e^- data at 1 TeV are also displayed in blue in Fig. 8(a).

While the existing bounds on λ_{HHH} are rather weak, they nevertheless already probe so far untested parameter regions of physics beyond the SM [95, 96] because λ_{HHH} can receive large mixing effects and/or very large loop corrections from the additional scalars (which we will generically denote Φ in the following) of models with extended Higgs sectors. These large radiative contributions to λ_{HHH} — often referred to as mass-splitting or non-decoupling effects — were first pointed out in Refs. [97, 98], but have now been shown to occur in various BSM models with extra scalars (see Refs. [96, 99–123] for studies in models with additional singlets, doublets, triplets, etc. or combinations thereof). Moreover, the physical nature of these effects was confirmed by explicit two-loop calculations [112, 113]. These corrections are driven by couplings of the generic form $g_{\mathrm{HH}\Phi\Phi} \propto (m_\Phi^2 - \mathscr{M}^2)/v^2$, where m_Φ denotes the physical mass of a BSM scalar Φ, $\mathscr{M}$ is the mass scale that controls the decoupling of the BSM scalar(s), and v is the EW vacuum expectation value. In scenarios (away from the decoupling limit) where a splitting occurs between $\mathscr{M}$ and m_Φ, the $g_{\mathrm{HH}\Phi\Phi}$ couplings can be substantial, resulting in large BSM contributions to κ_λ. It should be emphasised that these loop effects involving BSM scalars and $g_{\mathrm{HH}\Phi\Phi}$ couplings are not a perturbation of the tree-level expression of the trilinear

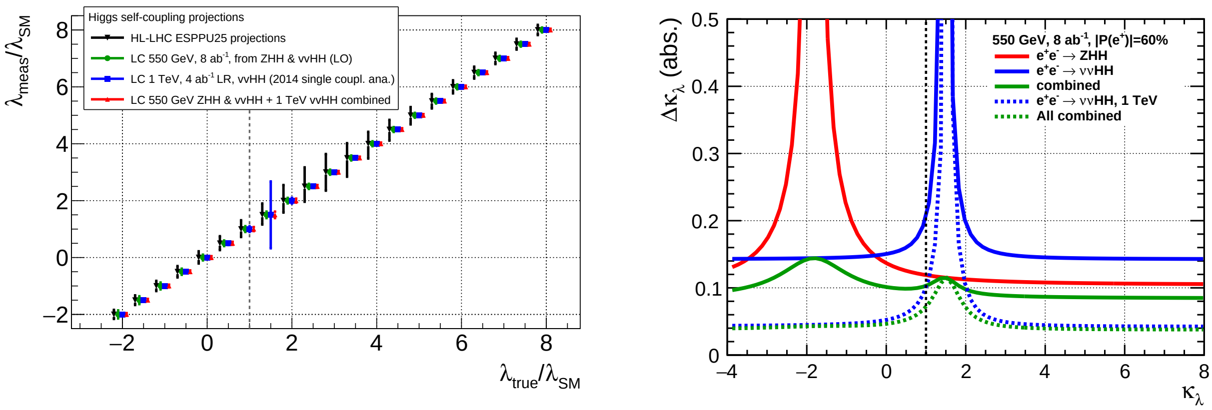

(a) (b)

Figure 8: (a) Projected accuracies for λ_{HHH} at the HL-LHC (black) [89] and an e^+e^- collider at a c.m. energy of 550 GeV (green), 1 TeV (blue) and the combination (red) in dependence of the actual value of λ_{HHH} that is realised in nature. (b) Absolute precision on trilinear Higgs self-coupling scaled to its SM value (κ_λ) as a function of κ_λ from the ZHH and WW fusion processes at the LCF at 550 GeV, and an outlook on 1 TeV based on ILC projections [14].

Higgs coupling, but rather a new class of contributions only entering at the loop level. They can therefore become larger than the tree-level contribution, without being associated with a violation of perturbative unitarity — this situation is analogous to that of loop-induced decays of the Higgs boson like e.g. $H \to \gamma\gamma$ or $H \to Z\gamma$. A very significant upward shift in λ_{HHH} is also motivated in many scenarios giving rise to a strong first-order EWPT which is required for electroweak baryogenesis, see Refs. [124, 125] or for more recent works e.g. Refs. [115, 126–128] for the cases of the (C)2HDM and N2HDM. In these latter cases, the parameter region featuring a strong first-order EWPT and a potentially detectable gravitational wave signal at the future space-based observatory LISA is correlated with an enhancement of λ_{HHH} compared to the SM value by about a factor of 2 (see also Fig. 11 below).

The existence of scenarios where λ_{HHH} receives large radiative corrections naturally raises the question of how sizeable higher-order corrections to other Higgs properties (e.g. single-Higgs couplings) involving $g_{HH\Phi\Phi}$ couplings can become. In turn, one may wonder in which observable, or which Higgs coupling extracted from the measurement(s), one would first observe a deviation from the SM prediction in these types of scenarios. It should be noted that deviations in λ_{HHH} may also be small or of the same order as those in single-Higgs couplings: this is for instance the case in decoupling scenarios of supersymmetric models [129–134] or in composite Higgs models [135–139]. On the other hand, various studies have found that there exist scenarios of new physics in which the size of the BSM deviations in λ_{HHH} can be significantly larger, by more than two orders of magnitude, than those in the couplings of H to gauge bosons and fermions, as will be discussed in more detail below — see for instance Refs. [95, 96, 99–123, 140–142] for investigations with explicit calculations in extended Higgs sectors and e.g. [143] for analyses based on EFT arguments. To be more specific, two main types of situations can be distinguished in which corrections to λ_{HHH} can be significantly larger than those in other (single) Higgs couplings: *(i)* models with some particular structure of the BSM sector, and *(ii)* scenarios, away from the decoupling limit, with relatively light new physics with significant couplings to the detected Higgs boson (as described above in terms of generic $g_{HH\Phi\Phi}$ couplings).

BSM models of the first case, which were systematically investigated in Ref. [143], include for instance the extension of the SM with a custodial EW quadruplet — a single field extension of the SM, where the enhancement of the effects in λ_{HHH} occurs already at the tree level — or the Gegenbauer's Twin models [144] where the Higgs boson is a pseudo Nambu-Goldstone boson. Turning next to the second case, with non-decoupling BSM physics, power counting arguments [96, 145] in the limit of large $g_{HH\Phi\Phi}$ couplings show that the leading one-loop BSM contributions to the trilinear Higgs coupling are of $\mathcal{O}(g^2_{HH\Phi\Phi})$, while those in Higgs couplings to fermions or gauge bosons grow at most linearly with $g_{HH\Phi\Phi}$.

A first simple but illustrative example is provided by the Z_2-SSM,[5] i.e. a real-singlet extension of the SM with an unbroken global Z_2 symmetry. Due to this symmetry, the BSM scalar S does not mix with the detected Higgs boson at 125 GeV. Its mass takes the form $m_S^2 = \mu_S^2 + \lambda_{H\Phi} v^2$, where μ_S is the singlet Lagrangian mass term and $\lambda_{\mathrm{H}\Phi}$ the portal quartic coupling between the singlet and the (SM-like) doublet. The coupling $\lambda_{\mathrm{H}\Phi}$ plays in the Z_2-SSM the exact role of the generic $g_{\mathrm{HH}\Phi\Phi}$ coupling in the discussion in above. In this model, single-Higgs couplings $g_{\mathrm{H}XX}$, where X can be a gauge boson or fermion, only receive BSM contributions via external-leg corrections — there are no mixing effects, and moreover vertex-type corrections do not appear because of the singlet nature of the BSM scalar and of the unbroken Z_2 symmetry. This allows obtaining compact expressions for the single-Higgs coupling modifier $c_{\mathrm{eff}} \equiv g_{\mathrm{H}XX}/g_{\mathrm{H}XX}^{\mathrm{SM}}$ at one and two loops [145]. The left panel of Figure 9 presents parameter scan results for the Z_2-SSM, in the plane of κ_λ and the BSM deviation in the g_{hZZ} coupling, denoted δg_{hZZ}, calculated at the one- and two-loop levels. Large shifts in κ_λ are found to be possible, e.g. at two loops up to $\kappa_\lambda^{(2)} \approx 3(2)$ for the case where one-loop (two-loop) corrections to the g_{HZZ} coupling are taken into account, while the effect in g_{HZZ} remains below the $1\,\sigma$ sensitivity of the FCC-ee (derived from Ref. [146], using the quoted precision on the measurement of the $\mathrm{e^+e^-} \to \mathrm{ZH}$ cross section at 240 GeV).

The Inert Doublet Model (IDM) is a second example of a BSM theory in which large BSM deviations can occur in λ_{HHH} while effects in other Higgs couplings would not be detectable, even with precision measurements. The IDM is a variant of the 2HDM in which the second doublet is charged under an unbroken $\mathbb{Z}_2$ symmetry — overviews of the model can be found e.g. in Refs. [147–149]. Similarly to the case of the Z_2-SSM, the masses of the BSM scalars $\Phi = h,\ A,\ H^\pm$ of the IDM take the form $m_\Phi^2 = \mu_2^2 + \frac{1}{2}\lambda_\Phi v^2$, with λ_Φ some combination of the Lagrangian quartic couplings and μ_2 the BSM mass scale of the IDM. However, to the difference of the previous model, single Higgs couplings in the IDM receive genuine BSM vertex corrections, which have here been evaluated consistently at the one-loop level (with also leading two-loop corrections from Ref. [121] included for the partial decay width of the Higgs to two photons). Results of parameter scans in the IDM are shown in the right panel of Figure 9, with predictions for κ_λ, including complete one-loop corrections — computed with the public tool `anyH3` [119] — together with leading two-loop corrections from Refs. [112, 113, 121], on the horizontal axis and the one-loop BSM deviation in the g_{HZZ} coupling on the vertical axis. For the latter, BSM vertex and external-leg corrections are included, with vanishing external momenta in order to obtain a quantity corresponding to κ_Z [150, 151]. The colour of the hexagonal bins corresponds to the minimal BSM deviation in the Higgs partial decay width to two photons, evaluated at two loops, among the points within the bin — this additional observable is relevant in the context of the IDM, due to the presence of a charged BSM Higgs boson in the model. Vertical blue lines correspond to 20% (dot-dashed) and 50% (dotted) levels of accuracy on the determination of λ_{HHH} (taking $\kappa_\lambda = 1$ as central value), while the red dotted horizontal corresponds to the 1σ precision expected for g_{HZZ} at FCC-ee. Interestingly, we observe that a significant population of scan points exhibit significant BSM deviations in κ_λ, with values up to $\kappa_\lambda \sim 2.8$, while maintaining $\delta^{(1)} g_{\mathrm{HZZ}}$ below the 1σ line of FCC-ee. Meanwhile, for the majority of these points a measurement of $\Gamma(\mathrm{H} \to \gamma\gamma)$ at the FCC-ee would also remain compatible with the SM up to the 1.5σ level. Finally, the impact of including both momentum dependence, as well as diagrams with an insertion of the modified value of κ_λ (while these are formally of two-loop order, the question of their size becomes relevant for large κ_λ) in the calculation of the g_{HZZ} coupling has been checked. Importantly, it was found for these IDM scan points that both effects lead overall to a reduction of the BSM deviation in g_{HZZ} — in other words, the results shown in the right panel of Figure 9 constitute a conservative representation of the possible deviations in κ_λ for IDM scenarios with BSM effects in g_{HZZ} below the 1σ sensitivity of the FCC-ee. While the discussion above was only done in two specific models — the $\mathbb{Z}_2$-SSM and the IDM — these cases offer a clear illustration of the important complementarity of measurements of the trilinear Higgs self-coupling with those of single-Higgs couplings, in order to probe the parameter space of BSM scenarios as thoroughly and completely as possible.

Finally, a qualitatively new feature at c.m. energies of about 1 TeV and above is the sensitivity to the triple Higgs-boson production processes $\mathrm{e^+e^-} \to \mathrm{ZHHH}$ and $\mathrm{e^+e^-} \to \nu\bar{\nu}\mathrm{HHH}$, which provide experimental access to the quartic Higgs-boson self-coupling λ_{HHHH}. Because of its dependence also on the trilinear Higgs-boson self-coupling λ_{HHH} (some contributions to the triple Higgs-boson production process even involve its square),

[5] We refer the reader to, e.g., Ref. [117] for an overview of the notations and conventions employed here (considering the $N = 1$ case of the $O(N)$-symmetric SSM discussed in Ref. [117]).

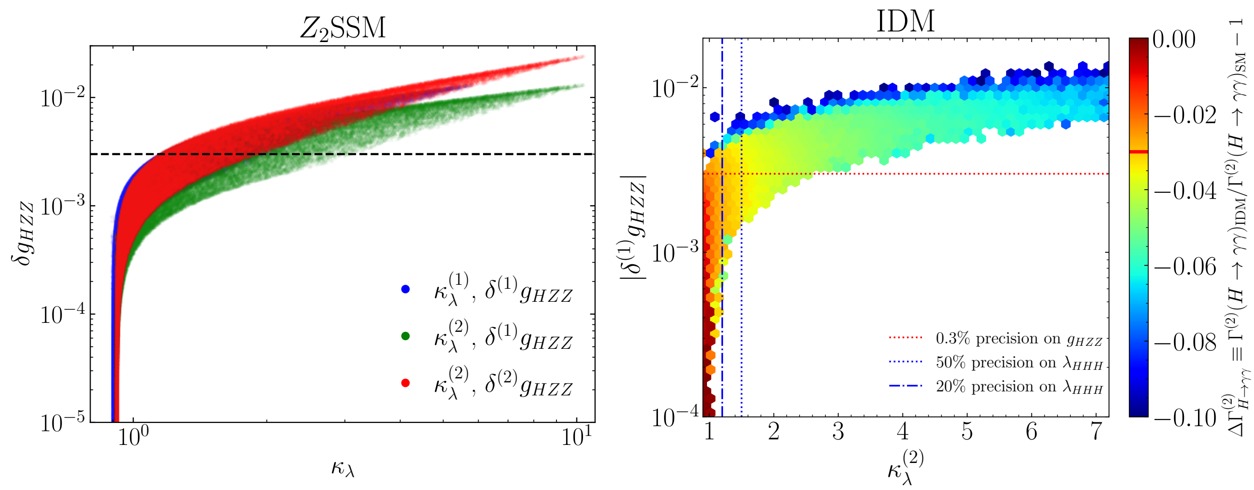

Figure 9: *Left*: parameter scan results for the Z_2-SSM, shown in the plane of κ_λ and $\delta g_{\rm HZZ}$. The colour of the points indicates the order (one or two loops) at which these two quantities are computed, and is explained in the legend of the plot. The black dashed line corresponds a precision of 0.3 % on the determination of the $g_{\rm HZZ}$ coupling (derived to the expected 1σ accuracy of FCC-ee on the $e^+e^- \to$ ZH cross section at 240 GeV [146]). *Right*: parameter scan results in the IDM, in the plane of $\kappa_\lambda^{(2)}$ (at two loops) and $\delta^{(1)} g_{\rm HZZ}$ (at one loop). The points are grouped in hexagonal bins, and the colour of each of these bins represents the minimal BSM deviation among the points of the bin. The red solid line in the colour bar corresponds to the expected 1σ accuracy of FCC-ee on $H \to \gamma\gamma$ [146], while the horizontal and vertical lines are described in the legend and the text.

the triple Higgs-boson production process also provides complementary information on $\lambda_{\rm HHH}$ that can be combined with the results that are obtained from the di-Higgs production processes.

Figure 10 illustrates the sensitivity of future lepton colliders with c.m. energies of 1 TeV, 3 TeV and 10 TeV to set constraints on the trilinear (horizontal axis) and quartic (vertical axis) Higgs-boson self-couplings, both normalised to the tree-level SM values [45]. The prospective sensitivities shown here are obtained only from the triple Higgs-boson production processes, without additional information from single- and di-Higgs production. The prospects for the lepton colliders are compared to the ones for the HL-LHC obtained in a recent exploratory study for the $5b$ channel and the $3b2\tau$ channel [45]. These prospective bounds go significantly beyond the current theoretical constraints from tree-level perturbative unitarity, shown in gray in Fig. 10. The displayed results indicate that the HL-LHC is competitive to a 1 TeV lepton collider in constraining $\lambda_{\rm HHHH}$, while higher-energetic lepton colliders (see also [152–155]) can significantly improve on the HL-LHC capabilities.

3.3.2 Overlap with other fields of science – Gravitational Waves

The determination of the trilinear Higgs self-coupling allows us to get insights in the cosmological evolution of the Higgs potential. Its phase history is closely connected to the generation of the baryon-antibaryon asymmetry. In particular, the requirement of a strong first-order EWPT (FOEWPT), i.e. departure from the thermal equilibrium, is one of the three Sakharov conditions [156] to be fulfilled for successful EWBG. While the SM cannot reproduce quantitatively the EWBG scenario, models with extended Higgs sectors may feature strong first-order EWPTs. A strong first-order EWPT typically comes along with a large trilinear Higgs self-coupling [115, 124–126, 128, 157, 158]. This in turn implies in general a mass gap between the lighter and heavier Higgs bosons of the Higgs spectrum, leading to typical signatures to be probed at present and future colliders [128, 159–164]. More generally, new physics effects in the scalar and/or Higgs-Yukawa sectors, as required for a strong first-order phase transition, have impact not only on BSM Higgs signatures [164–167] but also on the phenomenology of di- and triple Higgs production [45, 96, 119, 168]. Finally, strong first-order EWPTs can provoke gravitational waves that can be tested at a future space-based gravitational waves observatory such as LISA, cf. e.g. [122, 128, 164, 169–171]. The 2HDM contains a Higgs spectrum that could

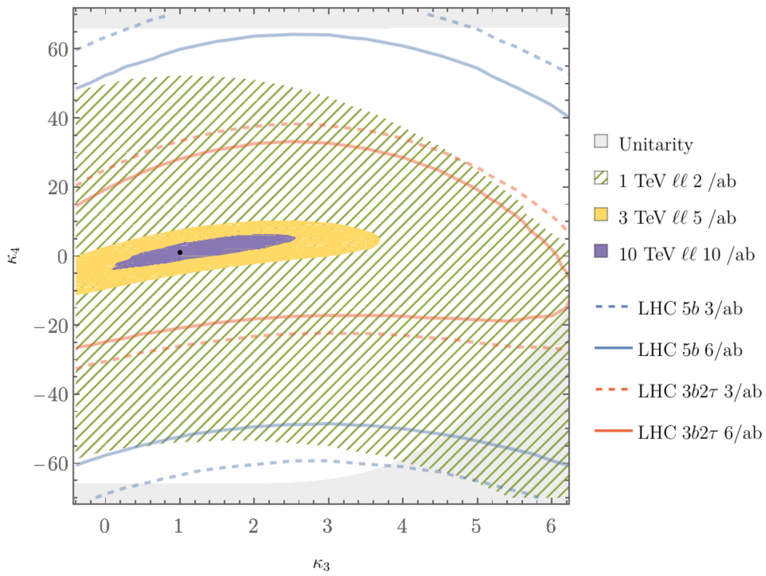

Figure 10: Prospects of future lepton colliders with a c.m. energy of 1 TeV, 3 TeV and 10 TeV for constraining the trilinear (horizontal axis) and quartic (vertical axis) Higgs self-couplings, both normalised to their tree-level values in the SM, at the 95% C.L. using exclusively searches for triple-Higgs production [45]. These prospects are presented in comparison to the projected 95% C.L. contours for the $5b$ and $3b2\tau$ analyses at the HL-LHC. The shaded gray area indicates the region that is excluded by the bound from (tree-level) perturbative unitarity.

trigger a FOEWPT. A case study is outlined below in Sec. 3.6.5. Figure 11 shows the result from a scan in the 2HDM parameter space. Shown in pink are the points in the κ_λ versus $m_A - m_H$ plane that feature a first-order EWPT that leads to a gravitational wave signal which is potentially detectable at LISA [128]. There is hence a strong interplay between the size of the Higgs self-interaction, the actual shape of the Higgs potential and EWBG, such that exploiting synergies between particle physics and cosmology will largely advance our knowledge about the true model underlying nature.

In general, in a first-order phase transition of the vacuum, a spatial and temporal contrast of vacuum energy density occurs. If the magnitude of the contrast exceeds a certain critical value, the spatial portion of the phase transition that is delayed can cause gravitational collapse and become a primordial black hole (PBH). The mass of a PBH derived from the EW first-order phase transition is expected to be about 10^{-5} of the solar mass. Searching for a PBH of this mass using microlensing experiments in the present or near future such as Subaru HSC, OGLE, PRIME and Roman Space Telescope may provide an early insight into the physics of the electroweak first-order phase transition. The search for PBHs will provide a new way to verify the physics of the electroweak first-order phase transition that is complementary to future Higgs self-coupling measurements and gravitational wave observations. The study of PBHs derived from the first-order phase transition with respect to the electroweak phase transition was studied in the context of the SMEFT in Ref [172]. Subsequently, an analysis using Higgs EFT, an effective theory that is more compatible with the physics causing strong first-order phase transitions, was performed, and a methodology was proposed to comprehensively verify the physics of first-order phase transitions using Higgs self-coupling measurement, gravitational wave observations, and PBH searches [173]. Furthermore, the analysis was extended to include correlation with the Higgs with di-photon coupling [174]. In Fig. 12, the region providing a 1st order phase transition is indicated by the coloured bands: the narrow red band can be tested by PBH searches, and the (dark and light) green bands can be examined by gravitational wave observation at DECIGO and LISA, respectively, but the blue band can only be probed by collider measurements, in particular of the Higgs di-photon decay and of the triple Higgs coupling. The purple band corresponds to the case when $\Delta\kappa_\gamma$ is determined to be –4% $\pm$ 1% by combining HL-LHC and Linear Collider data, c.f. Sec. 3.1. In this case, the possible allowed $\Delta\kappa_\lambda$ (denoted $\Delta\kappa_3$ in the figure) is narrowed down to 135 %> $\Delta\kappa_\lambda$ > 55 %. PBH production resulting from electroweak first-order phase transitions has also been studied in specific models [175] (and other references). These studies highlight that the parameter region in which the first-order phase transition can be verified through PBH searches and gravitational waves alone is limited, and that precise measurements of the Higgs self-coupling and Higgs di-photon coupling by future collider experiments are essential for a broader verification of the electroweak first-order phase transition.

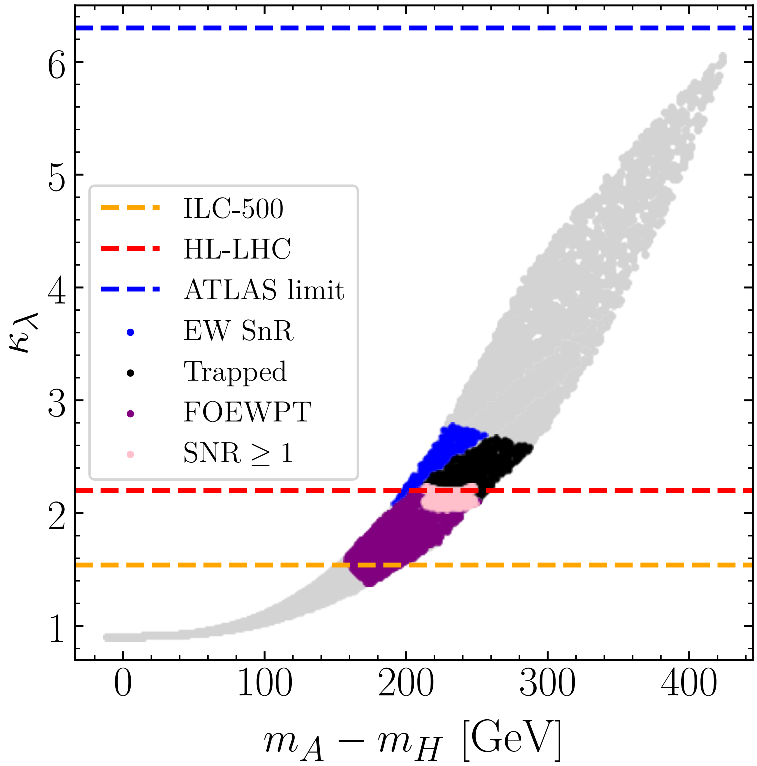

Figure 11: Results for a scan in the 2HDM of type II in the plane of the mass difference $m_A - m_H$ and κ_λ [128]. The parameter region giving rise to a first-order electroweak phase transition is displayed by the purple and pink regions, where in the latter region a gravitational wave signal is potentially detectable at the space-based gravitational wave observatory LISA. The current limit on κ_λ is indicated by the horizontal blue dashed line, while the projections for the HL-LHC and a 500 GeV linear collider are indicated by the horizontal red and orange dashed lines, respectively. Note that in the figure H denotes the CP-even Higgs boson that appears in the 2HDM in addition to the detected Higgs boson.

3.4 Electroweak physics at highest energies: multi-boson processes

3.4.1 Scrutinizing electroweak interactions at high(est) energies

Compared to QCD, our understanding of electroweak (EW) interactions as a quantum field theory is still relatively poor. The EW scale is three orders of magnitude above the QCD scale (v = 246 GeV compared to Λ_{QCD}), such that non-Abelian collinear phenomena like EW jets, EW showers, and EW (Sudakov) suppression of exclusive final states become visible only in the regime of a TeV and above. Exploring the non-Abelian EW structure is of utmost importance to understand this fundamental force of Nature. A first glimpse showed up in $e^+e^- \to WW, ZZ$ at LEP. In the recent years more insights could be gained at the LHC in dibosons and the first-ever observed EW triple-boson production and vector-boson scattering processes.

In general, multi (EW)-boson processes are needed to access the non-Abelian gauge structure and to ultimately disentangle transversal from longitudinal-scalar degrees of freedom, which are assigned to distinct sectors of the SM. In the SM, we expect to observe the restoration of electroweak symmetry at high energy such that transversal W and Z bosons become genuine gauge degrees of freedom, while longitudinal W and Z bosons combine with the Higgs boson to form a scalar multiplet which complements the fermionic matter of the SM. Multi-particle production and scattering in the multi-TeV regime can then be understood as electroweak-jet dynamics analogous to QCD. In extensions of the SM, the asymptotic symmetry pattern could

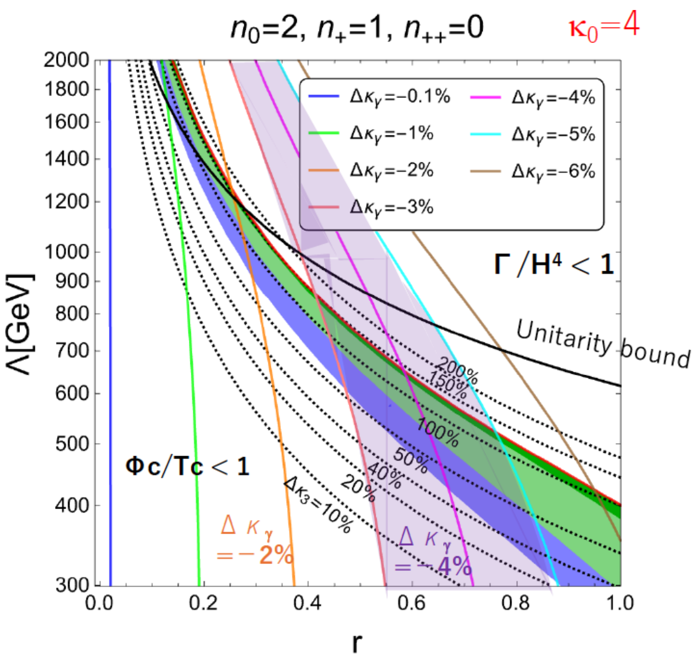

Figure 12: Region of 1st order phase transition indicated by colour in the r-Λ plane, where r represents non-decouplingness and Λ is the scale of new physics in the aligned Higgs EFT as discussed in [174]. The parameters n^0, n^+, and n^{++} correspond to the degrees of freedom of the electrically neutral, singly-charged and doubly-charged scalars in the model, respectively. The narrow red bad can be tested by PBH search, and the (dark and light) green bands can be examined by gravitational wave observation at DECIGO and LISA, respectively, and the blue region can only be tested by the measurements of the Higgs di-photon coupling and the triple Higgs coupling. The purple colored region corresponds to the case if $\Delta\kappa_\gamma$ is determined to be –4% ± 1% (using HL-LHC and ILC).

be different, which would typically result in a systematic enhancement of specific multi-boson final states as compared to the SM prediction shown in Fig. 13. Polarisation measurements at the LHC opened a first door to this. However, at a hadron collider EW effects are shadowed because QCD radiation and virtual corrections largely dominate over EW contributions. A detailed understanding of EW interactions in the complex structure of initial- and final-state radiation can be achieved at a TeV-scale lepton collider [176, 177].

Electroweak jets, most notably also neutrino jets can be studied in high-energetic lepton collisions [178]. Again, weak production and low-background environments make these precision studies more favourable than at a high-energy hadron collider. Besides electroweak multi-particle production these processes would also comprise electroweak fragmentation. It is essential that at a high-energy e^+e^- collider the analysis of fully hadronic final states provides a detailed picture of exclusive multi-boson states without significant loss of efficiency.

The observables here are 6-, 8-, 10-fermion final states which are complementary to corresponding processes at hadron colliders, limited mostly by statistics but with very low systematic uncertainties. The thresholds for the simplest multi-boson production processes are listed in Table 8, and the overall increase in particle multiplicity towards higher energies can be read off from Fig. 13.

3.4.2 Triple and quartic gauge couplings

The ILC prospects for triple gauge coupling measurements at $\sqrt{s} = 500$ GeV and 1 TeV have been studied based on full simulation of the ILD detector concept [180, 181], and extrapolated to 250 GeV [182]. With increasing energies, the relative effect on the differential cross section of the three TGC parameters g_Z, κ_γ, and λ_γ grows proportional to s/m_W^2. There are a number of experimental effects that become more challenging at higher energies — more forward-boosted event topologies, higher pile-up from beamstrahlung pairs and photoproduction of low-p_t hadrons — the fundamental gain in sensitivity with s dominates by far. Figure 14 summarizes the current state of the expected precisions, as discussed in more detail in the following

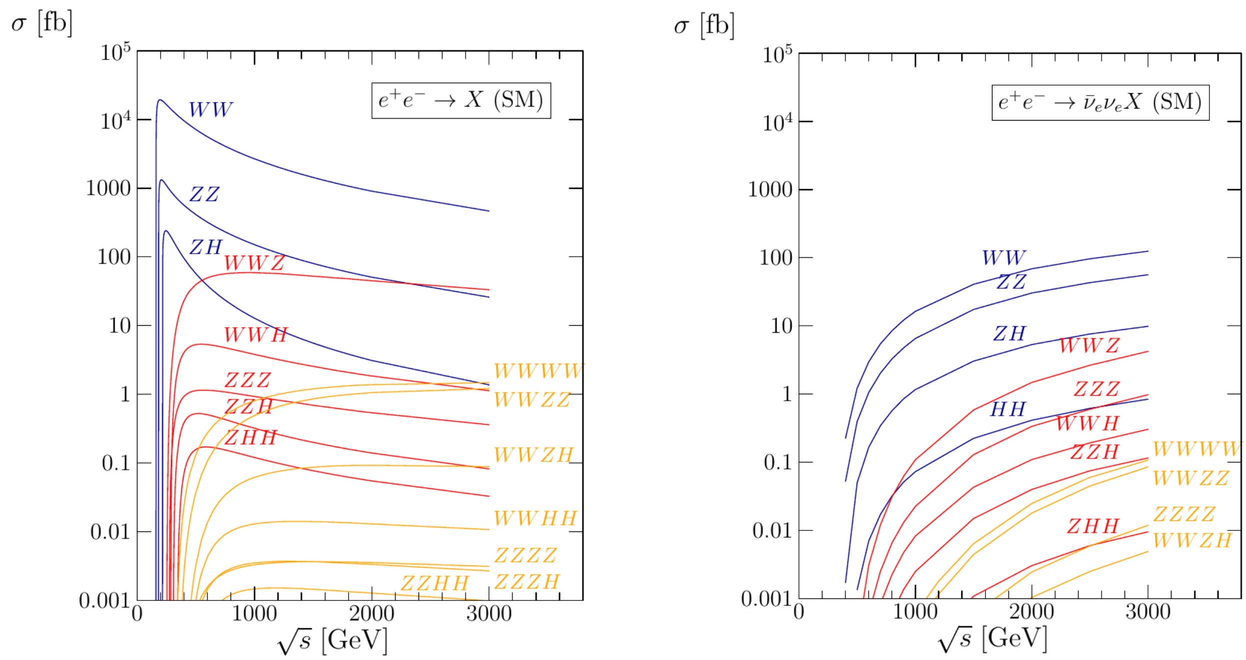

Figure 13: Unpolarised born-level cross sections for multi-boson production (LO) in annihilation (left) and vector-boson fusion processes (right) as probes of the electroweak sector.

ee →	threshold [GeV]	maximum [GeV]
ZH	160.8	195
ZZ	182.4	200
WW	216.3	240
WWZ	252.0	950
ZZZ	273.6	550
WWH	285.9	550
ZZH	307.5	520
ZHH	341.4	590
WWWW	321.5	3000
WWZZ	343.1	4000
WWZH	377.0	2000
WWHH	410.9	1400

Table 8: Production thresholds and peak cross section positions for 2-, 3- and 4 EW boson processes in e^+e^- collisions. From [179].

paragraphs.

The full simulation study at 500 GeV [180] was limited to a binned analysis of three (out of five) angles in the WW → $\mu\nu qq$ and WW → $e\nu qq$ channels. For an integrated luminosity of 500 fb^{-1}, this study found statistical uncertainties of $(6.1, 6.4, 7.2) \times 10^{-4}$ for g_1^Z, κ_γ and λ_γ, respectively. An unbinned likelihood or optimal observable analysis of all five angles, including also fully hadronic WW events as well as single-*W* events has been estimated [183] to improve these numbers by a factor of 2.4 for g_1^Z and by a factor of 1.9 for κ_γ and λ_γ. Assuming the full integrated luminosity of ILC500 instead of only 500 fb^{-1} gives another factor of 2 improvement to $(1.3, 1.7, 1.9) \times 10^{-4}$. At this level of precision, systematic uncertainties need to be considered. As shown in [184], the effects of a finite knowledge of the luminosity and the beam polarisations are negligible when including them as nuisance parameters in a global fit. The effect of different permil level uncertainties on the selection efficiency and percent-level uncertainties on the residual background has been evaluated in [180] by propagation through the whole analysis chain, thereby treating them as fully uncorrelated between data sets and observables, obviously a very pessimistic assumption. Based on considerations of correlated

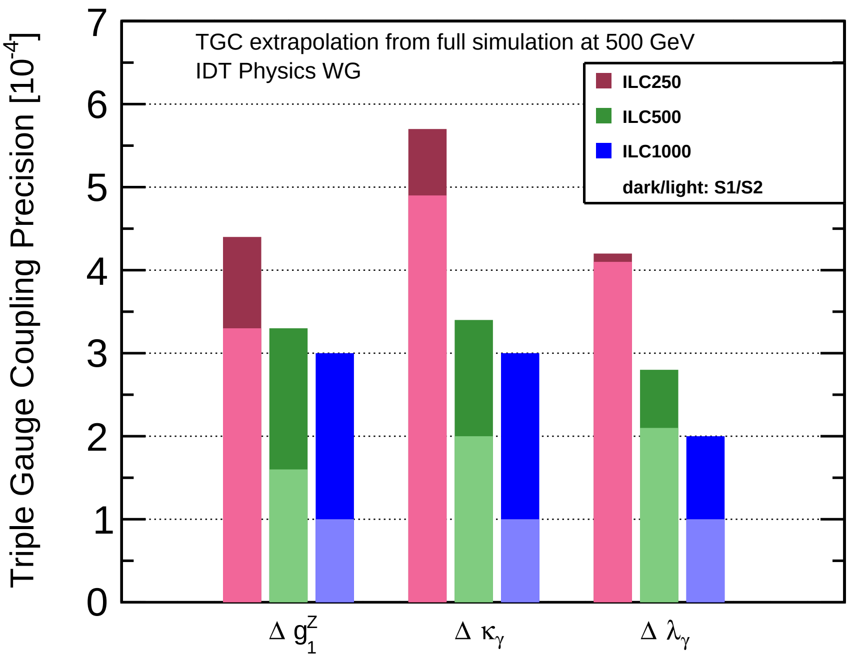

Figure 14: Expected precisions on the three triple gauge coupling parameters at the three energy stages of ILC. The results at 500 GeV and at 1 TeV are based on the ILD full simulation analyses of semi-leptonic W pair production, extrapolated to include improvements from the fully hadronic channel and single-W production as well as for upgrading from a binned analysis of three angles to an optimal observable technique [182]. The S1 scenario assumes the systematic uncertainties from [182], the S2 illustrates the hypothetical reduction by a further factor 2-3 to the level of 1×10^{-4}.

uncertainties and nuisance parameters in global fits, more recent studies expect that systematic uncertainties of $(3,3,2) \times 10^{-4}$ can be reached [182]. In total, the expected precisions on the three couplings thus reach $(3.3,3.4,2.8) \times 10^{-4}$ for ILC500.

The full simulation study at 1 TeV [181] found statistical precisions of $(1.9,1.7,2.7) \times 10^{-4}$ for a luminosity of 1 ab^{-1} with the same analysis technique as at 500 GeV (semileptonic W pairs, binned analysis using three angles). A simple scaling to the full luminosity of 8 ab^{-1} renders the statistical uncertainty negligible with respect to the systematic uncertainties as given above. Thus, an adequate estimate of the 1 TeV prospects requires a thorough re-analysis of the systematic effects. It has already been shown that any global scaling as well as the variation of a simple angular cut-off can be determined from the data without any loss of precision on the TGCs [184]. But a complete treatment of the remaining backgrounds in a multivariate fit still remains to be done. In Fig. 14 we present the expected precisions on the TGC paramters assuming the currently understood level of systematic uncertainties and the result of possible improvements by a factor 2-3 to the level of 1×10^{-4}.

3.4.3 Vector boson fusion and scattering

Vector boson scattering (VBS) is one of the most important processes to scrutinize the non-Abelian gauge structure of EW interactions, to connect to the Higgs mechanism and EW symmetry breaking and to compare transverse and longitudinal degrees of freedom. In addition, VBS (the Feynman diagrams are shown in 15 serves as a vehicle to potentially discover resonances that couple dominantly to either the gauge or Goldstone sector of particle physics. VBS starts at collider energies of 500 GeV and is therefore only accessible at linear e^+e^- colliders, not at circular ones. The advantage compared to VBS at hadron colliders is that fully hadronic final states are experimentally accessible; these allow the full reconstruction of the invariant mass of the diboson system. Also the reconstruction of polarisations of the intermediate vector bosons from fully

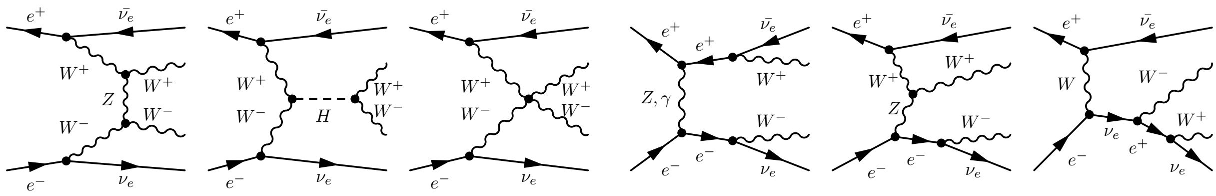

Figure 15: Feynman diagrams for vector boson scattering (VBS).Left: signal, right: irreducible background.

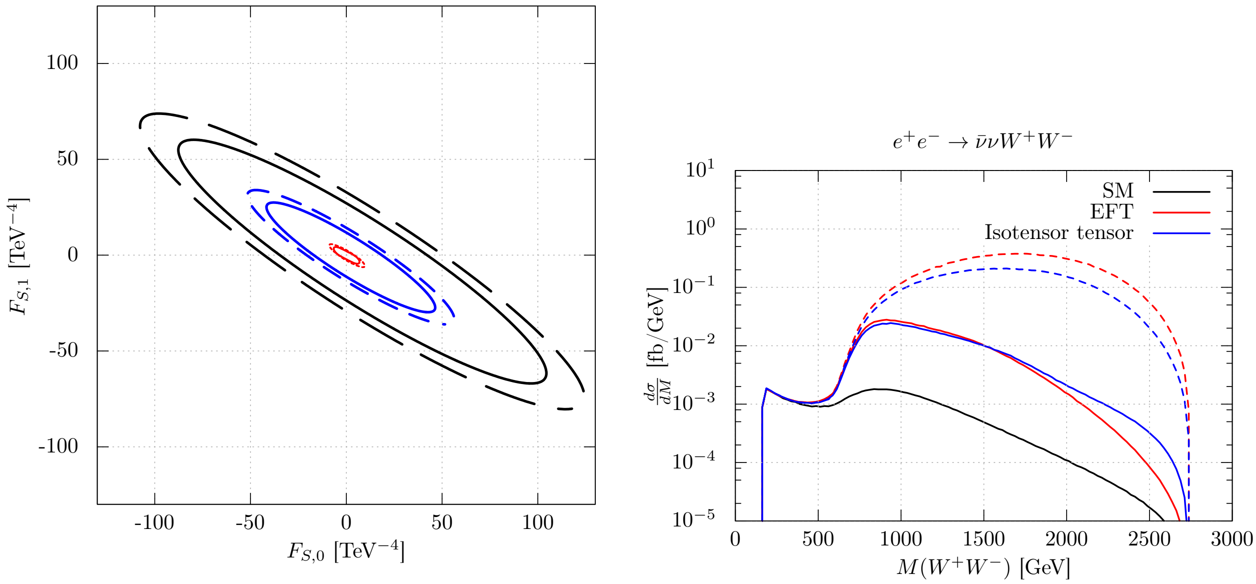

Figure 16: Left: reach for dim-8 operator coefficients for deviations in quartic longitudinal vector bosons at ILC-1000, CLIC 1.5 and 3 TeV in black, blue and red, respectively. Dashed curves are unpolarised, full lines with design polarisation fractions. Right: Isotensor tensor resonance in WW at 3 TeV CLIC. Full lines are the signal projected to a UV-complete scenario.

hadronic states is possible the LC. VBS can be used to search for deviations from the SM in terms of dim-6 or dim-8 operators in SMEFT or HEFT; indeed, VBS is one of the most sensitive processes to discriminate between the two EFT frameworks. Previously this has been studied as searches for deviations of quartic gauge couplings (QGCs) from the SM (aQGCs) [185–188]. To get physically meaningful results that obey the unitarity of the scattering matrix it is important to automatically implement such constraints in the signal modelling, cf. e.g. [189–191].

Vector boson scattering processes and multi-boson prompt production processes do, in general, probe the same physics, however, in kinematically vastly different regions and are, hence, complementary to each other. This has been shown e.g. in [187]. Prompt multi-boson production processes can be used to constrain deviations in triple and more importantly quartic gauge couplings and prove (or disprove) the equivalence of gauge and Goldstone degrees of freedom.

Beyond EFTs, VBS can be used for searches as generic di-boson resonances with spin and isospin quantum numbers of $S, I = 0, 1, 2$ each [188, 189, 192]. The right-hand side of Figure 16 shows a tensor resonance that could appear in a composite Higgs model. The invariant mass of the di-boson spectrum shows a broad excess that in this special case is difficult to distinguish from a dimension-8 EFT description.

3.5 Top physics programme – from threshold to highest energies

3.5.1 The top quark mass and width

The top quark mass is one of the fundamental parameters of the Standard Model that must be determined experimentally. The Tevatron experiments left a legacy top quark mass determination: $m_t = 174.34 \pm 0.64$

GeV, combining CDF and D0 results in several decay channels. Run 1 of the LHC yields a combination of 15 ATLAS and CMS measurements with an experimental precision of two per mille: $m_t = 172.52 \pm 0.33$ GeV. These results correspond to *direct* measurements, where templates from Monte Carlo generators are compared to the observed distributions of top quark decay products. The Monte Carlo mass parameter is identified with the top quark pole mass, within an uncertainty of about 500 MeV [193]. Extractions of the top quark mass from (differential) cross sections allow for a better control over the mass scheme, and have reached a precision of approximately 1 GeV [194, 195]. The High Luminosity program of the LHC is expected to improve the experimental precision of direct mass measurements to several 100 MeV [196].

A threshold scan at an electron-positron collider, scanning the centre-of-mass energy through the top-quark pair production threshold at $\sqrt{s} \sim 2m_t$ and mapping out the sharp rise of the cross section, provides a "golden" measurement of the top quark mass [197–202]. The location of the threshold is highly sensitive to the top-quark mass. A comparison of cross section measurements at several centre-of-mass energies to first-principle predictions gives access to the top quark mass in a well-controlled mass scheme. Typically threshold masses, such as the "1S" or "PS" mass are determined and then converted to the $\overline{\text{MS}}$ scheme. Non-relativistic QCD (NRQCD) calculations have reached N^{3}LO precision [203–207] and the conversion between mass schemes is known to to four-loop precision [208, 209].

Beyond the top quark mass, the shape of the threshold provides a direct handle on the top quark width. The cross section in the threshold region is moreover sensitive to the exchange of soft gluons and virtual Higgs bosons, leading to a strong dependence on the strong coupling and the top-quark Yukawa coupling. These parameters can be extracted from a precise measurement of the differential top quark pair production cross section versus centre-of-mass energy in a narrow window around the threshold.

Experimental studies have been performed by a number of groups [210–215]. The statistical uncertainty on the top quark mass can be reduced to below 20 MeV with approximately 200 fb^{-1} of data [211, 213]. The calibration of the beam energy and luminosity have an impact of a few MeV, provided the centre-of-mass energy is calibrated to 5 MeV and the luminosity to one per mille [215]. Both of these requirements are expected to be within reach. The luminosity spectrum must be reconstructed precisely, as demonstrated in Ref. [216], to benefit fully from the potential of the threshold scan.

The limiting factor in the extraction of the top quark mass is expected to be of a theoretical nature. Missing higher orders in today's state-of-the-art prediction of the cross section amount to approximately 35 MeV [215]. The conversion of the threshold mass (1S, MSR or PS mass) to the $\overline{MS}$ scheme [208, 209] contributes another 10-20 MeV.[6] The parametric uncertainties due to the current world average uncertainty in the strong coupling $\alpha_s(m_Z)$ has a non-negligible impact, through the impact on the prediction for the cross section and on the conversion to the $\overline{MS}$ mass. The impact of the uncertainty of the top Yukawa coupling is expected to be below 10 MeV assuming the uncertainty of $\delta y_t / y_t = 3\%$ projected by the HL-LHC [196], and can be further reduced with high-energy e^+e^- data, as discussed in the next section. The top quark $\overline{MS}$ mass can then be determined to approximately 50 MeV with the theory tools currently on the market and under reasonable assumptions for the impact of experimental systematic uncertainties.

The top quark width is extracted in the same fit, providing a direct measurement of the top quark width. A precision of about 50 MeV can be achieved, where statistical uncertainties, scale uncertainties in the prediction and the parametric uncertainty from the top quark Yukawa coupling all have a non-negligible impact.

The Yukawa coupling and α_s can be determined with a small statistical uncertainty from the threshold scan [211], but these measurements cannot compete with the most precise determinations once systematic uncertainties are fully accounted for. A very important reduction of the uncertainties from missing higher orders in the NRQCD predictions is required to enable precision measurements of these quantities.

While the threshold scan is definitely the *golden* top quark mass determination, high-luminosity runs at centre-of-mass energies above the top quark pair production threshold yield further opportunities. Very good statistical precision, below 100 MeV, can be achieved in a *direct* determination of the top quark mass from fits of MC templates to mass-sensitive observables formed with the top quark decay products [213]. These measurements may very valuable to connect the results of the threshold scan with the hadron collider measurements. Radiative events, where the top quark pair is produced in association with an ISR photon, enable a measurement with a precision of approximately 150 MeV using 4 ab^{-1} of data at $\sqrt{s} = 500$ GeV [217]. This

[6] Subtle issues in the use of the PS scheme are discussed in [209].

analysis maintains full flexibility in the choice of the top quark mass scheme and provides access to the top quark mass at several scales, thus probing the scale evolution ("running") of the top quark mass.

3.5.2 Top quark Yukawa coupling

The study of the top quark is important for providing precision inputs to the SM tests, but it is more important as a probe of the mechanism of mass generation. The top quark is the SM particle with strongest coupling to the Higgs boson. Thus, any modification of the Higgs sector and any new interactions involved in mass generation will be reflected in the properties of the top quark. The value of the top quark Yukawa coupling is expected to be close to 1. In the SM and other weakly coupled theories of electroweak symmetry breaking, the top quark enters in perturbation theory in the parameter $\alpha_t = y_t^2/4\pi \sim 1/12$. In models in which the Higgs boson is composite, the top quark will couple strongly to the Higgs constituents, giving rise to larger effects. This is called "top quark partial compositeness" [218]. A full exploration of the Higgs boson must include the search for this influence in the physics of the top quark.

Top quark partial compositeness can manifest itself in three distinct ways. First, it may lead to a larger than expected value of the top quark coupling to the Higgs boson. In this section, we will discuss the measurement of the top quark Yukawa coupling at colliders and searches for this effect. Second, it may lead to the mixing of the top quark with heavy vectorlike (composite) quarks, beyond the reach of the LHC. Third, it may lead to new four-fermion interactions involving the top quark that are seen at Higgs factories through the measurement of the reaction $e^+e^- \to t\bar{t}$. We will discuss those measurements in the next subsection.

We begin with the study of the top quark Yukawa coupling. It is important in any event to measure this couplings as part of the precision study of the Higgs boson and to gather any clues its value might provide on the nature of electroweak symmetry breaking and mass generation. We will argue that this requires e^+e^- measurements at high energy, above 500 GeV in the centre of mass.

The top quark Yukawa coupling is already constrained by the study of the Higgs boson at the LHC. The Higgs boson discovery channels at the LHC are sensitive to this coupling indirectly, through Higgs production and decay channels such as $gg \to H$ and $H \to \gamma\gamma$; in the SM, these proceed primarily through top quark loops. Under certain assumptions, the Higgs production and decay rates can yield a precise bound on the top quark Yukawa coupling. A more direct, and more robust, measurement is possible in the associated $pp \to t\bar{t}H$ production process, observed in 2018 [219, 220]. The projection for the HL-LHC envisages an uncertainty of approximately 3% on the signal multiplier κ_t dominated by theory uncertainties [221]. Several groups have studied the interplay between measurements in top quark and Higgs boson production processes in the framework of SMEFT fits [222, 223].

At an electron-positron collider, indirect probes are also available: the $H \to \gamma\gamma$, $H \to gg$ and $H \to Z\gamma$ channels provide sensitivity to the top Yukawa coupling already in 250 GeV data [224–226]. These measurements can determine the top Yukawa coupling with $\sim$1% precision, under the assumption that no new particles enter in the loops. These measurements may therefore provide an early indication of new physics, but a deviation of the SM cannot be unambiguously pinpointed. In more general EFT fits, the constraint on the coefficient $C_{t\phi}$ of the operator that shifts the top Yukawa coupling obtained from these indirect probes is not robust, as its effect is degenerate with poorly bounded degrees of freedom [226].

The $t\bar{t}$ threshold scan offers an indirect determination that is more specific for the top quark Yukawa coupling. The production rate close to threshold is sensitive to Higgs-exchange effects and can yield a competitive precision of 4 % on the top-quark Yukawa coupling [227]. However, the current uncertainty in state-of-the-art calculation would add a 20% theory uncertainty [228] and there is no clear perspective to reduce or circumvent this uncertainty.

The direct measurement in $e^+e^- \to t\bar{t}H$ production requires a centre-of-mass energy of at least 500 GeV. The cross section rises sharply around that energy; raising the centre-of-mass energy to 550 GeV enhances the production rate by a factor or approximately four and the measurement of the $t\bar{t}H$ coupling by a factor two. Several groups have performed detailed full-simulation studies at centre-of-mass energies ranging from 500 GeV to 1.4 TeV [47, 227, 229]. With 4 ab^{-1} at 550 GeV, a precision of 2.8% is expected on the top Yukawa coupling, which could improve to 1% with 8 ab^{-1} at 1 TeV. Measurements at multiple centre-of-mass energies and with different beam polarisations can further characterize the $t\bar{t}H$ coupling [230].

Another important target requiring centre-of-mass energies between 600 GeV and 1 TeV are the *CP* properties of the $t\bar{t}H$ coupling. Achievable constraints have been studied at the cross section level [54], showing a significant improvement due to polarised beams. A detailed detector-level study of the relevant observables remains an interesting task for future studies.

3.5.3 The top quark electroweak couplings

As we discussed in Sec 3.1, the basic processes of top quark pair production at Higgs factories can show signals of new physics related to the mechanism of top quark mass generation. These effects can arise in three different ways, (1) by top quark mixing with heavy vectorlike fermions, (2) by new four-fermion interactions between top quarks and electrons mediated by new vector bosons, and (3) by new four-fermion interactions among top and bottom quarks due to their intrinsic compositeness. The mechanism (1) appears in Little Higgs Models, e.g. [231]; the mechanism (2) appears in models with extra space dimensions, including Randall-Sundrum warped space models, e.g., [232]; the mechanism (3) appears in models of top compositeness with interactions described by effective field theory, e.g., [233]. All three mechanism predict especially large effects in models in which the Higgs boson is composite. In such models, the coupling of the Higgs boson to the top quark is sufficiently large that the top quark itself becomes fully or partially composite. The effects of this compositeness are limited in the top quark QCD couplings due to constraints from QCD gauge invariance, but they can be manifest in the top quark couplings to the massive electroweak gauge bosons W and Z. The search for modification of the top quark electroweak couplings thus nicely complements the searches for deviations from the SM in the Higgs couplings to W and Z and in the top quark Yukawa coupling.

A full description of beyond-SM effects on the top quark is given by Standard Model Effective Field Theory (SMEFT). We will discuss the results of SMEFT analysis below, but first we will present results in a simpler context, in which only the left- and right-handed couplings of the the top quark to the Z boson, g_L and g_R, are allowed to deviate from the SM. Discovery of non-SM values in this parameter space is sufficient to demonstrate a violation of the SM, though it is not sufficient to fully diagnose the origin of the new physics. Nevertheless, this first level of analysis is important, and a linear collider with polarised beams is well equipped to carry it out. The production mechanism for top quark pairs at an e^+e^- collider is s-channel γ and Z exchange, and, since these are in interference, there are strong constructive or destructive interferences, depending on beam polarisations, that distinguish the effects of g_L and g_R.

We illustrate this with two analyses from the literature. Ref. [234] studied effective theories of top quark compositeness in an effective field theory description. The authors found the regions of sensitivity in the model space shown in Figure 17. The horizontal axis is the compositeness scale m_*; note that the sensitivity extends into the 10's of TeV region. The vertical axis shows the hierarchy between a dimensionful scale f in the compositeness theory and the Higgs boson vacuum expectation value. Measurements of g_L and g_R probe the blue regions of the parameters space, while Higgs and diboson measurements probe the orange regions. The analysis nicely illustrates the complementarity discussed in the previous paragraph.

We illustrate this with two analyses from the literature. Reference [234] studied top quark compositeness in an effective field theory description. The authors found the regions of sensitivity in the model space shown in Figure 17. The horizontal axis is the mass scale of composite resonances m_*; note that the sensitivity extends into the 10's of TeV region. The vertical axis shows the hierarchy between the compositeness scale f and the Higgs boson vacuum expectation value. Measurements of top- and bottom-quark interactions probe the blue regions of the parameters space, while Higgs and di-boson measurements probe the orange regions. The analysis nicely illustrates the complementarity discussed in the previous paragraph.

Ref. [235] computed the polarisation-dependent cross sections for $e^+e^- \to \bar{t}t$ as a function of centre-of-mass energy in a class of models with a Randall-Sundrum fifth dimension and electroweak gauge bosons in the bulk. Figure 18 shows the relative deviations from the SM in the four helicity-dependent cross sections $e^-(L,R)e^+(R,L) \to t(L,R)\bar{t}(R,L)$ in two of these models. The figure shows the power using initial- and final-state polarisation in recognizing the beyond-SM effects, and also the dramatic increase in the size of these effects with centre-of-mass energy.

These are just two of the many models proposed that give significant deviations from SM in the top quark couplings to the Z. Predictions from many more models of all three types are collected in Figure 19. The points shown here correspond to individual parameter sets from the parameter spaces of the various models. We have rescaled the masses of new bosons to 5 TeV and the masses of vectorlike fermions to 2 TeV, so all

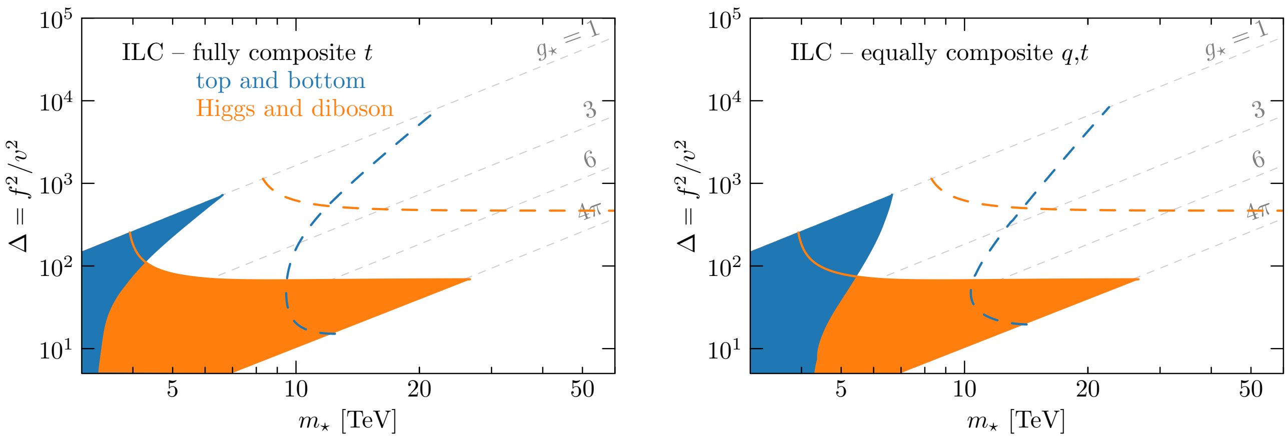

Figure 17: Five-sigma reach of top- and bottom-quark measurements in the parameter space of generic composite Higgs models. The model parameters on the axes are explained in the text. Runs at 500 GeV and 1 TeV are included, with 0.5 and 1 ab^{-1}, respectively and polarised beams. Note that this is 1/8 of the luminosity samples expected for the LCF. Blue and orange regions represent, respectively, the regions probed by measurements of t and b and regions probed by measurements of Higgs and diboson processes. The solid areas represent the potential reach in a pessimistic case with cancellations between the various contributions; the dashes lines are obtained in the optimistic case where no such cancellations occur. Figure reproduced from Ref. [234].

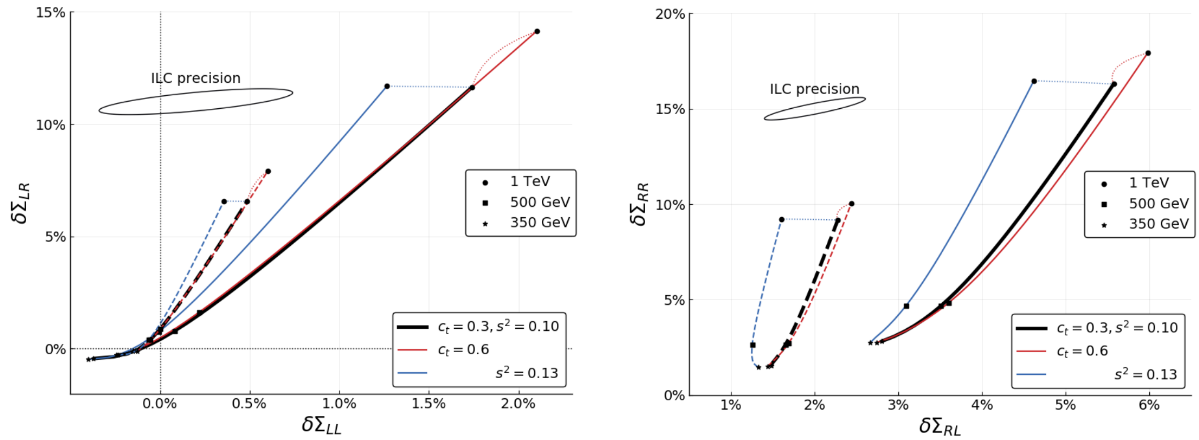

Figure 18: Deviations from the SM in helicity-dependent cross sections for $e^+e^- \to t\bar{t}$ in two examples of Randall-Sundrum theories, for centre-of-mass energies up to 1 TeV, from [235]. The ILC contour is the 68% 2-d uncertainty contour at 550 GeV, from [236].

of these points are well beyond current LHC limits.

The projected uncertainty contours presented in these figures are supported by full-simulation studies of the selection and reconstruction of $t\bar{t}$ final states [213, 236, 243]. The conspicuous six-fermion final state is readily isolated from backgrounds and the charged lepton yields a tag to distinguish the top and anti-top quark candidates up to ambiguities in the event reconstruction. The most recent projections are based on the analysis of optimal observables in Ref. [244], that propagates statistical uncertainties, taking into account a conservative energy dependent signal acceptance from the full-simulation studies. For bottom-quark production, the production cross section and forward-backward asymmetry are considered, based on the study of Ref. [75], see also Sec. 3.2.3.

As we noted above, disagreement between measurements and SM predictions for the value of g_L and g_R will demonstrate a deviation from the SM but will leave an ambiguity in the BSM model that leads to the effect. To gain more information, it is best to analyse the full data set for $e^+e^- \to t\bar{t}$ and $e^+e^- \to b\bar{b}$ parametrizing deviations from the SM as the coefficients of SMEFT dimension-6 operators. There are 30 dimension-6

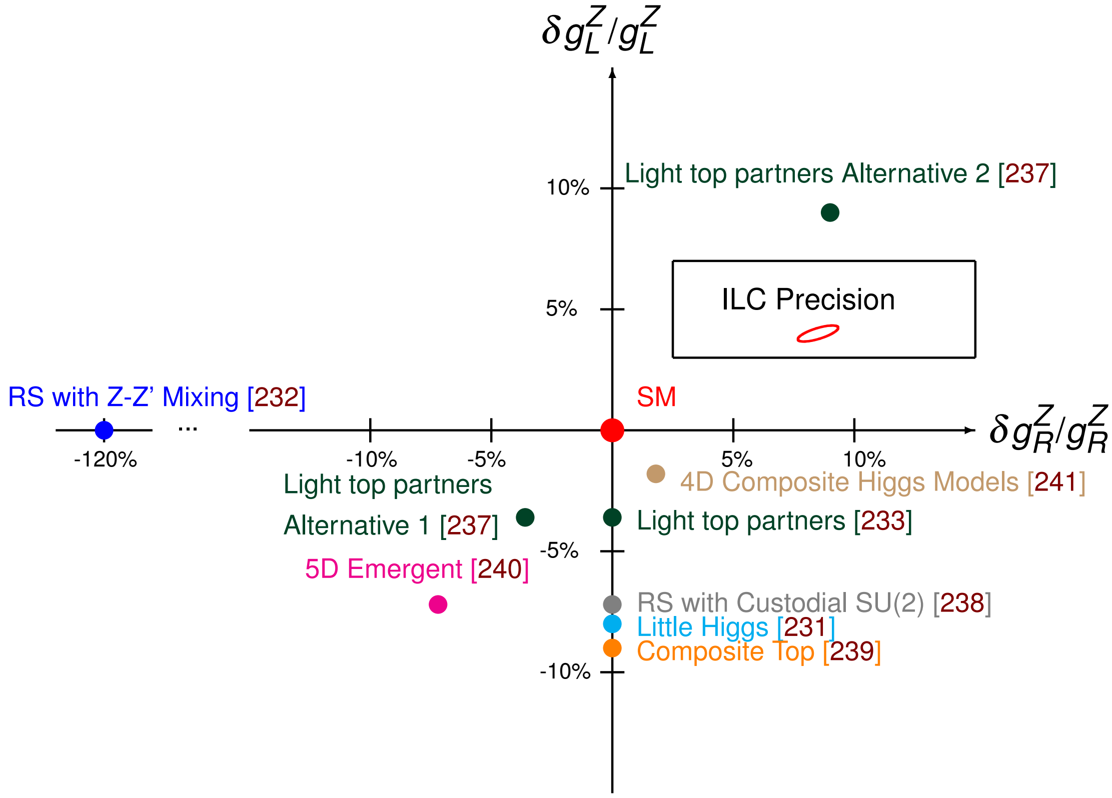

Figure 19: Predictions of a large number models of different types that predict deviations of the left- and right-handed couplings of the t quark to the Z boson. The ellipse in the frame in the upper right part indicates the precision that can be expected for the ILC running at a centre-of-mass energy of $\sqrt{s} = 500\,GeV$ after having accumulated $\mathscr{L} = 4\,\mathrm{ab}^{-1}$ of integrated luminosity shared equally between the beam polarisations $P(\mathrm{e}^-, \mathrm{e}^+) = (\pm 0.8, \mp 0.3)$. The original version of this figure can be found in [242]. We have rescaled the predictions to masses of new bosons or compositeness scales of 5 TeV and the masses of vector-like fermions to 2 TeV so that all points are well beyond current LHC limits.

SMEFT operators that couple to the top and bottom quarks, of which 14 are particularly important for $\mathrm{e}^+\mathrm{e}^-$ reactions. For orientation, the Wilson coefficient $c_{t\phi}$ modifies the top quark Yukawa coupling, the coefficients $c^{(1)}_{\phi Q}, c^{(3)}_{\phi Q}, c_{\phi t}$ modify the top quark vector and axial vector couplings to the Z boson, and the coefficients $c^{(1)}_{\ell Q}, c^{(3)}_{\ell Q}, c_{\ell t}, c_{et}$ give new four-fermion interactions.

We now report the projected uncertainties from such a fit to the full-simulation data [48, 245]. The 95% confidence level bounds on the SMEFT operator coefficients are shown in Fig. 20. The solid-colored bars show the limits from fits for individual Wilson coefficients; the lightly-shaded bars show the limits from a global fit including all operators. The HL-LHC projection (indicated in red) is based on an extrapolation of the current bounds of Ref. [246] to an integrated luminosity of 3 ab^{-1}, assuming that statistical and experimental uncertainties scale with the inverse square root of the integrated luminosity, while theory and modelling uncertainties are reduced to half of the current value. Global bounds are around $\mathscr{O}(0.1-1)$ TeV^{-2} for the two-fermion operator coefficients. No meaningful global bounds are found on the two-charged-lepton-two-top-quark operators, even if some LHC analyses of $\mathrm{t\bar{t}}l^+l^-$ production start to have some sensitivity [247]. The electron-positron data at $\sqrt{s} = 250$ GeV sharpen the bounds on the bottom operators, and coefficients that affect both bottom and top quark production such as $C^{(3)}_{\varphi Q}$, $C^{-}_{\varphi Q}$ and C^{-}_{lQ}, but bring no additional sensitivity for pure top quark operators.

The 500 GeV data yield an important improvement of all top operators. However, the global bounds remain an order of magnitude behind the individual bounds. The problem here is that there is a degeneracy between the effects of the two-fermion operators that modify the electroweak couplings and the four-fermion operators that generate contact interactions. Little Higgs models generate only the operators of the first type, while extra-dimensional models primarily generate operators of the second type, so it is important to break this degeneracy.

A second run above the $t\bar{t}$ threshold accomplishes this, since then the two-fermion and four-fermion operators can be disentangled using the strong energy dependence of the four-fermion operators. Operation at even higher energy yields stronger bounds still on the four-fermion operators. Note that the $1/s$ decrease of the top quark pair production cross section in the SM is compensated by the energy-growth of the sensitivity and the linear increase in instantaneous luminosity.

The study of top quark production at e^+e^- colliders can characterize the electro-weak interactions of the top quark and a complementary set of four-fermion operators to a precision that cannot be achieved at hadron colliders. High-energy operation and beam polarisation are key to robust global bounds. The stringent bounds on the top sector of the SMEFT correspond to a sensitivity well beyond the collider centre-of-mass energy in beyond-the-Standard-Model scenarios where the top quark and the Higgs boson are (partially) composite.

Several studies in Refs. [226, 248] explore the interplay between the top and Higgs and electro-weak sectors of the SMEFT, while Ref. [249] studies the impact of renormalization group evolution of operators. These studies include the e^+e^- projections from Ref. [244]. While these effects can be sizable, and should be part of future global analyses, the qualitative conclusions of this section remain unaltered.

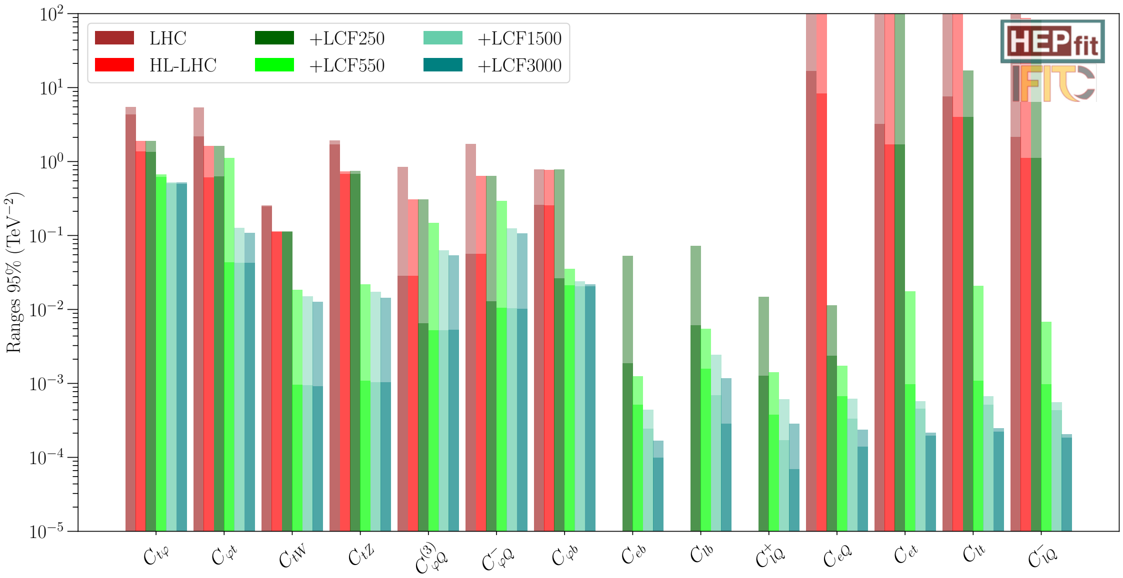

Figure 20: The 95% CL bounds from a global fit to 30 Wilson coefficients of SMEFT operators with top and bottom quarks. Coefficients are shown of two-fermion operators and four-fermion operators with charged leptons and heavy quarks. The fit includes also C_{tG} and fourteen $q\bar{q}t\bar{t}$ operators that are not shown. The four sets of results include the HL-LHC projection based on an extrapolation of current bounds in the S2 scenario [196] (indicated in red). Subsequent bars add the different stages of a linear collider facility, with e^+e^- data at increasing $\sqrt{t}$. Here, 3 ab^{-1} at 250 GeV, 5 ab^{-1} at 550 GeV, 3 ab^{-1} at 1.5 TeV and 5 ab^{-1} at 3 TeV are assumed. The dependence of the observables on the Wilson coefficients is parametrized at order $\mathcal{O}(\Lambda^{-2})$.

3.5.4 Quantum observables in top quark pair production

Following the proposal in Ref. [250], ATLAS and CMS have demonstrated that in top quark pair production at the LHC the top quark and top anti-quark are in a quantum-entangled state in regions of phase space close

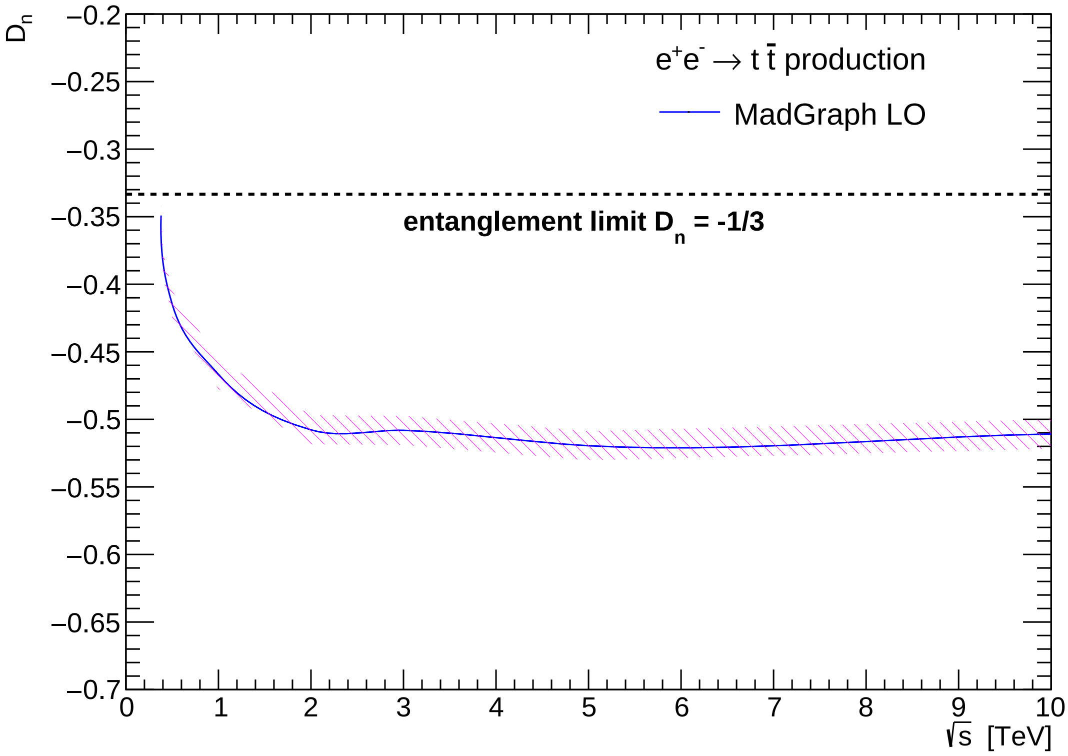

Figure 21: The SM prediction for the observable D_n defined in Ref. [255] versus the centre-of-mass energy. The $e^+e^- \to t\bar{t}$ process is generated at leading order in MadGraph and the top decays are simulated with MadSpin. The observable D_n is reconstructed from the charged leptons produced in the $t \to Wb \to l\nu b$ decay. Its value is used as an entanglement marker; a values below –1/3 indicate the top quark pair forms an entangled system.

to the $t\bar{t}$ threshold and in the boosted regime [251–253]. These results establish colliders as laboratories for the study of quantum phenomena at the highest energies. A steady flow of new ideas has been put forward since (see e.g. Ref. [254] for a recent review).

Top quark pairs at electron-positron colliders offer an interesting potential for the study of quantum observables. Unlike the LHC, top quark pairs are entangled in the entire phase space. The controlled initial state and clean final state allow for precise measurements. The SM prediction at leading order (generated with MadGraph/MadSpin) for the degree of entanglement is indicated in Fig. 21. The entanglement marker D_n exceeds the entanglement limit of –1/3 at all energies above the top quark pair production threshold. D_n initially grows strongly with the centre-of-mass energy [255] and reaches a value of approximately –0.5 at energies above 1–1.5 TeV. The prediction corresponds to unpolarised beams.

A study by Altomonte et al. [256] demonstrates a detailed quantum tomography of the $e^+e^- \to t\bar{t}$ process is possible at electron-positron colliders with polarised beams. The full Choi matrix — that determines the input-output transitions of the quantum process — can be experimentally reconstructed from measurements of top quark spin observables with different beam polarisation configurations. Note that this requires dedicated running periods where the longitudinal polarisation of the electron and positron beams must be rotated through spin rotator magnets.

The study of quantum observables in e^+e^- collisions offers a new approach to characterize the SMEFT and to probe potential extensions of the SM, but also tests the foundations of quantum mechanics at the highest energies.

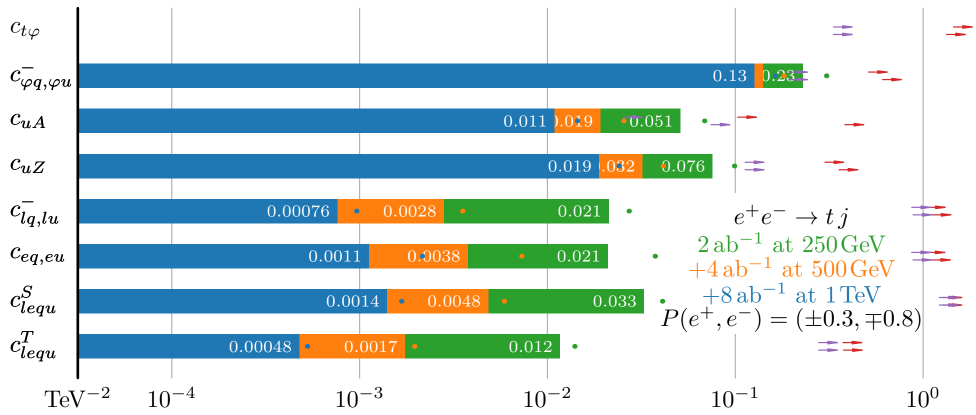

Figure 22: Global projected 95% C.L. constraints on dimension-six operator coefficient leading to $e^+e^- \to tj$ production at increasing centre-of-mass energies. Horizontal bars account for longitudinal beam polarisation, while the coloured dots would be obtained with unpolarised beams. For comparison, the red and purple arrows show present constraints and HL-LHC prospects respectively, for top-up (upper arrow) and top-charm (lower-arrow) flavour changes. Figure reproduced from Sec. 10.1.4 of Ref. [14].

3.5.5 Top quark FCNC interactions

Top-quark physics already starts at $\sqrt{s} \gtrsim m_t$ in electron-positron collisions. Single top-quark production in association with an up or charm quark, $e^+e^- \to tj$, can indeed be searched for. Such a quark-flavour-changing interaction (commonly denoted FCNC) is particularly suppressed in the SM, so that its observation would constitute an unambiguous sign of new physics.

If the underlying dynamics is heavier than the centre-of-mass energy, the SMEFT can be employed to model such FCNCs. They are first generated by dimension-six operators. At tree-level, those which contribute to $e^+e^- \to tj$ generate $t\bar{q}\gamma$, $t\bar{q}Z$, and $e\bar{e}t\bar{q}$ interactions. A new $t\bar{q}h$ interaction also generates top-quark decays, while a $t\bar{q}g$ one is efficiently probed in single-top-quark production at hadron colliders.

Predictions for top-quark FCNC processes, accurate to next-to-leading order in QCD, were computed in Refs. [257, 258] and a global analysis of existing constraints — including LEP2 ones — was performed in Ref. [259]. Based on this, HL-LHC prospects were provided in Sec. 8 of Ref. [260]. Single top-quark FCNC production at future lepton colliders was notably investigated in Refs. [261–263], in Sec. 3.1.2 of Ref. [179] for CLIC and in Sec. 10.1.4 of Ref. [14] for the ILC.

Figure 22, reproduced from Ref. [14], shows the constraints expected from collisions accumulated at 250, 500, and 1000 GeV centre-of-mass energies (coloured bars). Compared to HL-LHC prospects (purple arrows), the improvement in sensitivity mostly concerns four-fermion $e\bar{e}t\bar{q}$ interactions (lower four bars). It reaches almost two orders of magnitude with 2 ab^{-1} collected at 250 GeV. Higher-energy runs lead to even tighter constraints. This family of contact operators indeed generates amplitudes which grow quadratically with the centre-of-mass energy. Three BSM benchmarks for top-quark FCNC interactions will be provided in Sec. 5.3 of the ECFA focus topic study for Higgs, top-quark, and electroweak factories. Their contributions to four-fermion operators are however not estimated. It would be interesting to understand which new-physics scenarios generate sizeable such operators and therefore benefit the most from lepton collisions. The complementarity between FCNC and flavour-conserving channels (e.g. top-, bottom- and charm-quark pair production) also remains to be examined in specific scenarios where they would be correlated.

3.5.6 Top quarks and axions

The subject of Axions and Axion-like particles (ALPs) has become an important focus topic in the high energy physics community. ALPs represent a well-motivated, testable scenario of new physics hypothesising a new, relatively light pseudoscalar particle, a, that is a singlet under the SM gauge group. The lightness of this particle with respect to other putative new physics states is explained by the fact that the ALP is assumed to be pseudo Nambu-Goldstone boson (pNGB) of a spontaneously broken global symmetry in the UV. The pNGB nature manifests itself in a shift-symmetry of the ALP field, $a \to a + c$ where c is a constant, under which the ALP interaction Lagrangian should be approximately invariant. This means that the ALP couples preferentially via derivative interactions, built out of shift-invariants like $(\partial^\mu a)$. This fact, along with the ALP quantum numbers dictate that its interactions with the SM are necessarily described by an EFT, suppressed by a generic new physics scale, f_a. The leading, non-redundant set of interactions is described by the following dimension-5 effective Lagrangian,

$$\mathscr{L}_{\rm ALP}^{D=5} = \frac{1}{2}(\partial_\mu a)(\partial^\mu a) - \frac{m_a^2}{2}a^2 + c_{GG}\frac{a}{f_a}\frac{\alpha_s}{4\pi}G^A_{\mu\nu}\tilde{G}^{\mu\nu A} + c_{WW}\frac{\alpha_L}{4\pi}\frac{a}{f_a}W^I_{\mu\nu}\tilde{W}^{\mu\nu I}$$
$$+ c_{BB}\frac{\alpha_Y}{4\pi}\frac{a}{f_a}B_{\mu\nu}\tilde{B}^{\mu\nu} + \frac{\partial^\mu a}{f_a}\sum_F \bar{F}\mathbf{c}_F\gamma_\mu F, \tag{3}$$

where α_s, α_L and α_Y denote the $SU(3)_C$, $SU(2)_L$ and $U(1)_Y$ gauge couplings of the SM, $\tilde{X}^{\mu\nu} = \frac{1}{2}\varepsilon_{\mu\nu\rho\sigma}X^{\rho\sigma}$ is the dual field strength tensor, and F runs over the five fermionic representations of the SM, $\{Q, L, u, d, e\}$. The Wilson coefficients, $\mathbf{c}_F$, are 3×3 Hermitian matrices in flavour space.

The study of ALPs at colliders is a rich topic and its couplings to the heavier fermions, especially the top quark, has received relatively little attention to date. Focusing on final states involving the top quark probes, in particular, the ALP-top coupling

$$\mathscr{L}_{\rm ALP}^{\rm top} = c_{tt}\frac{\partial_\mu a}{f_a}\bar{t}\gamma^\mu\gamma^5 t, \quad c_{tt} \equiv [c_u]_{33} - [c_Q]_{33}. \tag{4}$$

Several works have considered the sensitivity of the LHC to this coupling in top-rich final states such as in the direct production of an ALP in association with a $\mathrm{t\bar{t}}$ pair, four-top production, as well as virtual ALP effects in $\mathrm{t\bar{t}}$ production [264–267]. The broad conclusion is that this coupling is quite challenging to test, and new physics scales on the order of a few hundred GeV are still permissible, with the sensitivity currently driven by precision measurements of $\mathrm{t\bar{t}}$ production. The precision measurement of the spin-density matrix has the potential to improve on this sensitivity [268].

At $\mathrm{e^+e^-}$ colliders, there are very few explicit studies of the sensitivity to c_{tt} or investigations of ALP signatures in top-quark final states. However, several ALP production mechanisms have been studied in this context. For example, it is known that ALP of mass $m_a < m_z$ can be efficiently produced via decays of the Z bosons which leads to bounds from LEP and LHC data [269–271] and promising sensitivity to its gauge boson interactions at a future collider Z-pole run [272, 273]. Several other production mechanisms, mostly focused on the gauge bosons couplings, have been investigated for future $\mathrm{e^+e^-}$ colliders [179, 270, 274–280].

In top quark final states, the direct sensitivity to c_{tt} can primarily be probed via direct production in the $\mathrm{t\bar{t}A}$ process or via indirect effects in $\mathrm{t\bar{t}}$. These would become accessible at energies about the top pair threshold and have the potential to improve on existing bounds, although no explicit studies exist to date. Precise measurements of spin correlations and scans across the top pair threshold would be particularly suited to testing these indirect effects. Associated production sensitivity would depend on the dominant ALP decay channel, and it is crucial to also consider loop-induced decay modes of the ALP [281]. Indeed, the clean environment of a future $\mathrm{e^+e^-}$ collider would facilitate the identification of the ALP decay products and therefore provide access to many of the ALPs couplings. For example, in the top-philic case, where c_{tt} is taken to dominate, the ALP preferentially decays at one-loop into a $b\bar{b}$ pair when its mass is below the top-pair threshold.

An interesting feature of ALP production is that its derivative couplings lead to enhanced off-shell effects, in which non-resonant diagrams with intermediate ALP contributions are comparatively important with respect to non derivatively-coupled particles [282]. These allow the possibility of studying $\mathrm{t\bar{t}}$ production mediated by off-shell ALPs, probing combinations of c_{tt} with other ALP couplings that mediate its production at $\mathrm{e^+e^-}$ colliders. Since derivative couplings to fermions can be shown to yield effects proportional to the fermion mass, direct production from $\mathrm{e^+e^-}$ annihilation is expected to be suppressed. However, at higher energy $\mathrm{e^+e^-}$ colliders, production via photon or vector boson fusion is a promising candidate. These channels have mostly been used to determine the sensitivity to gauge bosons couplings via gauge boson final states [283, 284], demonstrating substantial improvements over LHC bounds. A study of fermionic couplings, apart from the top quark, was also conducted in Ref. [285], considering vector boson fusion at the 1 TeV ILC, and assuming ALP decay via a universal coupling to fermions weighted by their mass. A promising sensitivity was determined for higher mass ALPs above a few tens of GeV for the $b\bar{b}$ decay mode. In the case of the $t\bar{t}$ final state, such searches would yield sensitivity to combinations of c_{tt} and c_{WW} or c_{BB}. The photon fusion case was investigated in Ref. [286], for e^+e^- centre-of-mass energies of 1.5 and 3 TeV. The study determined the best projected sensitivities of $(c_{BB}c_{tt})^{\frac{1}{2}} < 2.8\ \text{TeV}^{-1}$ and $(\sqrt{c_{WW}c_{tt}})^{\frac{1}{2}} < 4.3\ \text{TeV}^{-1}$ for $m_a = 10$ GeV, which decrease by about an order of magnitude for ultra-heavy ALPs with $m_a = 10$ TeV. This channel would benefit from further investigation.

Finally, it is worth noting that beyond dimension-5, the ALP EFT should strictly be considered alongside other potential dimension-6 deformations of the SM, encapsulated by, *e.g.*, the SMEFT. It is known, for instance, that at this order, the ALP EFT operators mix with the usual dimension-6 SMEFT operators under renormalisation group evolution [287, 288]. This means that ALP couplings can be probed in a global manner using SMEFT interpretations of collider data [289], and the precision SMEFT programme enabled by a future e^+e^- machine in the top sector would likely lead to better sensitivity to some ALP couplings. These should be complemented by the full future e^+e^- measurement programme, including EW precision tests, Higgs physics, W^+W^- production, etc.

3.6 Direct searches for BSM including SUSY

The previous sections highlighted the discovery potential of a linear collider facility by precision measurements, indirectly in most cases. It is evident that within the kinematic limit a linear collider facility can also directly detect new particles, example of ALP production has been discussed in the previous section. The following sections will focus on the search opportunities offered by the energy upgrade of the LC facility (see Sec. 4.4 for details on the upgrade options), the region between 500 GeV and ~1 TeV in particular. Extensive discussion of the discovery potential at the lower energies can be found in [14, 41].

When discussing LC discovery prospects one has to stress that lepton colliders are complementary to the hadron ones. Probed with the highest sensitivity are electroweak production channels and, thanks to the clean environment, the sensitivity extends down to the smallest masses or mass splittings, covering also the invisible final states in many cases. In addition to the direct BSM discovery potential in model parameter range not accessible at LHC, follow-up precision studies are possible in a much wider domain if any new state is observed at HL-LHC. Presented below are selected studies addressing discovery prospects at different LC energy stages: searches for light electroweak SUSY scenarios, light exotic scalars, Heavy Neutral Leptons and dark matter particles.

3.6.1 LC reach for light electroweak SUSY

Supersymmetry (SUSY) predicts the existence of spin-1/2 partners of the SM gauge bosons as well as for the Higgs bosons (which in the minimal version correspond to a 2HDM-like Higgs sector), the electroweakinos (EWinos). These states play a crucial role in gauge coupling unification, they are intimately tied to an understanding of the electroweak scale through the Higgs mixing parameter μ, and they are of primordial interest in the context of SUSY dark matter (DM). Naturally, EWinos are one of main goals of SUSY searches at the LHC, but limits are still relatively weak and stongly model dependent. The nature of the EWinos is determined by the hierarchies of the underlying mass parameters. Within the minimal supersymetric model, the MSSM, the relevant mass parameter are M_1 and M_2, the soft SUSY-breaking parameters corresponding to the $U(1)$ and $SU(2)$, respectively, as well as the Higgs mixing parameter μ. The motivation for light EWinos can be twofold. There are intersting theoretical arguments that favor $\mu \ll M_1, M_2$, corresponding to light higgsinos. On the other hand, there are some interesting anomalies in the LHC searches for light EWinos, possibly favoring $M_1, M_2 \ll \mu$, corresponding to a light wino/bino scenario. Both scenarios have their own implications for the searches at the LC, as will be briefly described below, focusing on the MSSM as the benchmark model.

Natural SUSY: LC reach for light higgsinos

While supersymmetry offers a 't Hooft technically natural solution to the Big Hierarchy problem, cumulative results from LHC Run 2 [290, 291] and WIMP direct detection searches have brought out a Little Hierarchy problem (LHP): why is there a gap between the weak scale $m_{weak} \sim m_{W,Z,h} \sim 100$ GeV and the apparently lowest-possible soft SUSY breaking scale $m_{\rm SUSY} > 1-2$ TeV?

The LHP is a problem of practical naturalness [292]: an observable is natural if all independent contributions to the observable are comparable to or less than the observable in question (this is how naturalness was successfully applied for instance by Gaillard and Lee in predicting the charm quark mass shortly before it was discovered). In the case of SUSY, the magnitude of the weak scale is related to the soft SUSY breaking terms and μ parameter by the electroweak minimization conditions:

$$m_Z^2/2 = \frac{m_{H_d}^2 + \Sigma_d^d - (m_{H_u}^2 + \Sigma_u^u)\tan^2\beta}{\tan^2\beta - 1} - \mu^2 \simeq -m_{H_u}^2 - \Sigma_u^u(\tilde{t}_{1,2}) - \mu^2 \tag{5}$$

where $m_{H_{u,d}}^2$ are soft SUSY breaking Higgs mass terms, the $\Sigma_{u,d}^{u,d}$ contain a large assortment of SUSY loop corrections and μ is the SUSY conserving μ parameter which feeds mass to W, Z, h and also to the SUSY higgsinos (the superpartners of the Higgs bosons). Practical naturalness requires all terms on the right-hand-side of Eq. (5) to be comparable (within a factor of a few) to $m_Z^2/2$. Note this is the most conservative and non-optional application of naturalness (plausibility) within the MSSM. Gluinos, top squarks and other SUSY particles have loop-suppressed contributions to the weak scale and so can live at the multi-TeV scale with little cost to naturalness, but higgsinos, with mass $m(higgsino) \sim \mu$, must lie close to the weak scale, with $\mu \lesssim 200-400$ GeV. Thus, higgsino pair production is a key target for an e^+e^- collider operating with $\sqrt{s} > 2m(higgsino)$ [293]. Indeed, there are at present some slight 2σ excesses for both ATLAS [294] and CMS [295] Run 2 data for the soft dilepton+jet+missing energy signature which could arise from light higgsino pair production at LHC.

In Fig. 23, we show the higgsino discovery plane [296] $m_{\tilde{\chi}_2^0}$ vs. $\Delta m^0 \equiv m_{\tilde{\chi}_2^0} - m_{\tilde{\chi}_1^0}$ along with theoretically preferred dots from (stringy) natural SUSY as expected from the string landscape: these prefer mass gaps $\Delta m^0 \sim 5-10$ GeV, making discovery at LHC difficult in searching for dileptons from $\tilde{\chi}_2^0 \to \ell^+\ell^-\tilde{\chi}_1^0$ decay since kinematically $m(\ell^+\ell^-) < m_{\tilde{\chi}_2^0} - m_{\tilde{\chi}_1^0}$. Several HL-LHC reach contours are shown which probe the left-side of the considered mass plane [297]. Whereas HL-LHC can see much of the theoretically-favored region, it cannot see all of it. We also show the LC500 and LC1000 reach contours. In particular, once $\sqrt{s} > m_{\tilde{\chi}_2^0} + m_{\tilde{\chi}_1^0}$ or $2m_{\tilde{\chi}_1^\pm}$, then a LC should have no problem picking up the soft decay debris from light higgsino pair production, and ultimately reconstructing the various higgsino masses and underlying SUSY parameters[298].

SUSY searches at the linear e^+e^- colliders profit from the well defined initial state, electron and positron beam polarisations, hermetic detectors, clean running environment and trigger-less operation, which is a huge advantage when looking for unexpected and most likely very soft final states. Prospects for SUSY particle discovery, identification and measurements were investigated in great detail, based on the full detector simulation, for selected scenarios [299–301]. Presented in Fig. 24 are example results from higgsino and stau search studies [302, 303] showing that a linear collider facility such as ILC can explore the full kinematic space of the considered models up to the kinematic limit.

LC reach for the light wino/bino scenario

Recent searches for the "golden channel" for EWinos, $pp \to \tilde{\chi}_2^0\tilde{\chi}_1^\pm \to \tilde{\chi}_1^0 Z^{(*)}\tilde{\chi}_1^0 W^{(*)}$ show consistent excesses between ATLAS and CMS in the 2 lepton and the 3-lepton searches, assuming $m_{\tilde{\chi}_2^0} \approx m_{\tilde{\chi}_1^\pm} \gtrsim 200$ GeV and $\Delta m := m_{\tilde{\chi}_2^0} - m_{\tilde{\chi}_1^0} \approx 25$ GeV [294, 295, 304, 305]. This mass configuration arises naturally in SUSY scenarios with wino/bino DM. In these scenarios the lightest supersymmetric particle (LSP), assumed to be the lightest neutralino, $\tilde{\chi}_1^0$, serves as a DM candidate.

Taking into account the relevant LHC search limits, the DM relic density [306] as well as the DM direct detection limits from LZ [307], it was shown in [308] that indeed wino/bino DM in the MSSM can fit the observed excesses. To this end, a parameter scan in the wino/bino scenario was performed with $|M_1|$ varied between 100 GeV and 400 GeV, $|M_1| \le M_2 \le 1.1|M_1| \le \mu$ and $2 \le \tan\beta \le 60$. The slepton masses were assumed to be heavier than the LSP. The result of the scan (in the case $M_1 \times \mu < 0$) is shown in the left plot of Figure 25 in the $m_{\tilde{\chi}_2^0}$–Δm plane of the MSSM. The gray points show all scan points, and the various colors indicate the effects of the experimental constraints taken into account. (Light slepton masses yield a large contribution for the

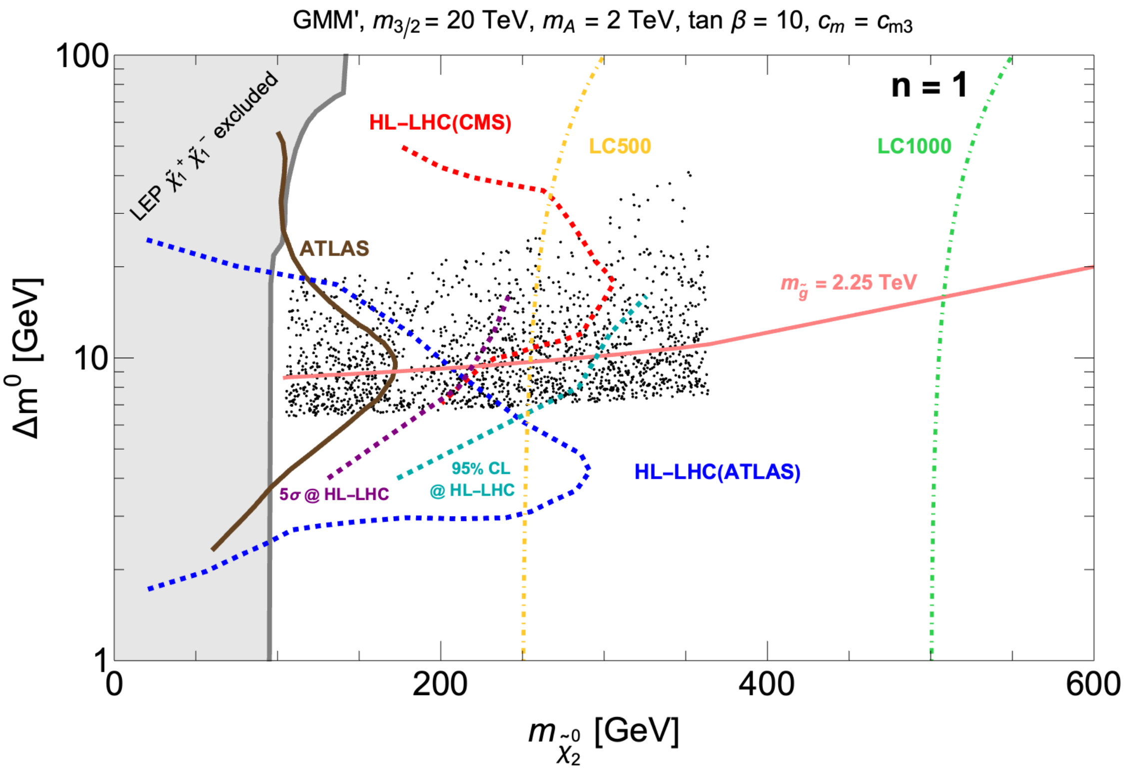

Figure 23: The higgsino discovery plane [296] along with predictions from a stringy natural landscape SUSY model (black dots: the greater the density, the more stringy natural it is) along with projected HL-LHC reach and the reach from LC500 and LC1000. The various colliders can probe the left-side of the reach contours.

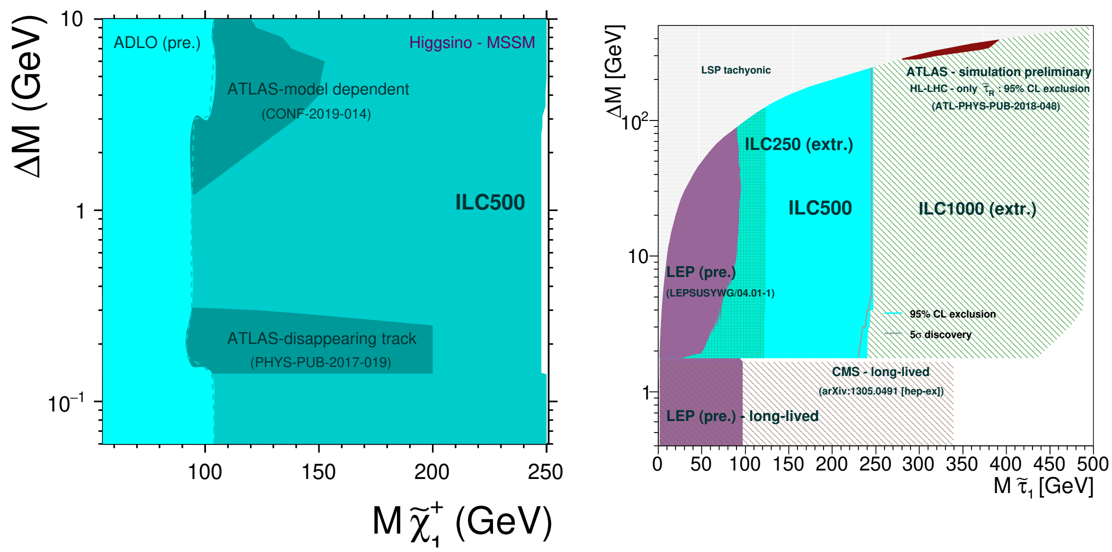

Figure 24: Comparison of the existing limits from LEP and LHC with the expected ILC limits for: $\tilde{\chi}_1^{\pm}$ search in the Higgsino-like scenario (left) [302] and $\tilde{\tau}$ search in the worst-case scenario (right) [303].

anomalous magnetic moment of the muon, whereas heavier slepton masses yield a negligible contribution.) The solid dark red (black) line show the search limits from ATLAS [294, 304] (CMS [295, 305]) in the two search channels discussed above, together with the corresponding theory uncertainties indicated by dashed lines. Shown in only the stronger of the two experimental limits. Consequently, the red stars indicate the scan points that fulfill all experimental constraints, including the LHC searches. One can observe that the part of the parameter space where ATLAS and CMS observe an excess in both their search channels is well populated. In [308] it was furthermore shown that for $m_{\tilde{\chi}_2^0} \approx m_{\tilde{\chi}_1^\pm} \leq 250$ GeV and $\Delta m \approx 25$ GeV the LHC production cross section for $pp \to \tilde{\chi}_2^0 \tilde{\chi}_1^\pm \to \tilde{\chi}_1^0 Z^{(*)} \tilde{\chi}_1^0 W^{(*)}$ has roughly the size to produce the observed excesses. Going a step further, [309] discussed the complementarity of the soft lepton excesses with other excesses in LHC monojet searches [310, 311], and showed that non-SUSY interpretations fit these excesses less well.

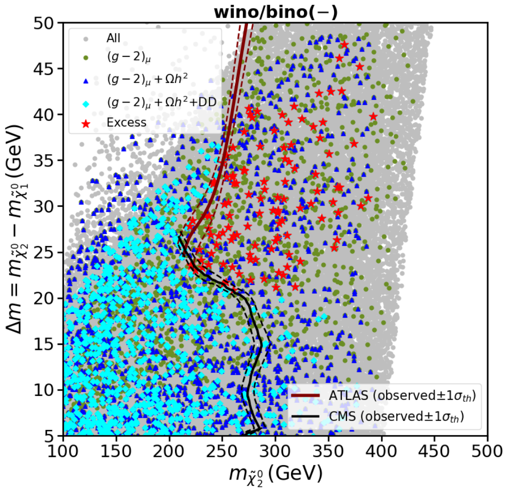

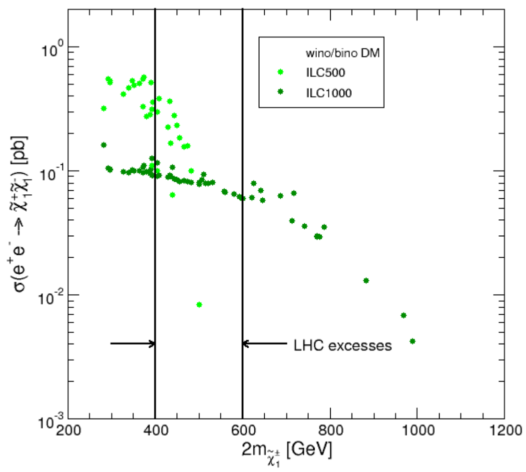

Figure 25: Left: Results of a parameter scan in the wino/bino DM scenario in the $m_{\tilde{\chi}_2^0}$–$\Delta m (:= m_{\tilde{\chi}_2^0} - m_{\tilde{\chi}_1^0})$ plane of the MSSM. For the color coding see text. The red stars show the points that are in agreement with all experimental constraints. Taken from [308]. Right: Cross section predictions for $e^+e^- \to \tilde{\chi}_1^\pm \tilde{\chi}_1^\mp$ in the wino/bino DM scenario for two centre-of-mass energies, $\sqrt{s} = 500, 1000$ GeV. The range that rougly corresponds to the observed LHC excesses is marked by two vertical lines. Adapted from [312].

This opens up very interesting prospects for the production of light SUSY particles at a LC. In a previous analysis [312] it was shown that the production cross section for $e^+e^- \to \tilde{\chi}_1^\pm \tilde{\chi}_1^\mp$ is in the range of $\mathcal{O}(100)\,\text{fb}^{-1}$ in this kind of scenarios. This is demonstrated in the right plot of Figure 25 (adapted from [312]), where for wino/bino DM the chargino production cross section is shown as a function of $2m_{\tilde{\chi}_1^\pm}$ for two centre-of-mass energies, $\sqrt{s} = 500, 1000$ GeV. The range that rougly corresponds to the observed LHC excesses is marked by two vertical lines. This prominent example demonstrates the possibility that BSM particles discovered by the LHC that are within the kinematic reach of a LC can be produced abundantly, and thus can also be studied in detail.

3.6.2 LC reach for light exotic scalars

BSM scenarios involving light scalars, with masses accessible at future lepton colliders, are not excluded even with the latest experimental data. Sizeable production cross sections for new scalars can also coincide with non-standard decay patterns, so a range of decay channels should be considered. Lepton colliders can be sensitive to exotic scalar production even for very light scalars, thanks to the clean environment, and precision and hermeticity of the detectors. Different production and decay channels, including invisible decays of a new scalar, S, can be considered, but the highest sensitivity is expected to come from the scalar-strahlung production process, $e^+e^- \to ZS$, where production of the new scalar can be tagged, independent of its decay, based on the recoil mass technique (similar to the approach used for the 125 GeV Higgs produced in the Higgs-strahlung process). Recent results on light exotic scalar searches in the scalar-strahlung process, submitted as input to the report of the ECFA Higgs/Electroweak/Top Factory Study, are summarized in Fig. 26. Strong limits on the light scalar production cross section are already expected from decay-mode-independent searches, based on the recoil mass reconstruction technique. If a light scalar preferentially decays to tau pairs, an improvement in search sensitivity by more than an order of magnitude is expected, making this channel the most sensitive one in this type of searches (in terms of limits on production cross section times corresponding branching fraction). Expected exclusion limits in the invisible scalar channel as well as limit estimates for the scalar decay to $b\bar{b}$ with hadronic Z boson decays, are slightly weaker due to much higher backgrounds, while constraints on scalar decays to $b\bar{b}$ with leptonic signature are limited by the leptonic branching fraction of the Z boson.

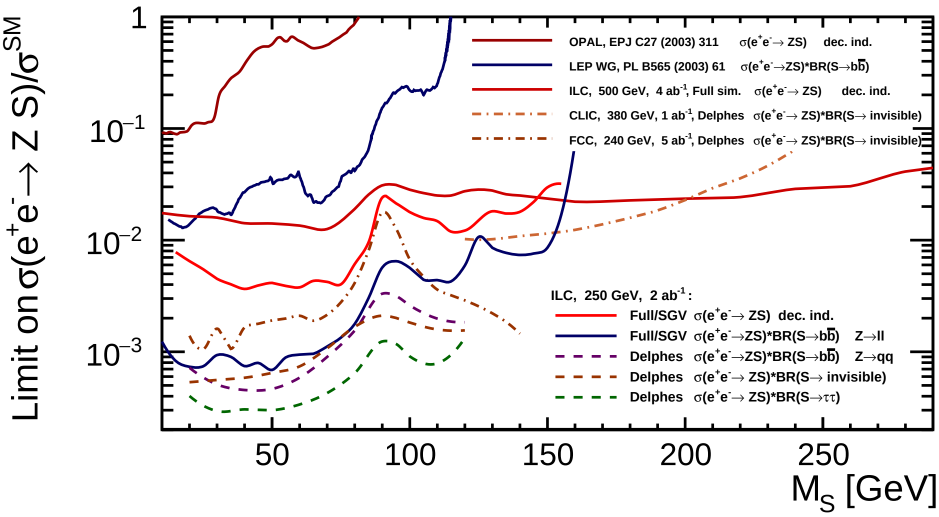

Figure 26: Comparison of expected exclusion limits for exotic light scalar production searches in the scalar-strahlung processes, for different search strategies and scalar decay channels considered. When particular decay channel is indicated, limits are set on the cross section ratio times the branching fraction [41].

As a concrete example we take the hints of a new Higgs boson at ~ 95.4 GeV (h_{95}) in the $gg \to h_{95} \to \gamma\gamma$ channel as reported by CMS [313] and ATLAS [314]; see [315] for a combination leading to an excess of $3.1\,\sigma$. In the same mass range LEP reported a $\sim 2\,\sigma$ excess in the $e^+e^- \to Z \to Zh_{95} \to Zb\bar{b}$ channel [316]. These two types of excesses can simultaneously be described in a variety of BSM models. It was shown in [317], that models extending the SM Higgs sector by one additional doublet and one additional singlet are an interesting option in this context. The interpretation of the h_{95} as a new light CP-even Higgs boson, receiving its couplings to SM particles from a mixing with the SM Higgs doublet, ensures a non-negligible coupling to Z bosons, falling into the regime accessible at future e^+e^- colliders as shown in Fig. 26. This results in an abundant production of the h_{95}, allowing an analysis of its decay patterns and couplings. The result of such an analysis is shown in Figure 27, based on an analysis within the S2HDM (the SM extended by a second complex doublet and one complex singlet) [318, 319]. Shown are points passing all relevant theoretical and experimental constraints that predict a di-photon signal strength $\mu\gamma\gamma$ in the preferred range by CMS [313] in the ($|c_{h_{95}\tau\tau}|$–$|c_{h_{95}VV}|$) plane. Here we denote with $c_{h_{95}xx}$ the coupling strength of the h_{95} to the particle x (where V denotes $W^\pm$ or Z) relative to the coupling strength of the SM Higgs boson. The Yukawa type II and the type IV parameter points are shown in blue and orange, respectively. The shaded ellipses around the dots indicate the projected experimental precision with which the couplings of h_{95} could be measured at the ILC250 with $2\,\text{ab}^{-1}$ of integrated luminosity following [320] (and references therein). One can observe the anticipated high precision of the coupling determination of the h_{95} that will allow to discriminate between various Yukawa types, identify the model realised in nature and pin down its parameters.

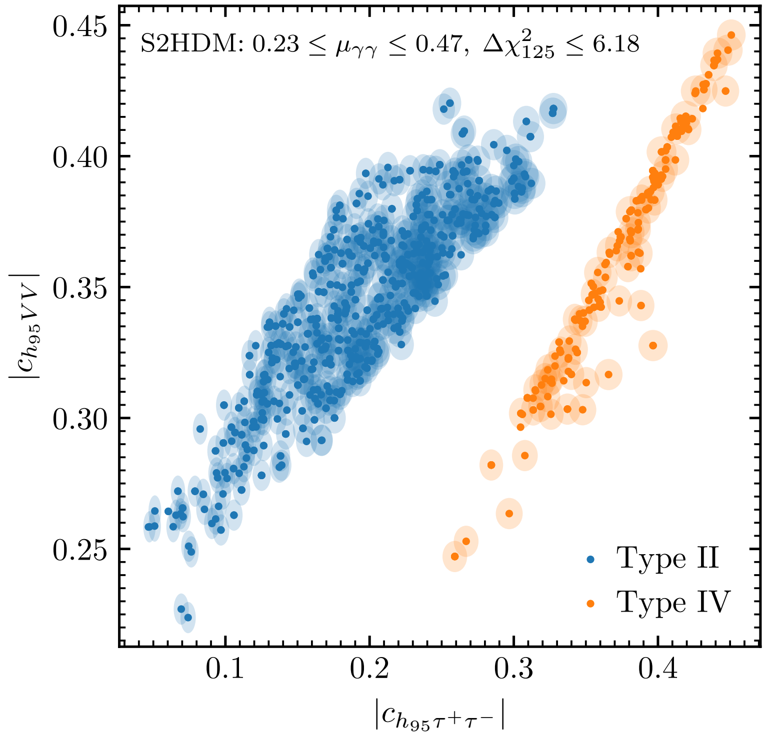

Figure 27: S2HDM parameter points passing the applied constraints that predict a di-photon signal strength in the preferred range by CMS [313] in the ($|c_{h_{95}\tau\tau}|$–$|c_{h_{95}VV}|$) plane (see text) The type II and the type IV parameter points are shown in blue and orange, respectively. The shaded ellipses around the dots indicate the projected experimental precision with which the couplings of h_{95} could be measured at the ILC250 with 2 ab^{-1} of integrated luminosity. Taken from [319].

3.6.3 LC reach for heavy neutral leptons

Observation of neutrino oscillations is a direct evidence that neutrinos have a non-zero mass. This indicates the existence of right-handed neutrinos, which are however not a part of the SM. Models with Heavy Neutral Leptons (HNLs) could explain a number of SM "mysteries", like the tiny neutrino masses (via seesaw mechanism), the baryon asymmetry of the universe (with additional source of CP violation) or existence of dark matter (with stable sterile neutrinos).

Lepton colliders are clearly the preferred option for the exotic lepton searches. Depending on the HNL's mass, width and coupling to the SM particles, as well as additional model details (for UV-complete models), many different experimental signatures can be considered. For light HNL states, up to the masses of the order of M_W, they could show up in rare or invisible decays of the Z, W or Higgs bosons. With very small SM couplings light states could also be long-lived, resulting in the striking signature of displaced vertices. However, for masses above M_W, only prompt decays of HNLs are expected. Sensitivity of future lepton colliders to production of heavy neutrinos was considered in the series of studies [321–323], and results are summarized in Fig. 28 (left). For each of the considered running scenarios, sensitivity range extends almost up to the centre-of-mass energy and the expected limits on the heavy neutrino coupling to the SM leptons, V^2_{lN}, are much more stringent than any results for high-energy hadron colliders. This is because, for the considered mass and energy range, single HNL production cross section in e^+e^- collisions is dominated by the contribution from the t-channel W boson exchange and depends very weakly on the heavy neutrino mass almost up to the kinematic limit. For pp colliders, only s-channel production processes (Drell-Yan) contribute, decreasing fast with the invariant mass of the produced final state.

Heavy Neutral Leptons can be of Dirac nature with only lepton-number conserving (LNC) decays or of Majorana nature, including also lepton-number violating (LNV) production and decay processes. If heavy neutrinos are discovered (at 5σ level) at the future lepton collider, we should also be able to identify their nature (on 95% C.L.), as shown in Fig. 28 (right).

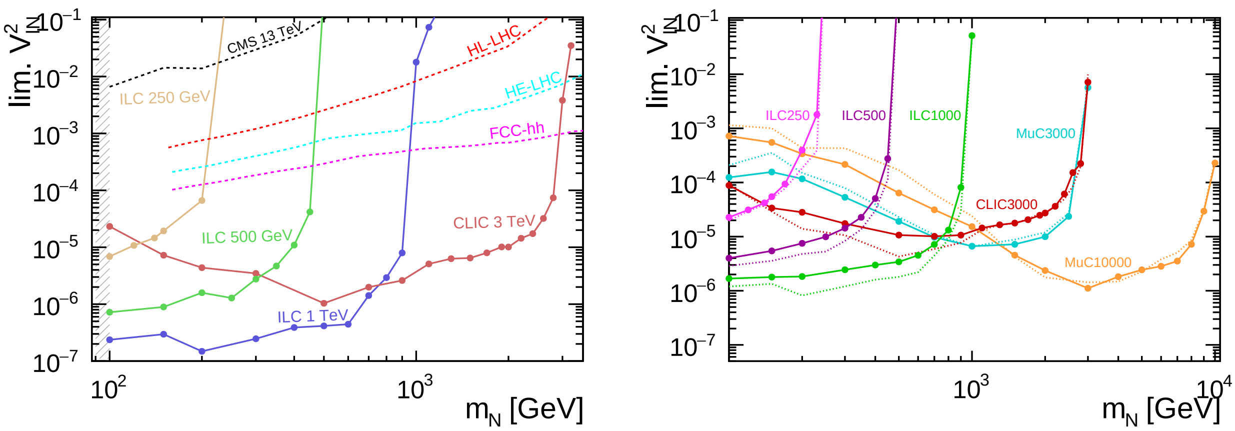

Figure 28: Expected 95% C.L. exclusion limits on the coupling $V^2_{\ell N}$ (left) and 95% C.L. discrimination limits between Majorana and Dirac nature (right), as a function of the heavy neutrino mass, m_N,for different lepton collider setups, as indicated in the plot. Dashed lines in the left plot indicate limits from current and future hadron colliders based on [324, 325]. Expected 5σ discovery sensitivity is also indicated in the right plot (dotted lines). Figures taken from [323].

3.6.4 LC reach for dark matter scenarios

High energy e^+e^- colliders offer a unique possibility for the most general search of dark matter (DM) particles based on the mono-photon signature. The advantage of this approach is that the photon radiation from the initial state is fully described within the Standard Model and depends only indirectly on the DM production mechanism. Prospects for DM searches were studied for ILC and CLIC, both in the heavy mediator approximation (using the EFT-based approach) [326, 327] as well as for the finite mediator masses, when contributions from resonant production of light mediators have to be taken into account [328].

Example limits on the mediator coupling to electrons, g_{eeY}, for the ILC running at 250 and 500 GeV, and CLIC running at 3 TeV are presented in Fig. 29. Considered are scenarios with light Dirac DM pair-production, m_χ=1 GeV for ILC and 50 GeV for CLIC, and different structures of mediator coupling to electrons. As mediator decays to DM particles are expected to dominante, mediator coupling to DM is fixed by setting its width to 3% of its mass. One has to note that for the coupling range considered, the analysis of mono-photon spectra gives higher sensitivity to processes with light mediator exchange than their direct searches in SM decay channels.

Results presented in Fig. 29 indicate also that, assuming couplings of the order of one, precision measurements in the mono-photon channel are sensitive to mediator mass scales significantly above the collision energy. In this domain, EFT approach is safely applicable, unlike in the hadron colliders, which often probe only the mass scales below the colision energy. In the EFT limit, for high mediator masses above the collision energy, constrained from the analysis of mono-photon events is the ratio of the mediator mass to the square root of the product of its couplings to electrons, g_{eeY}, and DM particles $g_{\chi\chi Y}$, $\Lambda = M_Y/\sqrt{g_{eeY}g_{\chi\chi Y}}$. Expected exclusion limits in the dark matter mass vs mediator mass scale can be calculated for the selected values of the couplings. Shown in Fig. 30 are the expected limit contours resulting from the ILD [327] and CLIC [326] studies, the latter assuming the product of the two couplings, $g_{eeY} \cdot g_{\chi\chi Y} = 1$. These results confirm that the mono-photon signature allow e^+e^- colliders to be sensitive to DM pair-production also for mediator mass scales much higher than the collision energy.

It is important to stress the key role of the beam polarisation in the mono-photon analysis. It is not only essential to reduce SM backgrounds, but also to control systematic uncertainties, which become important for large data sets expected. Compared in Fig. 31 are expected exclusion limits for different running scenarios for the future Higgs factory [327]. Even with 10 ab^{-1} CEPC and FCC-ee, circular colliders running without beam polarisation, can not compete with 2 ab^{-1} of pollarized data collected at 250 GeV ILC.

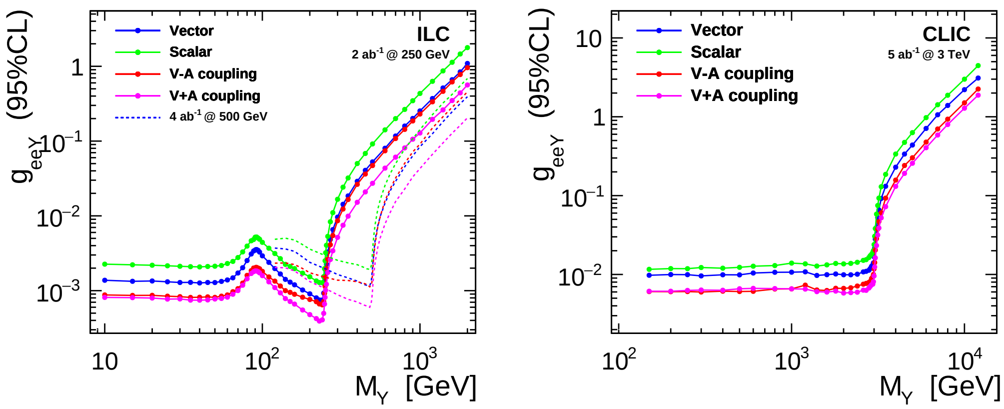

Figure 29: Expected limits on mediator coupling to electrons for the ILC running at 250 and 500 GeV (left) and CLIC running at 3 TeV (right), for relative mediator width, Γ/M = 0.03, and different mediator coupling scenarios, as indicated in the plot. Presented are combined limits corresponding to the baseline running scenarios, with systematic uncertainties taken into account [328].

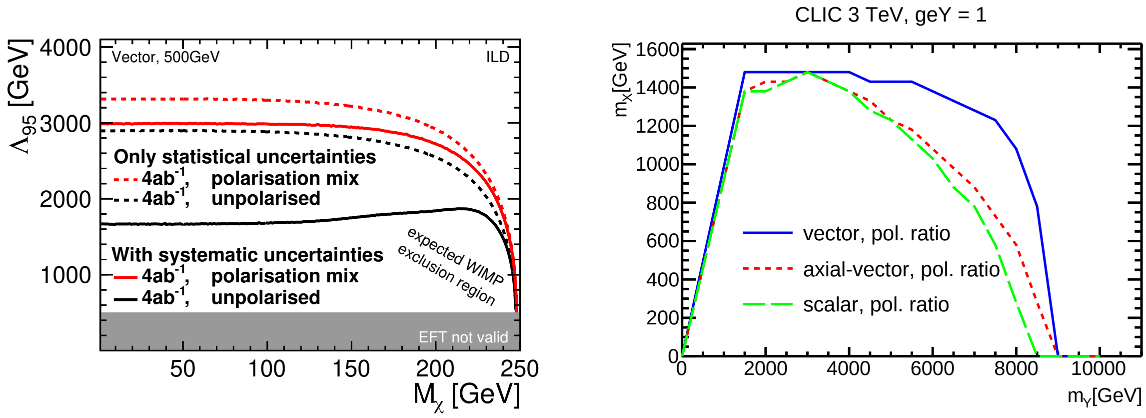

Figure 30: Expected exclusion limits in the dark matter mass vs mediator mass scale plane, from the search for dark matter pair-production with the mono-photon signature. Left: impact of systematic uncertainties and beam polarisation on the expected limits from the ILC running at 500 GeV, assuming vector mediator couplings [327]. Right: expected sensitivity of CLIC running at 3 TeV, based on the measured polarisation ratio, for different mediator coupling scenarios [326].

Dark matter charged under electroweak interactions can also be explored at e^+e^- colliders. In this scenario, DM corresponds to the neutral component of an electroweak multiplet. For a recent review on this class of DM candidates, see Ref. [329]. As it turns out, the thermal relic abundance of electroweak-charged DM agrees with the observed DM density for a mass $\gtrsim \mathcal{O}(1)$ TeV; *e.g.*, $\simeq$ 1 and 3 TeV for an $SU(2)_L$ doublet and triplet fermion DM, respectively [330, 331]. Lighter DM masses can also be viable if supplemented by other DM species (such as axions) or non-thermal production mechanisms [332]. At e^+e^- colliders, electroweak-charged DM can be probed for masses up to $\simeq \sqrt{s}/2$. The search strategy corresponds to that presented in Sec. 3.6.1 for light SUSY searches – results presented in Fig. 24 apply for the search of any $SU(2)_L$ doublet fermion. Precision measurements of di-fermion production cross sections could extend the mass reach by $\simeq \mathcal{O}(100)$ GeV [333, 334]. High energy e^+e^- colliders thus provide a crucial testing ground for electroweak-charged DM. In particular, CLIC at 3 TeV can fully test both the thermal and non-thermal scenarios for the $SU(2)_L$ doublet case.

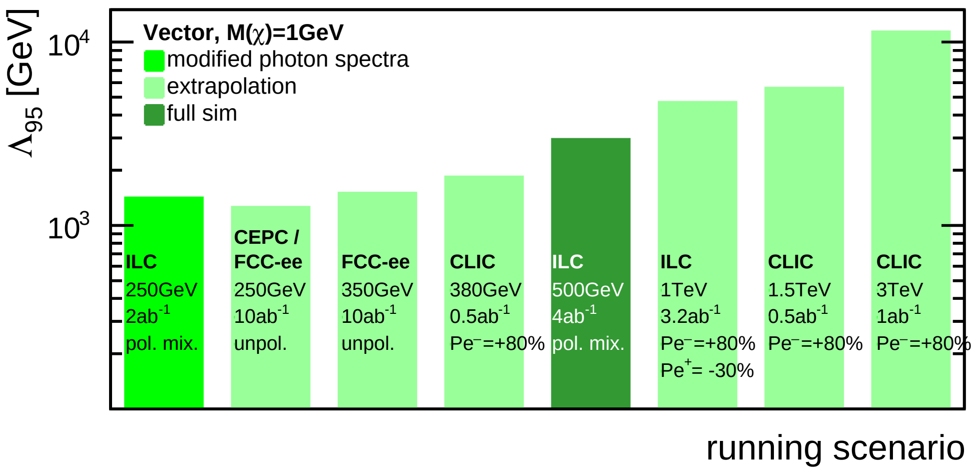

Figure 31: Results from the search for dark matter pair-production with the mono-photon signature, for vector mediator couplings and dark matter mass of 1 GeV. Compared are expected exclusion limits for different settings of centre-of-mass energy, integrated luminosity and polarisation combination [327].

3.6.5 BSM Higgs bosons and triple Higgs couplings at the LC

As argued already in Sec. 3.3.2, one of the most intriguing open questions is the origin of the matter-antimatter asymmetry of the Universe, which cannot be explained within the SM [335]. A broad class of models [336, 337] imply that the required first-order electroweak phase transition (FOEWPT) can only be realized if the mass of an additional Higgs boson, h, is not too large, $m_{\mathrm{h}} \leq 900-1000$ GeV. This makes the boson h a prime target for the HL-LHC, but also for future high-energy $\mathrm{e^+e^-}$ colliders. The related physics questions are two-fold. Firstly, can such a new, heavier Higgs boson, as favoured by a FOEWPT, be detected at (the HL-LHC and/or) a LC? Secondly, can we gain access to BSM triple Higgs couplings (THCs) through the processes $\mathrm{e^+e^-} \to \mathrm{ZHH}/\nu_l\bar{\nu}_l\mathrm{HH}$?

A case study carried out in the frame of the 2HDM is given by Ref. [338] (for a recent analysis in the Higgs Singlet extension of the SM, see [339].) In this work several benchmark points are evaluated, and the access to the THC λ_{HHh} (i.e. involving two CP-even Higgs bosons, assumed to correspond to the Higgs bosons discovered at the LHC, and one additional CP-even Higgs boson) is analyzed. In Figure 32 [338] results for one benchmark point in the 2HDM type I are given. The parameters are chosen as: $m_{\mathrm{H}} = 125$ GeV, $m_{\mathrm{h}} = 300$ GeV, $m_{\mathrm{A}} = m_{\mathrm{H^\pm}} = 650$ GeV, $\tan\beta = 12$, $\cos(\beta-\alpha) = 0.12$ and $m^2_{12}/(\sin\beta\,\cos\beta) = 400$ GeV. This yields $\kappa_\lambda^{(0)} = 0.95$, $\kappa_\lambda^{(1)} = 4.69$, $\lambda^{(0)}_{\mathrm{HHh}} = 0.02$ and $\lambda^{(1)}_{\mathrm{HHh}} = 0.21$, where ($i$) denotes the loop order. Shown are the differential cross sections of the process $\mathrm{e^+e^-} \to \mathrm{ZHH} \to \mathrm{Zb\bar{b}b\bar{b}}$ w.r.t. m_{HH}, the invariant mass of the di-Higgs system. The cross section is evaluated at $\sqrt{s} = 500$ GeV for $P_{\mathrm{e^-}} = -80\%$ and $P_{\mathrm{e^+}} = +30\%$. The blue lines include the one-loop values of $\kappa_\lambda^{(1)}$ and λ_{HHh} (evaluated via the effective potential approach), the yellow lines show the 2HDM tree-level prediction and the dotted black lines show the SM tree-level prediction. The number of events is calculated assuming an integrated luminosity of $\mathscr{L}_{int} = 1600\,\mathrm{fb}^{-1}$ for each choice of polarisation ($P_{\mathrm{e^-}} = -80\%$, $P_{\mathrm{e^+}} = +30\%$ and $P_{\mathrm{e^-}} = +80\%$, $P_{\mathrm{e^+}} = -30\%$ (not shown in the plots)). The m_{HH} distribution is binned with a bin size of 6 GeV, ensuring a minimum of at least 2 events per bin for each polarisation in the case of no smearing (indicated by the vertical lines), as shown in the left plot. The right plot shows the same curves, but with a smearing of 5%, which could be seen as a realistic value for the ILC detectors [340]. To estimate the significance of the peak-dip structure caused by the the resonant h-exchange (and thus the presence of a BSM THC, λ_{HHh}) cuts on the b-jet energy and momentum are introduced, together with a b-jet acceptance (see [338] for details). The significance, Z, is then calculated from the number of events expected with or without the peak-dip structure (and quadratically summed over the two polarisations). The results are given for tree-level THCs ($Z^{(0)}$) and one-loop THCs ($Z^{(1)}$ in the plots. One can observe that the significance in this benchmark point becomes very large only because of the large one-loop correction to λ_{HHh}, and degrades somewhat by the inclusion of a "realistic smearing" of 5%. However, even after including the smearing the significance is found at $Z^{(1)} \sim 13$, i.e. at a very high level. Clearly, a full experimental analysis is needed to realistically determine the precision with which λ_{HHh} can be measured at the ILC500. However, this example clearly indicates that BSM THC's can be accessible, if the BSM Higgs-boson mass is within the kinematical reach.

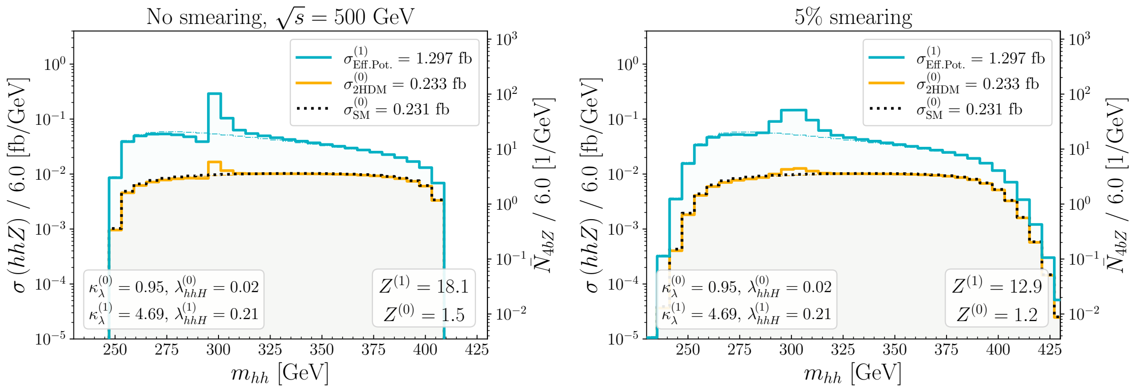

Figure 32: Differential cross section distribution w.r.t. m_{HH} in the 2HDM type I (for the parameters see text) at $\sqrt{s} = 500$ GeV for $P_{e^-} = -80\%$ and $P_{e^+} = +30\%$. Left (right) with 0% (5%) smearing. For the color coding: see text. Adapted from [338]. Note that in the figure h denotes the detected Higgs Boson.

3.6.6 LC sensitivity to unexpected new physics

While the above examples provide a panorama of well-motivated scenarios that address open questions of the SM, they remain speculative: we do not know what form BSM physics will take or at what scale it will manifest. Indeed, despite our theoretically well-founded ideas about BSM, it is possible that new physics shows up in an unexpected way. It is therefore important to search for new phenomena with an open mind, and with maximum experimental flexibility.

Not all is completely open, however. As stated in the introduction, the priority for the next collider is to gain understanding of the Higgs sector and electroweak symmetry breaking. And, dynamical explanations of the puzzles of the Higgs sector must come from new interactions and particles that couple to the Higgs. For new particles with electroweak interactions, the LC sensitivity essentially goes up to the kinematic limit. The extensibility in energy of a linear machine is thus a huge advantage, as it allows one to adapt future upgrades to the findings at the HL-LHC and/or early stages of LC operation. Moreover, one can exploit beam polarisation to maximize sensitivity to whatever new physics may show up. Indeed, as already advocated in section 3.6.1, the clean experimental environment with well defined initial state, precisely known collision energy, electron and positron polarisation, hermetic detectors and trigger-less operation make an e^+e^- LC an ideal machine for looking for unexpected and possibly very subtle new phenomena. Runs at different centre-of-mass energies (see section 2.1) and the $\gamma\gamma$ and $e\gamma$ options (see section 3.8) further increase this potential.

It is also important to stress here that indirect measurements, e.g. in the context of EFT fits discussed in the next section, may provide evidence of new physics, but will not be able to pinpoint its exact nature. For this, direct observation and precise measurements of on-shell processes are vital, which makes the possibility of energy upgrades and beam polarisation even more important.

3.7 Global Interpretations

Without any particular guidance in terms of what type of new physics signal we are looking for, and given the vast number of *Beyond the Standard Model* (BSM) deformations that could appear in physical observables with the expected precision at future e^+e^- colliders, global explorations covering as many different types observables as possible in new physics searches become a necessity. Indeed, while a significant deviation from the Standard Model prediction in a single observable would be sufficient as evidence of new physics, characterizing its origin requires to study the pattern of deviations that could appear in correlation with such a signal across different observables.

From the point of view of indirect searches, and assuming that new physics is somewhat heavier than the electroweak scale, as seem to be suggested by LHC direct searches[7], the low-energy effects of the new physics in the precision measurements that will be possible at future electroweak, Higgs and Top factories can be adequately described by an *Effective Field Theory* (EFT). In this section, we adopt the framework of the so-called *Standard Model Effective Field Theory* (SMEFT), which describes new physics in a model-independent way *under the assumptions* that at low energies the fields and symmetries are those of the Standard Model, and the effects of new states decouple as these become heavy. While some of these assumptions could be questioned, and one could use other EFTs [8], this is a minimal set that is consistent with current observations, it is well-motivated phenomenologically and has an ample coverage of BSM scenarios. These assumptions also introduce some simplifications, in the form of theory correlations between different types of effects, that allow the exploration of complementarities between different observables that can be measured at present and future colliders, exploiting also the benefits associated to, e.g., use of polarisation and measurements at different energies. Finally, compared to other alternative EFTs, the SMEFT is a significantly more mature framework in terms of formal and practical developments.

Current SMEFT studies at future colliders prepared for the 2020 European Strategy Update [341, 342] and the 2021 Snowmass process [48] were based on global fits to projections of measurements of EW and Higgs observables, while the top sector was either minimally described [341] or treated separately [48]. The studies were performed truncating the SMEFT Lagrangian to dimension six:

$$\mathscr{L}^{(6)}_{\text{SMEFT}} = \mathscr{L}_{\text{SM}} + \frac{1}{\Lambda^2}\sum_i C_i \mathscr{O}_i, \tag{6}$$

where Λ is the cutoff of the EFT, $\mathscr{O}_i$ are Lorentz and SM gauge-invariant operators of mass dimension six, with C_i the corresponding Wilson coefficients, and we have implicitly assumed lepton (and baryon) number conservation, thus removing the contribution from the dimension-five Weinberg operator. All the new physics effect are encoded in the C_i, which can be obtained matching the SMEFT to a given particular scenario. The different dimension-six operators will induce observable effects suppressed by $q^2/\Lambda^2 \ll 1$, with $q = v$ or the energy scale E of the process of interest. Effects from higher-dimensional operators will carry extra suppressions in q/Λ and are therefore expected to be subleading, unless the new states are relatively light.

In this section, we will update previous studies of the sensitivity to dimension-six SMEFT effects at Linear Colliders, focusing our attention on the LC Vision scenario described in this document. Details about this scenario, the assumptions of the SMEFT interpretation and the inputs used in the global interpretation are given in the next subsection, with references to the corresponding sections of this report for additional information. In Section 3.7.2 we will present and discuss the results of the SMEFT fit. For this version of the report, however, the full analysis is not yet complete and in Section 3.7.2 we provide partial results based on a more limited SMEFT fit, focused on the characterization of the Higgs boson properties.

3.7.1 Inputs and assumptions of the global SMEFT interpretation

The baseline of the SMEFT fit that will be used for comparison here is similar to that in [48], including current Electroweak Precision Observables from LEP/SLD, as well as the HL-LHC projections for Higgs measurements. This baseline will be combined with the information obtained from the observables that would be

[7] Many scenarios not excluded can be probed at the LCF; see Section 3.6 and Section 3.9.1.

[8] For instance, including extra light degrees of freedom or, staying with the SM spectrum at low energies, assuming that the electroweak symmetry is non-linearly realized, leading to what is known as the Higgs Effective Field Theory (HEFT), where the Higgs described by a singlet field.

measured at the different centre-of-mass energies that could be accessible at a future e^+e^- linear collider. In this regard, we consider two operating scenarios, based on Table 3:

- Scenario LCv_{250}^{550} consists of all the stages reported in Table 3 up to 550 GeV, with the luminosities indicated in that table.
- Scenario LCv_{250}^{1000} considers also an extension to high-energies up to 1 TeV, collecting a total of 8 ab^{-1} with the same distribution among polarisations described in Table 3. In this scenario we reduce the luminosity collected at 550 GeV to 4 ab^{-1}, which would allow to keep the same duration for the whole project.

In terms of observables included in the fit, we include the following list, where we also indicate the updates with respect to the analysis in previous global SMEFT studies in [48]:

- The full set of measurements for single-Higgs processes in Table 5 in Section 3.1. (We assume the same precisions at 500 and 550 GeV.) Compared to [48], the projected uncertainties have been scaled to the new luminosity in Table 3.
- The Higgs mass determination at 250 GeV with a precision of 12 MeV, as explained in Section 3.1.2.
- We use the same projections for $e^+e^- \to W^+W^-$ processes as in [48], but again updating the luminosity to the scenarios discussed above.
- The projections for electroweak precision measurements at linear e^+e^- colliders. These include the measurements taken during the Giga-Z run, which remain unchanged with respect to [48], as well as the electroweak precision observables that could be measured at 250 GeV, e.g. the Z-pole observables via radiative return, in which case we scale the uncertainties with the luminosity change from 2 to 3 ab^{-1}. For the W mass precision, we use the results in Section 3.2.2.
- On the electroweak side, we extend the set of observables with the projected measurements of $2 \to 2$ fermion processes above the Z pole, which were treated separately in [48]. For the leptonic channels we use the same information in [48], scaled to the appropriate luminosities, whereas for the hadronic final states we use the results in [41, 75].
- The top-quark mass measured in the $t\bar{t}$ threshold scan, see Section 3.5.1. This is particular relevance for the fit to electroweak precision observables.
- Similarly, we include the top sector directly in the global combination, using the results presented in Section 3.5. We also include from the study presented in that section the HL-LHC Top measurements used as a baseline.

On the technical side, we include the contributions to these processes from all the dimension six operators that contribute at leading-order. We restrict the analysis to CP-even operators and, to be consistent with flavour constraints, we assume an $U(2)_q \times U(2)_u \times U(2)_d$ flavour symmetry in the quark sector, while in the leptonic one we simply assume lepton family number conservation (without imposing lepton universality). The contributions from the different operators are kept at order $1/\Lambda^2$, given by the interference between the new physics amplitudes and the Standard Model ones. Finally, as in [48], we consider an extension of the SMEFT fit where we include the possibility of non-SM final states in Higgs decays via an extra fit parameter modelling "unclassified" contributions to the Higgs width. While technically this is not consistent with the EFT approach, as one would need to replace the SMEFT by the appropriate EFT considering the extra light degrees of freedom the Higgs is decaying to, we include this scenario to illustrate the e^+e^- capabilities of constraining the total Higgs width.

3.7.2 Global fit results

The full analysis described in the previous section is not yet complete. For this version of the report, we supply results from a more limited global SMEFT fit carried out with the assumptions of [343] used in previous

ILC reports [12, 32, 344]. This includes the expected uncertainties from precision electroweak measurements in the program discussed in Sec. 3.2 and from measurements of W pair production discussed in Sec. 3.4.1, as well as the Higgs measurements from the various stages of a linear collider program described in Sec. 3.1. The fit assumes lepton flavour universality and ignores CP-violating dimension-6 operators. It allows for exotic Higgs decays, parametrizing these by the branching fraction for Higgs decay to invisible final states and, separately, the branching fraction for Higgs decay to unclassified exotic modes. For a more detailed explanation of the assumptions of this fit, see [343].

This fit includes only tree-level effects. The triple-Higgs coupling affects single-Higgs production only through loop effects, which should be considered together with Standard Model 1-loop diagrams, including effects from CP-violating operators and operators involving the top quark. The full 1-loop SMEFT corrections to $e^+e^- \to ZH$ have now been computed [345, 346], and in principle these could be incorporated into a SMEFT analysis. However, this brings in many subtle points which we have, not, for the moment, resolved. We will present our analysis in a later version of this report.

Within this context, we present the Higgs coupling uncertainties predicted by this fit for the proposed LCF run plans. In principle, we could quote the results of the fit in terms of bounds on SMEFT coefficients. However, it is more illustrative to quote them in terms of fractional uncertainties in the Higgs couplings to various final states. We present these in Table 9. For the purpose of that table, we define the relative error in the coupling for $H \to A\bar{A}$ as

$$\delta g(HAA) = \frac{1}{2}\frac{\Delta\Gamma(H \to A\bar{A})}{\Gamma(H \to A\bar{A})} \ . \tag{7}$$

Note that, while each Higgs decay depends on several separate dimension-6 SMEFT operators, the uncertainties in these operator coefficients are conflated in this metric. This is rather different from the commonly used but oversimplified κ fit to Higgs couplings, where the separate effects of different SMEFT operators are ignored and also constraints from processes other than Higgs production and decay are not included.

In the LCF run plan, the initial stage will take 3 ab^{-1} of luminosity at 250 GeV in the centre of mass and carry out a separate run at the Z resonance, as described above. Longitudinally polarised beams are used, assuming 80% electron polarisation and 30% positron polarisation. With both dominantly left-handed (-) and dominantly right-handed (+) electron and positron beams, there are four possible modes of operation: –, -+, +-, and ++. In this analysis, the total luminosity is assumed to be divided among these modes as (10%, 40%, 40%, 10%), respectively. The like-sign modes contribute little to the rate of Higgs boson production but are important to measure 2-photon and beam-related backgrounds. All of the processes included in the fit have been studied in full simulation using the ILC beam conditions and model detectors, as described above. We use these results to obtain the measurement uncertainties associate with this data sample. Estimated systematic errors are included. The results for $\delta g(HAA)$ as defined in (7) are given in Table 9.

Figure 33 illustrates the projected uncertainties for 3 ab^{-1} at 250 GeV and 8 ab^{-1} at 550 GeV, i.e. the 3rd column of Table 9. The projected precisions on the top Yukawa and the trilinear Higgs self-coupling are from $t\bar{t}H$ and di-Higgs production, as discussed in Sec. 3.5.2 and Sec. 3.3.1, respectively.

In Table 9, we also give a similar set of LCF results for the full program of Higgs studies. For LCF, the full program would consist of 3 ab^{-1} at 250 GeV plus either 8 ab^{-1} at 550 GeV or 4 ab^{-1} at 550 GeV and 8 ab^{-1} at 1 TeV, plus additional short runs at the Z resonance and the top quark threshold. We also include the results for a program with only 4 ab^{-1} at 550 GeV for comparison.

With either extension at high energies, the Higgs program at the LCF would be comparable to that of any of the other Higgs factories that have been proposed, e.g. at circular colliders, bringing per-mille level sensitivity to potential new physics effects in Higgs couplings. It should be noted that the LCF program, more balanced between ZH and WW fusion Higgs production, also offers nontrivial checks of anomalies found in these two separate reactions. Of course, as we have discussed in the previous sections, the higher-energy program of the LCF also includes many reactions not accessible to circular colliders, including the measurements of the $t\bar{t}H$ and HH production processes, where one could test at tree-level the top quark Yukawa coupling and the Higgs self-coupling, respectively.

Higgs couplings	LCF, L[ab^{-1}]	250 GeV 3, pol.	250 + 550 GeV 3+4, pol.	250 + 550 GeV 3+8, pol.	250 +550 +1000 GeV 3+4+8, pol.
$g(Hb\bar{b})$		0.72	0.46	0.38	0.36
$g(Hc\bar{c})$		1.45	1.04	0.87	0.72
$g(Hgg)$		1.31	0.86	0.70	0.60
$g(H\tau\tau)$		0.83	0.61	0.53	0.52
$g(HWW)$		0.34	0.24	0.22	0.22
$g(HZZ)$		0.34	0.24	0.22	0.22
$g(H\gamma\gamma)$		1.02	0.98	0.94	0.90
$g(H\gamma Z)$		7.51	5.75	5.41	5.64
$g(H\mu\mu)$		3.87	3.68	3.53	3.36
Higgs widths					
total width		1.39	0.97	0.85	0.83
width to invisible (95%CL)		0.36	0.33	0.31	0.33
width to unclassified (95%CL)		1.53	1.23	1.11	1.19

Table 9: Expected measurement precision of Higgs boson coupling and width determinations, in percent, according to the SMEFT fit described in the text. Higgs coupling uncertainties are defined by (7). We show the results for the initial-stage program of the LCF at 250 GeV (first column of results), and for the full program, considering different possible upgrades to higher energies: an extension to 550 GeV collecting a total of 4 or 8 ab^{-1} (columns 2 and 3, respectively); an extension to 550 GeV collecting 4 ab^{-1}, followed by a 1 TeV run with a total of 8 ab^{-1} (fourth column). The inputs to the fit are the full-simulation results described in earlier sections of this chapter.

3.8 Photon-photon, electron-photon and electron-electron collisions

High-energy $\gamma\gamma$- and eγ-collisions offer a rich physics programme [347, 348], complementary to the e^+e^- linear collider both in kinematic as well as physics aspects [349–351]. An overview about the most important SM processes in e^+e^- as well as $\gamma\gamma$ collisions can be seen in Fig. 34 [351]. High polarisation of the photon beams (produced via Compton backscattering) can be achieved and easily be flipped by flipping also the laser polarisation. The development of XFEL-like lasers might allow to use a γ-beam with a peak-like beam-spectrum, whereas the option with an optical laser leads to a much broader energy spectrum [31]. Both laser-options are complementary as well.

3.8.1 Higgs sector

One of the most important physics in $\gamma\gamma$ collisions is in testing the properties of the Higgs boson(s) [351]: the Higgs bosons can be singly produced as s-channel resonances through one-loop triangle diagrams and observed in their subsequent decays into $b\bar{b}, \tau^+\tau^-, WW^*, ZZ$, etc.
Furthermore, the control of the polarisations of back-scattered photons provides a powerful tool for exploring the CP properties of any single neutral Higgs boson that can be produced with reasonable rate at the photon collider: parallel (perpendicular) $\gamma\gamma$ beams generate Higgs particles with quantum numbers $J^{PC} = 0^{++}$ (0^{-+}), respectively, e.g. [352–354].

Higgs width

Since the $\gamma\gamma$-option enhances the cross section of any charged particles by about a factor of 10 compared to the e^+e^- option [355–358], it also allows better access to the two-photon decay width of the Higgs boson, $\Gamma_{\gamma\gamma}$, due to the higher rates in $\gamma\gamma$ collisions. The two initial photon polarisations can be chosen to produce spin-zero resonant states and to simultaneously reduce the cross section for the background.

Combining the measurement of the $\gamma\gamma \to H \to b\bar{b}$ cross section at a $\gamma\gamma$ collider with its expected precision of 2 % with the $BR(H \to b\bar{b})$ measured in e^+e^- mode to the 1%-level allows to determine the partial width $\Gamma_{\gamma\gamma}$ with a precision of 2% on basis of $\mathscr{L}_{\gamma\gamma}$ = 410 fb^{-1} [359, 360]. This rate is particularly sensitive to new heavy charged particles in different beyond Standard Models and beyond the kinematic range [360, 361].

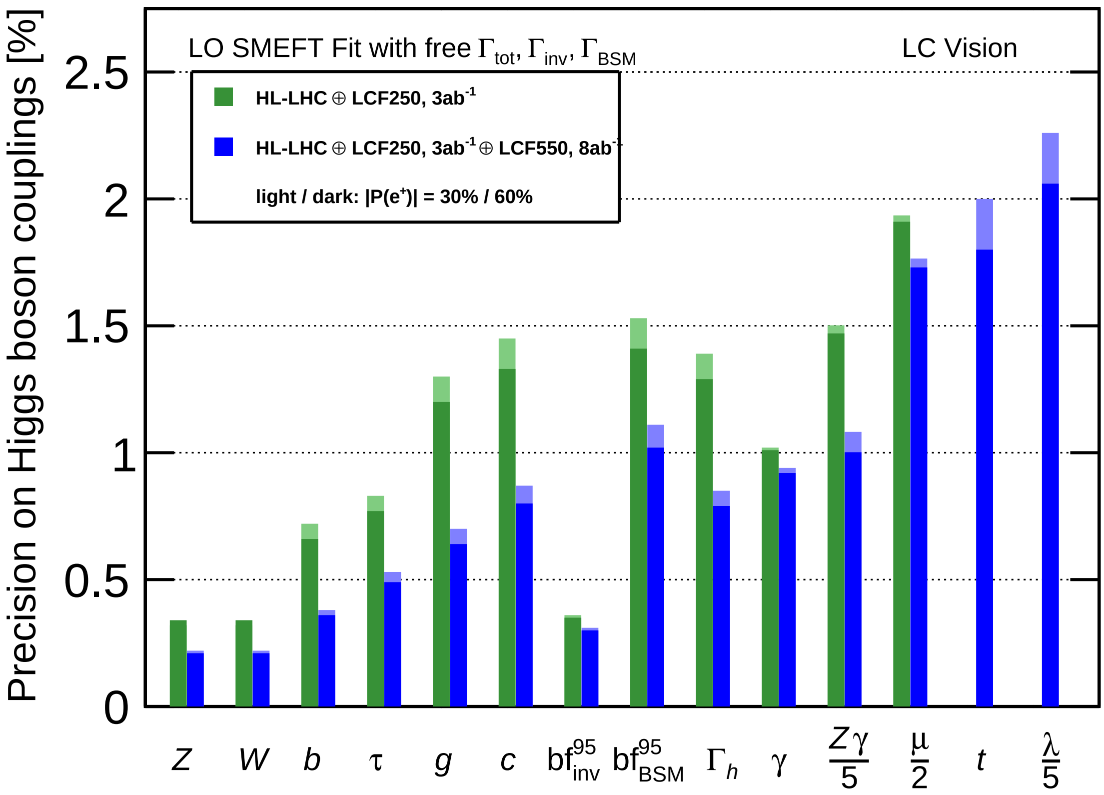

Figure 33: Projected uncertainties on Higgs boson couplings for 3 ab^{-1} at 250 GeV and 8 ab^{-1} at 550 GeV; the bars for the H – Z – γ coupling, the muon Yukawa and the trilinear Higgs self-coupling λ have been scaled by 1/5, 1/2 and 1/5, respectively. On the invisible and unclassified partial widths the expected 95 % CL limit is shown.

If e^+e^- colliders can also provide the branching fraction for $H \to \gamma\gamma$ at the 10% level, the total Higgs width can be determined with a comparable level of uncertainty.

Di-Higgs production and measurement of trilinear couplings

Particularly promising are di-Higgs processes and the measurement of the trilinear couplings [362–366]: the $\gamma\gamma$ set-up allows a direct measurement already at lower cms energies than at the e^+e^- mode, exploiting also the photon polarisation for disentangling the different contributions [366], see Fig 37.

An XFEL $\gamma\gamma$-option operating at 380 GeV centre-of-mass energy enables di-Higgs production and measurement of trilinear couplings. The HH cross section at 380 GeV centre-of-mass energy is almost double that of e^+e^- at 500 GeV, see Fig. 35, and with a simpler hadronic final state consisting of only four jets in the $H \to b\bar{b}$ channel. Therefore, a $\gamma\gamma$-option provides not only complementarity to the e^+e^- mode due to the production in a $J_z = 0$ state, c.f. Fig. 36, but also potentially higher precision. To assess the feasibility of the trilinear Higgs self-coupling measurement in a 380 GeV XFEL $\gamma\gamma$ collider option, a Delphes-based analysis was performed using simulated data produced with Pythia8 and Cain, interfaced with Whizard 3.14, including all sources of physics backgrounds from $\gamma\gamma$, $e^-\gamma$, and e^+e^-, properly accounting for the luminosity profile predicted by Cain. The e^+e^- background, not present in previous optical photon collider concepts, arises from the operation at very large x values where Compton photons interact with laser photons producing e^+e^- pairs. The process $e^+e^- \to ZH \to b\bar{b}b\bar{b}$ is in fact the dominant background to $\gamma\gamma \to HH \to b\bar{b}b\bar{b}$ after final selection. Pileup backgrounds were not considered but preliminary studies show that the $\gamma\gamma \to$hadrons pileup background is predominantly forward and can be suppressed at the analysis level.

Figure 38 shows an event display of $e^+e^- \to ZHH \to q\bar{q}b\bar{b}b\bar{b}$ at $\sqrt{s}$=550 GeV and $\gamma\gamma \to HH \to b\bar{b}b\bar{b}$ at $\sqrt{s}$=380 GeV, highlighting the simpler final state in the $\gamma\gamma$ mode.

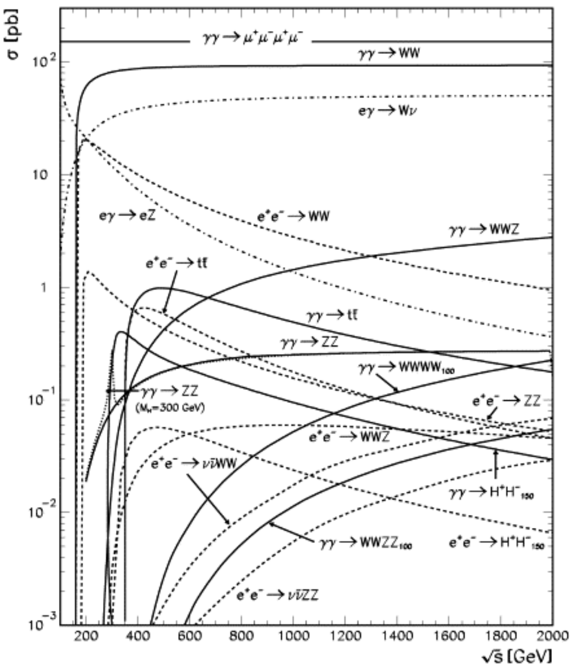

Figure 34: Fermion, gauge boson and Higgs production in e^+e^- and $\gamma\gamma$ and as a function of $\sqrt{s}$ [351]. The plots are done for a hypothetical Higgs sector $H^{\pm}$.

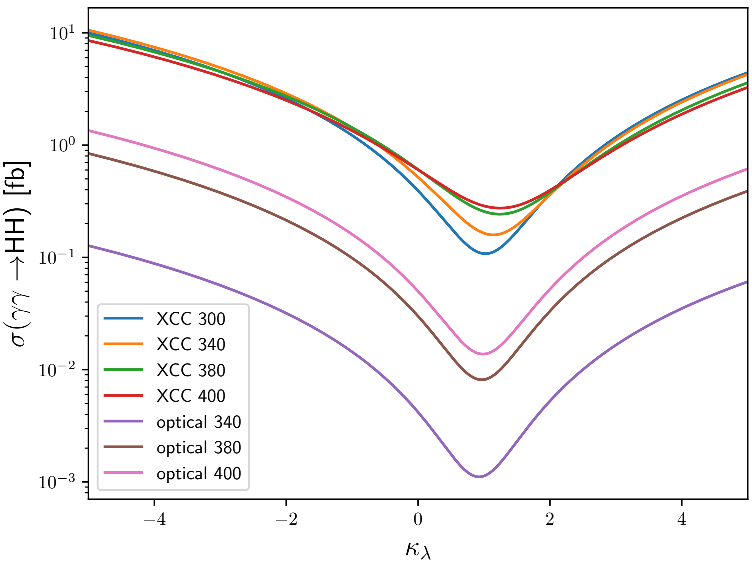

Figure 35: Di-Higgs production cross section at $\gamma\gamma$-collision for both the optical laser as well as the XCC-like laser for different c.m. energies in dependence on the trilinear Higgs couplings parameter κ_λ [366].

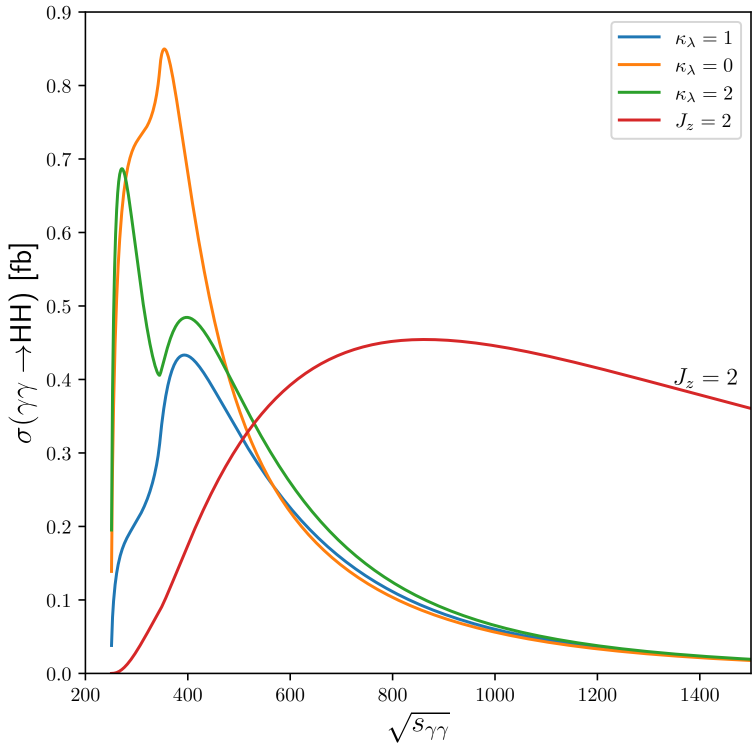

Figure 36: Di-Higgs production at the parton level at different $\sqrt{s_{\gamma\gamma}}$ for different κ_λ. The $J_z = 2$ case can clearly be separated [366].

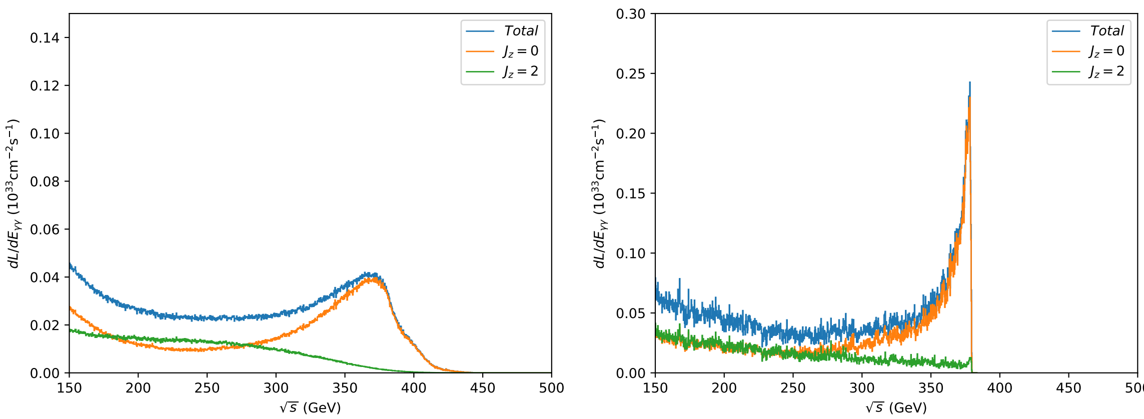

Figure 37: Comparison: Different contributions $J_z = 0$ and $J_z = 2$ in di-Higgs production in $\gamma\gamma$ collisions produced via an optical laser (left panel) and via XCC-like laser (right panel) [366].

Although the $e^-\gamma$ background processes have the largest cross sections, their final states are highly boosted and easily suppressed. This is illustrated in Fig. 39 which shows event displays of a typical $e^-\gamma \to qqH$ and $\gamma\gamma \to$ HH event.

Several Boosted Decision Trees (BDT) were trained to separate signal from the dominant backgrounds. A genetic algorithm was then used to pick the output cuts of each BDT that maximize sensitivity. Figure 40 shows the invariant mass of the leading b-jet pair before and after the multivariate discriminant.

A likelihood fit analysis yields a significance of 7.5 σ (statistical only) and a statistical uncertainty of 13% on the di-Higgs cross section in the $\gamma\gamma \to b\bar{b}b\bar{b}$ channel for an integrated $\gamma\gamma$ luminosity of 6.5 ab^{-1} for 260 GeV $< sqrt(s_{\gamma\gamma}) <$ 380 GeV i.e., the top 30 % of the luminosity spectrum. This result is expected to improve by utilizing a kinematic fit and a higher efficiency b-tagging operational point.

CP quantum numbers

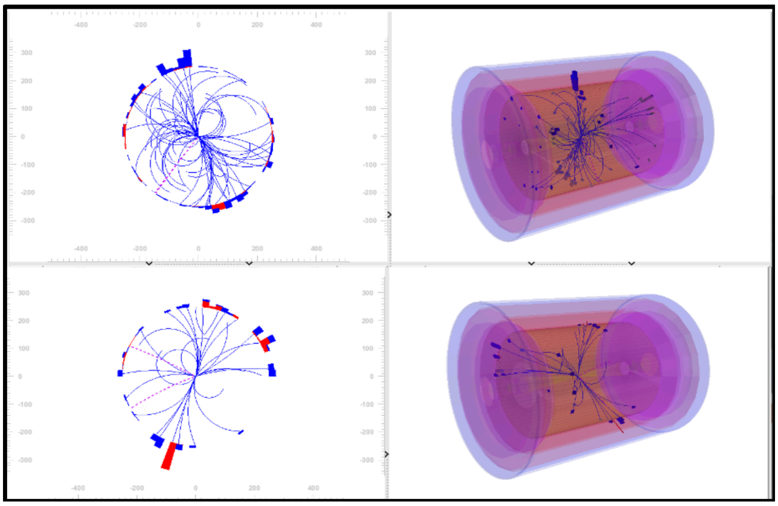

Figure 38: $e^+e^- \to ZHH \to qqb\bar{b}b\bar{b}$ at $\sqrt{s}$=550 GeV and $\gamma\gamma \to HH \to b\bar{b}b\bar{b}$ at $\sqrt{s}$=380 GeV event displays, highlighting the simpler final state in the $\gamma\gamma$ mode.

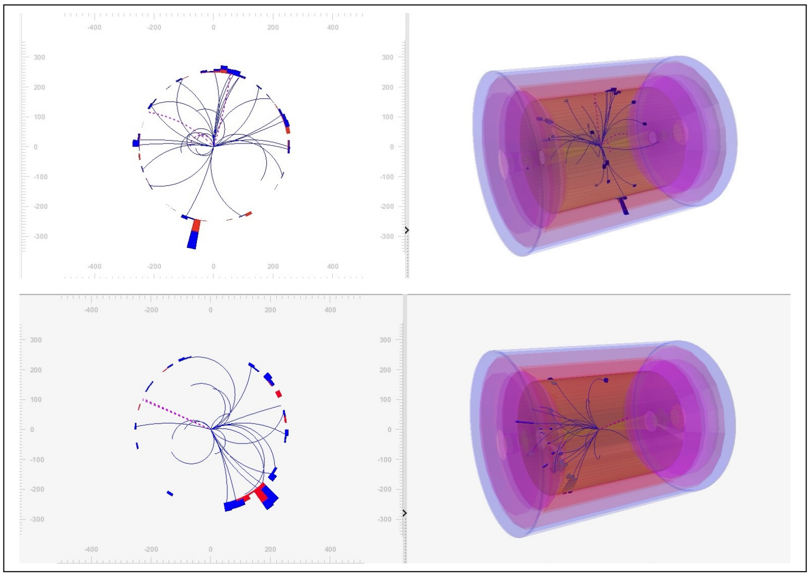

Figure 39: $\gamma\gamma \to HH \to b\bar{b}b\bar{b}$ and $e^-\gamma \to q\bar{q}H$+X at $\sqrt{s}$ = 380 GeV event displays. The $e^-\gamma$ background events are highly boosted and distinct from the di-Higgs signal.

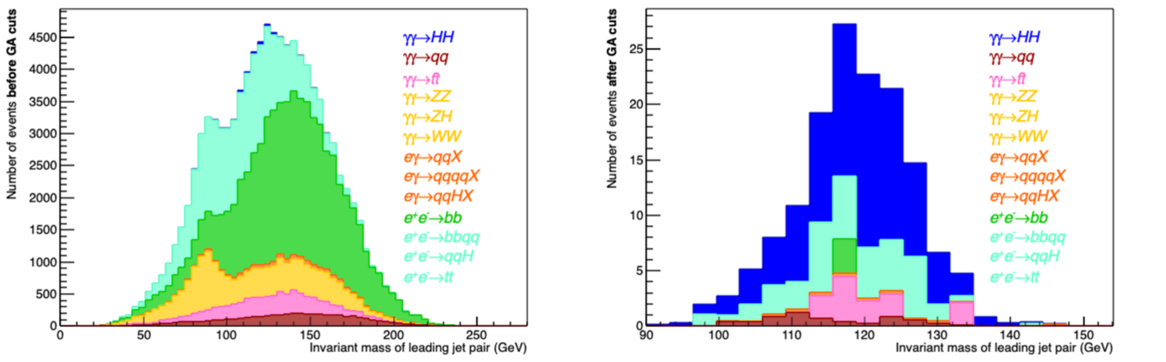

Figure 40: Invariant mass of the leading b-jet pair before and after BDT cuts.

	Optical	XFEL
Laser E_γ (eV)	1.17	1.04×10^3
$\sqrt{s_{ee}}$ (GeV)	216.00	125.72
$w_{\max}$ (GeV)	218.16	126.97
N_{bunch}/train	2820	165
Rep Rate (Hz)	5	120
$L_{\gamma\gamma}$ (cm^{-2}s^{-1})	3.618×10^{34}	3.570×10^{34}
$N_H/1.0 \times 10^7$s	25,000	72,200
$N_{bb}^{(1)}/1.0 \times 10^7$s	64,390	58,220$^{(2)}$
$N_{bb}^{(1)}/N_H$	2.58	0.81
$\langle\mu\rangle$	0.90	0.63

Table 10: Table of $\gamma\gamma$ collider parameters and number of single Higgs and $b\bar{b}$ backgrounds with $M_{b\bar{b}} \geq 100 GeV$ and $\beta_z \leq 0.1$ for an optical and XFEL laser.

For instance, the CP-properties of the Higgs sector [367] can directly be probed via the photon polarisation, complementing results from the LHC on this topic: CP-even Higgs bosons couple with maximal strength to linearly-polarised photons with parallel polarisation vectors whereas CP-odd Higgs bosons prefer linearly-polarised photons with perpendicular polarisation vectors [368, 369].

Single Higgs production

This physics reach at a $\gamma\gamma$-collider is accomplished by access to the single Higgs production, leading to complementary information and measurements of the couplings. This channel allows a determination of the g_{ZZH} coupling which in combination with the HZ-channel, both at $\sqrt{s} = 500$ GeV, leads to an accuracy that is comparable to a determination at HZ only but at $\sqrt{s} = 250$ GeV [370]. Combining this channel with the corresponding results from the e^-e^--option would enhance the accuracy furthermore due to the lower background [370].

Table 10 shows the comparison of a $\gamma\gamma$ collider mode using optical and XFEL lasers. The XFEL option produces a luminosity profile that is sharply peaked around the Higgs mass (see Fig. 63) leading to a much higher number of signal events and slightly smaller backgrounds. A full analysis of single Higgs production comparing both laser options is ongoing.

BSM Higgs production

Since, in principle at higher energy when the Higgs-strahlung (direct production of Higgs in association with a vector boson) is suppressed, the full phase space is available for Higgs production and one gets access to heavy Higgs masses that are higher by a factor of about 1.5 than those directly accessible at e^+e^-. This is particularly interesting for practically all BSM models with an extended Higgs sector, since they usually offer both CP-even H as well CP-odd A heavy Higgs bosons that become accessible in the $\gamma\gamma$ option, even allowing a precise determination of the two-photon width of those particles, respectively [351].

Furthermore, since $\gamma\gamma \to$ H is loop-induced, one can also probe new physics contributions to the SM-like Higgs couplings [353, 371, 372].

Case study: possible LHC excess at 750 GeV

Motivated by the former excess at 750 GeV in the 2015 LHC data, the implications for future colliders of such LHC excesses that show up in the invariant mass distribution of a pair of high-energy photons produced in the collisions, are discussed in [373] Such an excess is directly detectable at the $\gamma\gamma$ option at that energy even if the direct kinematical reach of the corresponding e^+e^- set-up is not high enough. Though the spin of the new particle will be measured from the angular distribution of the decay products at the LHC, the $\gamma\gamma$ option will test the spin assignment precisely via the polarisation of the initial photons. Even the CP numbers of such an excess can be measured directly using transversely polarised initial photons, see e.g. [373].

3.8.2 Non-Higgs physics

Multi-quarks resonances

In general, the $\gamma\gamma$ option allows a precise spectroscopy of C-even resonances in multi-quark states or glueballs [369]. These information might lead to new insights into the strong sector.

Photon structure functions

The polarised as well as unpolarised $\gamma\gamma$ as well as $e\gamma$- ption allows access to measuring the hadronic as well as electromagnetic structure of photons [374, 375].

ALPS and DM

The $\gamma\gamma$ option allows as well direct access to the dark sector. For instance, the direct access to light-by-light scattering opens a new plethora of "old" and "new" physics as Born-Infeld, constraints for non-linear extensions of QED, ALPS and dark matter candidates, complementary to high luminosity e^+e- options [376, 377].

3.8.3 $e\gamma$ physics

The $e^-\gamma$ collider option is a particularly promising option to produce single BSM heavy charged particles like heavy Higgs or supersymmetric fermions that were beyond the kinematical limit in direct production at e^+e^-. Similar as for the $\gamma\gamma$ case both beams $e^-\gamma$ are available highly polarised.

Higgs and electroweak physics

Anomalous top couplings are well accessible in particular in single top production at the $e^-\gamma$ option. The single top production is directly proportional to the *Wtb* coupling and its anomalous part contains terms $f_{L,R} \sim 1/\Lambda$, where Λ is the scale of new physics. At $\sqrt{s} = 500$ GeV rates for single top production of ≥ 100 fb are predicted, leading to much better limits in $F_{L,R}$ than at the LHC [351].

Supersymmetry

Supersymmetry (SUSY) is one of the best motivated extensions of physics of the Standard Model. Due to many free new parameters one applies further symmetries or constraints originating from unification assumptions at grand-unified theory (GUT) scale. Such constrained SUSY models lead to mass relations between the coloured and uncoloured particle SUSY sectors. Therefore, the LHC results lead to high SUSY mass scales in such models. The $e^-\gamma$ mode extends and complements the kinematic range of e^+e^- colliders in particular for heavy sfermions [378, 379] which might be absolutely substantial for the direct discovery of Supersymmetry!

3.8.4 e^-e^- physics

Electron-electron collisions extend the physics potential of e^+e^- and offer an extreme cleanliness since background processes are usually strongly suppressed. For instance, the annihilation processes from e^+e^- collisions are absent. Since both e^- beams are in the foreseen set-up highly-polarised ($P(e^-)$>85%), the weak quantum numbers of the initial state spin S_z, weak isospin I^3_w and hypercharge Y can be completely specified. The beam-beam interaction and implications for the luminosity tuning has been studied in [380].

Background processes involving W-bosons can be substantially suppressed using right-handed polarised electrons. The initial state with lepton number $L = 2$, but electron number $L_e = 2$ and electric charge $Q = -2$ opens a window to new classes of BSM model, for instance bi-lepton models or models with doubly-charged Higgs bosons as in Georgi-Machacek models [381, 382].

SM Higgs physics

At e^+e^- single Higgs production via ZZ-fusion becomes available which has particularly low backgrounds compared with the corresponding channel at e^+e^-. A cross section of about 10 fb is expected at $\sqrt{s} = 500$ GeV, leading to a precise and complementary measurement of the HZZ coupling [359, 370, 383, 384]. Combining this channel with the ZH channel at e^+e^- (at the same energy stage) leads to an accuracy in the coupling determination g_{HZZ} that is comparable to the determination at the low energy stage $\sqrt{s} = 250$ GeV via the

ZH-channel only [370].

BSM Higgs physics

Doubly-charged Higgs bosons exist in models with Higgs triplet fields and can potentially enhance the branching fraction into $\gamma\gamma$. Triplet models, however, often lead to problems with the ρ parameter and violate the custodial symmetry. The Georgi-Machacek model, however, offers a triplet but has also a value of $\rho = 1$. These models offer a very rich phenomenology for future colliders including the e^-e^- option for detecting H^{--} but can also embed a resonance at 95 GeV [385].

Majorana neutrino

The process $e^-e^- \to W^-W^-$, which violates lepton number conservation, is the inverse of neutrino-less double beta decay. It has a clear kinematical signature ($W^-W^- \to$ 4 jets). Its observation would indicate a model-independent evidence for the Majorana nature of the neutrino, and measurement of the cross-section could serve as input to distinguish between theoretical models [386–388].

3.9 Beyond-collider physics

The LC beam dumps absorb a huge number of electrons or positrons. The produced particles can be utilized for exploring BSM, QED in extreme conditions, material science, or future accelerator studies. The purpose of this section is to give an overview on the past linear collider study and how this can be realized at a linear collider facility.

3.9.1 Beam dumps

Physics at main dumps Main beam dumps are installed at the downstream end of the two beamlines of a linear collider. During collider experiments, the beams are continuously directed at the main beam dumps. Considering various experiments that use the secondary particles produced at the beam dump is essential in designing the beam dump area and maximizing the output of the LC program.

Unlike circular collider experiments, experiments using the main beam dumps can be conducted entirely in parallel with collider experiments. On the other hand, careful consideration must be made in advance because the LC facility is aligned along the beam line, and space available for the detectors is limited.

In a linear collider facility, almost all accelerated beams are injected into the beam dumps, so the main beam dumps must absorb high power. Using a low-Z material enhances the feasibility. Water absorbers have been developed. By forcibly circulating the water in the tank, efficient heat dissipation can be achieved. The integrity of high-power water beam dumps was first verified with SLAC's 2.2 MW beam dump [389]. At JLab-CEBAF, a mixed water and aluminium beam dump handling up to 1 MW is operational [390]. A cylindrical beam dump with a diameter of 1.8 m and a length of 11 m is adopted for ILC design which can handle up to 17 MW beam power [391]. We assume the ILC-like water dump in this section.

At the beam dump, $e^\pm$, γ, $\mu^\pm$, are produced through the EM showers, and they further interact with nucleons. Fig. 41 shows the effective luminosity of $e^\pm$, γ, $\mu^\pm$ to nucleons of water target inside the electron beam dump as a function of $\ln x$, where $x = E/E_{beam}$.

For a beam energy of 125 GeV and a power of 2.6 MW, corresponding to the "low power" option of ILC, the main beam dumps see $N_{EOT} = 4 \times 10^{21}$ in about 2.5 years. With these, high luminosities of 10^5 to 10^6 ab^{-1}/year for $e^\pm$ and γ, and approximately 10^2 ab^{-1}/year for muons can be achieved. This result considers only interactions with water inside the beam dump. If shielding is placed downstream of the beam dump, interactions with these materials can further increase the luminosity of muons. New particles that couple feebly to the Standard Model particle may also be created from electromagnetic shower particles.

The positron and electron behave similarly for EM showers. Important differences arise from the annihilation of the positron and electron in the target. For example, pairs of muons are produced more efficiently in the positron beam dump through the annihilation process between the e^+ beam and atomic electrons ($e^+e^- \to \mu^+\mu^-$). Fig. 42 shows the energy distribution of muons downstream of the beam dump. The contribution of muons from the annihilation process in the positron beam dump (red curve) is higher than the one in the electron beam dump (blue curve) and is dominant in the high energy region.

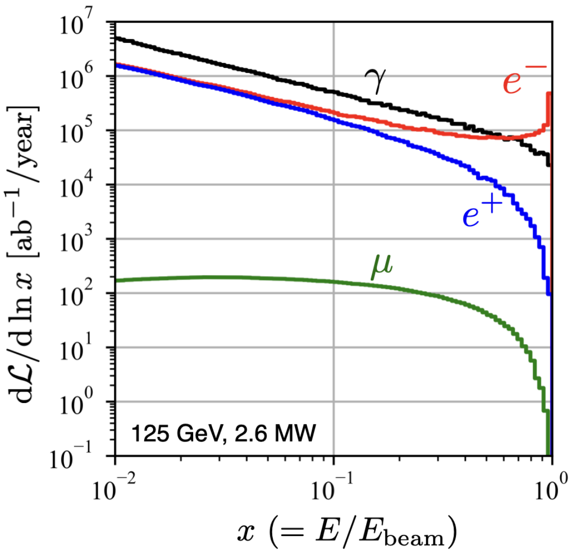

Figure 41: The luminosity of $e^{\pm}$, γ, $\mu^{\pm}$ to nucleons of water target inside the electron beam dump as the function of $\ln x$, where $x = E/E_{beam}$.

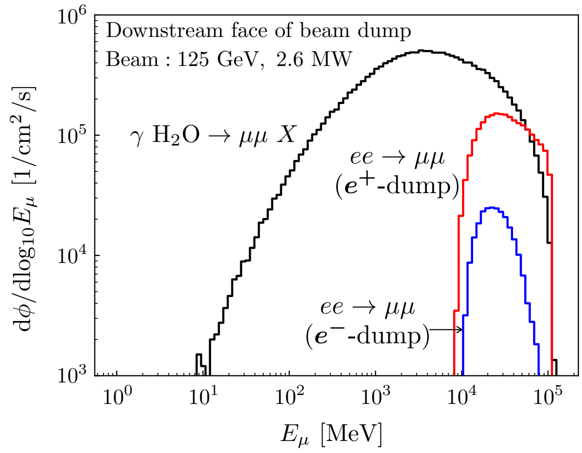

Figure 42: The energy distribution of muons downstream of the beam dump. The contribution of muons from the annihilation process in the positron beam dump (a red curve) is higher than the one in the electron beam dump (a blue curve) and is dominant in the high energy region.

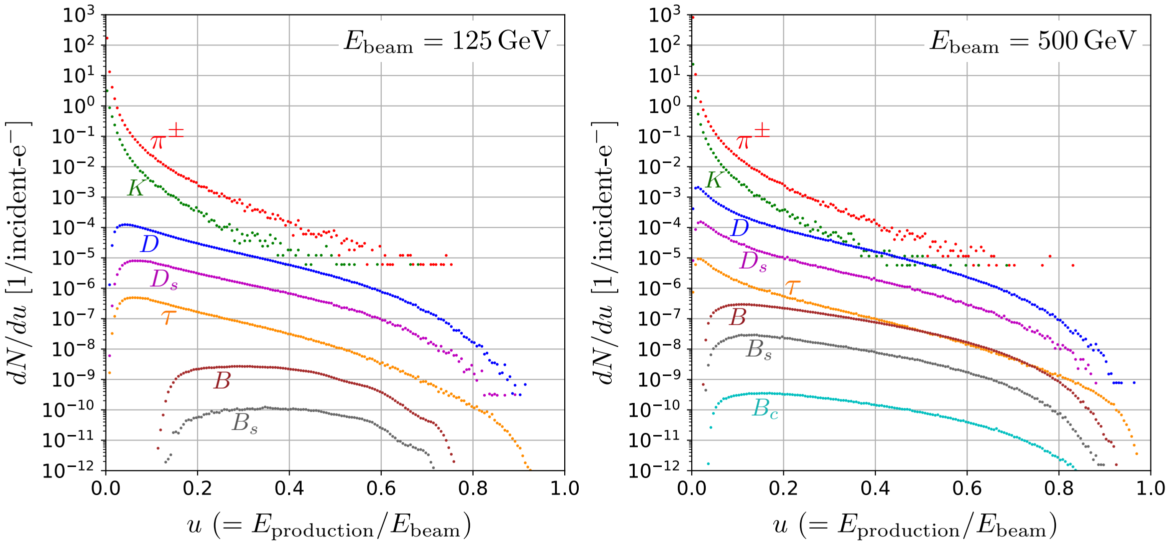

Figure 43: The energy distribution of mesons and tau leptons at its production inside the LC beam dump.

High-energy electron or positron beam dumps produce not only electromagnetic shower particles but also a large number of hadrons and tau leptons. Figure 43 shows the energy distribution of mesons and tau leptons at its production inside the LC beam dump. For this evaluation, meson production via photoproduction has been considered for hadron production because photons are dominant secondary particles in EM showers. In contrast, tau lepton production cross section includes both the contributions from D_s decay ($D_s \to \tau\nu_\tau$) and pair production from real photons ($\gamma N \to \tau^+\tau^- X$). In the high-energy region where $u > 0.65$, the pair production process becomes dominant, a characteristic feature of electron beam dumps. In the right panel, we show the same distribution of $E_{beam} = 500$ GeV. At the higher scale, the contributions of the D and B are more prominent. The total number of B mesons, D mesons, τ leptons per $N_{EOT} = 4 \times 10^{21}$ are 4×10^{12}, 7×10^{16} and 3×10^{14} for $E_{beam} = 125$ GeV, and 3×10^{14}, 5×10^{17} and 2×10^{15} for $E_{beam} = 500$ GeV.

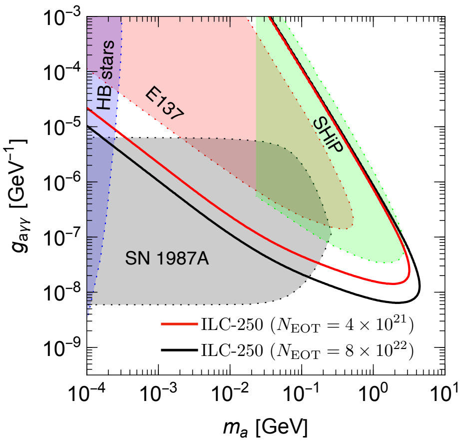

Figure 44: Sensitivity reach of the beam dump experiment to ALPs coupled to photons [393]. The SHiP limit is taken from [394]

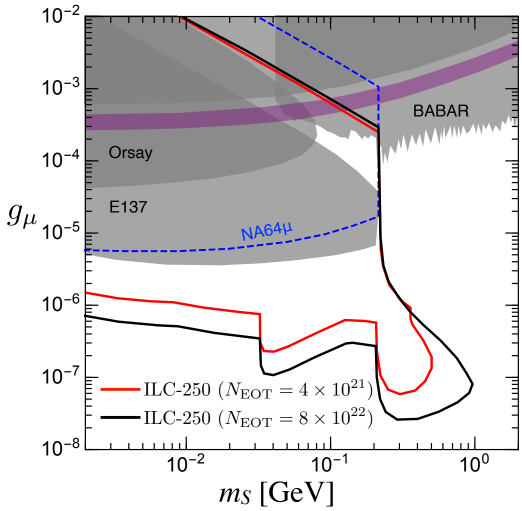

Figure 45: Excluded region of Leptophilic Scalar couple to muon. Figures are modified from [395].

Dark Sector particle searches Many extensions of the Standard Model contain particles that do not carry SM gauge charges, or "dark sector" particles. Dark sector particles often arise in models that address the hierarchy problem (e.g., relaxion models), the strong CP problem (models with axions or axion-like-particles (ALPs)), and very importantly Dark Matter (DM) models.

In the past decade, there has been a flourishing of new ideas to search for dark sector particles at accelerator-based experiments (colliders, meson factories, fixed target experiments, ...). For a recent review, see [392]. Dark sector particles can naturally have a long lifetime, making them a target for beam dump experiments.

Axion-like particles Axion-like particles (ALPs), A, are pseudoscalar particles whose Lagrangian has an approximate shift symmetry. ALPs can couple to the SM gauge bosons, V, with interactions of the type

$$\mathscr{L}_{VV} = g_{aVV}\, aV_{\mu\nu}\tilde{V}^{\mu\nu}/4, \tag{8}$$

where $V_{\mu\nu}$ is the field strength tensor and $\tilde{V}_{\mu\nu} = \varepsilon_{\mu\nu\alpha\beta}V^{\alpha\beta}/2$. ALPs can also couple to the SM fermions with derivative couplings, $\propto \partial_\mu a(\bar{f}\gamma^\mu\gamma_5 f)$.

These ALPs could be produced in the LC electron beam dump through the bremsstrahlung process initiated by the secondary photon beam. They could decay to two photons after the dump. Their lifetime can, in fact, be macroscopic and is given by

$$\tau_a = 4\pi/(c^2_{a\gamma\gamma}m_a^3) \simeq 4\pi\left(\frac{\mathrm{GeV}}{m_a}\right)^3\left(\frac{1}{g_{a\gamma\gamma}\mathrm{GeV}}\right)^2\frac{\mathrm{m}}{5\times10^{15}}\,. \tag{9}$$

Due to the setup of the ILC beam dumps, this experiment can be sensitive to GeV-scale ALPs with coupling to the photons of the order of $\mathscr{O}(10^{-8}/\mathrm{GeV})$. This is demonstrated in Fig. 44 where we show the sensitivity for ILC-250 GeV at 95% C.L. with 1- and 20-year statistics. Even 1-year of ILC beam dump could extend the SHiP reach by roughly an order of magnitude in couplings.

Apart from dumping charged particles on a fixed target to search for ALPs, high-energy photons can also be used. Such photons can be produced via Compton backscattering when colliding high-energy electrons with a high-intensity laser pulse, such as in setups of strong-field quantum electrodynamics experiments described in Sec. 3.9.2. Fixed-target searches using photons have been shown to have significantly lower background rates in certain cases [396]. Simulations showed that a linear collider facility can probe new phase space of the ALP-photon coupling compared to existing constraints and projections of current experiments in such a configuration [397]. Additionally, the approach remains highly complementary since this method leverages photon interactions via the Primakoff production mechanism directly.

Leptophilic Scalar ILC beam dump is a good place to search for light scalar particles coupled to electrons and muons (Leptophilic Scalar). The Lagrangian of the simplified model is expressed as follows[9],

$$\mathscr{L} = \frac{1}{2}(\partial_\mu S)^2 - \frac{1}{2}m_S^2 S^2 - \sum_l g_l S\bar{l}l - \frac{1}{4}SF_{\mu\nu}F^{\mu\nu}. \tag{10}$$

Figure 45 shows the expected limit on the Leptophilic scalar coupled to muons. Because of the high electron energy, $\mu^\pm$ is copiously produced, being the source of S particle. They can be detected if they decay back to the lepton pairs before the detector. The expected limit is shown in the figure. The peculiar shape of the excluded region comes from its competing production process of scalar boson (Bremsstrahlung, Primakoff and pair annihilation). [10].

Heavy neutral leptons(HNL) The Neutrino sector can be extended to include the right-handed neutrino. In that case, the heavy neutral lepton is predicted, and the constraint of the heavy neutral lepton is weak enough to allow this sector to play a pivotal role in the leptogenesis by introducing the CP violation to the sector. The charged current interaction between a charged lepton and HNL is expressed as;

$$\mathscr{L} = -\lambda_{IK}(\bar{L}_I\tilde{H})N_I - \frac{1}{2}M_I\bar{N}_I^c N_I + h.c., \tag{11}$$

where N_I express the extra neutral lepton that mixes with the SM neutrinos. When the coupling λ is small, the mixing angle is approximated as

$$U_{ll} = \frac{v|\lambda_{ll}|}{M_l}. \tag{12}$$

The interaction of charged lepton is already strongly constrained as low as $10^{-10} < U^2 < 10^{-4}$ depending on the m_{HNL} for mixing to the electron.

The phenomenology of HNL at the beam dump experiment is complex because various production processes contribute. The charged current interaction of electron or muon produces the HNL directly and dominant production cross section of the high mass region. The production cross section is proportional to the square of the mixing angle of U^2, while the probability of decaying inside the decay volume reduces if the mixing angle is either too large or too small. The corresponding accessible region is the nose-like region above a few GeV shown in the black (E_{beam} = 250 GeV) and the red lines (E_{beam} = 500 GeV). While the accessibility of the beam dump experiment to the HNL has been estimated, the effect of the beam polarisation has not been carefully studied yet. The electron beam is highly polarised at the injection of beam dumps so that the highest charged current interactions depend on the beam polarisation, while the effect is diminished for the electron and positron at the end of the EM showers. This should allow us to study the interaction of HNL or other BSM particles that are produced at the beam dump.

The heavy neutral leptons can also be produced by heavy meson decay. Any meson-weak decay process contributes to the HNL production through neutrino mixing. As already discussed, at the LC beam dump, HNL is copiously produced by photon nucleon interaction, and the leptonic decay of the heavy mesons is a source of HNLs. The effect can be seen in the edge-like structure of the excluded region at 500 MeV, 2 GeV and around 3 GeV, hidden behind the direct production limit.

Note that expected reach E_{beam} = 250 GeV of the Figure closely follows the SHiP limit. This is because the total flux of neutrinos at the beam dump is roughly equal to the expected SHiP neutrino. As we discuss the facility section, the SHiP limit assumes an active muon veto(need check). In contrast, the ILC limit assumes a rather simple director setup and the kinematical reduction of the background. Figure 46 compares the various limits of the HNL mixing with ν_e.

[9] The mixing of S to the SM Higgs bosons also has to be considered.

[10] This case is not explored in the SHiP report

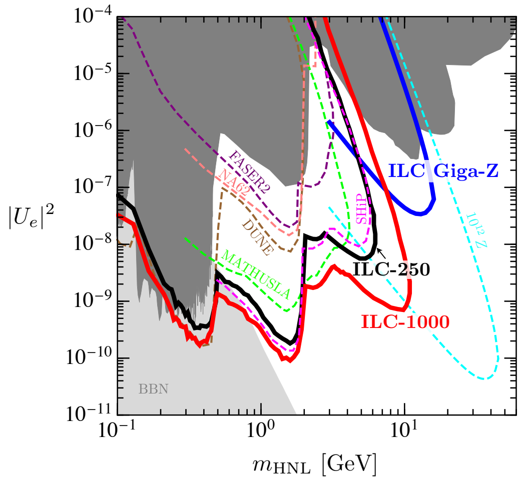

Figure 46: Sensitivity reach of the beam dump experiment to HNLs mixing with the electron neutrino in the mass and mixing plane, assuming 10 year run at ILC like set up with energy 250 GeV (black solid) and 1000 GeV (red solid) figures are taken from [398].

Dark Matter Light dark matter particles can be produced at the beam dumps of the ILC. Depending on the specific model, DM particles can be produced via bremsstrahlung at both electron and positron beam dumps or via pair-annihilation of positron on an atomic electron at the positron beam dump. The resulting DM particles can scatter off electrons in a detector placed after the muon shield and yield observable electron-recoil events. Several models predict the existence of heavier dark particles in addition to DM and the decay of heavy particles to dark matter can produce a signal at beam dump experiments. This is the case of e.g., inelastic DM models or models with strongly interacting massive particles. In Fig. 47, we show the reach in the case of pseudo-dirac inelastic dark matter, which is detected via decay (left panel) and for scalar inelastic dark matter detected by scattering (right). In both cases, the ILC will be able to extend the probed regions of parameter space, if compared to past and current experiments (in gray in the figure). Particularly, the ILC will have access to the "thermal lines" where DM acquires the measured relic abundance (shown in black in the figure). The future ILC beam dump reach will be complementary to the reach at the proposed LDMX experiments (blue lines in the figure). In the case of scalar inelastic DM, the ILC bound is expected to be weaker than the LDMX one. However, the beam dump experiment can potentially give additional information since it can characterize the DM interaction in detail by identifying the recoil objects. The reach in the figure was computed in the case of production at the positron beam dump. The ILC reach varies if the search is done at the electron beam dump or at the positron beam dump, with generally a broader reach in the case of positron beam dump, due to the increase in production coming from the pair-annihilation of positron on an atomic electron.

3.9.2 Strong-Field QED

Strong-field quantum electrodynamics (SFQED) describes the behavior of charged particles and photons in strong electromagnetic fields, where nonlinear effects become significant. These effects emerge when field strengths approach the QED field strength scale, which is sometimes also called the critical field or the Schwinger limit $E_{\mathrm{qed}} = \frac{m_e^2 c^3}{e\hbar} \approx 1.32 \times 10^{18}$ V/m, where m_e is the electron mass, c the speed of light in vacuum, e the elementary charge, and $\hbar$ the reduced Planck constant. Processes like nonlinear Compton scattering and nonlinear Breit-Wheeler pair production, as well as the effect of vacuum birefringence, can be observed. With advancements in high-intensity laser technology, SFQED is now experimentally accessible. A future linear collider facility with beam energy above 100 GeV will provide a unique opportunity to probe this largely unexplored regime of QED.

The strong-field QED phase space can be defined via two parameters. One is the classical nonlinearity parameter $\xi = eE\lambda_c/\hbar\omega$ also called the intensity parameter, although proportional to the square root of the laser intensity. $\lambda_c = \hbar/(m_e c)$ is the Compton wavelength and ω the angular frequency of the laser photons.

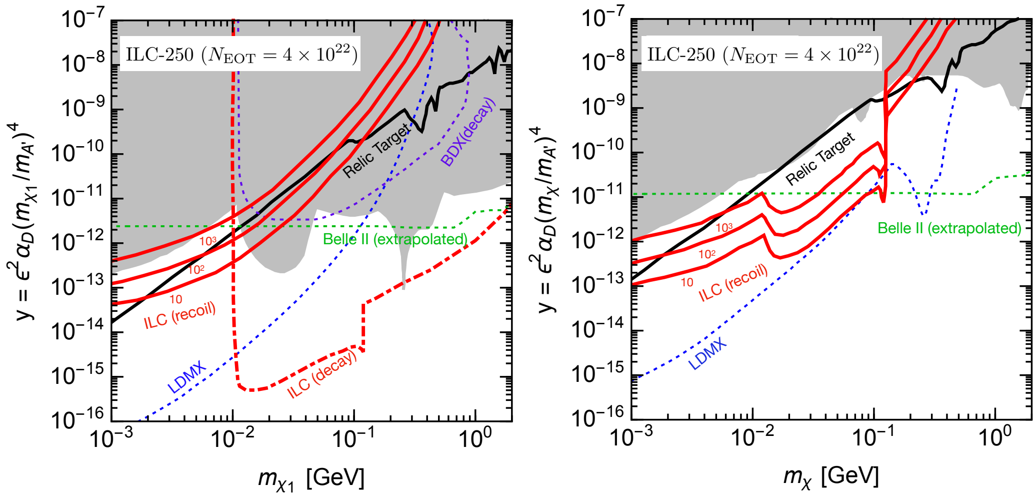

Figure 47: Projected sensitivity reach of a 10-year ILC-250 run in the pseudo-Dirac DM model (left panel) and in the scalar inelastic DM model (right panel). See [399] for the details on the specific benchmark chosen for the two models. The solid lines correspond to 10, 10^2, 10^3 signal events in the case of DM scattering. The dotted-dashed line in the left panel shows the reach of the decay signal search. In both panels, we show the reach at the positron beam dump.

The other one is the quantum nonlinearity parameter which in plane-wave approximation is $\chi = \gamma E/E_{\mathrm{qed}}$, where γ is the Lorentz boost of the electron and E the electric field strength of the laser pulse. In the context of electron-laser collisions it is convenient to also define the linear quantum parameter $\eta = \chi/\xi$ which is proportional to the momentum of the electron.

Electron-Laser Interaction So far, tests of strong-field QED by colliding electrons with a high-intensity laser have only been conducted with the E-144 experiment at SLAC (US). They collided electrons with an energy of 46.6 GeV with a 1 TW laser, resulting in a value of $\chi = 0.3$. They observed a total of 106 ± 14 positrons from the nonlinear Breit-Wheeler process [400]. Currently, the E-320 experiment at SLAC is testing SFQED with the FACET-II electron beam with an energy of 10 GeV and 10 TW available laser power [401]. At DESY (DE), the LUXE experiment is planned to be measuring in the near future at the 16.5 GeV electron beam of the European XFEL and also 10 TeV available laser power [402, 403]. Both experiments are considering laser upgrades in a second phase.

At the point when a linear collider facility becomes operational, advancements in high-power laser systems will likely result in the availability of laser systems capable of delivering 100 PW or more [404]. Electron-laser collisions could be performed at a dedicated facility in the tune-up dump area, described in Sec. 5.1.3.

Various measurements are of particular interest. With a slow-extraction beamline, the elementary electron-photon interaction can be investigated by colliding single electrons with a laser pulse at normal incidence [405]. Changing the configuration to head-on collisions would allow to measure the coherent electron-positron plasma creation [406] and with an electron bunch instead of single electrons the incoherent plasma creation can be tested, which is of astrophysical interest as such strong fields can appear in magnetars, neutron starts, and black holes [407, 408]. These cases have been discussed in the ILC report to Snowmass 2021 [14].

A linear collider facility has two peculiarities that makes it particularly suited to test strong-field QED. The high degree of electron polarisation of the electron beam of more than 80% allows for the measurements of the spin-dependent rates of the strong-field QED processes [409]. Furthermore, future energy upgrades will allow for a beam energy of $\mathcal{O}(1)$ TeV. This will allow to thoroughly test the Breit-Wheeler harmonic structure [410, 411] at low laser intensity and delve into the fully non-perturbative regime where there is no reliable QED theory at all. Both cases are indicated as dashed ellipses in Fig. 48 which shows the different regimes of the strong-field QED landscape of the Breit-Wheeler process.

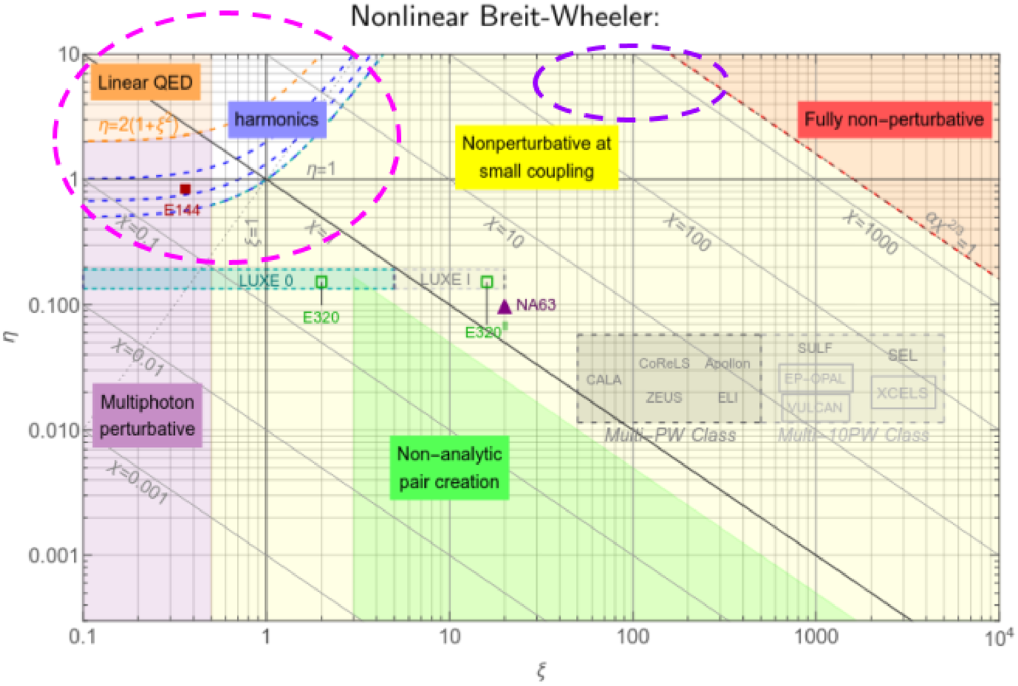

Figure 48: Phase space of the nonlinear Breit-Wheeler effect, adapted from [412], defined by the classical nonlinearity parameter ξ and the linear quantum parameter η. The different regimes are indicated by the colored areas. Two particularly interesting regimes that can be tested at a linear collider facility are the harmonic structure of the Breit-Wheeler process and the transition into the fully non-perturbative regime with no reliable QED theory, indicated by the pink and purple dashed lines, respectively.

Beam-Beam Interaction Beamstrahlung is a relevant process in future electron-positron colliders that is usually tried to be minimized. The particles in each beam radiate photons due to interaction with the electromagnetic fields generated by the opposite beam [413, 414]. In future Higgs factories the effects are in the linear regime, and the radiation is mitigated by having very flat beams. At higher beam energy, such as in a future energy upgrade of a linear collider facility, the beam-beam effects will become more significant because of the nonlinear effects. This is especially the case at energy of 1 TeV and above, where more than 10% of the energy is lost [4]. This was studied for CLIC at CERN for energies up to 5 TeV [415] and for future ultra-high energy linear colliders for energies up to 15 TeV [416]. However, the standard tools of the community to model beam-beam interaction, i.e. GUINEA-PIG [417] and CAIN [418], are not believed to accurately model all physics processes. Therefore, they should be tested and validated at low energy where the tools are reliable.

The beamstrahlung is characterized by the beamstrahlung parameter

$$\Upsilon_{\text{avg}} = \frac{5 r_e^2 \gamma N_e}{6\alpha\sigma_z(\sigma_x + \sigma_y)}, \tag{13}$$

where r_e is the classical electron radius, N_e the number of electrons, α the fine structure constant, and σ is the Gaussian sigma in the corresponding direction. From a strong-field QED perspective, this is the average quantum nonlinearity parameter that the particles experience in the collision $\Upsilon_{\text{avg}} \equiv \chi$. For a systematic investigation, various parameters can be tuned, such as the energy, the shape of the beam, and also the misalignment/offset between the two beam axes [419]. Such tests could be done at the second interaction point of the linear collider facility. The main diagnostics required is a detection system in the forward direction for the produced photons and, at higher energy, the coherent electron-positron pairs. Detailed studies are required.

The fully non-perturbative regime of strong-field QED, indicated in Fig. 48, can also be tested in the beam-beam interaction with highly focused beams of energy above 100 GeV. This approach may even be more easily accessible since it does not require a high-power laser facility. Simulations showed that in particular with slightly misaligned beams, very high values of $\chi \gtrsim 1000$ can be probed [419, 420].

4 A Linear Collider Facility - Baseline and Roadmap

This section takes a fresh look at various accelerator concepts and technologies proposed for linear colliders, aiming to develop a coherent picture of providing e^+e^- collisions at the earliest possible date, while remaining open to the many exciting R&D ideas which could gain maturity on short-, medium- and long-term timescales.

The timing here is important. The next collider should plan for data-taking on a schedule that will motivate young scientists involved in the LHC program to participate in the design and construction of Higgs factory detectors in parallel with late-stage HL-LHC data analysis. Delay and uncertainty will discourage young people and sap the vitality of collider physics. On the other hand, our field must be able to react in a flexible way to new scientific developments, be it from HL-LHC, Belle-II, other ongoing experiments – or the first stage of a linear collider itself.

Over the last year, the LC Vision team developed a compelling scenario to address this apparent contradiction: A Linear Collider Facility (LCF), with a first stage that is affordable and based on the technology which promises earliest realisation, implemented within an underground structure compatible with upgrading the facility with other, more advanced technologies in future. Following this guiding paradigm, this section is structured as follows: We will first discuss the two most mature technologies, which can be considered for a first stage, namely "ILC-like" SCRF (Sec 4.1) and "CLIC-like" warm copper (Sec 4.2) accelerating structures. These sections heavily rely on the mature designs of the ILC [4, 6, 14] and CLIC [10, 15] projects which also have been submitted to the EPPSU [16, 17]. Linear collider proposals have often been criticised for offering only one interaction region, usually a choice made for cost reasons. We will address this issue by discussing key aspects of the beam delivery system (BDS) in Sec. 4.3, in particular covering the existing designs with a double BDS catering two interaction regions and how they would need to be optimised for a linear collider facility. Section 4.4 then discusses opportunities to upgrade an initial linear collider facility to higher energies by exploiting technologies under development today, including advanced super-conducting RF, cool and warm copper RF as well as plasma wake-field acceleration. Upgrade opportunities leading to higher luminosity will be discussed in Sec. 4.5 – spanning from straightforward upgrades to the minimal ILC scenario to concepts for energy and particle recovery – before addressing alternative collider modes like in particular $\gamma\gamma$ collisions in Sec. 4.7. Opportunities for beyond-collider extensions of the facility will be discussed in Sec. 4.4.3.

4.1 First Stage based on Superconducting Radio Frequency (SCRF) Cavities

A Linear Collider based on SCRF has been studied in great detail in the context of the International Linear Collider ILC, as documented in a Technical Design Report [1–5] and several updates since [6, 14]. The ILC TDR considered three different sample sites for construction, at Fermilab, at CERN and in Japan. Following the discovery of the Higgs boson at the LHC [421, 422] in 2012, the Japanese HEP community expressed interest to host the ILC in Japan, and siting, civil construction and costing studies focused on a minimal version of the ILC in Japan [6]. In the last years, the ILC design has been guided by the International Development Team (IDT [423]), and important R&D aspects have been advanced by the International Technology Network (ITN [424]). In particular for the EPPSU, the cost estimate for the ILC in Japan has been updated. For about 2/3 of the costs, the update is based on new quotes from industry, whereas the remaining items have been escalated to 2024 costs. The cost update as well as the work of the ITN are summarized in the IDT's submission to the EPPSU [16].

Here, we discuss a SCRF-based linear collider in a more general context, for a project anywhere in the world, including opportunities to modernize the ILC design. We will refer to such a generalized and modernized SCRF-based linear collider as Linear Collider Facility (LCF). The underlying TESLA SCRF technology is by now well-established with several free electron laser facilities in operation (FLASH and European XFEL in Hamburg, Germany and LCLS-II at SLAC, USA) or under construction (energy upgrade of LCLS-II at SLAC and SHINE in Shanghai, China). We summarize the experience with cavity production for the European XFEL as part of Sec. 4.1.1, and discuss the experience from its operation in Sec. 4.1.2, both underpinning the maturity and reliability of the technology.

For an SCRF linear collider, the two main baseline options under consideration are 1) a cost-minimizing option and 2) a day-1 operation at 550 GeV. The first option has a centre-of-mass energy reach of 250 GeV within 20.5 km, following [32]. The second option, retained in [19] is similar to a collider presented in the ILC TDR [1–5] but with a slightly higher centre-of-mass energy of 550 GeV fitting into a 33.5 km long site. Both options can accommodate two interaction points as will be discussed in section 4.3. An option of a 27 km collider with a centre-of-mass energy between 350 and 380 GeV could be considered, however is not favoured from the point of view of an optimal science program (apart from the threshold mass determination, most top quark measurements achieve much better results at higher centre-of-mass energies of at least 550 GeV, which also enable the study of $t\bar{t}H$ and ZHH production, c.f. Sections 3.5.2 and 3.3). If desired, a path towards the 550 GeV collider could include construction a full-length tunnel and other civil infrastructure but with an initial installation of linacs sufficient to run at 250 GeV centre-of-mass only for the first physics runs. Subsequent installation of additional SCRF cryo-modules and other accelerator hardware would increase the machine energy to the full 550 GeV centre-of-mass energy.

Constructing the 33.5 km full length tunnel required for the desired final energy (of 550 GeV) provides attractive features at reasonable additional cost: It avoids the complications created by digging more tunnel, which causes vibration, during accelerator operation. In a geology that lends itself to the use of a tunnel boring machine (e.g., in the Geneva area), drilling a full length tunnel in a single go is considerably more economic than inserting and extracting a tunnel boring machine again at a later time. Cryo modules can be installed in several shorter shutdowns as they become available, avoiding very long interruptions of the physics programme. Also it avoids the relocation of the turn around arcs, the spin rotators and the bunch compressors, with a total length of about 1.2 km on each side, after a tunnel extension.

Even the 20.5 km includes some reserve length of tunnel, which is partially necessitated by a timing constraint between damping ring circumference and main linac length. Such a reserve is an important risk mitigation, as it would permit, if necessary, to install more cryomodules and thus reduce the gradient requirements, should producing cavities at the design gradient turn out to be economically less advantageous than producing and installing more cavities at slightly lower gradient.

Table 11: Key parameters for the updated superconducting Linear Collider Facility (LCF) compared to the ILC baseline options. Values for ILC250 and ILC500 are taken from Table 4.1 in [14]

Parameter	Unit	ILC250	ILC500	LCF250	LCF550
Centre-of-mass energy	GeV	250	500	250	550
Luminosity	$10^{34}\mathrm{cm}^{-2}\mathrm{s}^{-1}$	1.35/2.7/5.4	1.8/3.6	2.7/5.4	3.9/7.7
Polarisation, $P(e^-)/P(e^+)$	%	80 / 30	80 / 30	80 / 30	80 / 60
Number of interaction points		1	1	2	2
Repetition frequency	Hz	5/5/10	5	10	10
Number of bunches per train		1312/2625/2625	1312/2625	1312/2625	1312/2625
Bunch spacing	ns	554/366/366	554/366	554/366	554/366
Bunch train duration	μs	727/961/961	727/961	727/961	727/961
Cavity quality factor	10^{10}	1	1	2	2
Klystron efficiency	%	65	65	80	80
Bunch population	10^{10}	2	2	2	2
Accelerating gradient	MV/m	31.5	31.5	31.5	31.5
Length of 2 SCRF linacs	km	10	22.3	10	24.1
Total facility length	km	20.5	33.5	33.5	33.5
Site power consumption	MW	111/138/198	173/215	148/182	250/322

Previously reported ILC baseline options assumed that SCRF linacs operate at an accelerating gradient of 31.5 MV/m, see [1–5]. The worldwide R&D efforts continue to improve performance of SCRF cavities and efficiency of klystrons. Some of the recent advances can benefit the baselines of the SCRF linear collider already and are discussed in section 4.1.1. Taking into account an improved SCRF cavity performance with a quality factor of 2×10^{10} at 31.5 MV/m and a klystron efficiency of 80%, Table 11 shows the main parameters for an updated ILC-like Linear Collider Facility in comparison to the ILC itself. Notable differences comprise:

- centre-of-mass energy: the LCF targets operation at 550 GeV instead of 500 GeV for a much better precision on the top quark Yukawa coupling. Note that this does not increase the overall facility length as already the ILC main linac tunnel provides a sufficient length.

- repetition rate and instantaneous luminosity: the LCF proposes to operate at a repetition rate of 10 Hz, i.e. twice the repetition rate, at full gradient. For ILC, 10 Hz operation has only been considered when operating the physical 500 GeV machine at 250 GeV, i.e. when operating the main linacs at half their maximal gradient. Due to the improved Q_0 and the higher klystron efficiency of a modernised design, the impact of the 10 Hz operation at full gradient on the total site power is visible, but not outrageous and significantly improves the luminosity-to-power ratio. For instance at 550 GeV, the power increase by about 50 % more than doubles the luminosity. For more information on the luminosity upgrade options we refer to Sec. 4.5.2.

- beam polarisation: for the 500 GeV ILC, an upgrade of the positron polarisation from 30 % to 60 % was foreseen in the TDR [4] by installing a longer helical undulator and a collimation system. Due to more challenging positron production with a lower electron drive-beam energy, this was never considered for the 250 GeV ILC. Since the ILC TDR, there has been significant progress both in terms of the design of the positron source (c.f. [425] for a recent summary) as well as in terms of operation experience with long undulator systems, e.g. at the European XFEL. Thus, after several years of experience with operating the positron source in the more challenging 250 GeV configuration, the positron polarisation can be increased to $|P(e^{+})| = 60\%$ for the 550 GeV stage.

- number of interaction points: the LCF foresees two interaction points, while the original second interaction point was removed from the ILC design during the TDR phase in order to reduce the construction cost.

- total facility length: for the LCF, a 33.5 km tunnel is foreseen from the beginning. For an initial 250 GeV stage, the turn-arounds between the RTML and the ML will be built at the ends of the facility, and the outer half of the ML will be equipped with cryo-modules, followed by a transport line (e.g. with a simple FODO lattice) to the beginning of the BDS. While this adds about 0.65 BCHF to the initial construction cost, such a scenario enables a seamless upgrade to 550 GeV. Given sufficient resources, cryo-module production could continue after the installation of the 250 GeV machine, and cryo-modules could be added in the annual or bi-annual shutdowns as they become available, or stored and installed in one longer shutdown. Alternatively, one can consider a scenario in which a host country or region can decide to move ahead with the construction of the 250 GeV machine (in a 33.5 km tunnel) independently of – or only with a small number of – other contributors. Should, after a positive decision, other parties decide to join the project, providing additional cryo-modules produced in local industry as in-kind contribution offers a potentially attractive route, directly augmenting the energy reach of the facility. In any case the fact that no additional civil construction will be needed for the upgrade to 550 GeV, is considered a decisive advantage.

- more efficient components: given the necessarily longer preparation time for a new site in the Geneva area, more ambitious R&D goals for klystron efficiency (80 instead of 65 %) and cavity quality factor ($Q_0 = 2 \cdot 10^{10}$ instead of $1 \cdot 10^{10}$) have been formulated, based on recent technological advances.

While Table 11 focuses on 250 and 500/550 GeV, a SCRF linear collider can always be operated at lower energies, for instance at the Z pole or at the WW and $t\bar{t}$ production thresholds as physics demands. The overall accelerator parameters for these lower energies have not been optimized in as great detail as for the main energies yet. Some recent, preliminary ideas on how to improve the luminosity at the Z pole and WW threshold quite significantly will be discussed in Sec. 4.5.1.

4.1.1 SCRF Specifications for the Baseline

The ILC TDR [1–5] specifies an accelerating gradient of 31.5 MV/m and an intrinsic quality factor Q_0 of 1×10^{10}. This level of performance is by now firmly established, with recent R&D results pointing towards the possibility of increased performance, potentially combined with lower production costs, through novel surface treatments.

A statistical model, based on the European XFEL data, which accurately includes the gradient increase due to re-treatment of low performing cavities, shows that the ILC specification of an yield of 94% at 35 MV/m for the maximum gradient can be achieved after re-treatment of underperforming cavities.

Taking into account other limitations (field emission and low quality factor), the usable gradient is lower, 33.4 MV/m with a 82(91)% yield after one (two) re-treatments. The re-treatment would mostly be limited to a simple high-pressure rinse (HPR) rather than a more expensive electropolishing step. Thus, with a reasonable extrapolation, the European XFEL cavity production data demonstrate that it is possible to mass-produce cavities in industry meeting the ILC TDR specifications with the required yield [426].

Further, the ILC-like performance with beam was demonstrated in two laboratories. A cryo-module at Fermilab has reached total accelerating voltage of 267.9 MV, equivalent to an average gradient of 32.2 MV/m for eight cavities, thus exceeding the ILC goal. A beam with 3.2 nC bunch charge has obtained an energy gain of >255 MeV after passing through the cryo-module [427]. At KEK, nine (including one nitrogen-infused cavity) out of twelve cavities in a demonstration cryo-module at the STF test facility exceeded the ILC specification, achieving an average accelerating gradient of 33 MV/m during beam operation [428]. Three of these cavities exceeded 36 MV/m.

The results discussed above are obtained with the SCRF cavities subjected to the ILC-TDR cavity processing recipe, which include electrochemical polishing (EP), outgassing at 800°C in a furnace under high vacuum, HPR, and vacuum baking at 120°C. The cost estimate for ILC, for the TDR and the recent update for the EPPSU [16], is based on quotes from companies around the world which have demonstrated that they can produce cavities following the ILC recipe.

Recent advancements in surface tailoring techniques have led to groundbreaking results, as laboratories have successfully introduced nitrogen, oxygen, and other impurities into the niobium lattice. These innovative procedures have yielded increasing efficiency of cavities by a factor of 2 to 3 at medium accelerating fields, 20 to 30 MV/m. The best experiments employing medium temperature, or mid-T, vacuum bake produced 1.3 GHz SCRF cavities with a quality factor of 5×10^{10} at 30 MV/m and 2 K [429, 430]. The world's first SCRF cryo-module with nine 1.3 GHz mid-T baked cavities was developed and successfully tested at IHEP, China [430].

On the high-gradient side, new advances pushed accelerating gradients towards 50 MV/m in vertical tests of single-cell TESLA cavities, and demonstrated that with some additional R&D it should be practically achievable to operate TESLA cavities in cryo-modules at >35 MV/m while maintaining $Q_0 > 2 \times 10^{10}$. Examples of the new recipes are 1) a combination of cold electropolishing and two-step baking (75/120°C) [431] and 2) medium temperature (mid-T) baking followed by low-T baking [432]. Figure 49 shows curves of an intrinsic quality factor vs. accelerating gradient for three 1.3 GHz cavities after a combination of mid-T and low-T treatment. The performances of all three cavities are outstanding and very promising, indicating that large accelerating gradients accompanied by high quality factors are in reach. Following a short-term R&D to refine the cavity processing procedure, a well-funded industrialization program ($\sim$ 5 years) should be launched to demonstrate the required cavity production yield. While global availability of high-purity niobium remains a concern, there is progress with increasing SCRF cavity production capacity worldwide. Europe has traditionally been a cavity production hub with two strong companies qualified to make cavities per ILC specifications. With several SCRF-based accelerator projects under way, China has developed industrial capabilities to produce 1.3 GHz cavities. More recently, South Korea's industry has become interested in building up such a capability as well.

In parallel to industrialising the cavity processing advances, better strategies for mitigating the effect of field emissions should be deployed in order to minimise the difference between maximal and usable gradient and maximise the yield of high gradient cavities. Examples comprise a robot-assisted automation of the cryo-module assembly and plasma processing after installation [433].

Significant technical progress has been made in improving the efficiency of high-power klystrons. This will make L-band klystrons with > 80% efficiency a reality in the near future if current R&D efforts will continue

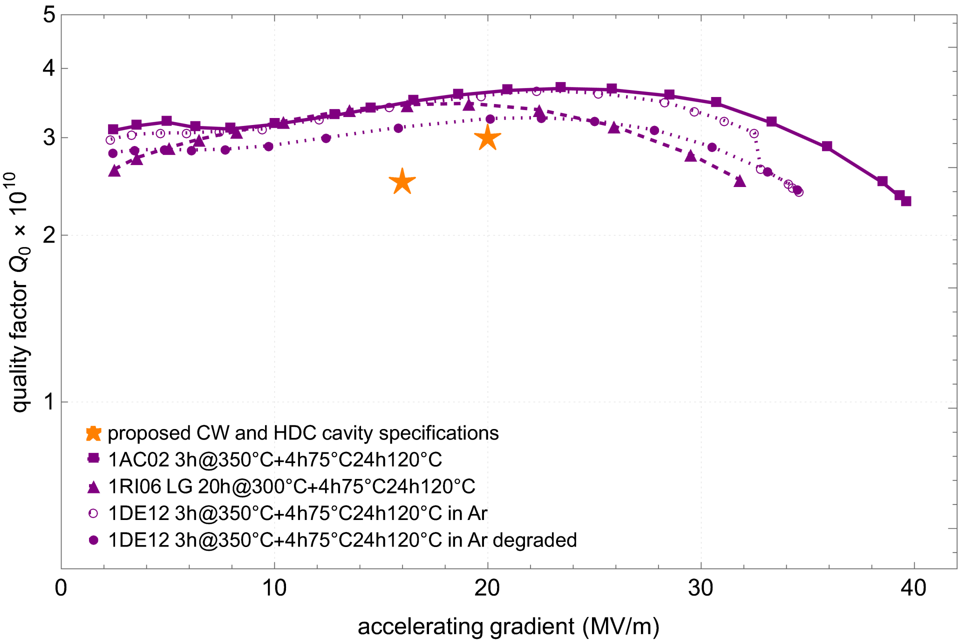

Figure 49: $Q_0(E_{acc})$ curves for three single-cell cavities at 2 K after the mid-T–low-T heat treatment combination. The stars indicate the two suggested specification points for EuXFEL upgrade cavities. [432]

with sufficient funding. Then the total RF source efficiency would be $\sim$ 70%, taking into account losses in a high-voltage modulator and waveguide distribution system. Another area where short-term R&D would greatly benefit the ILC SCRF performance is the waveguide distribution system. To avoid an issue when one low-performing cavity in an RF unit can limit the performance of the whole unit, a flexible, remotely-controlled, low-loss design must be developed.

None of these recent advances have been incorporated in the ILC baseline, which – in terms of SCRF specifications – remained effectively frozen since the TDR. Today, about 12 years later, it is time to modernize the design. A most conservative update maintains the ILC average gradient of 31.5 MV/m, but assumes a higher quality factor Q_0 of 2×10^{10}, to be achieved e.g. via the mid-T baking recipe discussed above. This recipe so far exhibits an excellent reproducibility, and is actually a slight simplification compared the standard ILC recipe. Therefore, after a short optimisation period and industrial test production, it is not expected to invalidate the careful cost evaluation for the ILC [16].

4.1.2 Experience with European XFEL

The 1.4 km 1.3 GHz superconducting linac of the European XFEL (Eu.XFEL) is the largest deployment of TESLA technology. With 100 cryo-modules (800 cavities) driven by a total of 25 klystrons, the Eu.XFEL can be considered a $\sim$ 10% prototype of an ILC linac. The numbers in this section are based to a large extent on the online monitoring of Eu.XFEL operation; for conference summaries see e.g. [434, 435]. In operation since 2018, the linac was turned on at 14 GeV beam energy, which was then ramped up to the Eu.XFEL maximum design energy of 17.5 GeV within the first 18 months of operation. The maximum average cavity gradient is 23.4 MV/m, with several cavities operating close to 30 MV/m. The accelerator now routinely operates for photon users with very high availability, accelerating up to 2700 bunches per 10 Hz pulse, using an RF pulse structure very similar to ILC. Typical pulse beam currents are 0.24-1.0 mA, with a demonstration of 4.5 mA planned in the near future. The 10 MW multi-beam klystrons (originally developed for linear collider application) show excellent and robust behaviour (albeit running at typical peak powers of 4-7 MW), as do the solid-state pulse modulators. Operationally the linac systems have accumulated close to 40 000 hours, which is the specified lifetime of the klystrons. To date only four klystrons have failed and needed to be exchanged, and only one of these could be considered an end-of-life event. The state-of-the-art low-level RF (LLRF) and related controls systems facilitate a high degree of automation and almost turn-key operation. Specifically, the LLRF feedback stabilises the electron beam energy to the level of 10^{-4} or better. The Eu.XFEL has also demonstrated that cavities can be routinely and robustly operated at gradients within 0.5 MV/m of their quench limits over very long periods of time, with quench-related RF trips being quite rare. This together with the high beam energy stability is aided by the sophisticated piezo control systems which actively keep the cavities tuned on resonance to within 15 Hz.

The exceptional high availability is in part achieved by sophisticated RF trip recovery which recovers over 50 % of the RF trips with 100 seconds. The mean time between trips is typically ∼12 hours (averaged over a half-year user run), although entire weeks of operation have been observed trip free (100 % availability). The 2 K liquid-helium cryoplant in general runs routinely and provides significantly better than specified liquid helium pressure stability at the cavities. However, cryoplant failures are a significant source of downtime. Although trips are rare (few per year), recovery of the liquid helium stability generally takes between 8 and 48 hours, depending on the nature of the fault. Fortunately due to the development of new technology (magnetic bearings in the cold compressors), the longer downtimes (resulting from the need to warm up the the cold compressors) are becoming less frequent, and there is good indication that this particular issue has been resolved. Even including these long downtimes, the linac availability over an entire six-month user run routinely achieves 98 %.

4.2 First Stage based on Drive-Beam Technology

CLIC will be proposed as a linear collider option at CERN [18] and it can also be a starting point for an upgradable linear collider facility as discussed in this document. CLIC as proposed would start at 380 GeV and can be upgraded to 1.5 TeV in 29 km. In a 33 km facility one could reach very close to 2 TeV. In all cases one drivebeam is sufficient to provide the RF power needed.

Currently the civil engineering studies for a linear collider at CERN are compatible with both starting options described in this document, as they use the same footprint. In the following section the main features and parameters of a CLIC technology based accelerator complex are summarised.

4.2.1 Design overview

The schematic layout of the baseline CLIC complex for 380 GeV operation is shown in Fig. 50 and the key parameters are listed in Table 12. The schematic layout of the baseline CLIC complex for 380 GeV operation is shown in Fig. 50 and the key parameters are listed in Table 12.

The main electron beam is produced in a conventional radio-frequency (RF) source and accelerated to 2.86 GeV. The beam emittance is then reduced in a damping ring. To produce the positron beam, an electron beam is accelerated to 5 GeV and sent into a crystal to produce energetic photons, which hit a second target and produce electron–positron pairs. The positrons are captured and accelerated to 2.86 GeV. Their beam emittance is reduced first in a pre-damping ring and then in a damping ring. The ring to main linac system (RTML) accelerates the beams to 9 GeV and compresses their bunch length. The main linacs accelerate the beams to the beam energy at collision of 190 GeV. The beam delivery system removes transverse tails and off-energy particles with collimators and compresses the beam to the small sizes required at the collision point. After the collision the beams are transported by the post collision lines to the respective beam dumps.

The RF power for each main linac is provided by a high current, low-energy drive beam that runs parallel to the colliding beam through a sequence of power extraction and transfer structures (PETS). The drive beam generates RF power in the PETS that is then transferred to the accelerating structures by waveguides.

The drive beam is generated in a central complex with a fundamental frequency of 1 GHz. A 48 μs long beam pulse is produced in the injector and fills every other bucket, i.e. with a bunch spacing of 0.6 m. Every 244 ns, the injector switches from filling even buckets to filling odd buckets and vice versa, creating 244 ns long sub-pulses. The beam is accelerated in the drive-beam linac to 1.91 GeV. A 0.5 GHz resonant RF deflector sends half of the sub-pulses through a delay loop such that its bunches can be interleaved with those of the following sub-pulse that is not delayed. This generates a sequence of 244 ns trains in which every bucket is filled, followed by gaps of the same 244 ns length. In a similar fashion three of the new sub-pulses are merged in the first combiner ring. Groups of four of the new sub-pulses, now with 0.1 m bunch distance, are

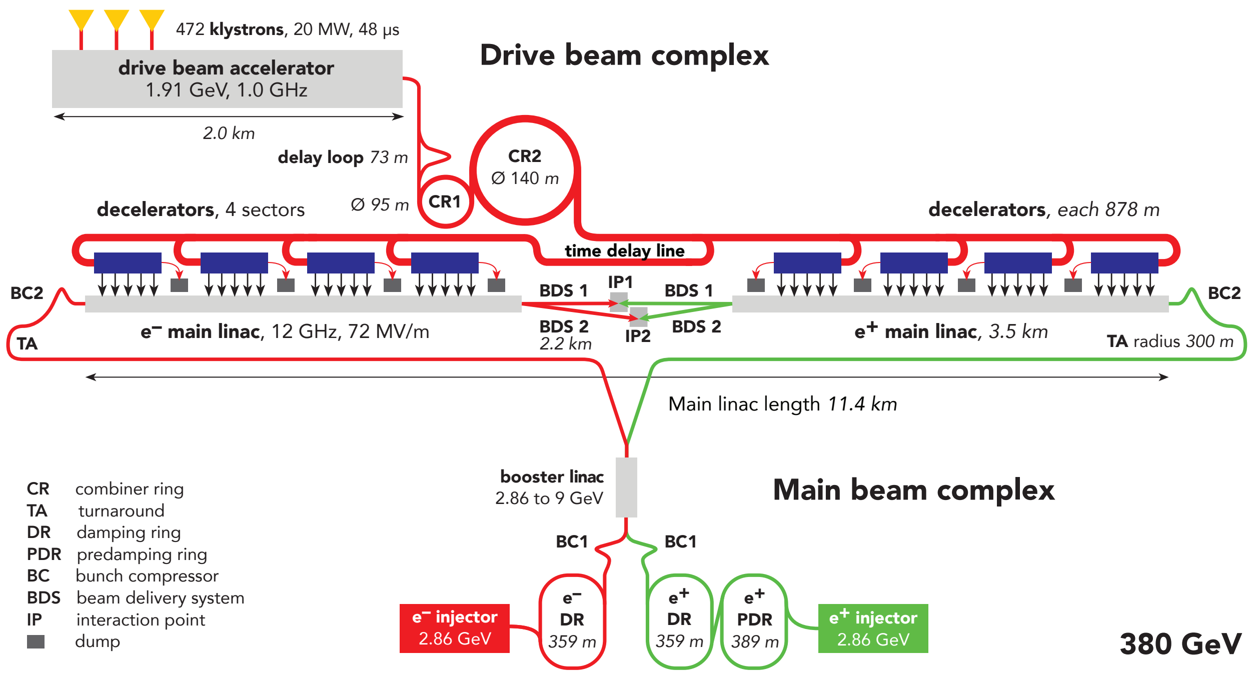

Figure 50: Schematic layout of the CLIC complex at 380 GeV, with a double beam-delivery system and two detectors.

then merged in the second combiner ring. The final pulses are thus 244 ns long and have a bunch spacing of 2.5 cm, i.e. providing 24 times the initial beam current. The distance between the pulses has increased to 24 $\times$ 244 ns, which corresponds to twice the length of a 878 m decelerator. The first four sub-pulses are transported through a delay line before they are used to power one of the linacs while the next four sub-pulses are used to power the other linac directly. The first sub-pulse feeds the first drive-beam decelerator, which runs in parallel to the colliding beam. When the sub-pulse reaches the decelerator end, the second sub-pulse has reached the beginning of the second drive-beam decelerator and will feed it, while the colliding beam has meanwhile reached the same location along the linac.

4.2.2 Extension to higher energy stages

The CLIC 380 GeV energy stage can be efficiently upgraded to higher energies. This flexibility has been an integral part of the design choices for the first energy stage. With a single drive beam and running at 100 Hz, the machine can be upgraded to 550 GeV. With a single drive beam and running at 50 Hz, the machine can be upgraded to 1.5 TeV, and possibly to 2 TeV. Parameters for a 1.5 TeV stage a given in Table 13. The table also contains numbers for a 250 GeV and 550 GeV CLIC. The power and luminosity at these energies are scalings, based on the 380 GeV and 1500 GeV designs. The key parameters for the different energy stages of CLIC are given in Table 13.

In the 380 GeV stage, the linac consists of modules that contain accelerating structures that are optimised for this energy. At higher energies these modules are reused and new modules are added to the linac. First, the linac tunnel is extended and a new main-beam turn-around is constructed at its new end. The technical installations in the old turn-around and the subsequent bunch compressor are then moved to this new location. Similarly, the existing main linac installation is moved to the beginning of the new tunnel. Finally, the new modules that are optimised for the new energy are added to the main linac. Their accelerating structures have smaller apertures and can reach a higher gradient of 100 MV/m; the increased wakefield effect is mitigated by the reduced bunch charge and length. The beam delivery system has to be modified by installing magnets that are suited for the higher energy and it will be extended in length. The beam extraction line also has to be modified to accept the larger beam energy but the dump remains untouched. Alternative scenarios exist. In particular one could replace the existing modules with new, higher-gradient ones; however, this would increase

Table 12: Key parameters of the baseline machine, a drive-beam based CLIC at $\sqrt{s}$ = 380 GeV, running at 100 Hz, operating with two detectors.
Parameters for an alternative machine, using ca. 40 % lower power consumption, running at 50 Hz with a single beam delivery system and one detector, are also given.
* The main linac crossing angle is 20 mrad. The crossing angle at the IP depends on the BDS design, and the number of IPs. See Sec. 4.3 for details.

Parameter	Symbol	Unit	380 GeV, 100 Hz	380 GeV, 50 Hz
Centre-of-mass energy	$\sqrt{s}$	GeV	380	380
Number of interaction points	N_{IP}		2	1
Repetition frequency	f_{rep}	Hz	100	50
Number of bunches per train	n_b		352	352
Bunch separation	Δt	ns	0.5	0.5
Pulse length	τ_{RF}	ns	244	244
Accelerating gradient	G	MV/m	72	72
Total luminosity	$\mathscr{L}$	$1\times10^{34}\,\mathrm{cm}^{-2}\mathrm{s}^{-1}$	4.5	2.3
Luminosity above 99% of $\sqrt{s}$	$\mathscr{L}_{0.01}$	$1\times10^{34}\,\mathrm{cm}^{-2}\mathrm{s}^{-1}$	2.6	1.3
Beamstrahlung photons per particle	n_γ		1.5	1.5
Total integrated luminosity per year	$\mathscr{L}_{\mathrm{int}}$	fb^{-1}	540	270
Average power consumption	P	MW	166	105
Main linac tunnel length		km	11.4	11.4
Number of particles per bunch	N	10^9	5.2	5.2
Bunch length	σ_z	μm	70	70
IP beam size	σ_x/σ_y	nm	149/2.0	149/2.0
Final RMS energy spread		%	0.35	0.35
Crossing angle*		mrad	26.0/16.5	16.5

the cost of the upgrade. In the following only the baseline is being discussed.

The design of the first stage considers the baseline upgrade scenario from the beginning. For the luminosity target at 380 GeV, the resulting cost increase of the first stage is 50 MCHF compared to the fully optimised first energy stage (without the constraints imposed by a future energy upgrade beyond 380 GeV). To minimise the integrated cost of all stages, the upgrades reuse the main-beam injectors and the drive-beam complex with limited modifications and reuse all main linac modules.

In order to minimise modifications to the drive-beam complex, the drive-beam current is the same at all energy stages. The existing drive-beam RF units can therefore continue to be used without modification. In addition, the RF pulse length of the first stage is chosen to be the same as in the subsequent energy stages. This is important since the lengths of the delay loop and the combiner rings, as well as the spacings of the turn-around loops in the main linac, are directly proportional to the RF pulse length. Hence, the constant RF pulse length allows the reuse of the whole drive-beam combination complex. For the upgrade from 380 GeV to 1.5 TeV, only minor modifications are required for the drive-beam production complex. The drive-beam accelerator pulse length is increased in order to feed all of the new decelerators, and also its beam energy is increased by 20%. The energy increase is achieved by adding more drive-beam modules. The pulse length increase is achieved by increasing the stored energy in the modulators to produce longer pulses. The klystron parameters in the first energy stage have been chosen to be compatible with the operation using longer pulses and higher average power. The remainder of the drive-beam complex remains unchanged, except that all magnets after the drive-beam linac need to operate at a 20% larger field, which is also foreseen in the magnet design.

The impact of the upgrades on the main-beam complex has also been minimised by design. The bunches of the main-beam pulses have the same spacing at all energy stages, while at higher energies the number

Table 13: Key parameters for different centre-of-mass energies. The power and luminosity at 250 GeV and 550 GeV energies are scalings, based on the 380 GeV and 1500 GeV designs.
*The luminosity for the 1500 GeV machine has not been updated to reflect recent alignment studies [436].

Parameter	Unit	250 GeV	380 GeV	550 GeV	1500 GeV
Centre-of-mass energy	GeV	250	380	550	1500
Repetition frequency	Hz	100	100	100	50
Nb. of bunches per train		352	352	352	312
Bunch separation	ns	0.5	0.5	0.5	0.5
Pulse length	ns	244	244	244	244
Accelerating gradient	MV/m	72	72	72	72/100
Total luminosity	$10^{34}\,\mathrm{cm}^{-2}\,\mathrm{s}^{-1}$	$\sim$3.0	4.5	$\sim$6.5	3.7*
Lum. above 99% of $\sqrt{s}$	$10^{34}\,\mathrm{cm}^{-2}\,\mathrm{s}^{-1}$	(n/c)	1.3	(n/c)	1.4
Total int. lum. per year	fb^{-1}	$\sim$350	540	$\sim$780	444
Average power consumption	MW	$\sim$130	166	$\sim$210	287
Main linac tunnel length	km	11.4	11.4	$\sim$15	29.0
Nb. of particles per bunch	10^9	5.2	5.2	5.2	3.7
Bunch length	µm	70	70	70	44
IP beam size	nm	$\sim$180/2.5	149/2.0	$\sim$120/1.7	60/1.5
Final RMS energy spread	%	0.35	0.35	0.35	0.35
Crossing angle (of main linacs)	mrad	16.5	16.5	16.5	20

of bunches per train and their charge is smaller. Therefore the main linac modules of the first stage can accelerate the trains of the second and third stage without modification. Since the drive-beam current does not change, also the powering of the modules is the same at all energies. The upgrade to 1.5 TeV requires an additional nine decelerator stages per side and the 3 TeV needs another 12. An upgrade from 380 GeV to 550 GeV requires an additional two decelerator stages per side.

Still some modifications are required in the main-beam complex. The injectors need to produce fewer bunches with a smaller charge than before, but a smaller horizontal emittance and bunch length is required at the start of the main linac. The smaller beam current requires less RF, so the klystrons can be operated at lower power and the emittance growth due to collective effects will be reduced. The smaller horizontal emittance is mainly achieved by some adjustment of the damping rings. The reduction of the collective effects that result from the lower bunch charge will allow to reach the new value with the same risk as in the first energy stage.

The preservation of the beam quality in the main linac is slightly more challenging at the higher energies. However, the specifications for the performance of alignment and stabilisation systems for the 380 GeV stage are based on the requirements for the 3 TeV stage. They are therefore sufficient for the high energy stages and no upgrades of these systems are required.

The collimation system is longer at 1.5 TeV and 3 TeV to ensure the collimator survival at the higher beam energies. Similarly the final focus system is slightly longer to limit the amount of synchrotron radiation and emittance degradation in the indispensable bending of the beams. The systems have to be re-built using higher field magnets. However, the integration into the existing tunnel is possible by design. The extraction line that guides the beams from the detector to the beam dump will also need to be equipped with new magnets.

4.3 Beam Delivery System Considerations

The BDS baseline and the energy upgrades The current baseline ILC BDS at 250 GeV (BDS-250) has been designed to be scaled until 1 TeV (BDS-1000), keeping the same geometry. The total length is around

2400 m with a crossing angle of 14 mrad. The optics has been designed taking as starting point the BDS-250 magnet configuration. The BDS-500 optics has been matched with the same magnet configuration (location) than the BDS-250 one, but with different quadrupole strengths. The field strength of the Final Doublet (FD) quadrupoles (QD0, QF1) for the BDS-250 is half of the BDS-500. The BDS-1000 needs some additional magnets, in dedicated locations that are free magnet areas for the lower energy operation modes. The ILC-BDS optics for 250 and 500 GeV are shown in Fig. 51. Beam dynamics studies taking into account the

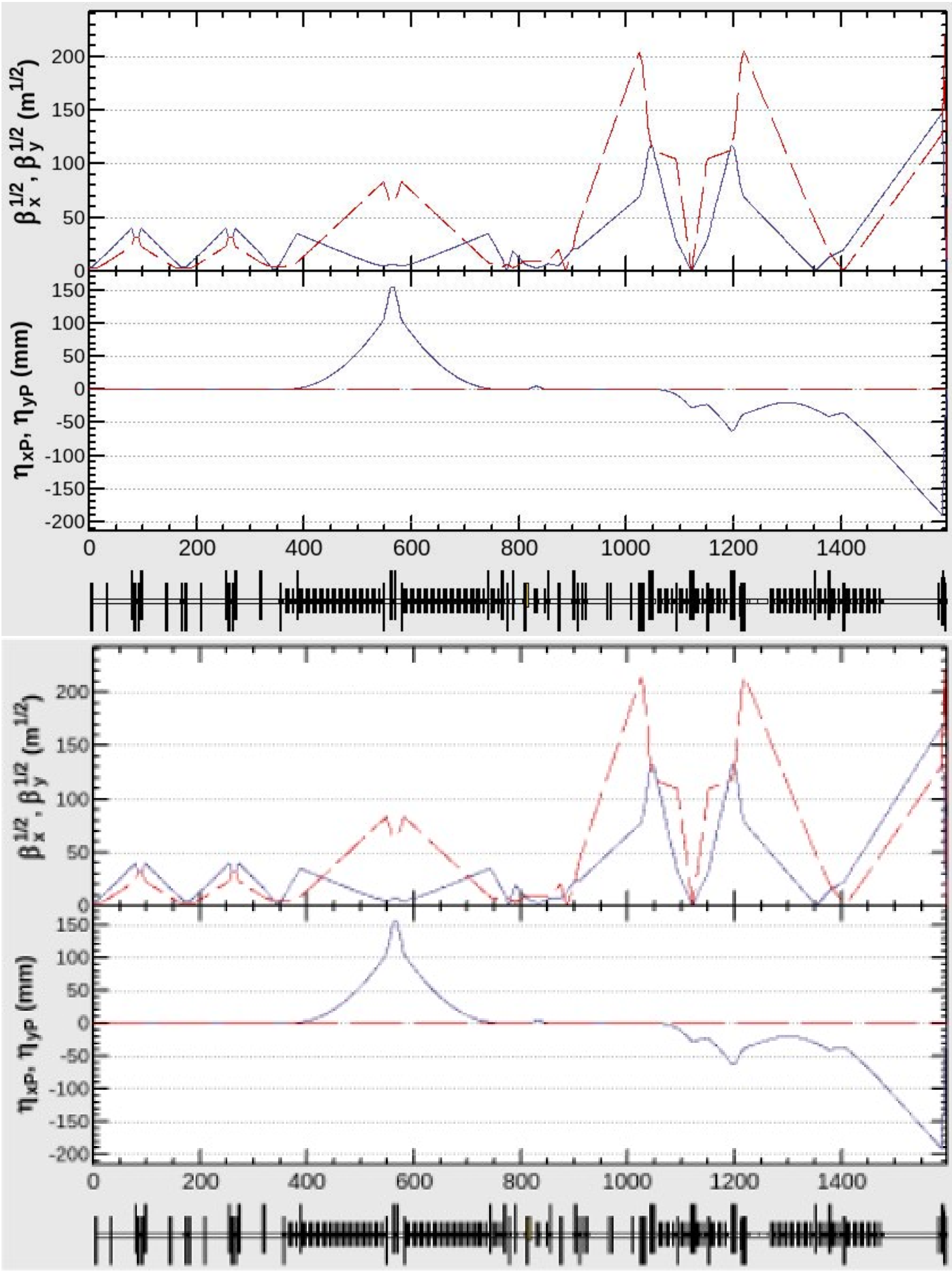

Figure 51: ILC BDS optics design. Top: BDS for 250 GeV with half-length FD (β_x^* = 13 mm, β_y^* = 0.41 mm); Bottom: BDS for 500 GeV (β_x^* = 11 mm, β_y^* = 0.48 mm).

multipoles but not the Synchrotron Radiation (SR) have been made for all the beam energy range. The performance and tolerances optimization, including different bending magnets strengths compatible for all the energies, collimation depths and different possible beamline geometries between others, are ongoing. More details can be found in [437].

The crossing angle choice The long ILC inter-bunch spacing of 554 ns (366 ns for upgrade luminosity), gives the possibility of having a large range of crossing angle configurations from large (20 mrad) to quasi-head-on (2 mrad).

Larger crossing angle solutions separate the incoming beam from spent beam, with no shared Final Focus (FF) magnets. This separation facilitates the beam optics for the spent beam extraction line at the expense of some detector hermeticity in the forward region and the more complex tracking calibration procedures. In addition larger crossing angles are more reliant on a Crab Cavity (CC) system, which rotates the bunches, in order to maximize their overlap and hence the luminosity.

Small crossing angles are generally favoured from the point of view of detector hermeticity and are less reliant on the CC system. However the fact that the incoming and outgoing beams must to share the inner most magnets reduces significantly the design flexibility that has to deal with the reduction of the backgrounds and the minimisation of energy losses in the critical elements. A detailed study for the 2 mrad scheme including the design of the magnets involved in the extraction line has been carried out [438, 439]. Detailed studies and discussions about the pros and cons of each crossing scheme can be found in [440–442].

The present ILC baseline configuration has a 14 mrad crossing angle at the Interaction Point (IP). The 14 mrad option is the minimum angle allowing on one hand independent magnetic channels for ingoing and outgoing beams by means of compact Superconducting (SC) magnets and on the other hand makes easier the straightforward spent beam extraction while facilitating post-IP diagnostics to serve precision physics studies, such as polarimetry and spectrometry complementing similar devices planned upstream the BDS.

The 2 IPs BDS configuration The full realization of the scientific potential of the ILC argues for the construction and operation of two complementary detectors. The value of having two detectors with different designs, technologies, collaborations and emphasis has proven to be a very effective way to exploit the science. In the ILC Baseline Conceptual Design [440], the ILC was designed with 2 BDS sections and two independent IRs with 20 and 2 mrads crossing angles respectively as shown schematically on Figure 52 and is described in some detail [441]. At that time other schemes were under study, including one of 14 mrad [443] and a head-on scheme [444]. Since 2007, the two IRs evolved to only one IR with 14 mrad crossing angle and two detectors in push-pull configuration sharing the beam time. This configuration is the baseline for the ILC located in Japan, [1–5], [12].

A detailed study of a dual BDS serving two IPs has been realized in the framework of the CLIC project, this work could be taken as reference for future studies [445]. The main objective of this work was the design of a dual BDS system optimized to minimize the luminosity loss due to emittance increase and related widening of the beam sizes caused by the emission of synchrotron radiation (SR) as generated in the bending magnet section in the first added part of the BDS, to separate the two IRs. This effect is much more significant for CLIC at high energies such as the 3 TeV case, since the contribution to the IP beam size scales with the fifth power of energy [446]. To mitigate luminosity loss from this contribution, the bending angle needs to be as large as possible, which determines the length of the BDS. Another important design parameter is the crossing angle at the IP. In fact, the SR in the final quadrupole and the solenoid increases the vertical spot size at the IP. Simulations with a 4 T solenoid field at CLIC 3 TeV give an acceptable growth if the crossing angle is around 20 mrad, leading to the current baseline value of 20 mrad. An interesting consequence of adding a new IR with larger crossing angle is its compatibility with $\gamma\gamma$ collisions [447]. A crossing angle of about 25 mrad is considered optimal for this type of collisions using optical lasers [448].

Figure 53 shows the layout of the CLIC dual BDS at 380 GeV with 16.5/20 mrad crossing angles and 3 TeV with 20/25.5 mrad crossing angles. The BDS layout is constructed by adding FODO cells in the existing DS, with an additional total length of about 300 m for 380 GeV and 1 km for the 3 TeV. The four BDS systems at either side of the two IPs need to have different DS lengths to provide the desired longitudinal and transverse separations at the IP. Further improvements can still be performed for the dual BDS layout in order to recover part of the luminosity performance, especially for the BDS2 of the CLIC 3 TeV case. Currently all DS bending is placed in BDS2 however this could be distributed between BDS1 and BDS2 (with opposite angle). This would reduce luminosity loss in IR2 and increase it in IR1. Another option could be to do a longer BDS to reduce the impact of the SR in the BDS2, followed by optics improvements of the dual BDS.

For the LCF at CERN, the idea of having two IPs is being revisited as baseline. The angle choice has

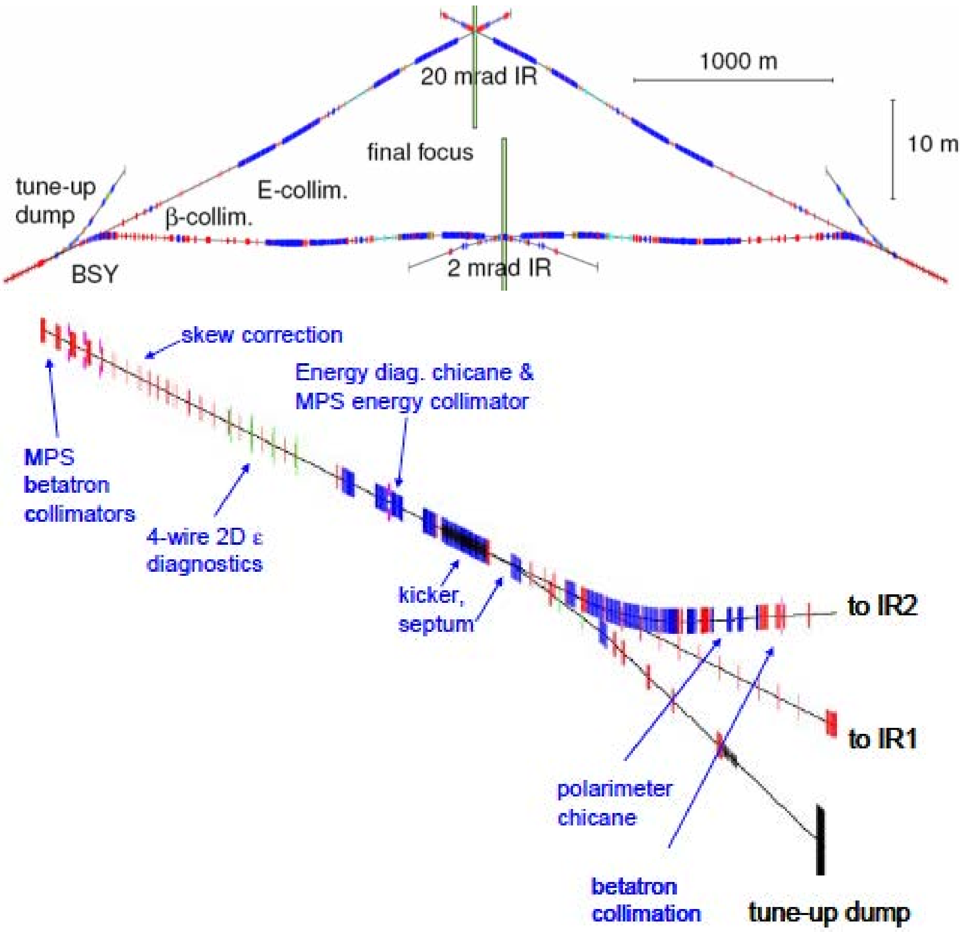

Figure 52: ILC BDS optics design with 2 IPs. Top: Layout of the two IRs with 20 and 2 mrad crossing angle; Bottom: Layout of the BDS section after the Main Linac and the FF section.

not been finally determined, but in principle the two angles will be different to have physics complementarity between the two detectors. Preliminary design studies and CFS cost with 20 mrad between the Main Linacs (MLs), and with two IPs with 14 and 26 mrad crossing angle with the two detectors in the same longitudinal position, are being performed but no detailed design of the optics is currently being developed. Discussions are ongoing to find an optimal solution; some issues have been identified and could be the the subject of focused R&D over the next five years. These topics are:

- The “quasi-head on” (2 mrad) crossing angle configuration will be very difficult to implement from the outgoing beams and dumps point of view.
- In the same longitudinal position for the two IPs, an optimization of the two IPs cavern has to be performed to provide a minimum distance of 30 m between two detectors.
- The beam dumps have to be reconfigured and special attention has to be paid to the photon dump location. In particular, the photon dump location at the centre (between two tilted beams) becomes a critical issue in the case of the undulator positron source.
- Options for different longitudinal positions for the two IPs, indeed they have the advantage of allowing less separation between the two detectors will have timing issues due to the different lengths for the two BDSs. The implementation of these type of options will be complex, and will suppose a global optimization design for all the accelerator systems as the Damping Rings (DR) (for instance, the length of the BDSs has to be half-integer of the DR length) or the injection system. In this scenario the implementation of two inter-bunch space as expected for the the baseline ILC operation with 554 ns and

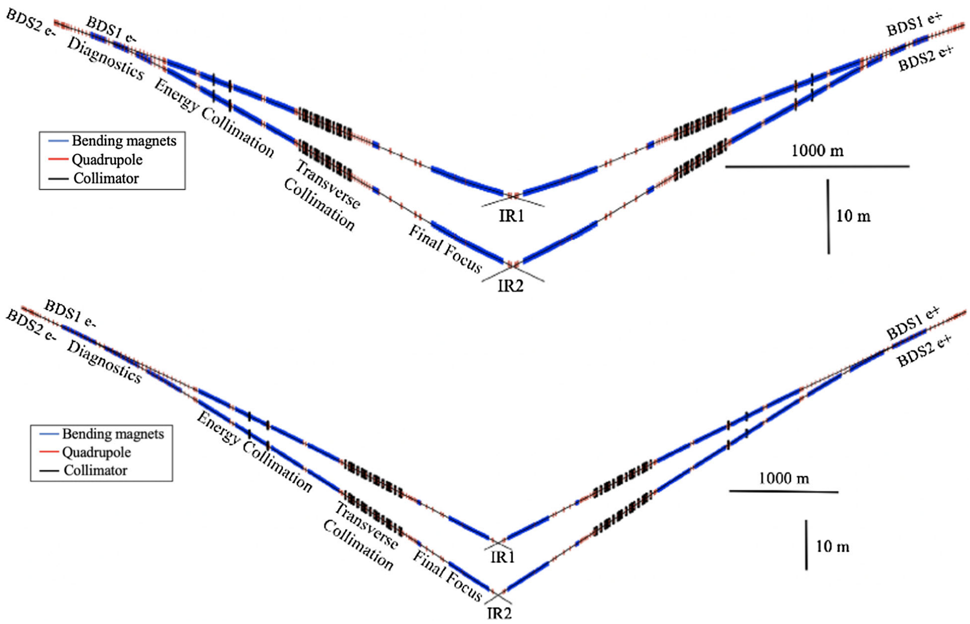

Figure 53: CLIC BDS optics design with 2 IPs. Top: Layout of the two IRs at 380 GeV with 16.5 and 20 mrad crossing angle; Bottom: Layout of the two IRs at 3 TeV with 20 and 25.5 mrad crossing angle

with 366 ns for high-luminosity will be very difficult. More in detail, if the path length condition is satisfied by one of the IPs, the other IP can see the bunch collisions only when the distance of the two IPs is a multiple of 554 ns/2 this means 83 m (though 1-2 collisions among 1312 are missed). But this cannot be a multiple of 366 ns/2 equivalent to 55 m.

- The angle between the MLs has to be optimized to minimize the SR generated by the bending magnets of the BDS separation region, taking into account the two IPs crossing angle choice.
- The idea of having parallel MLs is also being considered and this option could be better for the future implementation of an upgrade by means of ERLs, nevertheless the impact of the increase of total length and the SR losses in the splitting section should be considered.
- The split location of the BDSs has to studied in detail, as well as the split magnet technology for the high-energy upgrades.
- Both, bunch-by-bunch switching or train-by-train separation should be possible. In particular train-by-train switching by pulsed magnets are used for the Z-pole operation and also the polarization switching of positron beam.
- Compatibility with a possible future $\gamma\gamma$ collision mode have to be evaluated, with both optical lasers or FEL options. Options with Eu.XFEL lasers are optimal when the crossing angle is "quasi-head on" contrary to the optical ones.

4.4 Energy upgrades

4.4.1 Upgrade of an SCRF-based machine with higher gradient cavities

The European Strategy for Particle Physics - Accelerator R&D Roadmap [449] and Snowmass'2021 [450–452] emphasized strategic trends in SCRF development. In particular, the former stated: "In SCRF the development is focused in two areas, bulk niobium and thin-film (including high-T_c) superconductors. In bulk SCRF new treatments are allowing niobium cavities to exceed previous record Q factors and avoiding degradation with increasing gradients. This includes nitrogen infusion and doping, and two-step baking processes. There is also an emphasis on limiting field emission. For thin-films the community is investigating creating coated cavities that perform as good as or better than bulk niobium (but with reduced cost and better thermal stability), as well as developing cavities coated with materials that can operate at higher temperatures or sustain higher fields. One method of achieving this is to use multi-layer coatings. Innovative cooling schemes for coated cavities are also being developed. Coupled to the cavity development is improvement in the cost and complexity of power couplers for SCRF cavities."

The performance limit of superconducting radio frequency (SCRF) cavities made of pure niobium is determined by the two key parameters: the RF critical, or superheating, magnetic field B_{sh} and the surface resistance R_s. The RF critical magnetic field limits the maximal achievable accelerating gradient $E_{acc} = B_{sh}/k_m$, where k_m is a coefficient specific to the cavity shape. For example, $k_m = 4.26$ mT/(MV/m) for 1.3 GHz TESLA-shape cavities. The surface resistance determines efficiency of the SCRF cavity: the cavity intrinsic quality factor $Q_0 = G/R_s$ is inversely proportional to the surface resistance with the cavity geometry factor $G \approx 270$ Ohm. Recent advancements in surface tailoring techniques have led to groundbreaking results, as laboratories have successfully introduced nitrogen, oxygen, and other impurities into the niobium lattice.

The superheating field of approximately 210 mT[11] at 2 K was reached experimentally on single cell cavities, resulting in an accelerating field of about 50 MV/m for TESLA-shape cavities [431, 454]. At ~ 50 MV/m the quality factor is still limited to $< 2 \times 10^{10}$ at 2 K[12]. To date, the experiments show that only low-temperature surface treatments are beneficial for increasing of RF critical field. Mid-T bake and nitrogen doping tend to lower the achievable quench field of SCRF cavities.

With additional investments, further developments in the bulk niobium SCRF technology could be impactful for the ILC upgrades on a 5-year time scale. On a longer time scale, about 10 years, traveling wave SCRF structures could be developed to bring the gradient to > 60 MV/m [455]. Finally, if there is a breakthrough, thin films and superconductors beyond niobium could potentially bring higher accelerating gradients, higher quality factors at 4 K, or both. This would open a horizon to more efficient (e.g., ERL-based) and higher energy linear collider options.

Bulk-Niobium and Travelling wave SCRF: The most promising surface treatment of SCRF bulk niobium cavities for high gradient applications is a combination of cold electropolishing and two-step (75/120°C) baking. It has paved the way for gradients near 50 MV/m in single-cell TESLA-shape cavities. Applying this advanced treatment to improved shape standing-wave SCRF structures – such as Ichiro, low-Loss (LL), re-entrant, and Low Surface field (LSF) cavities – holds the prospect of gradients close to 60 MV/m in single-cell cavities and 50 MV/m in 9-cell cavities in a cryo-module.

Further improvements in accelerating gradients of bulk Nb structures are possible but require developing an alternative approach. Utilizing travelling wave (TW) in a resonant ring configuration offers such an approach [456]. The SCRF TW structure has several advantages compared to the standing wave structures, see, e.g., [455, 457, 458]. The most salient advantages are as follows. Substantially lower k_m promises achieving higher E_{acc} at the same magnetic quench limit. Approximately a factor of 2 higher R/Q (even at somewhat lower G) would ensure lower cryogenic losses. See [459] for more details on the structure optimization. In addition, the TW structure provides high stability of the field distribution along the structure with respect to geometrical perturbations. This allows for much longer accelerating structures than TESLA cavities, limited by the manufacturing technology only.

Assuming a realistically achievable accelerating gradient of 60 MV/m (about 20% reduction from the ultimate gradient of 73.7 MV/m) and the quality factor of 1.4×10^{10} (for the surface resistance corresponding to $Q_0 = 2 \times 10^{10}$ of TESLA cavity), a superconducting linear collider built with TW cavities could reach 500 GeV centre-of-mass collision energy within the 20.5 km footprint and 1 TeV within the 33.5 km footprint. Some parameters of SCRF traveling-wave based linear collider (TWLC) are presented in Table 14.

While there is progress towards proof-of-principle experimental demonstration on a 3-cell structure and developing a longer structure [460], it is slow due to intermittent funding. Proper investment in this technology could bring it to "prime time" readiness – demonstrated performance in a full-scale cryomodule – on a 10-year

[11]Typically, it is assumed that the RF critical magnetic field is equal to the DC superheating field [453], although no definitive theory yet exist that can calculate The RF critical filed.

[12]Note, a 4 K operation of niobium cavities at this frequency is not practical, as the Q_0 becomes low, $\sim 5 \times 10^8$ resulting in an excessive heat dissipation.

time scale. After that TW-based linear collider should be feasible.

Table 14: Key parameters for a linear collider based on traveling-wave SCRF.

Parameter	Unit	TWLC550	TWLC1000
Centre-of-mass energy	GeV	550	1000
Luminosity	10^{34}cm^{-2}s^{-1}	3.9/7.7	5.1
Number of interaction points		2	2
Repetition frequency	Hz	10	4
Bunch population	10^{10}	2	1.74
Number of bunches per train		1312/2625	2450
Bunch spacing	ns	554/366	366
Bunch train duration	μs	727/961	897
Accelerating gradient	MV/m	60	60
Cavity quality factor at 60 MV/m	10^{10}	1.4	1.4
Klystron efficiency	%	80	80
Length of 2 SCRF linacs	km	11.9	21.8
Total machine length	km	20.5	33.5
Site power consumption	MW	225/299	223

Advanced SCRF superconductors (Nb_3Sn, thin films, mutilayers): Over the years, many high-temperature superconductors have been investigated. Some of them (cuprates, bisthmuthates, etc.) have not found to be useful for high-field accelerating cavities [453]. Others, such as A15 compounds, MgB_2 are still under investigation. The most progress to date in advanced SCRF superconductors has been made with Nb_3Sn using the vapour diffusion process [461]. Superconducting accelerating cavities using Nb_3Sn are expected to be a game changer, bringing higher gradients with more efficient cooling, because Nb_3Sn has higher transition temperature (T_c) of 18.3 K, compared to the 9.2 K transition temperature of Nb. Development of 1.3 GHz accelerating cavities has been progressing since the mid-2010s at Cornell University, Fermi National Accelerator Laboratory (FNAL), and Jefferson Laboratory (JLAB) in the United States [461–463], and now is being actively pursued worldwide [464].

Normally, 1.3 GHz Nb cavities operate at 2 K to reduce the surface resistance and achieve high intrinsic quality factors Q_0 of greater than 1×10^{10}. Large cryogenic systems, like the one required for ILC, are very inefficient, with about 800 W of wall-plug power needed for every watt dissipated at 2 K. On the other hand, Nb_3Sn can achieve the same surface resistance as Nb, but at at 4.2 K. For example, a single-cell cavity having surface resistance of 20 nΩ and operating at an accelerating gradient of 10 MV/m would dissipate approximately 1 W at 4.2 K, where the efficiency of cryogenic systems is almost a factor of 3 better. Such cavities would not only benefit future colliders but are also suitable for compact conduction-cooled accelerators, as commercial cryocoolers have capacity of 1 – 2 W at 4.2 K.

For making higher gradients, Nb_3Sn has a potential advantage due to its high DC superheating field (B_{sh}), approximately twice that of Nb [453]. This means that it could be expected that Nb_3Sn SCRF cavities might reach accelerating gradients as high as 90 – 100 MV/m providing good system efficiency at the same time. However, despite continuous efforts to improve the gradient performance of Nb_3Sn SCRF cavities, the maximum accelerating gradients achieved to date remain quite modest, $\leq$ 24 MV/m [461]. Processes other than vapor diffusion are being investigated at different institutions: electroplating, CVD deposition, magnetron sputtering, just to mention a few. As these techniques mature, we should expect further progress to be made. If there is a breakthrough, one could potentially apply Nb_3Sn to travelling wave structures, making even higher accelerating gradients reachable.

Another approach was proposed by Gurevich and further developed by Kubo [465–467], taking advantage of superconductors with higher T_c than niobium without being penalized by their lower B_{sh}. The idea is to coat SCRF cavities with alternating superconducting and insulating layers (SIS structures) with a thickness *d* smaller than the London penetration depth λ. The surface resistance will be strongly reduced because those superconducting materials have a higher energy gap Δ (Nb_3Sn, NbTiN, NbN, ...) than Nb and the surface resistance depends inverse exponentially on the energy gap Δ.Theory suggests that by employing such structures, the performance of superconducting cavities can be significantly increased by achieving *Q*-values of a factor of 2-5 higher than values typically obtained for pure niobium. Since induced currents and fields in the bulk material are reduced as well by additional shielding provided by the interfaces between the layers, an application of SIS multilayers would in addition enable a significant increase of the maximum achievable accelerating fields above 70 MV/m. This would allow an operation of cavities above 50 MV/m at 4 K with a Q_0 of greater than 1×10^{10}. The benefit would then be, that a 4 K operation would allow an overall higher cooling efficiency and reduced operational cost of an accelerator the same way as for Nb_3Sn and the higher gradient would increase the energy reach of a machine.

The SIS multilayer research is in its initial stage, at the technological readiness level two. Teams in America, Asia, and Europe are developing coating processes, investigating the parameter phase space, trying various materials, etc. A sustained investment into the basic R&D studies, infrastructure, analytical instruments is needed before we can expect first practical multilayer SCRF cavities. Yet, sample studies have shown already, that a field enhancement and a higher external magnetic field can be sustained compared to bulk Nb [468], proving the underlying principle [469–472]. Very first RF tests on prototypes showed weak to no improvement or even deterioration of the surface resistance compared to baseline measurements [473–475], which can be explained by magnetic flux pinning during cooldown or a non-optimal, faulty post-processing of the films after deposition. Hence, the major focus of the ongoing R&D is to transfer the promising sample results to cavities, and optimize the post-processing strategy which heavily relies on the deposition technique itself. First decisive results can be expected within a 5- to 10-year time frame.

Upgrading the initial facility In case of a replacement of the original main linac with better SCRF technology, most of the other infrastructure could be retained, including the cryogenic system. R&D results expected in the coming ten years will form an important basis for a more detailed design study for such an upgrade.

4.4.2 Upgrade using CLIC technology

Basic idea In this section we describe the possible upgrade of the SCRF based accelerator described before, by replacing the SCRF linac in the case of a total site length of 20.5 and 33.5 km with the CLIC high-gradient RF cavities with an energy reach up to 2 TeV in the same footprint.

The current performances of the CLIC project are described in detail in [18] and is summarized in section 4.2 above. The key parameters of the baseline machine, a drive-beam based CLIC at $\sqrt{s} = 380$ GeV, running at 100 Hz, operating with two detectors are listed in Table 12. Accelerating gradients of up to 145 MV/m were reached with the two-beam concept at CTF3, and breakdown rates of the accelerating structures well below the limit of $3 \times 10^7 \mathrm{m}^{-1}$ are stably achieved at X-band test platforms. For the first energy stage, an alternative scenario, with X-band klystrons powering the main-beam accelerating structures has also been studied. When considering using CLIC X-band technology as an upgrade, the klystron-powered solution is the easiest, as it minimises changes to the infrastructure and in particular does not require construction and integration of a drivebeam complex. With this strategy we estimate the energy reach for a 20.5 km (15 km linac) and 33.5 km site length (seeTable 15).

Timeline and R&D needed The key technologies needed for such an upgrade are related to the powering and in particular high-efficiency X-band klystrons: Efficiencies between 80–90 % and more than 70 % are being achieved currently in L-band and S-band klystrons respectively [476]. For X-band achieving such high efficiency is very difficult, due to the small distances involved. A focused R&D is needed to overcome the issues and get higher efficiencies to be able the reach of high-energies a reality. These klystrons and associated modulators are also cost-drivers and require reliabilities beyond what is needed for the drivebeam based CLIC.

Table 15: Main parameters for a CLIC based upgrades showing the different possible energy versions.

Parameter	Unit	550 GeV	1500 GeV
Centre-of-mass energy	GeV	550	1500
Repetition frequency	Hz	100	50
Nb. of bunches per train		352	312
Bunch separation	ns	0.5	0.5
Pulse length	ns	244	244
Accelerating gradient	MV/m	72	100
Total luminosity	$10^{34}\,\mathrm{cm}^{-2}\,\mathrm{s}^{-1}$	$\sim$6.5	3.7
Lum. above 99% of $\sqrt{s}$	$10^{34}\,\mathrm{cm}^{-2}\,\mathrm{s}^{-1}$	(n/c)	1.4
Total int. lum. per year	fb^{-1}	$\sim$782	444
Average power consumption	MW	$\sim$209	287
Main linac tunnel length	km	$\sim$15	29.0
Nb. of particles per bunch	10^9	5.2	3.7
Bunch length	µm	70	44
Final RMS energy spread	%	0.35	0.35
Crossing angle (of main linacs)	mrad	16.5	20

4.4.3 Upgrade using C^3 technology

The construction of a linear collider facility provides us with the opportunity to consider various pathways for future energy upgrades. These upgrades may allow for more advanced technologies presently in development to replace the original technological choices if they provide a significant advantage. Ideally, significant portions of the accelerator complex can be re-utilized to leverage the existing common hardware of a linear collider facility and the research and development investment that went into those sub-systems (e.g. injectors, positron source, damping ring, beam delivery).

C^3 is a concept for a linear collider that aims to achieve a compact, high-gradient facility with a normal-conducting distributed-coupling accelerator that is operated at cryogenic temperatures [20]. C^3 is designed and optimized with a wholistic approach that aims to optimize the main linac, collider subsystems, and beam dynamics to deliver the required luminosity at the overall lowest cost. C^3 was originally optimized for physics program at 250 and 550 GeV centre of mass to allow for a Higgs physics program that could also perform measurements of the Higgs self-coupling. A total facility length of 8 km is sufficient for operation at 250 and 550 GeV centre of mass. The initial operation at 250 GeV is upgraded to 550 GeV simply with the addition of RF power sources to the main linac. This is possible because the increase in gradient and resulting increased power requirement is balanced with an adjustment to the beam format to maintain a constant beam-loading, or fraction of the RF power delivered to the beam, which preserves the RF efficiency of the system. By optimizing the cavity geometry, RF distribution, and operating at liquid nitrogen temperatures where the conductivity of copper is increased significantly, the peak-power requirement from the high-power RF sources are significantly reduced. This allows for a high beam loading, nearly 50 %, making for a compact and efficient machine. It is important to emphasize that for a normal conducting machine the cost driver for the main linac is the RF, and through the adoption of distributed-coupling and cold-copper technology peak RF power requirements are reduced by a factor of six.

The present optimized parameters for C^3 are listed in Table 16. The original and sustainability update parameters (s.u.) are shown. The s.u. parameters have now been adopted as the baseline after careful analysis [477].

C^3 was optimized based on the incredible advances that were made as part of the ILC and CLIC programs in the development of electron and positron sources, injector linacs, damping rings, bunch compressors, beam transport, beam dynamics, beam delivery and detectors. These highly complex and optimized systems serve as the baseline for what is technologically achievable in the linear collider complex and allow for the

Scenario	C^3-250	C^3-550	C^3-250 s.u.	C^3-550 s.u.
Luminosity [x10^{34}]	1.3	2.4	1.3	2.4
Gradient [MeV/m]	70	120	70	120
Effective Gradient [MeV/m]	63	108	63	108
Length [km]	8	8	8	8
Num. Bunches per Train	133	75	266	150
Train Rep. Rate [Hz]	120	120	60	60
Bunch Spacing [ns]	5.26	3.5	2.65	1.65
Bunch Charge [nC]	1	1	1	1
Crossing Angle [rad]	0.014	0.014	0.014	0.014
Single Beam Power [MW]	2	2.45	2	2.45
Site Power [MW]	$\sim$150	$\sim$175	$\sim$110	$\sim$125

Table 16: Baseline C^3 parameters.

optimization of the main linac using the C^3 approach with minor modifications to the relevant sub-systems. Indeed, a critical point is that C^3 is compatible with the injector complex and beam delivery system that will be installed in the first phase of a linear collider facility with an SCRF technology that reaches 250 GeV centre of mass in 20.5 km. The present design of the damping ring and bunch compressors for C^3 will be presented below. As is shown there, the size and beam format for the ILC damping ring is compatible with the size of the damping ring of C^3. The extraction kicker for the damping ring would need to be replaced with from a fast to a slow kicker. The bunch spacing at injection into the damping ring, which is set by the fast kicker into the ring, would need to be optimized to match the bunch format required for the C^3 upgrade, in the range of 1–5 ns.

Of a 20.5 km Linear Collider Facility, 15 km consist of the main linac for the collider. After completing the initial run of a Linear Collider facility, we envision the possibility of replacing these 15 km with a cold-copper distributed-coupling linac with an energy reach of up to 2 TeV in the same footprint. Analogously, a centre-of-mass energy of up to 3 TeV is possible in a 33.5 km facility. No additional civil construction (i.e. additional tunnel length) would be required.

The linacs could operate at any energy below 2 TeV by a combination of bypass lines or by adjusting the gradient and beam format to maintain a constant beam loading and providing a linear scaling in luminosity with energy and beam power. The parameters for 1 and 2 TeV operation are shown in Table 17, and would be accomplished only with the addition of RF sources, upgrades to the beam delivery system and modifications to the bunch format. More details on upgrading an SCRF-based LCF with C^3-technology can be found in [21].

Significant technical progress has been made recently in the development of C^3 technology. In particular, the accelerating structures that can achieve this gradient have been built and demonstrated. Further research and development is needed for the integration of higher order mode damping, cryo-module integration and demonstration of alignment and vibration tolerances. A C^3 demonstrator plan was developed to identify the required metrics and experiments that would be needed to advance the technical maturity of the main linac to a level required for a collider design [478]. Since this demonstrator plan was published, significant progress has been made on structure design [479], high gradient testing [480], structure vibration measurements [481], damping materials [482], alignment system [483], low-level RF [484] and cryo-module design. Ongoing efforts are focused on integration of higher order mode damping, cryo-module design and integration, alignment and vibration measurements, and ultimately the construction and testing of a "quarter cryo-module (QCM)" with RF power, beam and full instrumentation for alignment and vibrations. The QCM represents an essential step in the process as it contains all of the repeating element that make up the full cryo-modules in the main linac. On the intermediate timescale a demonstration is needed on the few GeV scale to provide technical maturity for the full scale cryo-modules (9 m) that would be used C^3. Such an R&D program as proposed at Snowmass is technically achievable before 2030 allowing for C^3 technology to be integrated into plans for an upgrade to the Linear Collider Facility.

The injector complex and the damping rings represent a major capital investment for the LCF. Fortunately, with C^3 we can reutilise this infrastructure for an energy upgrade of the LCF. This is because the damping ring

Parameter	Unit	Value	Value	Value
Centre-of-Mass Energy	GeV	1000	2000	3000
Site Length	km	20	20	33
Main Linac Length (per side)	km	7.5	7	10.5
Accel. Grad.	MeV/m	75	155	155
Flat-Top Pulse Length	ns	500	195	195
Cryogenic Load at 77 K	MW	14	20	30
Est. AC Power for RF Sources	MW	68	65	100
Est. Electrical Power for Cryogenic Cooling	MW	81	116	175
Est. Site Power	MW	200	230	320
RF Pulse Compression		N/A	3X	3X
RF Source efficiency (AC line to linac)	%	50	80	80
Luminosity	$x10^{34}$ $cm^{-2}s^{-1}$	$\sim$4.5	$\sim$9	$\sim$14
Single Beam Power	MW	5	9	14
Injection Energy Main Linac	GeV	10	10	10
Train Rep. Rate	Hz	60	60	60
Bunch Charge	nC	1	1	1
Bunch Spacing	ns	3	1.2	1.2

Table 17: Main Linac parameters for C^3 at 1 TeV to 3 TeV centre-of-mass energy.

offers an opportunity to adjust the bunch train format from the electron and positron source linacs to match the bunch structure needed for C^3.

In the original configuration for a SCRF based LCF the damping ring operates with fast kickers for both the injection and extraction of the electron and positron bunches. This is due to the fact that the bunch spacing (hundreds of nanoseconds) is too large to maintain in the damping ring without and excessively large circumference. The fast kickers place the bunches with a spacing on the order of five nanoseconds into the damping ring. This spacing is well suited for the use of a normal conducting technology such as C^3. Small adjustments to the timing of the injection system and RF system of the damping ring would allow the bunch spacing in the damping ring to match the desired spacing of C^3. The bunch spacing for C^3 is nominally in the 3-5 nanosecond range and possibly as small as 1.5 nanoseconds. The fast kicker in the extraction system would be replaced with a slow kicker to extract the full bunch train which is accelerated in the main linac.

When considering this scheme, it is essential that the circumference of the damping ring be sufficient to provide enough space for the C^3 bunch train and enough time for the beam to be damped. This also requires that the emittance at the exit of the damping ring be low enough and preserved through the bunch compressors prior to acceleration in the main linac. The footprint of the bunch compressor could also limit the energy reach of the collider and should be accounted for. In the following sections we show that the size needed for the damping ring is smaller than the SCRF baseline for the LCF. A larger damping ring would be lower risk and is therefore acceptable. We also show that the emittance is low enough through bunch compression, and the length of the bunch compressors and associated RF is small and on the order of 100 m. With this preliminary study we can conclude that there is a significant amount of infrastructure that can be reutilised in the injector complex and damping rings of the LCF for a C^3 upgrade. Future studies should investigate a configuration that matches the circumference of the LCF damping ring. Furthermore, R&D is needed in fast kickers to get down to the single nanosecond timescale for the most tightly spaced bunch formats being considered.

Damping Ring The goal of the damping ring is to produce a flat beam with as small an emittance as possible subject to the constraint of having a sufficiently fast damping time to match the collider repetition rate, f. Generally, multiple damping cycles are required to allow the injected beam to reach its equilibrium emittance. This requirement along with the collider bunch structure which informs the choice of ring circumference, sets roughly the beam energy:

$$\tau_y = \frac{3C}{r_e c \gamma^3 I_2} \tag{14}$$

where C is the ring circumference, γ is the relativistic factor, r_e is the classical electron radius and I_2 is the second radiation integral.

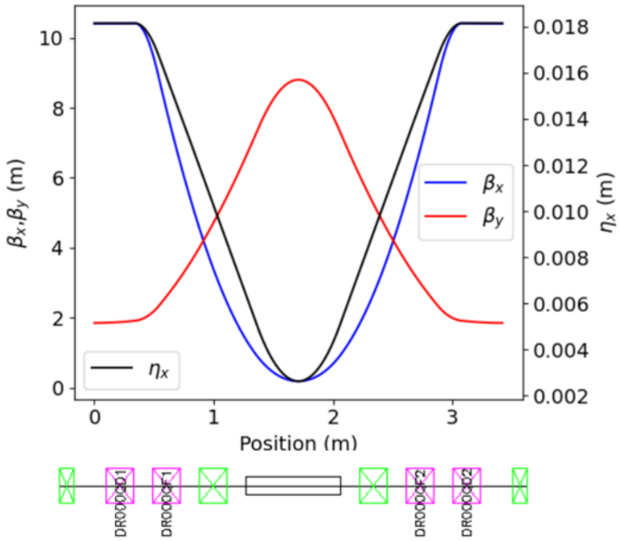

Figure 54: Beta functions and dispersion for a TME cell.

For the C^3 collider the main electron and positron damping rings will have a racetrack layout. The arcs are comprised of Theoretical Minimum Emittance (TME) cells while the straight sections are used for injection and extraction and to provide space for damping wigglers. An analytic study varying the major parameters (beam energy, number of stored bunches, wiggler strengths and lengths) was performed and a choice of storing two bunch trains was made as a trade-off between size of the machine and achievable emittance resulting in an energy of 4.6 GeV. Each bunch train is stored for approximately 7.9 damping times. While this number is relatively large, lowering it by reducing the beam energy results in a larger final emittance when IBS is accounted.

The zero-charge horizontal emittance is largely determined by the number of TME cells in the ring:

$$\gamma\varepsilon_x = \frac{C_q \gamma^3 \theta^3}{12\sqrt{15}} \tag{15}$$

where $\gamma\varepsilon_x$ is the normalized horizontal emittance, C_q is a numerical constant and θ is the bend angle per TME cell. The above implies 248 cells are required for a baseline zero-charge normalized emittance of 65 nm. However, at optimal emittance TME cells require tight focusing which introduces a large chromaticity in both planes. We therefore moved off of the optimum settings until the normalized chromaticity in each plane was <3 resulting in a zero-charge emittance of 170 nm. For a cell length of 3.4 m the total arc length is 843 m. Each straight section is 172 m long with the majority of that length used for wiggler magnets, but additional space is also included for beam extraction/injection, RF cavities to replenish energy loss from synchrotron radiation and optics for matching the straight sections and arcs and zeroing dispersion.

In the current design the ring circumference is 1190 m which fits 2.8 bunch trains. It may be possible to reduce the ring circumference by making the TME cells more compact but for an initial study a conservative estimate of 3.4 m was used. Note that reducing the number of cells would increase the emittance which is not preferable. Another possibility may be to increase the circumference to fit 3 bunch trains.

With the major design parameters selected a model of the ring was produced in BMAD. A code available in the BMAD ecosystem to model IBS based on the Completely Integrated Modified Piwinski (CIMP) formalism was used (see Fig. 55). Final normalized emittances range from 300–500 nm in the horizontal plane depending on RF voltage and bunch charge, while the vertical emittance remains below 1 nm for all RF settings and bunch charges considered. It is important to note that the vertical emittance value will likely be dominated by magnet tolerances and not IBS, which is an ongoing study.

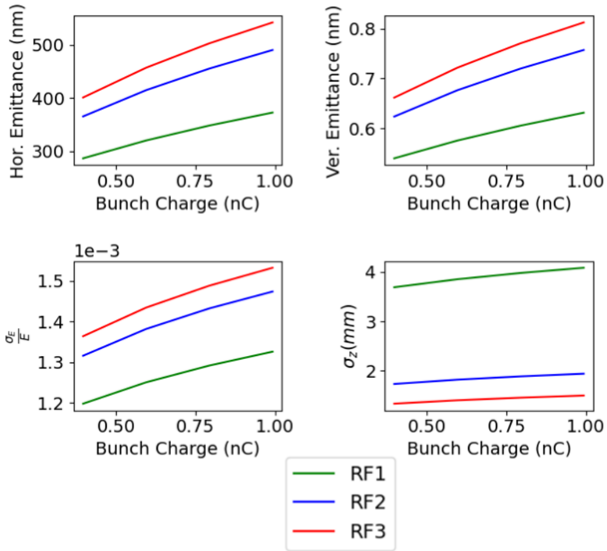

Figure 55: Horizontal, verticle normalized emittances, RMS relative energy spread and bunch length as a function of charge due to IBS. Each color refers to a different RF voltage in the ring.

Bunch Compressors Particle bunches leaving the damping ring (DR) have been damped strongly in the transverse plane but are too long to be accepted into the main linac where they will be boosted to collision energy. Therefore, a bunch compression scheme between the damping ring and main linac is required. Because the beam energy leaving the DR is 4.6 GeV, ballistic compression is not an option. Instead, the compressor consist of two parts: an RF linac which imparts an energy-position correlation (energy chirp) on the bunch, and a magnetic chicane which has a path length that depends strongly on a particle's energy.

Leaving the damping ring, the particle bunch is uncorrelated in position with a bunch length of the order of a few mm and a relative energy spread of approximately 0.1 % (depending on bunch charge and RF setting in the DR). The compression goal is 100 μm. In the absence beam intensity effects (in particular Coherent Synchrotron Radiation (CSR)) the longitudinal emittance is conserved which implies an energy spread on the order of 1 % is expected after compression.

Analytic formulae derived from linear transfer matrices of an RF cavity, bend magnet and drift were used to determine the required M_{65} of the RF system and M_{56} of the chicane for the case of operating at the RF zero-crossing. To compensate for a non-negligible T_{566} from the chicane the beam is moved slightly off the zero-crossing to take advantage of the curvature present in the RF field. This results in a slight deceleration of the beam from 4.6 GeV to about 3.9 GeV.

An RF frequency of 2.85 GHz was chosen since it is a sub-harmonic of the main linac. As a reasonable starting point a 15-cell cavity with gradient of approximately 9 MV/m was assumed. To achieve the required energy chirp for a 100 μm final bunch length, 80 total RF cavities are needed resulting in an approximately 130 m long RF section. Dipole magnets where chosen to be 2 metres in length separated by 4 metre drifts. Typical strengths are 0.5 T resulting in a bending angle of 4.5 degrees per dipole. For focusing, a FODO cell comprising the length of 8 RF cavities is used. The chicane does not contain any quadrupoles. 4 quadrupoles on each side of the chicane were tuned to keep the beta functions under 30 m with relatively weak divergence through it. The effect of CSR was modeled using BMAD's built-in 1D CSR calculation. Tracking was done with 10K particles and 100 longitudinal bins (see Fig. 56). We are currently looking into 3D CSR effects. However, we note that due to the small transverse emittance and well controlled beta functions in the chicane, the common rule-of-thumb for when 3D effects become non-negligible $\sigma_{x,y} < \rho^{1/3}\sigma_Z^{2/3}$ suggest that the 1D model should be accurate.

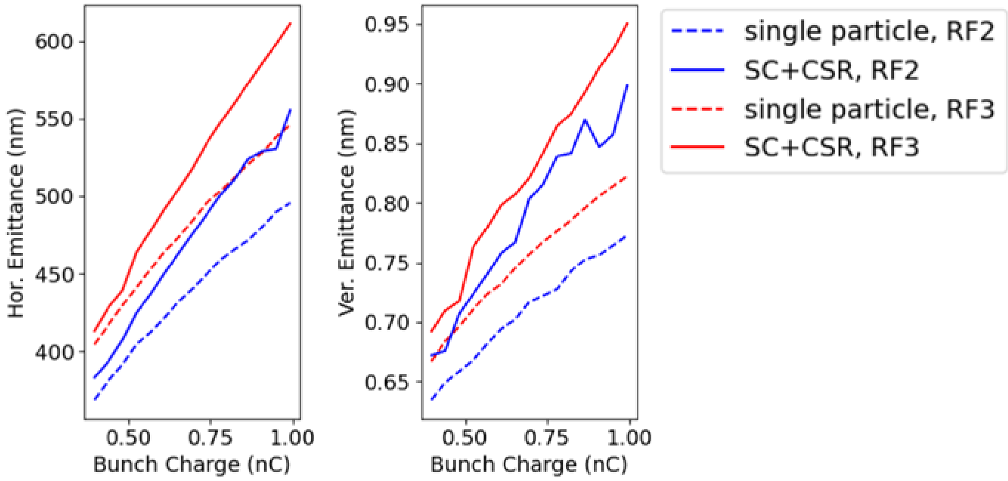

Figure 56: The horizontal and vertical normalized emittances at the end of the bunch compressor. Red and Blue are for two different RF settings in the DR while solid lines include a 1D-CSR calculation while dashed lines do not.

Environmental Considerations Due the the presence of liquid nitrogen in the tunnel, the presence of humans during the cold state of the machine will require proper safety measures. These include adequate ventilation, oxygen deficiency monitors, etc. Requirements will need to be considered concerning relevant regulations.

4.4.4 Upgrade using Plasma Wakefield Accelerator Technology

A particular strength of a linear collider at the electroweak scale is that it can be a first step towards a discovery machine that can reach 10 TeV parton-centre-of-mass (pCM) collisions. Such a machine must necessarily be based on novel accelerator technology with GeV-per-meter accelerating gradients in order to fit within a reasonable facility footprint. The 2023 P5 Report [485] calls for "vigorous R&D toward a cost-effective 10 TeV pCM collider based on ... wakefield technologies" and goes on to state "Wakefield concepts for a collider are in the early stage of development. A critical next step is the delivery of an end-to-end design concept, including cost scales, with self-consistent parameters throughout." The 10 TeV Wakefield Collider Design Study has been formed in response to the P5 Report [29].

There are several design studies on future wakefield accelerator (WFA) collider concepts currently underway. First, the HALHF concept [486] proposes an asymmetric collider where high-energy, plasma-accelerated electrons collide with low-energy positrons accelerated in conventional RF linacs, thus avoiding the challenge of positron acceleration in plasma [487]. Second, ALIVE [488] considers the proton beam-driven plasma wakefield acceleration where the enormous energy stored in the LHC proton beam is harnassed to accelerate electrons to the TeV scale in a single plasma stage. The 10 TeV pCM Wakefield Collider Design Study aims to develop a self-consistent design of an energy-frontier linear collider based on beam-driven plasma, laser-driven, or structure-based wakefield acclerators [29].

Plasma Booster The idea of upgrading a linear collider using newer technology with a higher accelerating gradient has long been discussed and is a major advantage of a linear compared to a circular collider. The difficulty of such an upgrade depends on the similarity of the technologies involved. Beam-driven plasma-wakefield acceleration (PWFA), the only WFA technology currently capable of achieving the efficiencies required for collider applications, is rather dissimilar to that of the RF cavities of the baseline facility. Implementing it with minimal changes to a running Higgs factory is complex but seems at least in principle feasible.

Because no efficient and tested scheme to accelerate positrons in a plasma exists, the booster is only used in the electron arm, which leads to a boost to the CoM of the electron-positron system as in the HALHF concept. However, the boost is much smaller than in HALHF, since achieving a CoM energy of 550 GeV is achieved with a positron energy of 137.5 GeV and an electron energy of 550 GeV , which corresponds to a boost of ≈ 1.25. This is sufficiently small to not require significant changes to the detector, except for the luminosity monitoring. Should efficient positron acceleration be developed in future, then boosters could be used in both arms, restoring symmetric collisions.

For this exercise, it is assumed that the Higgs factory to be boosted is based on the ILC TDR design at the baseline luminosity. The CoM energy is increased from 250 GeV to 550 GeV , appropriate for top-pair and Higgs-pair production. This requires a slight increase in the positron energy to 137.5 GeV , achieved by assuming that the cavities can be run at a gradient of 35 MV/m, and an electron energy of 550 GeV , produced by the PWFA booster. The major complication in using PWFA is the necessity to produce the drive beams required to “blow-out” the electrons to form the accelerating cavity in the plasma. The number of drive beams required depends on the number of “stages”, or plasma cells, in the design. This depends on a detailed optimisation of costs, operational feasibility, cooling etc. for the required application [25] that is beyond the scope of this exercise. To be concrete, the number of stages used in the original HALHF design, 16, is used. Thus, 16 drive beams must be manufactured, fed to the PWFA cells and synchronised so as to accelerate the electron bunch coherently. The most cost-efficient way to do this is to repurpose the original cavity-based electron arm to produce the required number of low-energy drive bunches in addition to the high-quality bunch destined for collision at the IP. Overall, the cavities are run at lower gradient but accelerate higher currents; an additional factor of 2.7 in the RF power in the electron arm is required because of the addition power required for the drive beams. This is somewhat higher than the doubling that was forseen for the ILC luminosity upgrade in the TDR. It can be achieved by providing six klystrons per nine cryo-modules rather than the baseline of two; sufficient space is available, and the segmentation of the power distribution system makes this modification easy. The number of colliding bunches per bunch train is halved in order to keep the power/colliding bunch approximately constant; the bunch charge for the positrons can then be doubled for the same RF power. If 5 Hz running is assumed, then the produced luminosity would be half that assumed for a 500 GeV standard ILC upgrade. Running at 10 Hz of bunch trains, which may be possible, would restore the luminosity.

The area in which the booster is situated is assumed to be that containing the undulator that produces polarized positrons. Since additional space perpendicular to the beam line is required for the drive-beam distribution, this must either have been planned during the original construction or the cavern must be extended somewhat, since polarized positrons will still be required in the upgrade.

Complications arise from the bunch-compressor design for the ILC, which also accelerates from 5 to 15 GeV. This is unable to cope with the necessary drive-beam current. It is therefore necessary to construct a separate drive-beam injector. However, injecting at 15 GeV would be too expensive. A possible solution is to reduce the injection energy for the drive beams to 2 GeV and to construct a bypass for the 15 GeV colliding beam from the bunch compressor, returning it to the main beam axis just before the PWFA cells. Such a bypass requiring only a simple FODO lattice would be inexpensive and would fit inside the main tunnel.

Other complications include the bunch length of the colliding bunch. This must be sufficiently short to fit within the plasma blow-out bubble, whose length is approximately the plasma wavelength, which is inversely proportional to the plasma density. The relatively low plasma densities used in HALHF, which facilitate the operation of the PWFA arm, around 6×10^{14} cm^{-3}, still require much shorter bunch lengths than typical for ILC, of around 40 μm rather than 300 μm. The ILC TDR bunch length is mostly determined by the electron-damping-ring characteristics. The HALHF baseline assumption is that polarised sources of characteristics such as to obviate the necessity for a damping ring will be available before construction. This would make the production of short pulses much easier. Additionally, the shape of the drive bunches, which should provide a Transformer Ratio of around 2, are asymmetrical and therefore lead to an increase in high-order mode losses (HOMs) which must be damped, leading to a concomitant increase in the cryoload, which is power hungry.

In summary, there are a number of challenges that need to be addressed if a detailed design of a PWFA-based energy booster were to be pursued. It should be remarked that CLIC technology is much more compatible with a PWFA booster, in terms of bunch patterns, bunch lengths etc., than is ILC. However, it seems possible that either technology can be made compatible with a PFWA booster. There do not appear at this stage to be show stoppers; such a booster could provide a cost-effective way to increase the energy of an initial linear-collider Higgs factory. It also would provide an important proof of principle for a much higher energy linear collider, as discussed in the next section.

Fully Wakefield-based accelerator The alternative to a booster-upgrade is a multi-TeV upgrade (up to 10 TeV) of the LC facility based on wakefield accelerators (either beam-driven plasma, laser-driven plasma, or structure-based wakefield accelerators, depending on technological developments). The accelerating gradient in the plasma or structure may well-exceed 10 GV/m. One of the primary challenges the 10 TeV Wakefield Collider faces is the staging of multiple wakefield stages in succession. In the case of beam-driven plasma acceleration, the wakefield stages are separated by magnetic chicanes and focusing lattices, which may be longer than the accelerating plasma in each stage. This results in a reduction of the *geometric gradient*. If the ILC 550 GeV option is built, each linac will be 11 km in length. Therefore, the minimum geometric gradient to achieve 5 TeV beam energy in this 11 km tunnel is 450 MV/m. It is important to examine tradeoffs between the local maximum gradient in the plasma, the length of the interstage optics, and the number of plasma stages in order to achieve this geometric gradient. Such problems would be solved if the ALIVE concept [488, 489] of proton-driven PWFA can be successfully developed, since this is envisaged to achieve high energies in a single stage. It does however also require a high-energy proton accelerator on site, which would be available if the facility were built at CERN or Fermilab. In addition to the staging challenge, the 10 TeV Wakefield Collider must either solve the problems of accelerating positrons in plasma efficiently [487], or further develop the $\gamma\gamma$ collider concept for ultra-high energy collisions.

The 10 TeV Wakefield Collider Design Study is currently being formed to address these challenges [29]. The design study has been initiated by the 2023 P5 Report [485], which calls for "vigorous R&D toward a cost-effective 10 TeV pCM collider based on proton, muon, or possible wakefield technologies." Specifically, the P5 Report requests "the delivery of an end-to-end design concept, including cost scales, with self-consistent parameters throughout." The Design Study is working in close collaboration with the ongoing HALHF [25], ALIVE [488], and ALEGRO [27, 28] efforts to design colliders based on wakefield technologies.

The 10 TeV Wakefield Collider Design Study must deliver solutions to the following challenges in order to achieve high-energy, high-luminosity collisions.

- Full acceleration of beams with charge > 100 pc and emittance < 100 nm.
- Emittance preservation and stability of staged plasma acceleration.
- Beam Delivery Systems for 5 TeV beams.
- Mitigation of beam-beam effects at 10 TeV pCM.

In addition, if an electron-positron collider is required, the efficient acceleration of positrons in plasmas must be solved.

Assuming that these challenges can be addressed both in theory and in proof-of-principle demonstrations, the next step is to understand their implementation in the context of an existing LC facility. For example, beam-driven plasma staging requires multiple parallel beamlines to deliver drive and main beams to each plasma stage. Are the ILC tunnels wide enough to accommodate the necessary separation between the beamlines? In the case of a collider based on laser-driven accelerators, large laser rooms must be built near the beamline. Both of these design choices impact the civil engineering of the LC facility, but current wakefield collider designs are not mature enough to make specific recommendations for facility enhancements that might accommodate a 10 TeV upgrade. The 10 TeV Wakefield Collider Design Study aims to address questions related to civil engineering and deliver its report by 2028, well in-time to provide input to the construction process.

Timeline and R&D needed

- **Electron beam-driven plasma** Table 18 indicates the timescale necessary for the required development of PWFA technology to produce a Technical Design Report for the HALHF project and its current technological readiness. The technology and design thus developed would have far-reaching implications and be applicable to all plasma-wakefield accelerator facilities.
- **Proton beam-driven plasma** The ideas for proton-driven acceleration for a collider are being explored in the ALIVE project. The major gain of such a facility would be the possibility of accelerating to TeV

energies in a single stage, leading in principle to significantly higher geometric gradients because inter-stage optics inserts which grow in length with energy is avoided. However, significant R&D is required, in particular in areas such as rapid-cycling proton accelerators, if the luminosity of such machines is to be large enough to be interesting.

- **Laser-driven plasma** There is very substantial activity in laser-driven plasma acceleration, which, not needing powerful accelerators, is more widely spread worldwide than is the case for PWFA. Investigations with LWFA can illuminate many of the areas that require development in plasma-acceleration facilities, particularly single-stage properties, emittance preservation, etc. The implementation of a laser-driven collider must however await an orders-of-magnitude improvement in the efficiency and repetition rate of the high-power lasers required. The good news is that such developments are required in a much broader scientific field than particle physics and are driven by major industrial actors. There is therefore hope that by the time that a plasma-wakefield accelerator could be seriously contemplated, the required advances will have been made. Scientists inside the ALEGRO framework [27, 28] are pursuing research in this area.

- **Structure wakefield acceleration** The idea of using dielectric structures to maintain high accelerating fields has been developed in recent decades. Very interesting results have been obtained for a variety of configurations [490]. Two of these have been investigated in the context of upgrades to HALHF [25].

Facilities and Timelines There are several facilities world-wide are carrying out work relevant for wakefield-based colliders. A summary of research goals and capabilities for Beam Test Facilities in the US was created for the recent Snowmass process [491], and a summary of research goals and capabilities for Beam Test Facilities in Europe was created for the LDG process [492].

- **AWAKE** [493] is engaged in a long-term development programme to explore the parameters of proton-driven wakefield acceleration. It has a variety of "spin-off" applications for physics, in particular for high-field QED and fixed-target experiments. Developments that could lead to a collider based on these techniques are concentrated in the ALIVE project.

- The **FACET-II** programme at SLAC focuses on high-efficiency, high-quality two-bunch PWFA with parameters relevant for future colliders [494]. FACET-II provides 10 GeV electron beams at extremely high peak currents [495]. Its advantages include the ability to carefully control the drive-witness separation and bunch profiles. FACET-II has some infrastructure creating positron beams and accelerating them in plasma, but further investment is required to enable this capability.

- The **FLASHForward** facility at DESY has been running for several years and produced results, particularly in emittance preservation and plasma recovery time, of direct relevance to collider applications [496]. It is particularly suited to the study of high-power effects as it can run with multiple bunches closely separated to study large instantaneous power deposition in the plasma cell.

- The **Argonne Wakefield Accelerator (AWA)** facility specializes in beam-driven wakefield acceleration, with a focus on the structure wakefield accelerator technology [491]. It has pioneered advanced phase space manipulation techniques for temporal bunch shaping, and is capable of producing electron-bunch trains having charges up to $\simeq 400\,$nC. Operating at beam energies of approximately 70 MeV, the facility contributes significantly to developing next-generation compact accelerators through collaborations with institutions worldwide.

- The **BELLA** centre at LBNL has been performing research on laser-plasma accelerators (LPAs) for over two decades. The main research objectives are the development of LPA modules at the 10 GeV level [497] and the staging (coupling) of LPA modules, which are two essential R&D components for a future plasma-based linear collider. BELLA is pursuing research into coherent combination of fiber lasers for high repetition rate LWFA.

Critical parameters	TRL	R&D time (y) (Design/Total)	R&D current (MSF)	R&D needed (M€) (Design/Total)	FTE current	FTE needed	Comments
Electron beams > 100 GeV	1	7-8/11-13		7/100	1	40	No PWFA-test facilities have produced >100 GeV beams
Acceleration in one stage (∼10 GeV)	5	5/9-10		10/100	3	50	AWAKE demonstration but technology may not be suitable
Plasma uniformity (long & trans.)	4	5/9-10		2/100	2	15	AWAKE demonstration but technology may not be suitable
Preserving beam quality/emittance	3.5	7-8/11-13	0.5 (ERC + Oslo national)	3/100	5	25	Normalized emittance preserved at <3 um levels with small currents
Spin, polarization	2	5/9-10	0.1 (DESY)	3/100	1	16	Technology concept formulated
Stabilisation (active and passive)	3	7-8/11-13		1/100	1	10	Studies at AWAKE and LWFA, but not at HALHF requirements
Ultra-low-emittance beams	2	7-8Y/11-13		3/100	0	20	Not yet at collider emittance. Better test facilities required.
External injection and timing	4	7-8/11-13		1/100	0	10	Precise timing for external injection demonstrated at AWAKE
High rep-rate targetry with heat management	2	5/9-10		7/100	3	40	Heat modification of plasma properties/profile and target cooling requires inew concepts
Temporal plasma uniformity/stability	4	5/9-10		3/100	0	10	AWAKE demonstration but technology may not be suitable
Driver removal	2	7-8/11-13		2/100	0.5	10	HALHF concept exists
Drivers @ high rep. rate & wall-plug eff.	5	5/9-10		5/100	0.5	10	Similar to CLIC driver, demonstrated in CTF3
Interstage coupling	2	7-8/11-13	1 (ERC)	3/100	3	10	HALHF concept exists
Total system design with end-to-end	3	3-4	0.5 (Oslo, Oxford)	3	2	20	Not yet at pre-CDR level. Aim for pre-CDR document early in 2026.
Simulations	5	part of above	0.5 (ERC + Oslo national)	part of above	4	5	Single-stage simulation (HIPACE++) well developed - dedicated framework (ABEL) for start-to-end
Self-consistent design	4	part of above	part of above	part of above	in previous 2 rows	5	Plasma linac start-to-end simulations performed using HIPACE++/ABEL

Table 18: HALHF Plasma Arm R&D: Technology Readiness Levels (TRL), required resources and timescales to produce TDR. “FTE current” means currently in place; “needed” is integrated total requirement. “R&D current” is only non-zero if dedicated to HALHF. (Adapted from LDG Accelerator Roadmap review submission, Feb. 2025).

- **SPARC-LAB** at INFN Frascati develops plasma source technologies and has demonstrated precision applications of beam-driven plasma accelerators, such as FELs [498]. The R&D at SPARC-LAB lays the groundwork for EuPRAXIA, the world's first plasma accelerator-based User Facility [499].
- **High-Intensity Laser Facilities**: A number of laser facilities, including ZEUS, ELI, APOLLON, GEMINI and others pursue LWFA research with very high intensity lasers. Goals for these facilities include single-stage very high energy acceleration.

If a PWFA facility such as HALHF is to make progress, it will be necessary to build a substantial test facility to test the various parts of the system if a real accelerator. Such a test facility, as proposed for example by the SPARTA project [500], would produce beams of around 100 GeV, which can additionally be very useful for e.g. strong-field QED studies or beam-dump experiments. The time-scale for such a facility, assuming sufficient resources are obtained for the necessary R&D, could be around a decade. In fact, as discussed in Sect. 5.2, a linear collider facility in an initial, SCRF driven configuration, could itself provide opportunities for an R&D facility with the necessary beams and experimental environment to conduct and finalise this research.

Necessary civil construction and environmental impact The strength of PWFA colliders is precisely in the area of civil construction and environmental impact. Since the effective accelerating gradient is at least an order of magnitude greater than for metallic cavities, the length for a particular application is greatly reduced, and thereby the construction cost and the environmental impact. The latter is usually dominated by the carbon footprint of the concrete required for the tunnel. For the case of the HALHF Higgs factory, for example, the length of the 250 GeV CoM version is around 5 km, much shorter than ILC.

For many of the PWFA upgrades to an existing ILC discussed in this section, the additional construction and environmental impact is negligible. For example, for the PWFA booster discussed above, the only major impact would be the requirement for a larger alcove/cavern at the site of the undulator in order to make space for the drive-beam distribution system. This would preferably be part of the initial construction, or a subsequent minor excavation.

4.4.5 Upgrade using Structure Wakefield Accelerator Technology

As mentioned in the previous section, Structure Wakefield Acceleration (SWFA), the acceleration of beams in fixed dielectric or metal structures at very high frequency, has also been explored as an approach to high gradient electron acceleration [490]. Though this cannot reach such high gradients are are possible in Plasma Wakefield Acceleration, SWFA is e^-/e^+-symmetric and makes the problem of staging somewhat simpler.

In this section, we explore two applications of SWFA to a future $\sqrt{s} = 10$ TeV pCM linear collider housed in the LCF tunnel. The first application is (*i*) a fully SWFA-based linear collider, while the second option is (*ii*) a hybrid-WFA that uses SWFA for the positron (e^+) linac and plasma-WFA for the electron (e^-) linac. By assessing the feasibility of these options, we explore how SWFA can offer a viable quasi-conventional high-gradient solution alongside PWFA and LWFA. This assessment draws on collaborative efforts from the newly formed 10 TeV pCM Wakefield Collider Design Study [29] and updated beam-delivery system (BDS) scaling from the CLIC 7 TeV design report at CERN while leveraging recent SWFA progress at Argonne National Laboratory (ANL).

SWFA includes two configurations: collinear wakefield accelerator (CWA), where the drive and main beams share the same path (similar to PWFA), and two-beam acceleration (TBA), pioneered at CERN's CLIC test facility, where the two beams follow parallel paths. For the two linear collider applications considered here, we focus on TBA-SWFA, given its maturity compared to CWA-SWFA. Specifically, we consider the short-pulse TBA-SWFA scheme under development at ANL that employs structures driven by short RF pulses to achieve high gradients.

The short-pulse TBA-SWFA approach is motivated by the CLIC program's empirical scaling law,

$$\mathrm{BDR} \propto E^{30} \times \tau^5 \,, \tag{16}$$

where E is the electric-field gradient [MV/m] and τ is the RF pulse duration [501] and $E \propto G$, where G is the average-energy gradient [MeV/m]. This equation indicates that shorter pulses enable higher gradients. While the CLIC 3 TeV collider [7] is based on $\tau = 240$ ns pulses to achieve $G = 100$ MV/m, the Argonne Flexible Linear Collider (AFLC) uses $\tau = 22$ ns pulses to operate at $G = 267$ MV/m [502]. This trend of shorter pulses enabling higher gradients continues with recent short-pulse TBA research at ANL that has demonstrated $G \simeq 300$ MV/m in a 3-cell traveling-wave structure and $E \simeq 400$ MV/m (corresponding to $G \simeq 200$ MV/m) in a standing-wave RF gun, both driven by 9 nsec X-band (11.7 GHz) RF pulses [503]. The ongoing research at ANL is targeting $E \simeq 1$ GV/m.

1. **Fully SWFA-Based Linear Collider.** This application proposes a 10 TeV linear collider employing short-pulse TBA-SWFA for both the electron (e^-) and the positron (e^+) linac, each operating with an average energy gradient of $G \simeq 500$ MeV/m over 10 km. This configuration yields 5 TeV per linac with a total linac length of 20 km. The CERN BDS analysis for a 7-TeV collider, which requires 7 km per linac, scales to approximately 8 km for 10 TeV, leaving 5 km for the injector complex and interaction point (IP). This layout fits within the 33.5-km ILC tunnel. Note, the proposed short pulse TBA-SWFA 10 TeV design is an extension of the previous short pulse TBA-SWFA 3 TeV , AFLC strawman by ANL [502].

2. **Hybrid-WFA.** This application proposes a hybrid 10 TeV linear collider that uses short-pulse TBA-SWFA for the e^+ linac and plasma-WFA for the e^- linac. The advantage of TBA-SWFA is that it is charge-independent and can easily serve as the e^+ linac, which remains a challenge for plasma-WFA. This application can be considered for both ILC baseline options based on tunnel lengths of 20.5-km and 33.5-km. While the 33.5-km option was already outlined above, the case for a 20 km tunnel is similar to the asymmetric Higgs Factory, HALHF [486]. As a motivating example, one could use a 5-km e+ TBA-SWFA linac (2.5 TeV) and a 5 km e- plasma-WFA linac (10 TeV) to give $\sqrt{s} = 10$ TeV. Assuming 8 km for BDS this leaves 2.5 km for the injector and IP; further optimization is needed.

These two applications toward a 10 TeV pCM collider based on short-pulse TBA-SWFA with average-energy gradient of 500 MeV/m appear feasible within both the 33.5 km and 20.5 km LCF tunnels. They are encouraged by current designs and ongoing experimental progress in TBA-SWFA. This approach enables effective reuse of the ILC tunnel once its Higgs-factory program has concluded, thus offering an opportunity to extend the program to the energy frontier. Continued validation of the gradient will strengthen the Linear Collider Facility's contribution to CERN, advancing the energy-frontier program through collaborative wakefield research.

4.5 Luminosity upgrades

4.5.1 Higher luminosity at lower energies: Z-pole and WW threshold

The initial accelerator configuration for ILC-250 can also run at the Z-pole with an instantaneous luminosity of 2.05×10^{33} cm^{-2}s^{-1} with polarised electron and positron beams as described in [14] and in detail in [67]. It can also run around the WW threshold if desired; interpolating between the Z-pole and 250 GeV to running at $\sqrt{s} = 161$ GeV leads to an instantaneous luminosity[13] of 3.65×10^{33} cm^{-2}s^{-1}. The luminosity at the Z-pole exceeds that of LEP by two orders of magnitude and together with the polarisation is sufficient to produce five billion Z's and accumulate 100 fb^{-1} in a couple of years. Given the likely investment in a facility that can reach to much higher energy including to 500 GeV and above, it makes sense to consider how to efficiently address the physics goals at lower energy as part of the integrated physics program of a TeV-scale linear collider. Two of the primary physics drivers discussed in Sec. 3.2 that showcase unique linear collider capabilities are the measurement of A_{LR} at the Z-pole [504] and the option for a dedicated m_W measurement from a polarised threshold scan [505]. The two relevant aspects are the potential for higher luminosity at lower centre-of-mass energies, and the provision of the highest possible polarisation of both beams, thus enabling target physics precisions to be reached in modest running times.

At lower energies, especially at the Z-pole, beamstrahlung is naturally suppressed. The characteristic centre-of-mass energy spread at the Z-pole, including the effects of beamstrahlung, σ_{eff}[14], is 0.25%; this is much less than the related fractional half-width of the Z (1.4%). Therefore, the physics constraints leave

[13] This assumes a repetition rate of 3.0 Hz for specifically WW threshold operation with the initial ILC-250 configuration.

[14] Defined as half of the range covered by the central 68% of the centre-of-mass energy luminosity distribution normalized to the nominal centre-of-mass energy.

considerable scope for adopting collision conditions that lead to higher luminosities per bunch crossing, while modestly broadening the luminosity spectrum. A number of potential improvements have been investigated that may lead to combined luminosity increase factors in the range of 2.0–10.

These include both "straightforward" repetition rate, f_{rep}, and/or bunch number, n_{b}, increases, and changes that increase the luminosity per bunch crossing, $\mathscr{L}_{\mathrm{BX}}$, by accepting increased beamstrahlung leading to higher luminosities. The latter involves both increases to the geometric luminosity, $\mathscr{L}_{\mathrm{geo}}$, that is a function of the number of electrons/positrons per bunch, N, and the beam-sizes at the interaction point ($\sigma^*_{x,y}$), and potentially additional increases, over that from $\mathscr{L}_{\mathrm{geo}}$ alone, from corresponding increases to the luminosity enhancement factor associated with the pinch effect, H_D. The facility instantaneous luminosity is

$$\mathscr{L} = f_{\mathrm{rep}}\, n_{\mathrm{b}} \left(\frac{N^2}{4\pi\sigma^*_x \sigma^*_y} \right) H_D = f_{\mathrm{rep}}\, n_{\mathrm{b}}\, \mathscr{L}_{\mathrm{BX}} = f_{\mathrm{rep}}\, n_{\mathrm{b}}\, \mathscr{L}_{\mathrm{geo}}\, H_D \ ,$$

where $\mathscr{L}_{\mathrm{BX}}$ and consequently H_D are evaluated with beam-beam simulations. In practice, the vertical disruption parameter, D_y, defined as

$$D_y = \frac{2\, r_{\mathrm{e}}\, N\, \sigma_z}{\gamma \sigma^*_y\, (\sigma^*_x + \sigma^*_y)} \ ,$$

plays a key role in determining H_D [413].

The "straightforward" changes are:

- Doubling the bunch number to 2625 as already assumed feasible in [67].
- Once the electron linac can reach beam energies significantly higher than thos required for for Z-pole/WW threshold operation, there will be enough power to permit $5+5$ Hz operation[15]. Consequently the collision repetition rate can increase to 5.0 Hz for both Z and WW threshold operation (from 3.7/3.0 Hz for Z-pole/WW threshold).

Combined, these changes lead to luminosities of $5.54 \times 10^{33}\mathrm{cm}^{-2}\mathrm{s}^{-1}$ and $12.2 \times 10^{33}\mathrm{cm}^{-2}\mathrm{s}^{-1}$ at the Z-pole and WW threshold respectively.

Individual changes were investigated affecting the luminosity per bunch crossing. The studies were done for a centre-of-mass energy of 91.2 GeV using Guinea-PIG++ [506] starting from the ILC-250 baseline Z-pole operation beam parameters with $D_y = 31.4$.

- Increasing the bunch length (σ_z). E.g. increasing σ_z from 410 μm to 615 μm by reducing the compression in the bunch compressor. This also reduces the linac beam energy spread from 0.30% to 0.20%. The 50% increase in D_y leads to a modelled 4.6% increase in luminosity and a *decrease* in σ_{eff} by a factor of 1.34.
- Decreased horizontal and vertical normalized emittances. For instance, if these could be decreased from 6.2 μm/48.5 nm to 5.6 μm/42 nm, the modelled $\mathscr{L}_{\mathrm{BX}}$ increases by 20% with a 2% increase in σ_{eff}.
- Decreased horizontal beta function. E.g., decreasing β^*_x from 18 mm to 12 mm leads to a modelled overall increase of 53% in $\mathscr{L}_{\mathrm{BX}}$ with a factor of 1.26 increase in σ_{eff}.
- Increased bunch population (N) at fixed beam power. E.g. increasing N from 2.0×10^{10} to 2.5×10^{10} while decreasing n_{b} by a factor of 1.25 leads to a 56% increase in $\mathscr{L}_{\mathrm{geo}}$, a modelled overall increase of 79% in $\mathscr{L}_{\mathrm{BX}}$, and 43% in instantaneous luminosity, with a factor of 1.16 increase in σ_{eff}.

Overall, if all four types of change could be implemented, with the discussed magnitudes, the net effect is simulated to be a factor of 3.1 increase in facility luminosity with a tolerable increase of σ_{eff} to 0.62%. Together with the "straightforward" luminosity upgrades, there is thus potential for luminosities of $1.7 \times 10^{34}\ \mathrm{cm}^{-2}\mathrm{s}^{-1}$ at the Z-pole and an estimated $3.8 \times 10^{34}\ \mathrm{cm}^{-2}\mathrm{s}^{-1}$ near WW threshold corresponding to factors of 8.5 and 10 beyond the ILC-250 baseline. Further study is needed to assess the feasibility of such changes, to verify the

[15] Where the electron linac uses one cycle for undulator-based positron production at 125 GeV or above, and one cycle for 45.6 GeV or 80.5 GeV beams for physics collisions. This requires a linac capable of achieving at least 170 GeV/205 GeV in nominal operatoon.

fidelity of the simulation estimates in the presence of machine imperfections and offsets in the high disruption regime, and to characterize fully the effects on the physics observables. There are a number of inter-related issues for the overall accelerator/detectors design:

1. Beam dynamics (i.e. less emittance dilution) is facilitated if beams are accelerated at full gradient. This would need a bypass line (and corresponding tunnel area) and may be essential for operating well an energy-upgraded machine at the Z-pole.

2. Study of the beam control at the IP for the high disruption case including the feedback system.

3. Beam backgrounds in the detectors will increase, especially for smaller β_x^*, and need to be assessed.

4. Increasing the bunch populations has wide-ranging challenges across the accelerator complex and may not be practical. The design bunch charge at the sources is 3.0×10^{10}e. This includes a 50% margin over the nominal 2.0×10^{10}e in collision.

The baseline scenario for ILC is 80% electron polarisation and 30% positron polarisation leading to an effective polarization [33] of 88.7%. Higher polarisation values of up to 90% for electrons and 60% for positrons are conceivable, leading to an effective polarization of up to 97.4%. A 40–45% positron polarization is already believed to be feasible with the current ILC-250 baseline [425].

4.5.2 Higher luminosity at all energies by increasing the collision rate

L-band SCRF cavities as employed at the ILC store a considerable amount of energy in the oscillating accelerating field, which is lost at the end of each pulse and must be replenished before the next beam pulse; in the ILC baseline design, as discussed in Sect. 4.1.1, approximately one third of the total RF pulse of 1.65 ms duration is required for the filling of the cavity. Therefore accelerating more bunches, or overall charge, per pulse improves the ratio of RF power transferred to the beam vs RF power lost in the filling, and thus improves the overall efficiency. This is also reflected in the fact that increasing the number of bunches from 1312 to 2625 bunches per pulse requires only 50 % more klystrons in the Main Linac, not twice as many.

Increasing the number of bunches per pulse (or the bunch charge) further would require to overcome several limitations together:

- The beam current in the damping rings, which is given by the total accelerated charge per pulse times the DR revolution frequency, is limited to about 400 (800) mA for positrons (electrons) by electron and ion cloud instabilities. More accelerated charge per pulse would thus require a larger damping ring circumference or stacking several damping rings in the same tunnel (which is already required for positrons when operating at 2625 bunches).

- The pulse length that the existing klystron designs deliver is limited to about 1.65 ms. Operation at significantly longer pulses would require changes to the klystron design. Alternatively, the bunch separation could be reduced to accelerate more bunches within the 1.65 ms pulse duration, which would require the installation of more klystrons (this is the solution chosen for 2625 bunches operation).

- Increasing the overall amount of accelerated positrons per second (i.e., if the repetition rate is not reduced when the charge per pulse is increased) raises the requirements on the positron source's production rate.

10Hz operation at full gradient The ILC baseline design calls for a repetition rate of 5 Hz. To permit the 5+5 Hz operating mode that is necessary for operation below the minimum energy of about 120 GeV needed by the undulator positron source to work effectively, a number of key systems have been specified for 10 Hz operation, notably: The electron source, the damping rings, the bunch compressors, the HLRF system (modulators, klystrons, and couplers) of the main linac, and the BDS. 10 Hz operation for physics operation at reduced gradient has also been studied, which is challenging for the undulator positron source, but deemed feasible. Operating the damping rings at 10 Hz repetition rate requires more damping wigglers in order to reduce the damping time, and more RF power to replenish the increased synchrotron radiation power; this is already foreseen in the damping ring design as an option. The raised RF power requirements of the sources, bunch compressors and main linacs would lead to a doubling of the electric power demand of the modulators, which needs to be taken into account in the dimensioning of the modulator electric supply, but is not a problem.

The limiting factor for 10 Hz operation at full gradient in the Main Linac is the increased cryogenic load from the dynamic heating of the cavities, which dominates the cryogenic load and doubles at a doubled repetition rate. Dynamic heating is dominated by the heat losses in the cavity walls, which are proportional to $1/Q_0$. An doubling of Q_0 (from the design value of 1×10^{10} to 2×10^{10}, which appears feasible given recent advances in cavity performance, would make it easier to provide the necessary cooling capacity to go to 10 Hz. However, as not all dynamic cryogenic losses scale with the cavity wall losses, i.e. $1/Q_0$, doubling the repetition rate does require an increase in cryogenic capacity.

Designing the Main Linac for operation at full gradient with a repetition rate is possible. Increasing the cryogenic cooling capacity involves an increased throughput of helium through the helium pipes of the cryo-modules, increased capacity of the cold compressor system serving one supply area (2 to 2.5 km of cryo-strings), and an increased helium plant capacity. Helium plants are commercially available up to approximately 20 kW equivalent cooling power at 4.5 K, and the ILC design is optimised to fully utilise such a plant. Therefore, more helium plants would be required to supply a given supply area. It would require to re-optimise the overall cryogenic layout concerning the number of cryo-modules in a cryo-string (connected to a single feed cap) and the number of strings supplied by one helium plant, and possibly to increase the helium gas pipe in the cryo-module for increased helium flow, as has been successfully done for the LCLS-II cryo-module. Provided that the overall distance between access shafts with helium plants stays the same, the cost impact of such a design change would be dominated by the increased number of cryo-modules.

Overall, if 10 Hz operation at full gradient is required for a linear collider facility, this is entirely feasible, with a cost impact dominated by the need for more cryogenic capacity, i.e., more helium plants. This requirement is to be taken into account during the dimensioning of the relevant components and systems, considering the assumed cavity operating gradient and quality factor. Revisiting these design assumptions would be part of the value engineering part of a design study.

4.5.3 Energy recovery technologies

Increasing luminosity by orders of magnitude from O(10^{34} cm^{-2}s^{-1}) requires significant modifications in overall approach to the beam parameters and some system choices for the linear collider. Simple-minded increase of the collision frequency would require increased AC power and particle production. Hence, an efficient recycling of both the beam energy and of the collided particles is required for any significant luminosity boost. All these requirements naturally lead to CW operation of Energy Recovery Linacs. In this section we present two possible upgrade of the proposed linear collider to average luminosity exceeding 10^{34} cm^{-2}s^{-1}.

Status of Energy Recovery Technology

Energy-Recovery Linacs (ERLs) are a highly efficient technique for accelerating high-average-current electron beams. In an ERL, a high-average-current electron beam is accelerated to relativistic energies in (typically) a superconducting RF continuous-wave (CW) linear accelerator. The beam is then used for its intended application, such as serving as a gain medium for a free-electron laser, producing synchrotron light, acting as a cooling source for ion beams, or generating a beam to collide with ions. These applications typically lead to a significant increase in energy spread or emittance of the electron beam, although the majority of the beam power is retained. To recover this power, the beam is sent back through the accelerator, but this time it is approximately 180° out of phase with the accelerating RF field. As a result, the beam is decelerated, transferring its energy back into the RF fields, allowing a new beam acceleration. Eventually, the beam's energy drops to a point where further transport becomes impractical, and the beam is dumped with a small residual energy. In the case of e^+e^- ERL-based colliders, all the beams are recycled and not dumped.

In high-energy physics, ERLs could be used on producing an intense, low-emittance electron beam for interactions with hadrons (e-hadron), positrons (e^+e^-), or photons (e γ). For e^+e^- colliders, both beams could be accelerated and decelerated in ERLs as it will be described in the following proposals.

The 2020 update to the European Strategy for Particle Physics (ESPP) emphasized that ERLs represent one of the most innovative technologies for future high-energy physics accelerator infrastructures. It also highlighted that the R&D roadmap for critical technologies needed for future colliders, should include research on high-intensity, multi-turn ERL machines. Thus, two projects were identified as essential pillar for future ERL development:

- The **bERLinPro** project in Helmholtz-Zentrum Berlin (HZB)- Germany: A single turn ERL (50 MeV) to demonstrate high current (up to 100 mA), low-emittance continuous wave (CW) electron beams using SCRF technology.
- The **PERLE** project at Irène Joliot-Curie Laboratory (IJCLab) at Orsay-France: A three-pass ERL facility designed to operate ultimately at 10 MW beam power (20 mA $\times$ 500 MV), aiming at testing the technologies increasing the efficiency of the accelerators and necessary for future high-energy physics applications, including SCRF development.

The two projects have the ambitions to explore a new power range (5 to 10 MW) never reached by ERLs, paving the way to a new generation of powerful machines and appending new milestones toward future large-scale, ERL-based colliders. However, several challenges have to be addressed along the way:

- **Development of High-Q_0 SCRF Systems for High Beam Currents**: The development of high-Q_0 SCRF systems capable of handling high beam currents (typically 100 mA or higher) and continuous wave (CW) mode operation while mitigating higher-order mode (HOM) excitations is a key focus. In addition to the widely-used Tesla cavities (1.3 GHz) adapted for CW operation, which have been implemented in projects such as bERLinPro, CBETA, and cERL, the PERLE project has led to the design and optimization of a new 802 MHz, 5-cell Nb cavity. This cavity has been optimized to facilitate the efficient extraction of parasitic HOMs through features like fewer cells, larger iris apertures, and an optimized end-group, all while enabling the handling of multi-bunch operations.
- **Innovations in HOM Couplers and Beam Line Absorbers (BLA)**: Recent advancements include the development of new HOM damping waveguides, which were implemented in the bERLinPro project to address the challenges of high-current operations. Additionally, for the PERLE project, three coaxial HOM coupler designs (Hook, Probe, and DQW) were studied and optimized. An optimized damping scheme was selected for the end-group to efficiently extract harmful modes. For the next generation of high-current ERLs, HOM couplers alone are often insufficient to eliminate all critical modes. To address this, Beam Line Absorbers (BLAs) are employed between cavities to capture and dissipate the modes that propagate along the beamline.
- **Enhancing ERL Efficiency**: Research is focused on advancing the performance of Energy Recovery Linacs (ERLs) by developing Nb3Sn coatings. These coatings have shown higher superconducting transition temperatures and potential for reduced surface resistance compared to traditional niobium cavities. Additionally, efforts are being made to develop multilayered Superconductor-Insulator-Superconductor (SIS) structures, utilizing materials like NbN and MgB2. These innovations aim to overcome the performance limitations of bulk niobium, offering the possibility of more efficient and higher-performing Superconducting Radio Frequency (SCRF) cavities. ERLs using these advancements could operate at higher cryogenic temperatures (4.2 K vs. 2 K), reducing the need for costly cryogenic cooling systems. Another promising technology under development is the Ferroelectric Fast Reactive Tuners (FE-FRTs). These innovative devices are designed to rapidly adjust the resonant frequency of SCRF cavities, compensating for frequency shifts caused by microphonics. Their integration could significantly improve the performance and efficiency of ERLs and other accelerator systems.

Many of the developments mentioned above are part of the European program “Innovate for Sustainable Accelerating Systems” (iSAS) [507]. This program is dedicated to enhancing accelerator efficiency, with a particular emphasis on Energy Recovery Linacs (ERLs). It focuses on optimising energy consumption and improving the performance of various systems, including cryogenics, RF power, and beam energy recovery.

ReLiC This luminosity upgrade of linear collider explores and extend ideas of recycling energy and colliding particles that were developed in Refs. [30, 508, 509] for a concept called ReLiC, illustrated in Fig. 57.

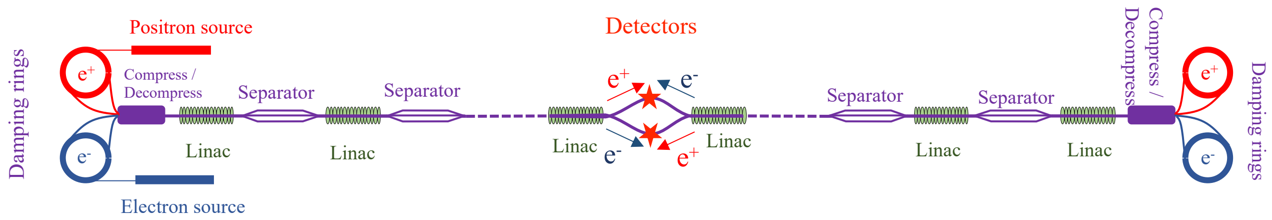

Figure 57: Schematic of ReLiC with two detectors. One the most important feature of ReLiC design is it capability of collide highly polarized electron and positions beams. Beam polarization is maintained by Sokolov-Ternov effects in the damping rings.

ReLiC is based on conventional standing wave (SW) single-axis SCRF linacs which are used both for accelerating and decelerating electron and positron beams. The Linacs are split into sections where separators are used to avoid parasitic collision of the accelerating and decelerating beams. It is worth noting that similar concept, but without separators, was discussed by Gerke and Steffen in 1979 [510], but the use of separators is needed to achieve high luminosity. Using combination of electric and magnetic field in separators provides for on-axis propagation of accelerating beams, preserving their emittance, and deflection only of the decelerating beams [30], as shown in Fig. 58.

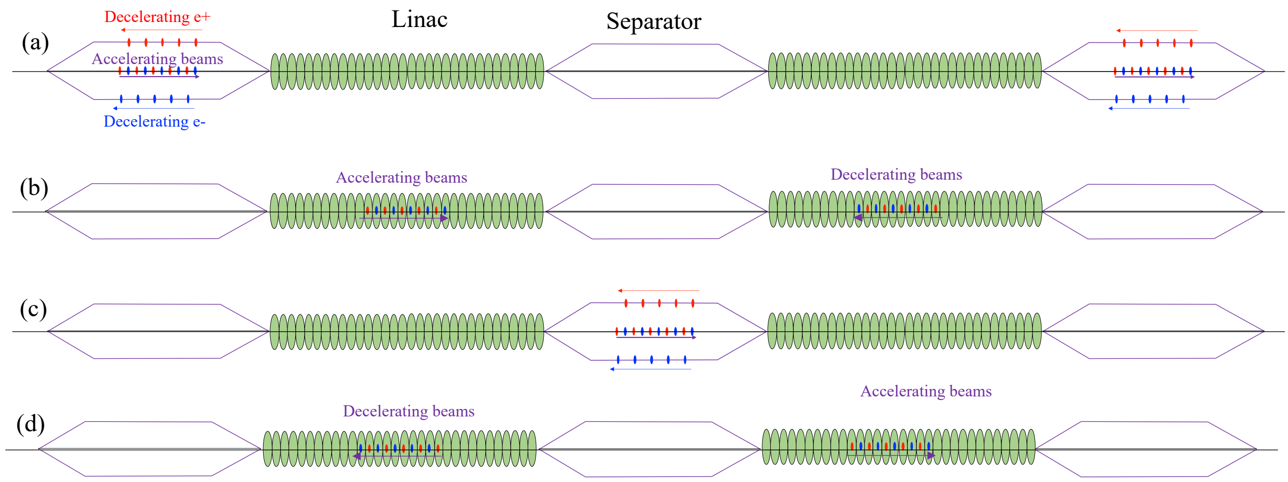

Figure 58: Details of separating accelerating and decelerating electron and positron bunches which repeats with the bunch train frequency, $f_{\text{train}} = 1/T_{\text{train}}$: (a) at $t = 0$ trains of N_{train} accelerating and decelerating bunches are separated horizontally in two separators; (b) at $t = T_{\text{train}}/4$ beams propagating towards the centre accelerate and decelerate on-axis in corresponding linacs; (c) at $t = T_{\text{train}}/2$, the contra propagating beams are separated again; (d) at $t = 3T_{\text{train}}/4$ beams accelerate and decelerate on-axis in opposite linacs. Then the process repeats itself. Note that scales are greatly distorted for visibility.

High luminosity is attained by relatively high collision frequency $f_c = N_{\text{bunches}} \times f_{\text{train}}$ of flat beams with large vertical disruption parameter, which are typical for linear colliders. As shown in [511], such violent collisions can result in significant ($\sim$ 2 fold) increase in vertical emittance, which requires cooling of decelerated beam in damping ring from one to two damping times.

ReLiC operation provides for recycling not only of the beam energy but also of the collided particles. Efficient particles recovery requires the damping ring to accept particles with energy deviation resulting from the synchrotron radiation in beam separator and IR optics and beamstrahlung during beam collision. An analysis shows that for high energy colliders at the centre-of-mass energy of interest the beamstrahlung plays the dominant role and requires increasing both horizontal beam size (and horizontal β^*) and bunch lengths when compared with the LCF baseline parameters (see Table 19). While this results in reduction of the luminosity, it also significantly reduces energy spread in colliding beam and should provide for improved energy resolution.

The energy efficiency of such collider depends on the energy of the damping ring: as mentioned above, we expect that each particle should lose about twice the particle energy in the damping ring per each collision. For a damping beam energy of 2 GeV and 4 GeV for centre-of-mass energies of 250 GeV and 500 GeV correspondingly, we would need a 20-fold decompression of the beams and 10 % energy acceptance of the damping rings to provide losses operation of the collider. In this case only particles lost ("burned") in IPs and in collision with residual gas would be replaced by top-off from electron and position injectors.

Current technology provides us with limited choices for 1.3 GHz SCRF linacs: the quality parameter is limited to $Q_0 = 4 \times 10^{10}$ at 2 K temperatures [512] where the coefficient of performance (COP) of liquid Helium refrigerators is $\sim$ 6-fold below the theoretical Carnot limit. While we list possible ReLiC parameters with existing technology, we also exploring options of engineering development of improved of 2 K liquid Helium refrigerator COP or a breakthrough with Nb3Sn SCRF cavities operating at 4.5 K temperature with high Q_0.

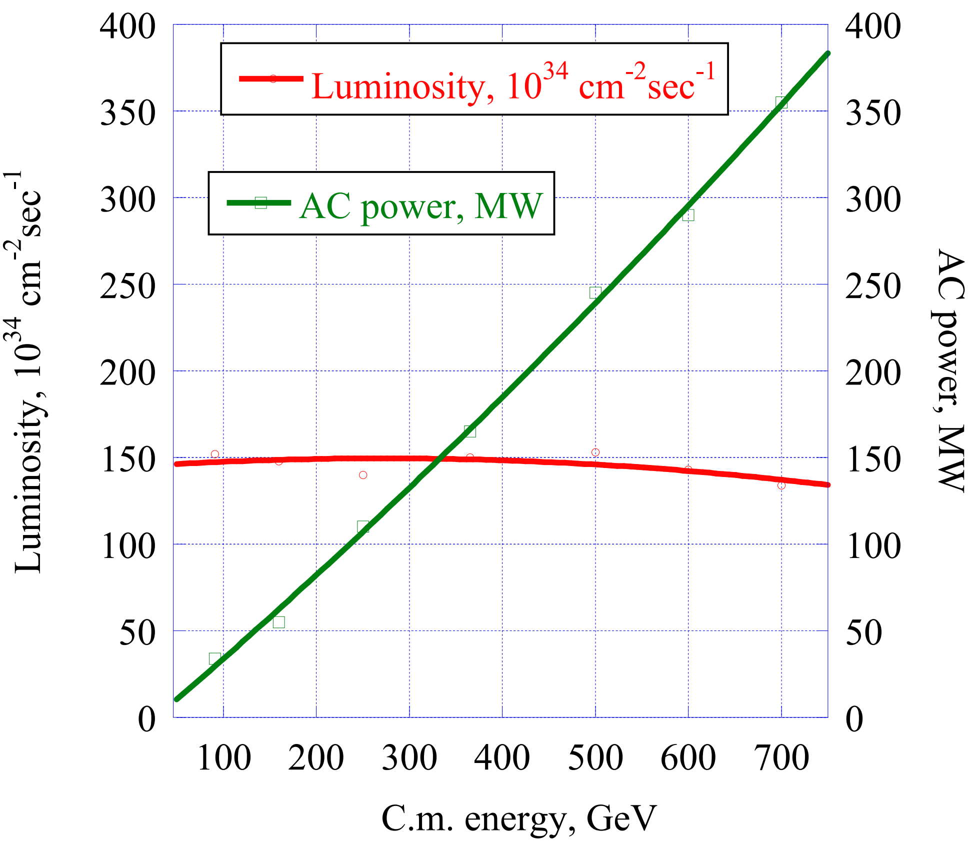

Figure 59: Estimated luminosity and AC power consumption for ReLiC operating with futuristic Nb3Sn SCRF linac with fixed linac length. At high centre-of-mass energies above 500 GeV, the AC power consumption is nearly proportionally split between that used by the cryogenic system and by the damping rings.

The table shows total luminosity of the collider, which is split 50/50 between two detectors. The collision time structure in each detector is determined by that of the bunch trains. Using five electron and five position bunches per train requires the linacs to be split in one kilometer sections. In addition, we assume that electron and positron bunches are separated by ten 1.3 GHz RF cycles. In this case, each detector will see five collisions, separated by 7.7 nanoseconds, repeated with frequency of 150 kHz. Separating contra-propagating bunch trains by 1 cm would require 62-meter-long separators, which reduces the real-estate gradient of the

Table 19: Parameters of ReLiC options with two 14.25 km linacs

	LCF	ReLiC[1]	ReLiC[2]	ReLiC[3]	ReLiC[3]
Centre-of-mass energy [GeV]	250	250	250	250	550
Accel. Grad. [MeV/m]	31.5	12.55	12.55	12.55	27.6
Cavity Q_0 [10^{10}]	2	4	4	4	4
Liquid He temperature [K]	2	2	2	4.5	4.5
Bunch population [10^{10}]	2	2.5	2.5	2.5	2.5
Collision frequency [MHz]	2.62	1.5	1.5	1.5	1.5
Duty cycle	0.0012	cw	cw	cw	cw
Beam current, all beams [mA]	0.042	12	12	12	12
Normalised emittance hor.[μm] / vert.[nm]	5/25	4/1	4/1	4/1	4/1
β_x / β_y [m] / [mm]	0.013/0.41	2.2/0.19	2.2/0.19	2.2/0.19	4/0.36
σ_x / σ_y at IP [μm] / [nm]	0.52/7.7	6/0.9	6/0.9	6/0.9	6/0.9
D_x / D_y	0.5/34.5	0.01/87	0.01/87	0.01/87	0.01/88
Υ_{max}	0.068	0.0028	0.0028	0.0028	0.0031
Luminosity [10^{34} cm^{-2}s^{-1}]	2.7	140	140	140	153
AC Site Power [MW]	111	$\sim$135	$\sim$105	$\sim$95	$\sim$ 250

[1] ReLiC based on current “conventional" Nb SW SCRF technology [512]. Cryogenics system: 80 MW, damping rings: 70 MW + others

[2] ReLiC based on Nb SW SCRF technology, but COP of 2 K LiHe refrigerators improved 2-fold. Cryogenics system: 45 MW, damping rings: 70 MW + others

[3] ReLiC based on futuristic SCRF technology for Nb3Sn SW cavity with $Q_0 = 4E10$.
250GeV: Cryogenics system: 35 MW, damping rings: 70 MW;
500GeV: Cryogenics system: 95 MW, damping rings: 140 MW

linacs by $\sim$6 %. While Table 1 shows case for c.m. energy of 250 GeV and 500 GeV, ReLiC would provide luminosity above 10^{36} cm^{-2}s^{-1}in polarized beam collision for large range of c.m. energies from 45 GeV to 700 GeV. Fig. 59 shows our estimations for luminosity and AC power consumption.

The fact that ReLiC can operate with a single cavity is important advantage of this upgrade option making it cost effective. Doubling the number of linac cavities, in the manner similar to ERLC, would allow to eliminate separators [509], reduce collider length by $\sim$6 % while doubling cryo-plant power and cost of the linac.

For power estimation we assumed that electron and positron beams circulate in damping rings for two emittance damping time (i.e. will lose energy equal to two of that of the damping ring). Such operation will provide for 7.4-fold reduction of transverse emittances and 54.6-fold reduction of the longitudinal emittance growths accumulated during each collision pass. Our simulations [511] indicated that head-on collisions with vertical disruption parameters below 150 results in less than factor 2 of vertical emittance growth, which could require only a single damping time if the orbit feedback system will maintain nearly head-on collisions.

Possible issues for ReLiC upgrade

1. ReLiC designs do not require a large crossing angle as in the ILC design. Since energy recovery requires returning beams into the opposite linac for deceleration, the beam's trajectory should be bent. Such bending and aligning of the beam's trajectory would result in synchrotron radiation and growth of energy spread and horizontal emittances. In ReLiC case operating at the 500 GeV centre-of-mass collider energy this will result in 15.4 MeV loss of energy with a critical photon energy of 0.7 MeV, and 3.3 MeV growth of the RMS energy spread per pass. This level of energy loss and increase in energy spread is fully acceptable for ReLiC.

2. Strong 2-fold damping in ReLiC system is sufficient to counteract additional contributions of the energy spread and emittance growth resulting from synchrotron radiation and intra-beam scattering. Still,

self-consistent simulations are required to establish loss level caused by beamstrahlung, Touschek scattering, scattering on residual gas and particle burn-off in collisions.

Time and R&D needed

1. Development of efficient SCRF and cryogenic technology (efficient LiHe refrigerators, development of high Q_0 SCRF cavities, including but not limited to Nb3Sn) are critically important for reduction of the energy consumption. While RLC and ReLiC can be build using existing SCRF/cryo technology, power consumption could be close to 500 MW for 500 GeV collider.

2. Demonstration of flat beams with 2,000 to 4,000 emittance ratios.

3. High rep-rate and accurate kickers

4. Start-to-end simulations of the beam and spin dynamics.

ERLC

Basic idea The idea of ERLC (Energy Recovery Linear Collider) has been proposed by V. Telnov[513]. Fig. 60 shows the concept of ERLC. In the steady state the positron beam goes as follows. It is accelerated in the linac (a) and, after collision with the electron beam, it is decelerated in the linac (b) down to about 5 GeV. After the bunch length is decompressed in (c), the beam looses about 25 MeV of energy in the wiggler section (d). Then the beam is compressed in (e) and again accelerated in (a).

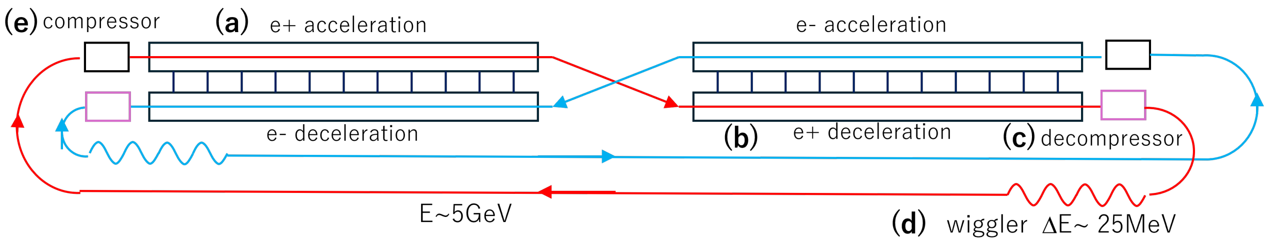

Figure 60: Schematic plot showing the concept of ERLC. Some systems such as injectors, beam dumps, etc. are omitted for simplicity.

During deceleration the electro-magnetic field generated by the positron beam is transferred to the electron linac running in parallel and accelerates the electron beam. Thus, the two linacs are connected electro-magnetically by twin-axis cavities.

The beam-beam collision at the IP (Interaction Point) is not as strong as in linear colliders like the ILC, but is quite moderate so that the beam quality is restored by the weak synchrotron radiation in the wiggler section. The whole system works like circular colliders rather than linear colliders.

Optimization From the beam dynamics point of view the following three issues must be considered:

1. The beam-beam tune-shift limit must be obeyed as in circular colliders.
2. The average energy spread coming from the turn-by-turn effects of the beamstrahlung must be taken into account.
3. The low energy tail of the beam due to the high energy tail of the single beamstrahlung demands large energy acceptance of the beam line. The beam life time is limited by this effect. The bunchlength compressor/decompressor are required to relax the third point.

The AC power consumption is dominated by the two effects, i.e., RF losses in the cavities and the HOM (Higher Order Modes). The RF loss is proportional to $GE/[(r/Q)Q_0]$ where E is the collision energy, G the accelerating gradient, (r/Q) is the R/Q per unit length and Q_0 is the cavity parameter. This is independent of the beam current. To compensate for this heating the efficiency of the cryogenics system (COP) is important.

The beam energy loss by HOM is proportional to $N\langle I\rangle(E/G)/a^2$, where N is the number of particles per bunch, $\langle I\rangle$ is the average beam current and a the aperture radius of the cavity. The HOM loss itself must be compensated by RF but a larger power consumption comes from the heat load, in particular the HOM component lost in the low (helium) temperature region. The design of the cavity and cavity module is important.

Thus, the sum of the powers of these two must be optimized.

Twin-Axis Cavity In this ERLC scheme "Twin-Axis Cavity" is indispensable, since the beam to be accelerated and the beam to be decelerated are running along opposite directions. Such cavities have already been proposed and some experiments are going on.

On the other hand, as an improvement of ILC accelerating cavity, a new idea called HELEN [22, 23] has been proposed. Standing Wave (SW), like the RF wave in ILC, consists of two travelling wave (TW) travelling in opposite direction. Only the TW travelling along the direction of the beam contributes to the acceleration. In the HELEN cavity a wave guide is attached such that only the TW to the 'right' direction goes through the waveguide and returns to the input port. In this way the maximum surface field and the RF heat loss is reduced if the accelerating gradient is the same. In principle the accelerating gradient can be increased if it is limited by the maximum field.

Starting from this idea a new type of twin axis cavity has been proposed [514],where the waveguide in the HELEN scheme is replaced with another cavity which decelerates the beam going to the left (see Fig. 61).

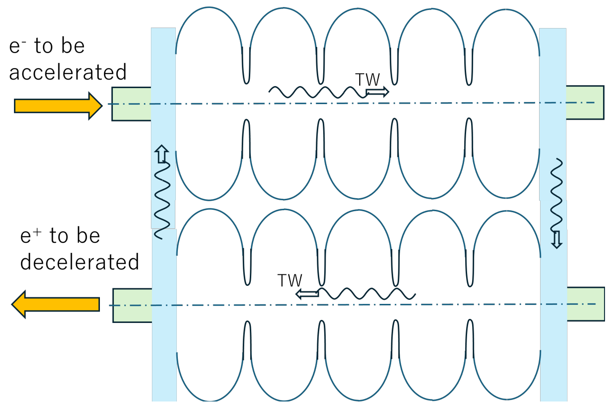

Figure 61: Concept of the twin axis cavity of TW type. There exists TW only in the clockwise direction in this figure. The upper cavity accelerates the electron beam going to the right and the lower cavity decelerates the positron beam going to the left.

An optimization of the HELEN cavity is described in [459]. It aims at an accelerating gradient as high as possible and, therefore, adoped the iris diameter 50 mm, narrower than 70 mm in ILC. For our purpose, however, 70 mm is appropriate for lower HOM generation and presumably easier absorption. The shunt impedance in Tab. 20 is taken from [459].

Issues as an ILC Upgrade The original idea of ERLC was proposed independently from the existing linear collider plans such as ILC. Once it is considered as an upgrade of a linear collider like ILC, several practical problems must be taken into account. An obvious problem is whether the Twin Axis Cavity can be accommodated in the tunnel. Here, we have to assume yes. Detailed design of the cavity and cryo-module and consideration of civil engineering are required.

Another problem is the emittance preservation. As is mentioned in Fig. 60 the 5 GeV beam looses 25 MeV in the wigglers. This means the transverse damping time is $\sim$ 400 turns. ILC assumes the vertical emittance increase of O(10nm) in the single pass from the damping ring to the IP. ERLC systtem would not work if this increase be accumulated over 400 turns, but the major part of this increase will be coherent turn by turn. On the other hand, the effects of the synchrotron radiation will certainly be accumulated. There are several places in the ILC such as the doglegs in the bunch compressor and the final focus system. To upgrade the ILC to ERLC the beam after IP (crossing angle 14 mrad) must be bent back to the main linac tunnel. A rough evaluation shows this is marginal for E_{CM} = 500 GeV. (The energy loss must also be taken into account as a source of total power consumption.) If this is severe, it is possible to shorten the damping time to $\sim$ 200 turns and/or increase the horizontal design emittance by factor of 2, for example.

Possible Parameters The first issue for the choice of the parameters is the choice of the available technology: Nb or Nb_3Sn, Q, cavity type (SW or TW), etc. Here, we choose the most demanding technology, TW twin-axis, Nb_3Sn cavity. Some tentative parameter sets for ERLC are shown in Table.20, which shows the parameter sets for E_{CM} = 250 and 500 GeV with ILC 250 for comparison. [513] suggests an advantage of a frequency of 650 MHz over 1.3 GHz, but here we adopt 1.3 GHz because twin-axis cavities for 650 MHz may not be accommodated in the ILC tunnel.

The accelerating gradient is chosen here so as to accommodate the linacs in the ILC tunnel of the same energy, taking into account the possible space for HOM absorption.

In this table CW operation is assumed. Reference [513] discusses the possibility of pulsed operation (duty cycle operation). It allows more flexible choice of parameters. For the case $Q_0 = 1 \times 10^{10}$ the luminosity would be some 60% of the CW luminosity with the same AC power.

Table 20: Tentative Parameters of ERLC for E_{CM} =250 and 500 GeV

	ILC	ERLC	ERLC	
centre-of-mass energy	250	250	500	GeV
Accelerating gradient	31.5	40	40	MV/m
Cavity Q_0	1	3	3	$\times 10^{10}$
Aperture radius	35	35	35	mm
Shunt impedance per unit length	996	1690	1690	Ohm/m
Operating temperature	2	4.5	4.5	K
Bunch population	2	0.075	0.081	$\times 10^{10}$
Bunch distance	166	0.23	0.23	m
Average beam current	0.021	157	169	mA
Beam energy in the return line		5	5	GeV
Total HOM power	0.014	2.9	5.85	MW
Energy acceptance of the return line		3	3	%
Radiation loss in the wiggler		25	25	MeV
Bunch length in main linac and IP	0.3	0.31	0.89	mm
Normalized emittance at IP (x/y)	5/35	10/35	10/35	μm / nm
Beta function at IP(x/y)	13/0.41	12/0.31	40/0.89	mm
Beam size at IP(x/y)	515/7.66	700/6.2	900/7.4	nm
Disruption parameter (x/y)	0.5/34.5	0.011/1.14	0.010/1.14	
Beam-beam tune shift (x/y)		0.033/0.097	0.036/0.098	
Upsilon (max)	0.068	0.00182	0.00106	
Luminosity	1.35	135	102	10^{34}/cm^2/s
AC power for RF heat cooling	5	91	181	MW
AC power for HOM cooling	1	35	71	MW
Total site power	111	170	320	MW

Timeline and R&D needed

There are several R&D issues.

1. Development of the twin axis cavity of SW or TW type is the key. TW type is desired (higher shunt impedance and lower surface field). The first step is the HELEN cavity, which may need more than 5-10 years. Obviously, the TW twin axis cavity requires a higher level of R&D. It is difficult to estimate the required R&D time. The structure fabrication is more complex.The surface polishing method must be developed. The tuning of the two cavities can be a serious problem. Possible trapped modes must be examined. Transverse deflection of the beam must also be investigated since the cavity is quite asymmetric and the beam current is very high.
2. Development of the cavity material, in particular Nb_3Sn which can be operated at 4.5 K. A high Q_0 value $\gtrsim 3 \times 10^{10}$ is desired.

3. HOM absorber/damper. As is seen in the table the HOM loss per unit length is a little higher than in the latest designs of ERL for light sources (the bunch charge and the average current). Tab. 20 assumes 1% of the HOM power is deposited in the helium temperature region.
4. High efficiency cryogenics system. Tab. 20 assumes COP 230 at 4.5K.
5. Beam dynamics issues
   - Vertical emittance increase in the main linac
   - Horizantal emittance increase due to symchrotron radiation in various parts, in particular the beding section after IP.
   - Background in the BDS section (the average beam current is 4 orders of magnirtude higher than in ILC.)

The items (2) to (4) are more or less common to energy recovery colliders.

Acknowledgement
This section on ERLC has been written after discussions with V. Telnov.

4.6 Running and Upgrade scenarios for an initial machine based on SCRF

The technologies discussed in Sections 4.1 and 4.2 enable us to pursue a comprehensive program to study the Higgs boson and its closest relatives in the SM today. At the same time, the energy and luminosity upgrade options discussed in the previous sections provide attractive long-term visions for a linear collider facility.

Figure 62 illustrates some of the possible choices. The instantaneous luminosities follow those for the LCF in Fig. 1(a) up to 550 GeV, and for C^3 above that energy. After each major change to the accelerator, a ramp-up of efficiency is assumed following the prescription developed in [34]. Figures 62(a) and 62(b) cover the integrated luminosities given in the first four columns of Table 3, corresponding to the Higgs coupling results in the third column of Table 9, differing by the initial luminosity (at low power (1312 bunches per train) or directly at full power (2625 bunches per train)). Figures 62(e) and 62(f) cover all stages given in 3, corresponding to the forth column of Table 9, differing in when a new technology would be decision- and production-ready. In the case that scientific competition makes a start at 550 GeV desirable, it would still be possible to collect (polarised) data lower energies later in the program if science requires (Fig. 62(c), or to directly upgrade the facility for exploring the 1 –3 TeV regime.

Many other choices are possible. We'd like to re-emphasize that one of the central advantages of a linear collider facility is that the upgrade path remains flexible, and should be chosen according to scientific and technological advances or even revolutions.

4.7 Alternative collider modes

A collider based on the Compton backscattering of laser light off colliding high-energy electron beams provides $\gamma\gamma$, $e^-\gamma$, and e^-e^- collisions with centre-of-mass energies up to the highest e^+e^- $\sqrt{s}$ at comparable luminosities. Such a collider nicely complements the e^+e^- physics program and is a natural fit for the second IP of the LCF.

Three $\gamma\gamma$ collider designs are considered:

1. SCRF accelerator + 1.2 eV optical laser
2. SCRF accelerator + 1.0 keV XFEL
3. C3 accelerator + 1.0 keV XFEL

Design (1) is well developed and was seriously considered for the second interaction region of the ILC before the second interaction region was dropped to save money. The XFEL laser in designs (2) and (3) leads to a greater physics reach, but significant R&D on the production and focusing of $\sim$ Joule per pulse XFEL light is required, among other issues. Design (3) has been included mainly because a parameter set for design (2) is not yet ready and all the existing literature on XFEL Compton colliders [31, 515, 516] assumes a C3

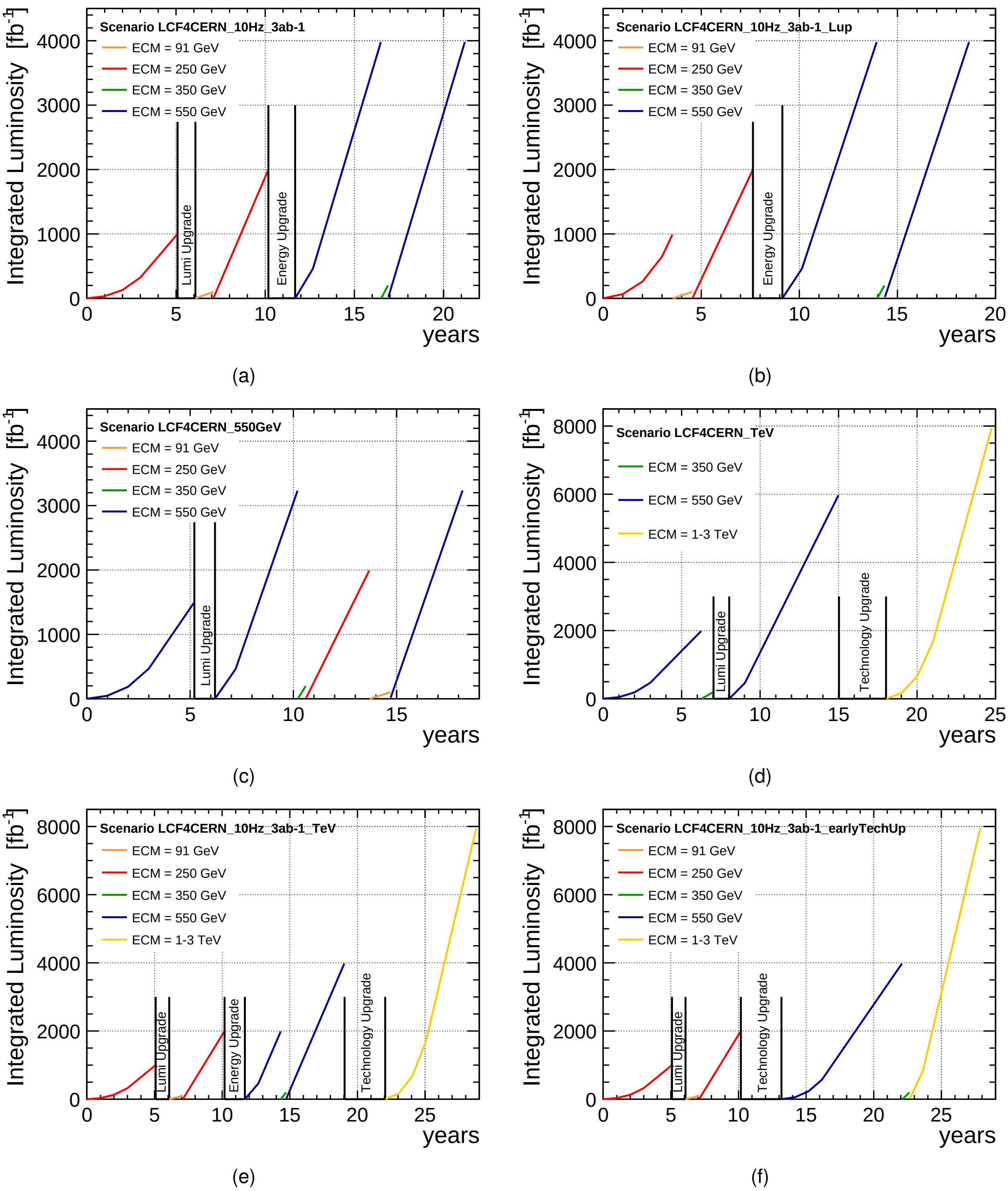

Figure 62: Various examples of operation and upgrade scenarios for a Linear Collider Facility, all starting with a SCRF-based machine, labelled LCF in Fig. 1(a). (a) starting at 250 GeV, low power and upgrade to full power and then to 550 GeV; (b) starting directly with full power at 250 GeV and then upgrading to 550 GeV; (c) start at 550 GeV, taking smaller sets of polarised data at lower energies later; (d) starting at 550 GeV and upgrading to 1 TeV or beyond; (e) like (a), but with a shortened run at 550 GeV in favour of an earlier upgrade to 1 TeV or beyond; (f) starting at 250 GeV, but then changing technology already for 550 GeV (here assuming C^3 parameters).

Final Focus parameters	SCRF + Optical Laser	C3 + XFEL
Electron energy [GeV]	108	62.8
Electron beam power [MW]	4.5	1.2
β_x/β_y [mm]	1.5/0.3	0.03/0.03
$\gamma\varepsilon_x/\gamma\varepsilon_y$ [nm]	2500/30	120/120
σ_x/σ_y at e^-e^- IP [nm]	133/6.5	5.4/5.4
σ_z [μm]	300	20
Bunch charge [$10^{10} e^-$]	2	0.62
Bunches/train at IP	2625	165
Train Rep. Rate at IP [Hz]	5	120
Bunch spacing at IP [ns]	366	4.2
σ_x/σ_y at IPC [nm]	266/56.7	12.1/12.1
$\mathscr{L}_{\text{geometric}}$ [$10^{34}\text{cm}^2\ \text{s}^{-1}$]	4.8	21
δ_E/E [%]		0.1
L^* (QD0 exit to e^-e^- IP) [m]	3.8	1.5 or 3.0
d_{cp} (IPC to IP) [μm]	2600	60
crossing angle [mrad]	20	2 or 20

Table 21: e^- beam parameters for $\gamma\gamma$ collider with peak luminosity at $\sqrt{s} \approx 125$ GeV

Laser parameters	SCRF + Optical Laser	C3 + XFEL
Electron energy [GeV]	n.a.	31
Normalized emittance [nm]	n.a.	120
RMS energy spread $\langle\Delta\gamma/\gamma\rangle$ [%]	n.a.	0.05
Bunch charge [nC]	n.a.	1
Undulator B field [T]	n.a.	$\gtrsim 1$
Undulator period λ_u [cm]	n.a.	9
Average β function [m]	n.a.	12
photon λ (energy) [nm (keV)]	1056 (0.0012)	1.2 (1.0)
photon pulse energy [J]	2.4	0.7
rms pulse length [μm]	450	20
$a_{\gamma x}/a_{\gamma y}$ (x/y waist) [nm]	5000/5000	21/21
non-linear QED ξ^2	0.21	0.10

Table 22: Laser parameters for $\gamma\gamma$ collider with peak luminosity at $\sqrt{s} \approx 125$ GeV

accelerator. However, it may not be out of the question to consider an independent pair of C3 linacs at the LCF given the relatively short length involved (4 km total for up to $\sqrt{s} = 380$ GeV) and the potential practical advantages of using two separate pairs of linacs for two very different applications.

The electron beam parameters for a $\gamma\gamma$ collider with peak luminosity at $\sqrt{s} \approx 125$ GeV are given in Table 21, and the laser parameters are shown in Table 22.The luminosity spectra for different colliding particle species for a $\gamma\gamma$ collider with peak luminosity at $\sqrt{s} \approx 125$ GeV are shown in Fig. 63.

The electron beam parameters for a $\gamma\gamma$ collider with peak luminosity at $\sqrt{s} \approx 380$ GeV are given in Table 23, and the laser parameters are shown in Table 24. The luminosity spectra for different colliding particle species for a $\gamma\gamma$ collider with peak luminosity at $\sqrt{s} \approx 380$ GeV are shown in Fig. 64.

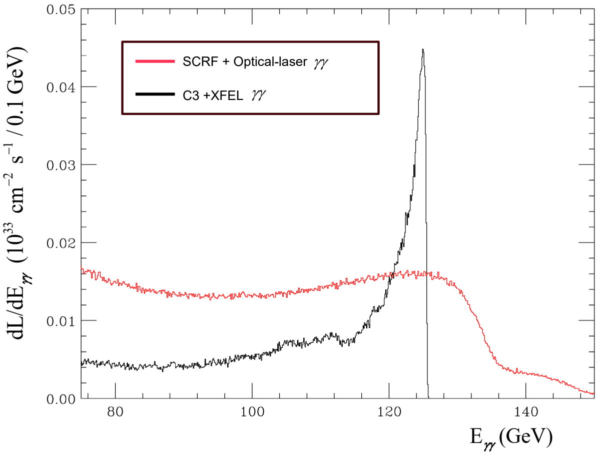

(a)

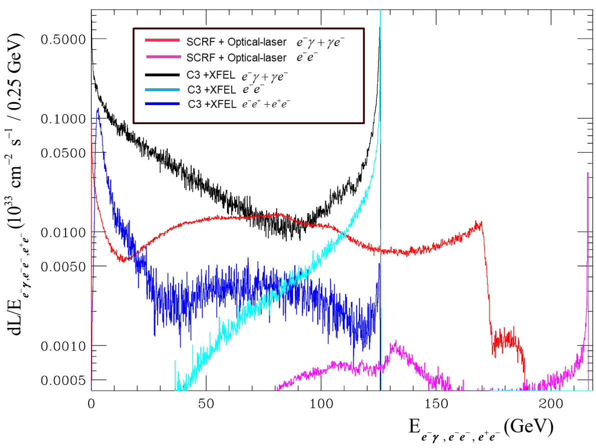

(b)

Figure 63: $\sqrt{s} \approx 125$ GeV $\gamma\gamma$ collider luminosity spectra for (a) $\gamma\gamma$ collisions and (b) $e^-\gamma$, e^-e^-, and e^+e^- collisions.

Final Focus parameters	SCRF + Optical Laser	C3 + XFEL
Electron energy [GeV]	250	190
Electron beam power [MW]	10.5	2.1
β_x/β_y [mm]	1.5/0.3	0.01/0.01
$\gamma\varepsilon_x/\gamma\varepsilon_y$ [nm]	2500/30	60/60
σ_x/σ_y at e^-e^- IP [nm]	88/4.3	1.3/1.3
σ_z [μm]	300	10
Bunch charge [$10^{10}e^-$]	2	0.62
Bunches/train at IP	2625	93
Train Rep. Rate at IP [Hz]	5	120
Bunch spacing at IP [ns]	366	5.2
σ_x/σ_y at IPC [nm]	176/37.5	5,2/5.2
$\mathscr{L}_{\text{geometric}}$ [$10^{34}\text{cm}^2\ \text{s}^{-1}$]	12	180
δ_E/E [%]		0.1
L^* (QD0 exit to e^-e^- IP) [m]	3.8	1.5 or 3.0
d_{cp} (IPC to IP) [μm]	2600	40
crossing angle [mrad]	20	2 or 20

Table 23: e^- beam parameters for $\gamma\gamma$ collider with peak luminosity at $\sqrt{s} \approx 380$ GeV

5 Beyond-Collider Facilities

One purpose of the Linear Collider Vision is to plan for a facility that exploits all aspects of it as well as possible and fully integrates facilities that are not directly related to the collider physics program. The beyond-collider physics topics are discussed in Sec. 3.9. In this section, the facilities required at the beam dumps to investigate beyond-collider physics and for neutron and muon facilities are described in Sec. 5.1. In Sec. 5.2, we elaborate on the possible integration of a plasma-wakefield accelerator R&D facility.

5.1 Beam Dump Facilities

A key difference of a linear collider facility compared to a circular collider is the continuous dumping of the electron and positron beams in the main beam dumps. In addition, other dumps, such as the tune-up dumps, are installed in the collider complex for setup and commissioning. The locations of the various beam dumps and the power they are designed to absorb are indicated in Fig. 65 for the example of the ILC [14]. In the

Laser parameters	SCRF + Optical Laser	C3 + XFEL
Electron energy [GeV]	n.a.	31
Normalized emittance [nm]	n.a.	60
RMS energy spread $\langle \Delta\gamma/\gamma \rangle$ [%]	n.a.	0.05
Bunch charge [nC]	n.a.	1
Undulator B field [T]	n.a.	-
Undulator period λ_u [cm]	n.a.	-
Average β function [m]	n.a.	-
photon λ (energy) [nm (keV)]	1056 (0.0012)	2.5 (0.05)
photon pulse energy [J]	2.4	1.0
rms pulse length [μm]	450	20
$a_{\gamma x}/a_{\gamma y}$ (x/y waist) [nm]	5000/5000	21/21
non-linear QED ξ^2	0.21	1.1

Table 24: Laser parameters for $\gamma\gamma$ collider with peak luminosity at $\sqrt{s} \approx 380$ GeV

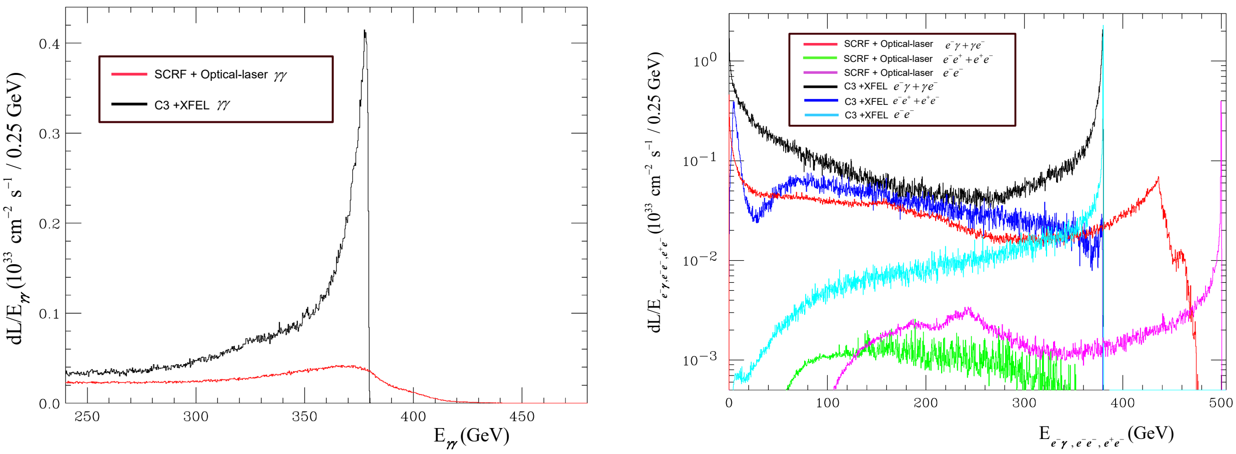

(a) (b)

Figure 64: $\sqrt{s} \approx 380$ GeV $\gamma\gamma$ collider luminosity spectra for (a) $\gamma\gamma$ collisions and (b) $e^-\gamma$, e^-e^-, and e^+e^- collisions.

following, we elaborate on the facilities that could be built to use them for additional functions and provide some preliminary assessments of the requirements.

5.1.1 Main Beam Dump Facility

For the main beam dump experiments, a long muon shield is required to reduce the secondary muon backgrounds. In previous studies, a muon shield of length $l_{sh} = 70$ m is assumed [393, 395]. The muons penetrating behind the shield cannot be neglected for $E_{beam} = 500$ GeV at LC-1000. After the muon shield, a decay volume of comparable length and a downstream detector would be placed.

Neutrino interactions near the end of the muon shied induce additional background. High-energy neutrinos can produce neutral hadrons, such as $K_{S,L}$ decaying to charged pions. A multi-layer tracker may be placed in the decay volume to veto them. This type of background has been estimated with GEANT 4 in the SHiP setup [517, 518]. They found that the relevant hadrons are always produced at the edge of the muon shield and can be significantly reduced by requiring charged tracks consistent with the HNL kinematics.

The background in the LC beam dump experiments can be inferred by comparing the number of produced neutrinos with SHiP. The SHiP experiment expects 7×10^{17} neutrinos per 2×10^{20} protons on target. Many of the background events with charged tracks can be reduced by simple topological cuts. At a beam energy of 125 GeV (500 GeV), we estimate 8×10^{15} (3×10^{16}) neutrinos for $N_{EOT} = 4 \times 10^{21}$ electrons on target. At the

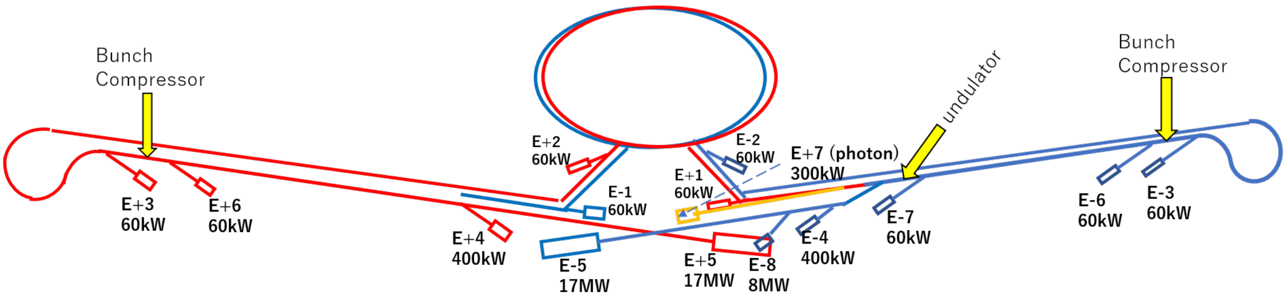

Figure 65: The layout of the ILC and its beam dumps [14]. The main beam dumps (E-5 for the electrons and E+5 for the positrons) are designed to absorb 17 MW each, The tune-up dumps (E-4 and E+4) for 0.4 MW each. For a Linear Collider Facility with two interaction points, c.f. Sec. 4.3, the arrangement of beam dump facilities still needs to be optimised.

LCF operated at an e^+e^- centre-of-mass energy of 250 GeV with 1312 bunches per train, $N_{\mathrm{EOT}} = 4 \times 10^{21}$ would be collected in about 1.2 years, at the ILC in about 2.5 years. Similar reduction factors using the topology cuts are assumed in [398].

The active veto system of SHiP reduces the muons pointing to the decay volume by a magnet, thereby reducing the neutrino background further by a factor of $O(10^{-4})$. Given the high neutrino flux, such an option may be considered for the LC beam dump experiments.

The location of the beam dump in the ILC design, with its 14 mrad crossing angle, is about 300 m away from the IP, where the transverse separation between the incoming and outgoing beams is roughly 4 m. In case one of the LCF IPs has a small crossing angle of e.g. 2 mrad, a location 2 km from the IP would be needed to provide the same separation, which we consider close to the minimum required to install an experiment. Integrating a beam dump detector into the LC accelerator would require careful consideration by accelerator and experimental physicists. If the second IP has a larger crossing angle of e.g. 20 mrad, a reasonable transverse separation can be achieved in a much shorter distance, constraints are much less severe, and the experimental site can be planned independently of the main accelerator system. Since it is planned to share the luminosity equally between the two IPs, it is advantageous to use the beam dump of the second IP for the beam dump facilities.

5.1.2 Neutron and Muon Facilities

At the main dump of the linear collider facility, a high number of high-energy neutrons and muons are produced. They can be used for auxiliary purposes such as irradiation tests of integrated circuits or to produce radionuclides as described in the following. In both cases, remote access and changes of the devices under test in the radiation cavern must be possible during beam operation. Furthermore, the facility must be large enough to accommodate entire devices, which will require a meter-sized cavern.

Irradiation Facility Our daily lives increasingly depend on larger integrated circuits with ever-smaller transistor structures. The demand for verifying their reliability grows. One possible source of malfunctions are soft errors induced by cosmic neutrons and muons [519]. They can induce a change of state (a bit flip) that can be reset by a power cycle (a cold reboot). In a soft error, the device itself is not damaged, but only the data on it. Assessing the soft error rate of an entire circuit requires a high-intensity radiation field with an atmospheric-like energy spectrum over a large area to irradiate a system as a whole. The vicinity of a linear collider beam dump meets all these requirements [520]. Other irradiation facilities exist, e.g. at RCNP in Osaka (Japan) or at TRIUMF in Vancouver (Canada). However, they can only provide neutrons with energy up to a few hundred MeV in small irradiation areas.

Neutrons and muons have different production characteristics in a beam dump as shown in Fig. 66. The neutrons are mostly produced through photonuclear reactions of the photons from the electromagnetic shower. They are emitted almost isotropically from the dump, with the core of the production being 2-4 m in the beam direction from the beam injection point. Therefore, high-intensity neutrons can be obtained close to the neut-

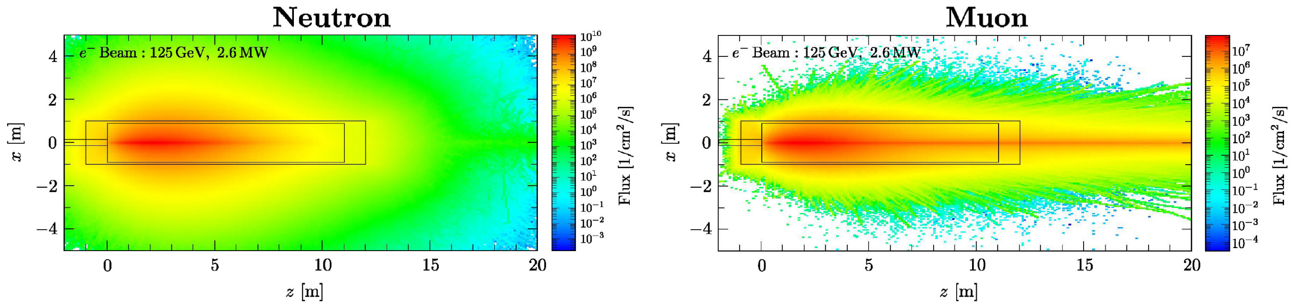

Figure 66: Neutron and muon fluxes around the electron beam dump of an LCF. The water beam dump (inner rectangle) is in a cavern (outer rectangle) which is surrounded by a uniform concrete shield. Figure from [520].

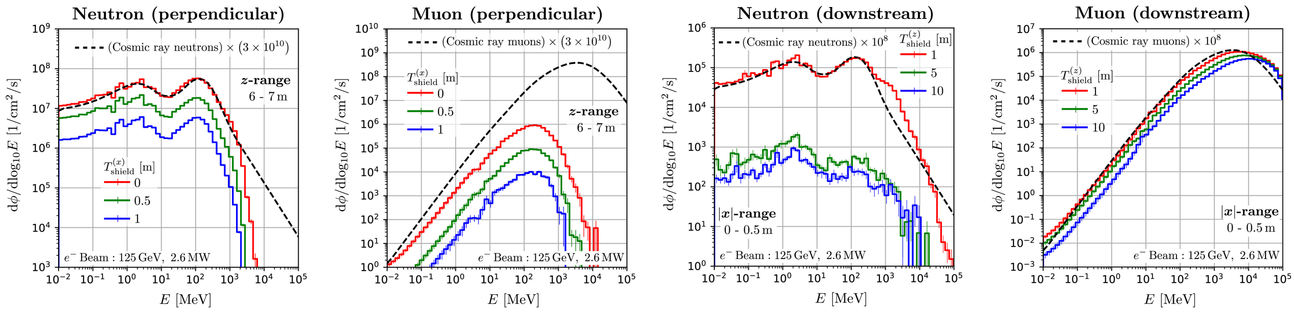

(a) (b)

Figure 67: Energy distribution of neutrons and muons for various concrete shield thicknesses (colors) and in comparison to cosmic rays (dashed line). (a) Spectra on the side of the dump at $z = 6-7$ m. (b) Spectra downstream of the beam dump at $|x| \leq 0.5$ m.

ron emission region on the side of the beam dump. The muons are mainly produced by pair production from bremsstrahlung and tend to be scattered in the beam direction.

As described in [520], there are two possible locations for the irradiation facilities at the beam dump of a linear collider. A cavern on the side of the dump at $z = 6-7$ m is mainly suitable for neutron irradiation. The neutron spectrum is atmospheric-like up to an energy of about 2 GeV with a flux more than a factor 10^{10} higher than cosmic rays at sea level. The muon flux in this area is much lower and can be further reduced by increasing the thickness of the concrete shield between the dump and the irradiation cavern. A cavern downstream of the dump on-axis is well suited for a combined neutron and muon irradiation facility. With a concrete shielding of the order of 1 m, both spectra are atmospheric-like but with a flux higher by a factor of 10^8. Since the shield thickness has almost no effect on the muons, but reduces the neutron flux significantly, a thicker concrete shield can be used if only muons are desired for the irradiation facility. The neutron and muon energy spectra for both locations are shown in Fig. 67.

Facility for Radionuclide Production Radionuclides or radioactive isotopes find applications in many fields such as nuclear physics, but most notably in nuclear medicine for diagnosis, treatment, and research. These are primarily produced through the exposure of stable targets to neutrons or charged particles. The result of such irradiation is an activated target material that has to undergo further processing to be usable. As part of the PRISMAP project network, European facilities provide a wide variety of radionuclides for medical research [521].

As described above, the beam dump of a linear collider facility can provide a high flux of high-energy neutrons that can possibly also be used for radionuclide production. Furthermore, a study for the ILC showed that the photon dump after the undulator for positron generation (E+7) could also be used, especially for ^{99}Mo production [522]. The detailed potential and competitiveness must be studied with a suitable tool such as ActiWiz [523].

5.1.3 Tune-Up Dump Facility

One suitable location for beyond-collider experiments is in the area of the tune-up dump. This section of the linear collider facility is after the linear accelerator and before the beam delivery system. Therefore, the maximum beam energy is available. When the accelerator is commissioned, the beam is guided to the tune-up dump to protect the rest of the facility. However, while the main physics program is running, it can be used to extract single bunches from the bunch trains. This facility could be used for thin-target beam dump searches as described in the following, but also for tests of strong-field QED (Sec. 3.9.2), plasma-wakefield acceleration R&D (Sec. 5.2), and others. The size of the facility may vary depending on the usage, and the details have to be worked out. For strong-field QED experiments, an energy spectrometer is needed which leads to a length requirement of about 100 m for the maximum energy of 1 TeV after the upgrade. For plasma-wakefield acceleration R&D at 100 GeV, this requirement may increase by a factor of ten.

Slow Extraction For many applications, having a low bunch charge even down to quasi-single electrons has advantages. Two examples are fixed-target experiments with a thin target and strong-field QED experiments with electron-laser collisions. The former allows access to bigger couplings in new-physics searches since these particles do not decay within the target and can therefore be detected, due to the short target length. This option was studied for the linear accelerator facility at KEK [524]. The latter allows for studying the elementary electron-photon interaction in a strong field and coherent electron-positron plasma creation, as described in more detail in Sec. 3.9.2.

Slow extraction usually refers to the gradual extraction of particles in a circulating beam. At a linear collider facility, the problem is more delicate due to the different bunch structure. However, similar approaches can be applied. One of those is the extraction of particles from the beam halo with the channelling effect in a bent crystal, as successfully demonstrated at CERN's Large Hadron Collider LHC with 6.5 TeV/c protons [525]. This could be done at the location of the tune-up dump, where first a single bunch can first be extracted from each bunch train with the full energy. Afterwards, the crystal can be brought to close proximity of the beam such that the desired number of particles can be extracted. The rate can be tuned by the distance from the crystal to the beam. Depending on the charge of the particle, different orientations of the crystal planes are advantageous. For energy of 120 GeV, deflections of $100-150$ μrad are possible for electrons and positrons with axial channelling and even more in the case of planar channelling of positrons [526, 527].

Laser Facility To test the fundamental physics of the strong-field QED described in Sec. 3.9.2, a high-power laser is required. Usually, laser facilities are built above ground, and the laser pulse is guided through a laser beam pipe to the electron-laser interaction point.

Nowadays, systems with 200 TW peak power can be bought off the shelf and have a small, container-sized footprint of approximately 4×4 m^2 [528]. They can deliver a pulse energy of about 5 J which, depending on the waist at the beam focus, leads to an intensity parameter of $\xi \approx 20$. The laser systems with the highest intensities currently available have a peak power of 10 PW and can reach intensity parameters of $\xi \gtrsim 200$ [529, 530]. However, they require hall-sized clean rooms of roughly 20×50 m^2.

5.2 Plasma-Wakefield Accelerator R&D Facility

Plasma-wakefield acceleration (PWA) shows considerable promise for the future of high-energy physics because it can provide exceptionally high acceleration gradients and focusing capabilities [531]. Also within the framework of the linear collider vision, it is considered one of the main upgrade options for the future energy upgrade of the collider as described in Sec. 4.4. The higher acceleration gradient compared to classic acceleration with superconducting cavities leads to a reduction in accelerator length.

In a PWA, a driver is shot into a plasma, creating a wakefield that can be used to transfer the energy of the driver into a witness bunch of charged particles. There are three options for the driver, namely a laser, a proton, or an electron pulse. For the applicability of this new technology to a high-energy electron-positron collider, only electrons are currently suitable as a driver. So far, lasers are not efficient enough and protons cannot be provided at high enough rates to be feasible.

For electron-driven plasma-wakefield acceleration, one of the major problems today is staging [532]. Since a single cell offers only limited capability of transfering energy into the witness bunch, many shorter acceleration cells have to be added/staged together. This issue is being addressed and will probably be solved by the time a linear collider facility is built. However, other challenges may persist and need to be overcome before a collider can be upgraded to PWA technology. They may include the acceleration of positrons [533] and the achievement of the required high beam currents to reach the luminosity goals [534].

A linear collider facility offers various options for the R&D of electron-driven PWA. For many applications, a low-energy beam is sufficient and easier to handle. Therefore, the beam before the bunch compressor with an energy of about 5 GeV could be used. In the layout of the linear collider facility, an extraction beamline with a low-power beam dump is planned (called E-3 in the ILC design). This cavern could be enlarged to host a facility for the PWA R&D. A tunnel with a length of a few hundred meters is required. For applications requiring high-energy, the beam after the full accelerator is needed. A possible location is the area of the tune-up dump (E-4). Since the length of a PWA facility scales roughly with $\sqrt{E}$, a km-long complex would be necessary. Such a beam could also be used for high-field QED experimentation, c.f. Sec. 3.9.2.

6 Detectors - Opportunities for the community

Detectors at a collider are an integral part of the facility, and need to be part of the planning the development from its very early stages. The detectors should be able to extract science as efficiently and as easily as possible from the enormous amounts of data produced by these facilities. They rely on technologies which in many case go well beyond currently established boundaries, and utilise advanced concepts and methodologies to handle, curate and eventually use the data. They need to be tightly integrated into the design of the accelerator, and in particular, with the needs of the collider in the immediate area of the interaction region.

Detectors at a linear collider need to be optimized towards the particular environment of the linear colliders. These facilities operate in a pulsed mode, at very high energies, but in a relatively background free environment. The intrinsically clean events, the absence of very large hadronic backgrounds, offer a great opportunity to the community to concentrate on the development of technologies which stress precision, and an as complete as possible feature extraction from the collisions. These detectors thus are not only very powerful detectors for the science at a linear collider facility, but also platforms to develop and proof cutting edge detector technologies.

6.1 Achievements

Ideas for the construction of a linear collider and their associated detectors have been around for a very long time. The first workshop for a Japan Linear Collider (JLC) took place in 1989 and a zeroth-order design report for a next linear collider (NLC) at SLAC was published in 1996. A conceptual design report of a superconducting linear accelerator (TESLA) was published in 1997 [535]. Concurrent with the development of the accelerator design, new detector technologies were proposed for the experiments at these new facilities. In November 2003 an International Technology Recommendation Panel was formed to decide on the accelerator technology for a future linear collider. This was followed in 2005 by the formation of the Global Design Effort by an international team of physicists to develop the Technical Design for a linear collider based on SCRF with their associated detectors. A global effort emerged for the development of new technologies for a linear collider detector, building on the strong foundation laid by the NLC, the JLC and the TESLA efforts.

In 2003 and following the proposal of the TESLA accelerator a number of R&D collaborations formed, with the goal to advance the state of detector technologies to be used in any linear collider. The collaborations were organised under the auspices of ECFA, but were drawing on a fully international membership and participation.

The CALICE (Calorimeter for Linear Collider Experiment) collaboration has pursued a broad spectrum of novel calorimeter technologies to address the critical issue of jet energy resolution to discriminate between W and Z-bosons in the jet final state for an ILC. A focus of the collaboration has been the study of particle flow, where the combined tracker and calorimeter is used to identify charged and electromagnetic particles in a hadronic shower and the calorimeter is used to match energy deposits with each track and the remaining energy is associated with neutrals. To achieve the best energy resolution, a very fine grained readout was required. The collaboration has pioneered the silicon-tungsten and SiPM-on-tile calorimeter and demonstrated that is was a viable technology. The concept has been adopted for the HL-LHC upgrade of the CMS experiment where the technology is being implemented in the High-Grained Endcap Calorimeter. The technology is currently also being implemented for the forward hadron calorimeter of the ePIC detector for the EIC. The silicon-tungsten calorimeter design has also been adopted by the ALICE experiment for the forward calorimeter (FoCal), that will enable a new and unique program at the LHC focused on small-x gluon distributions of hadrons and nuclei. Similar designs are being considered to instrument the forward region for the ePIC detector.

A demonstration of a full digital hadron calorimeter was also demonstrated by the CALICE collaboration. A 1 m^3 digital calorimeter was built, with one million readout channels using iron absorber plates interspersed with RPC readout chambers. The technique was been refined by developing the semi-digital hadronic calorimetry, where the deposits from a hadronic shower are recorded with high granularity with only a coarse energy information (2 - 3 thresholds). Different readout technologies were explored besides RPCs including MICROMEGAS chambers.

The linear collider community has been deeply engaged in the advancement of technologies for tracking detectors with major contributions in three distinct areas. The linear collider TPC (LCTPC) collaboration has explored novel technologies to improve the performance of a TPC. A large prototype TPC was built and tested deploying four different readout technologies. A triple GEM design minimized the inactive area and targeted an improvement in the operational stability of a triple GEM stack. An alternative design was based on a double GEM where the dead area pointing towards the interaction point was minimized. Using thicker GEM stacks that favor higher gas gains, only two GEM chambers were needed. To cover larger areas with fewer and thus larger pads without degrading the performance a new readout concept was developed using a resistive layer on the pads, spreading the narrow charge distribution of a Micromegas gas amplification stage over several pads thus enabling a more precise charge interpolation than otherwise possible. An inverted HV scheme was developed where the amplification mesh was on ground potential and the resistive layer on a positive high voltage. This configuration showed a reduction of field distortions between the modules by one order of magnitude. A fourth technology studied used the GridPix technology. A GridPix uses a highly pixelized readout ASIC. For the linear collider studies the Timepix ASIC was used. The ASIC was covered with a resistive layer to protect it from discharges and a Micromegas was mounted on top using photolithographic post-processing techniques. It was shown that this concept offers the best possible resolution only limited by the diffusion in the drift region. Many of these studies have informed the construction of new TPCs and the development of MPGDs. In particular it is noted that the desing of the new TPC for the ND280 near detector for the T2K experiment was informed by studies within the framework of a linear collider.

The readout of MPGDs was based on the AFTER and ALTRO ASICs. The Alice TPC Readout (ALTRO) chip was an existing chip that was later adapted to the SAMPA chip to read out the ALICE GEM-based upgraded tracker. The AFTER chip, that was heavily exercised during the linear collider studies is currently used in the readout of the ND280 near detector of the T2K experiment.

Given the stringent requirements on the material budget the PLUME (Pixelated Ladder with Ultralow Material Embedding) collaboration advanced the development of low-mass support structures for vertex detectors. In parallel, there was a very strong effort on the development of CMOS sensors for vertex detectors that has resulted in opening a new paradigm for vertex detectors with the introduction of monolithic active pixel sensors (MAPS). The Mimosa series of pixel sensors were candidate sensors for a vertex detector. The telescope for the beam test facility at DESY was equipped with Mimosa sensors under the EUDET program. The linear collider detector R&D program provided a fertile ground for the development of this new technology that is now being implemented at scale in the ALICE experiment. The Chronopixel design was developed to provide for single bunch-crossing time stamping in a CMOS process. These efforts targeted pixel sizes of 20x20 μm^2 or smaller.

One of the first silicon-based pixel detectors that reached very low mass budget by thinning the sensor itself was the DEPFET sensor. This technology provides very high signal-to-noise hits while only requiring 50 μm of silicon per layer in the tracking volume. The device can store signals over the readout cycle. Through very active development as a possible ILC vertex detector, the technology became mature enough to form the basis of the vertex detector for the upgrade of the Belle experiment.

The community has also been at the forefront in developing alternative bonding technologies. With the advent of the through-silicon-via (TSV) technology an intense effort on developing a direct-bond interface techniques was initiated. With this approach, different functionalities of the readout can be separated in different wafers, that then can be thinned resulting in very thin readout addressing the mass budget of vertex detectors. Initial devices have been produced, but given the cost, the early stages of the development of this technology and the promise of MAPS detectors, it never took hold for large-scale implementation. Capacitive coupled pixel detectors in which a sensor is capacitively coupled to the readout through, for example, a glue layer that eliminated bump bonding is another example of an approach pioneered by the linear collider community.

The challenges to instrument the forward detector region are significant in an e^+e^--environment. Novel ideas have been proposed within this community to advance calorimetry forward calorimetry with fast readout in high occupancy and high radiation environments to measure the luminosity. Three-tiered detector systems have been proposed and tested. A Lumi-Cal, covering the region from about 40-140 mrad from the beam axis, would provide a measurement of the luminosity with a precision of 10^{-3} using Bhabha events. A Beam-Cal (5-40 mrad) would be used for beam diagnostics and a Gam-Cal even closer to the beam axis would be used for beam diagnostics using beamstrahlung photons. Sensors studied are PCVD diamond, GaAs and SiC sensors.

The concept of particle flow calorimetry has been a central notion for linear collider detectors. This type of calorimetry fully integrates tracking with calorimetry and requires very high granularity in the calorimeter. If tracking provides the best possible energy or momentum resolution, that measurement is taken and the hits associated with the track in the calorimeter are removed. This has led to designing detectors not as a sum of individual subsystems, but the detector is viewed as a well choreographed integrated system where there is a mutual dependence of the overall performance of the integrated performance of each sub-detector. Optimization of the overall geometry and technologies was emphasized from the inception of a detector concept and is an idea that is now being adopted, where applicable, by other new detector designs.

6.2 Concepts

The linear collider community has developed several integrated detector concepts, adapted to the different linear accelerator options under discussion. ILD, SID and CLICdp [13, 40, 536] have all undergone intense optimization efforts, and have been subjected to a series of international reviews.

These detectors are all conceived as multi-purpose detectors, optimized for precision physics in the area of Higgs and electroweak physics. They should be able to cover a collision energy range from 90 GeV up to several TeV, in the case of the CLICdp, or 1 TeV for a detector at the ILC. Over the course of the development of these systems, the concept of particle flow as a method to optimally reconstruct the event properties has been developed and has been integrated into the detector design for all concepts. Particle flow has profound consequences for the design of the detector, as it stresses the need for high granularity throughout the detector, and in particular in the calorimeter system, and stresses the need for very high reconstruction efficiency in the tracker combined with an excellent capability to link objects in the tracker with objects in the calorimeter.

Regardless of the concrete linear collider option, the linear accelerator technologies define a number of boundary conditions, which have a significant impact on the way these detectors are designed, in addition to the requirements coming from the science program at these facilities.

Most prominently, linear colliders are pulsed machines. Collisions will happen during bunch trains, followed by relatively long periods of no collisions. The detailed timing requirement, the length of the bunch trains, and, most importantly, the time differences between pulses within a train, however, do vary a lot, with somewhat different constraints then put on the detailed detector design.

The pulsed operation allows the detectors to operate at high speed - and thus high power consumption - for the duration of the active pulse, but then be ramped down to reduced power consumption in the inter-bunch times. This significantly reduces the average power consumption of the detectors, and, with proper design, reduces very much the need for active cooling of many detector components. This has very advantageous consequences on the overall material budget, and reduces particularly in the inner part of the detector the amount of insensitive material needed to thermally control the detectors.

The pulsed mode of operation in addition makes it much easier to collect data during the collision part of the train locally, and then ship the data out during the inter-bunch times. This makes a triggerless operation of these detectors much easier to achieve.

The requirements for the detector concepts at a linear collider derive from the science requirements, which are described elsewhere in this document. They can be summarized by the requirements that have been introduced in Sec. 2.3 and are recalled here for convenience:

- **Impact parameter resolution:** An impact parameter resolution of $5\ \mu\mathrm{m} \oplus 10\ \mu\mathrm{m}/[p\ [\mathrm{GeV}/c] \sin^{3/2}\theta]$ has been defined as a goal, where θ is the angle between the particle and the beamline.

- **Momentum resolution:** An inverse momentum resolution of $\Delta(1/p) = 2 \times 10^{-5}\ [(\mathrm{GeV/c})^{-1}]$ asymptotically at high momenta should be reached with the combined silicon–TPC tracker, or silicon tracker alone. Maintaining excellent tracking efficiency and very good momentum resolution at lower momenta will be achieved by an aggressive design to minimise the detector's material budget.

- **Jet energy resolution:** Using the paradigm of particle flow a jet energy resolution $\Delta E/E = 3-4\%$ or better for light flavour jets should be reached. The resolution is defined in reference to light-quark jets, as the R.M.S. of the inner 90 % of the energy distribution.

- **Readout:** The detector readout will not use a hardware trigger, ensuring full efficiency for all possible event topologies.

- **Powering** The power of major systems will be cycled between bunch trains. This will reduce the power consumption of the detectors and minimise the amount of material in the detector. The corresponding smaller need of services will also be beneficial for the acceptance and hermeticity of the detectors.

6.2.1 Vertexing system

The system closest to the interaction region is a pixel detector designed to reconstruct decay vertices of short lived particles with great precision as well as low momentum tracks barely reaching the main tracker. Over the past few years, the CMOS technology has been adapted as baseline by all three concepts. It has matured to a point where all the requirements (material budget, readout speed, granularity) needed for an ILC detector can be met. The technology has seen a first large scale use in the STAR vertex detector [537], and more recently in the upgrade of the ALICE Inner Tracking System (ITS-2) [538].

The detailed system design is a matter of active R&D. Typically several layers of high precision pixel detectors form a barrel, complemented by endcap disks. In the CLICdp design, the endcap disks are arranged in a screw-like pattern, which allows efficient air-cooling of the detectors. In ILD sensors are arranged in pairs, which allow the combination of sensors with high spatial resolution with sensors with optimized timing resolution, in one super layer. A range of different technologies for the sensors and the readout are being explored, in close cooperation with the DRD groups recently initiated at CERN.

With current technology, a spatial resolution around 3 μm at a pitch of about 17 μm is in reach, and a timing resolution of around 2–4 μs, possibly lower, per (super-)layer can be obtained. R&D is directed towards improving this even further, to a point which would allow hits from individual bunch crossings to be resolved.

A key challenge for an integrated detector design is the development of an extremely light weight support structure, which bring the goal of 0.15% of a radiation length per layer within reach. Structures that reach 0.21% X_0 in most of the fiducial volume are now used in the Belle II vertex detector [539]. At a linear collider, the intrinsically pulsed operation of the system, which opens the possibility to have no liquid cooling system at all, is a significant boost of the efforts towards achieving passive-material budgets of around 0,1% of a radiation length.

In figure 68 the purity of the flavour identification in ILD is shown as a function of its efficiency. The performance for b-jet identification is excellent, and charm-jet identification is also good, providing a purity of about 70% at an efficiency of 60%. The system also allows the accurate determination of the charge of displaced vertices, and contributes strongly to the low-momentum tracking capabilities of the overall system, down to a few 10's of MeV.

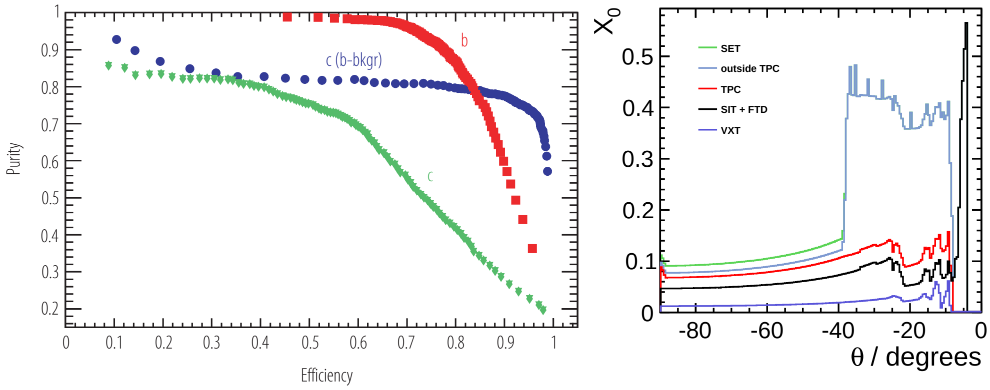

Figure 68: Left: Purity of the flavour tag as a function of the efficiency, for different flavours tagged. Right: Cumulative material budget in ILD up to the calorimeter, in fraction of a radiation length (figures from [40]).

6.2.2 Tracking System

The central tracking system in an LC detector is a key ingredient in the quest to optimize the detector towards particle flow. The system needs to deliver excellent momentum resolution, combined with outstanding efficiency, and overall low mass. Two different design routes are being followed:

ILD has decided to approach the problem of charged particle tracking with a hybrid solution, which combines a high resolution time-projection chamber (TPC) with a few layers of strategically placed strip or pixel detectors before and after the TPC. The inner layers could use CMOS detectors, the extended part is still open, including the possibility of using the first ECAL layer instead of extra detectors.

SiD and CLICdp have opted for a fully Silicon tracking option. The baseline designs call for strip sensors, arranged in layers surrounding the vertex detectors, and a system of endcap disks to maximise the solid angle coverage. As for the vertex detector, a solution which would require no or only minimal liquid cooling is anticipated.

The SiD concept has developed an integrated solution, where the readout ASIC is made part of the Silicon strip detector, simplifying the design and minimizing the overall material budget. With the rapid technological developments in the area of Silicon sensors and readout architectures, the option of a fully pixel-based central tracker is under investigation.

The time-projection chamber of ILD will fill a large volume about 4.6 m in length, spanning radii from 33 to 180 cm. In this volume the TPC provides up to 220 three dimensional points for continuous tracking with a single-hit resolution of better than 100 μm in $r\phi$, and about 1 mm in z. For momenta above 100 MeV, and within the acceptance of the TPC, greater than 99.9% tracking efficiency has been found in events simulated realistically with full backgrounds. The complete TPC system will introduce about 10% of a radiation length into the detector [540].

Inside and outside of the TPC volume a few layers of silicon detectors provide high resolution points, at a point resolution of 10μm. Combined with the TPC track, this will result in an asymptotic momentum resolution of $\delta p_t/p_t^2 = 2 \times 10^{-5}$ ((GeV/c)$^{-1}$) for the complete system.

Both options have demonstrated excellent momentum resolution over a large range of momenta. Differences between the options are mostly visible at lower momenta, where the lower material of the TPC tracker offers some advantages. The achievable resolution is illustrated in figure 69, where the $1/p_t$-resolution is shown as a function of the momentum of the charged particle, and is compared for a full-Silicon tracker in

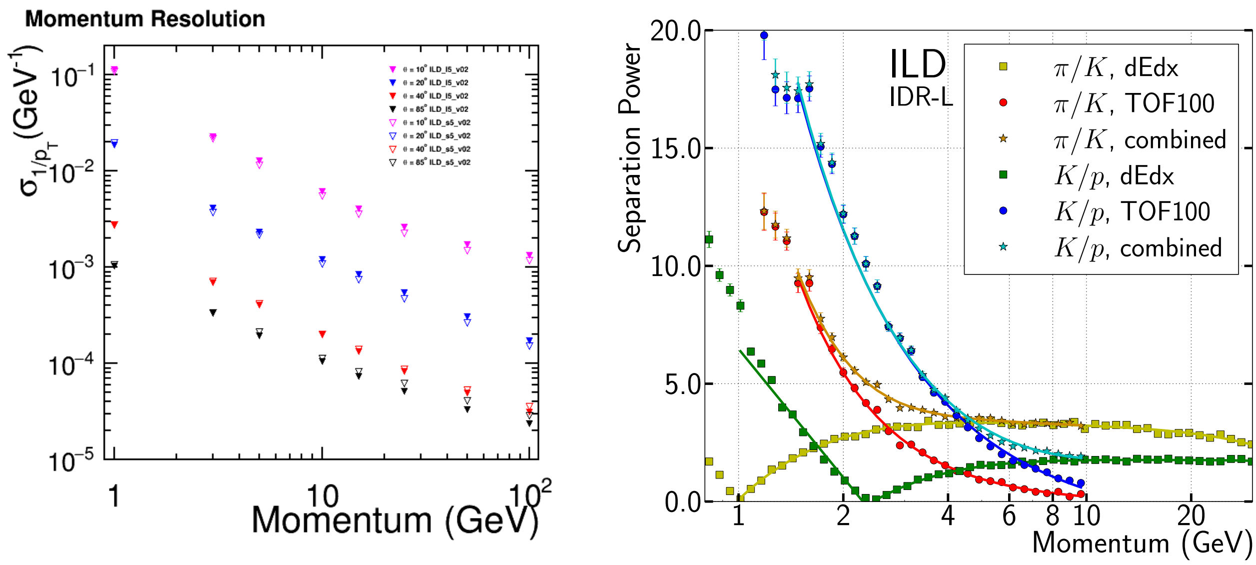

Figure 69: Left: Simulated resolution in $1/p_t$ as a function of the momentum for single muons. The different curves correspond to different polar angles. Right: Simulated separation power (probability for a particle to be reconstructed as another one) between pions and kaons (and between kaons and protons), from dE/dx and from timing, assuming a 100 ps timing resolution of the first ECAL layer (figures from [40]).

CLICdp (or SiD) and a TPC hybrid tracker.

Particle ID is an important additional role the tracking system should be able to deliver. For the all Silicon option, time of flight measurements provide Kaon-Pion separation for momenta up to XXX GeV, assuming a timing precision at the outer radius of the tracker of 10 ps. The TPC based option can extend this separation power up to momenta of 20 GeV for a Kaon-pion separation above XXX, based on dE/dx

6.2.3 Calorimeter- and Muon-System

A very powerful calorimeter system is essential to the performance of a detector designed for particle flow reconstruction. Particle flow stresses the ability to separate the individual particles in a jet, both charged and neutral. This puts the imaging capabilities of the system at a premium, and pushes the calorimeter development in the direction of a system with very high granularity in all parts of the system, both transverse to and along the shower development direction. A highly granular sampling calorimeter is the chosen solution to this challenge [541]. The conceptual and technological development of the particle flow calorimeter have been largely done by the CALICE collaboration (for a review of recent CALICE results see e.g. [542]), and are now integrated into the newly formed DRD6 collaboration.

Baseline for all three LC concepts is a sampling calorimeter equipped with silicon diodes as one option for the electromagnetic calorimeter. Diodes with pads of about $5 \times 5\,\mathrm{mm}^2$ are used, to sample a shower up to 40 times in the electromagnetic section. Extensive prototyping work and test beam experiments have demonstrated the feasibility of the system.

A self-sustaining structure holding tungsten plates in a Carbon-Fiber-Reinforced-Polymer (CFRP) supports the detector elements while minimizing non-instrumented spaces. A very similar system has been adopted by the CMS experiment for the upgrade of the endcap calorimeter, and will deliver invaluable information on the scalability and engineering details of such a system.

In recent years, the capabilities of the system to also provide precise timing information on the shower has been studied. The most obvious application of this is the instrumentation of the first (or early) layers of the ECAL with very good timing capacity, to provide time-of-flight measurements on charged particles, hitting the face of the calorimeter,

As an alternative to the silicon-based system, sensitive layers made from thin scintillator strips are also investigated. Orienting the strips perpendicular to each other has the potential to realize an effective cell size of $5 \times 5\,\text{mm}^2$, with the number of read-out channels reduced by an order of magnitude compared to the all silicon case. Also here, extensive prototyping work has been performed, though not as complete as for the Silicon ECAL option.

For the hadronic part of the calorimeter, several technologies are studied, based on either silicon photo diode (SiPM) on scintillator tile technology [543] or resistive plate chambers [544]. The SiPM-on-tile option has a moderate granularity, with $3 \times 3\,\text{cm}^2$ tiles, and provides an analogue readout of the signal in each tile (AHCAL). The RPC technology has a better granularity, of $1 \times 1\,\text{cm}^2$, but provides only 2-bit amplitude information (SDHCAL). For both technologies, significant prototypes have been built and operated. As for the ECAL the SiPM-on-tile technology has been selected as baseline for part of the upgrade of the CMS hadronic end-cap calorimeter, and will thus see a major application in the near future.

A key challenge for any of these technologies is the demonstration that the chosen technology scales to the large areas and large channel counts needed for a detector at an LC facility. Here great progress has been made through coordinated test beam campaigns and engineering efforts, to develop, demonstrate and cost scaling to large systems.

A rendering of the barrel calorimeter is shown in figure 70 (left).

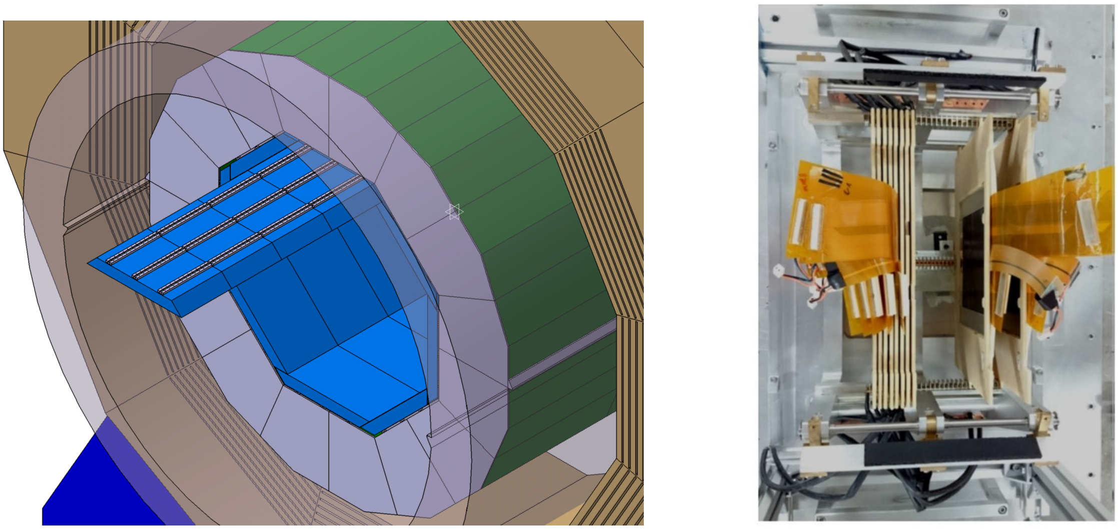

Figure 70: Left: Three-dimensional rendering of the barrel calorimeter system, with one ECAL module partially extracted. Right: Prototype module of the lumical calorimeter.

The iron return yoke of the detector, located outside of the coil, is instrumented to act as a tail catcher and as a muon identification system. The size and thickness of the iron return yoke scales with the ultimate energy for which the detector is designed. Several technologies are under study for the instrumented layers. The main challenge here is however primarily one of finding a cost efficient, robust technology, and not so much one of pushing technological limits.

The current ILD and SiD designs in addition were optimized for the so-called push-pull scheme, in which both detectors are housed in one common experimental hall, but share one interaction point. Servicing one detector while the other takes data requires additional shielding of the detector, most efficiently realised through a combination of additional Yoke thickness and added inactive shielding walls. In case, as anticipated for the LCvision scheme, two separate interaction regions are available, this additional complexity of the detector is not needed.

6.2.4 The Interaction Region

In a linear collider, electron and positron beams which are highly collimated are brought into collision. This creates a volume of extremely high energy density, which is the source of an very intense background radiation, the so called beamstrahlung. This effect is more pronounced at the currently considered linear collider options than it is at an FCC-ee, since the focus of the linear colliders is more intense.

The interaction region thus needs to be optimised to be able to extract as much as possible the background from the detector, without interacting with active or passive detector elements.

Compared to circular colliders, the final focus length L^* are larger at the linear colliders, which allows for more space for instrumentation and background mitigation. In particular, no need exists in the linear collider case to protect the inner region with a massive mask reaching inside the detector acceptance.

The region around the beam-pipe is instrumented with a series of smaller calorimeters, optimized to measure the luminosity, and to close the solid angle coverage of the electromagnetic calorimeter. Compared to the main calorimetric detectors, technologies need to be employed in this region which are significantly more radiation hard, to survive the intense electromagnetic background from the beam-beam interaction. These areas thus require rather special instrumentation.

The area surrounding the beam pipe is equipped with a set of compact calorimeters, including LumiCal and BeamCal, which are based on sampling calorimeter technologies. These detectors are designed to measure luminosity and extend the solid-angle coverage of the electromagnetic calorimeter. While both calorimeters utilize tungsten planes as absorbers, LumiCal employs silicon sensors as the active material, whereas BeamCal uses gallium arsenide sensors to withstand the intense electromagnetic background generated by beam-beam interactions. Figure 70(right) shows a 10-layer lumical prototype used during a test beam campaign.

6.2.5 Experimental Magnet

The three LC concepts all utilise a strong solenoid to provide fields between 3.5 and 5 T in the central region. This field is needed to measure charged tracks with high precision, and to focus and then remove charged background created in the beam beam interaction from the detector.

Technologically these magnets are based on the CMS experiment at CERN. A special challenge will be to build these magnets as thin as possible, to introduce minimal inactive material into the detector system. For all three concepts the current baseline calls for these magnets to be positioned outside of the hadronic calorimeter, to minimize the interference with the calorimeter measurement. Recent technological developments promise a significant reduction in thickness of the coils. Whether or not this then would allow to move the coil to smaller radii, at significant savings, is an area of active investigation.

6.3 New Ideas

Particle physics detectors are the eyes of the scientists to reveal the underlying laws of nature. The precision with which processes can be measured is limited by the precision with which the measurements can be performed. The experimentalist always needs to be prepared for the unexpected. History has many examples of detector systems discovering new phenomena for which the experiment was not originally designed. Key to these breakthroughs is building detectors that provide measurements with the highest precision. The pace of technology development is astounding and holds great promise for the next generation of detectors. The timescale from invention to application is sometimes remarkably short. A striking example is the origination of the time projection chamber (TPC). The idea arose in 1974 with a very small prototype [545] and it took a mere two years before it was adopted as the tracking technology of choice for the PEP-4 experiment [546]. In 1983 the ALEPH experiment at LEP chose the TPC as its main tracking detector.

One of the workhorses of current detectors is the silicon photomultiplier (SiPM), sometimes also called the multi-pixel photon counter (MPPC). A precursor to the current SiPM was the visible light photon counter (VLPC) developed by the company Rockwell. The devices had to be operated at cryogenic temperatures and their implementation in detectors was far from trivial. The development was significantly advanced in Russia in the late nineties and early twenties with first excellent devices produced by the Moscow Engineering and Physics Institute [547].

Given the challenges of the experimental environment of the LHC detectors, where events have many interactions per bunch crossing, the impact of high timing resolution was quickly realized and addressed with the development of the low-gain avalance diode (LGAD) technology. The idea for the implementation of a low-gain amplification region in a silicon detector was first proposed in 2012 and the technology has been advanced to the level where it can be implemented at scale has been at an impressive pace [548]. Both the ATLAS and CMS experiment now have large-area timing layers as integral part of their upgrades to help disambiguate the multiple interactions in an event. Within a timespan of seven years or so this technology has gone from a mere idea to an essential element of new detectors.

Another astounding technological revolution has been the development of the monolithic active pixel sensor (MAPS) CMOS technology. Although the hybrid pixel technology was recognized as a most powerful technology for vertex detectors, where the separation of readout and sensor allowed the devices to be made radiation hard for the very harsh environments at the LHC, integration on the two was considered the next logical step with potential access to commercial foundries for the production of the sensors. The MIMOSA (Minimum Ionizing MOS Active pixel sensor) series of sensors was the first venture into this area of sensor development that started around 1999. Using ever more advanced technologies, moving from AMS 0.6 μm to TSMC 180 nm, the technology was matured with the first deployment of a MAPS vertex detector for the STAR experiment at RHIC in 2014 [537]. The technology has advanced unabatedly and a major milestone was reached with the construction of the large MAPS-based vertex detector for the ALICE experiment, ITS2, that has 12.5 billion pixels of 27 x 29 μm, a spatial resolution of 5 μm and a material budget of 0.36% X_0 [549]. It has one of the lowest material budgets of any vertex detector and intense efforts aim at reducing that even further. It is the most promising candidate technology for future collider vertex detectors.

With sensors being thinned to be flexible, embedding sensors in thin flexible circuits will become feasible. This opens up the possibility to study geometries that have been out of reach to date. Current geometries have by necessity, due to the constraints imposed by the sensors, relatively large uninstrumented areas. With flexible sensors, continuous cylindrical or even spherical geometries could be considered, which could allow for significant advantages. An example of a study in this direction is the idea to embed a Timepix4 chip with through-silicon vias laminated onto a polyimide microRWELL flexible PCB, with the connection to the readout system on one side and the amplification stage on the other side, leading to a detector with full active coverage.

The emergence of quantum sensors could also enable the development of new detectors for particle physics to reach unimaginable precision in the measurement of certain quantities. A long-held goal of the community, for example, has been to construct calorimeters with superb energy resolution for hadronic jets. Quantum dots could be a first step in this direction. One-dimensional materials offer the capability to tune the fluorescence spectrum. Both crystals and scintillators can be doped with the appropriate quantum dots to enhance the properties of the light emission and improve the measurement of the energy resolution. Using different doping schemes for separate longitudinal sections in the calorimeter, chromatic calorimetry can developed and the calorimeter response tuned to different particles. A further example for improving vertex detectors is DoTPiX technology [550], which can be described as a technology for vertexing to in a semi-classical way, using quantum wells

As these few examples show, new technologies can be developed on a relatively short time scale that truly have a transformative impact on the next generation of experiments. The timescale for the development of new techniques is not many decades as the previous examples have shown, but can happen within a decade. The opportunity exists now to introduce a complete new paradigm for the next-generation experiments that will have capabilities that transcend the current state of the art significantly. This is a very exciting prospect. Given that the experiments will need to operate for many decades, at different centre of mass energies where the physics topologies will be different, it provides an opportunity to develop an approach to detector design, potentially using advanced AI and ML techniques, that integrates not only all detector technologies but also the full lifetime of the experiments with its full physics program.

7 Summary and Conclusion

In this report, we have surveyed the physics opportunities offered by linear e^+e^- collisions. The most urgent problem in particle physics is to understand the nature of the Higgs boson, its structure and couplings to quarks, leptons, and gauge bosons, and the physics responsible for their mass generation. As the energy of an e^+e^- collider is raised from the Higgs boson threshold, a series of different reactions allow us to measure the Higgs boson's properties in different ways. This is the way to obtain the most complete and most precise data to address the Higgs' mysteries. Precision electroweak measurements, measurements on the weak interaction bosons, and measurements on the top quark contribute to this story. Only a linear e^+e^- collider capable of observing the full evolution up to an energy of 1 TeV can see the full picture.

We have reviewed the technologies available for construction of a linear e^+e^- collider. For experiments at the peak of the cross section for $e^+e^- \to ZH$ at 250 GeV, there is a well-understood technology based on superconducting RF cavities that can provide a first-stage collider readily and with little risk. This can solve the problem of assuring a continuous program of collider experiments beyond the lifetime of the LHC. But also, new technologies with higher accelerating gradients and luminosities contribute new possibilities for the future of a linear collider program. These will make it possible to reach higher energies in an economical way. Ideas such as the $\gamma\gamma$ collider will add new observables. A linear collider can also provide a testbed for ideas such as plasma wakefield acceleration that someday will deliver colliders with parton collisions at 10 TeV and above.

The low-background environment of an e^+e^- colliders allows the development of new particle detector technologies that could not survive in the intense setting of high-energy proton colliders. These new technologies are needed to supply measurements of the Higgs boson at the highest possible precision. Some ideas for highly capable trackers and calorimeters are already included in the current designs for linear collider detectors. But we are looking forward to new and powerful ideas to emerge as young scientists educated at the LHC turn their creativity to this new challenge.

In all of these aspects – compelling physics, novel accelerators, high-precision detectors – construction of a linear collider facility will lead to a fresh and exciting era of experimental particle physics.

As for applications from our field to other areas of science, the future is linear. Spallation neutron sources and free-electron lasers are based on technologies invented to build linear colliders, and now these have become the workhorses of materials science, structural biology, and ultrafast chemistry. Our highly capable detectors and our experience with massive data sets are already needed, and are already being applied, to make sense of the results of new experiments that these facilities host. As we advance along this line, our colleagues will advance along with us.

Linear e^+e^- colliders promise a bright future for physics, for technology, and for the advance of science along many fronts. Members of our field, and our colleagues in physical science, need this future as soon as possible. The next step to that era is the construction of a linear collider Higgs factory.

Acknowledgements

This work was supported by EAJADE, a Marie Sklodowska-Curie Research and Innovation Staff Exchange (SE) action, funded by the EU under Horizon-Europe Grant agreement ID: 101086276; by AIDAinnova, a project within the European Union's Horizon 2020 Research and Innovation programme under GA no. 101004761; by the Deutsche Forschungsgemeinschaft (DFG, German Research Foundation) under grant 491245950 and under Germany's Excellence Strategy – EXC 2121 "Quantum Universe" – 390833306, and the DFG Emmy Noether Grant no. BR 6995/1-1; by a Department of Science and Technology and Anusandhan National Research Foundation Government of India Startup Research Grant, grant agreement no. SRG/2022/000363 and Core Research Grant, grant agreement no. CRG/2022/004120; by the National Science Centre (Poland) under the OPUS research project no. 2021/43/B/ST2/01778 and by Narodowe Centrum Nauki, Poland, grant no. 2023/50/A/ST2/00224; by the Spanish Ministry of Science under grant agreement PID2021-122134NB-C21, by the Generalitat Valenciana under CIPROM/2021/073 and ASFAE2022/013 and 015, by the Severo Ochao excellence program, and by the Atracción de Talento Grant no. 2022-T1/TIC-24176 of the Comunidad Autónoma de Madrid, Spain; by the Swiss National Science Foundation under grant no. 214492; by the Science and Technology Facilities Council, United Kingdom; by the US Department of Energy under contracts No. DE–AC02–76SF00515, no. 89243024CSC000002, no. DE-SC0010107, and no. DE-SC0010107, and by the US National Science Foundation through the award NSF2310030; by the CNRS/IN2P3, France.

References

[1] *The International Linear Collider Technical Design Report - Volume 1: Executive Summary* (2013), ed. by T. Behnke et al., arXiv: 1306.6327 [physics.acc-ph].

[2] *The International Linear Collider Technical Design Report - Volume 2: Physics* (2013), ed. by H. Baer et al., arXiv: 1306.6352 [hep-ph].

[3] *The International Linear Collider Technical Design Report - Volume 3.I: Accelerator \& in the Technical Design Phase* (2013), ed. by C. Adolphsen et al., arXiv: 1306.6353 [physics.acc-ph].

[4] *The International Linear Collider Technical Design Report - Volume 3.II: Accelerator Baseline Design* (2013), ed. by C. Adolphsen et al., arXiv: 1306.6328 [physics.acc-ph].

[5] H. Abramowicz et al., *The International Linear Collider Technical Design Report - Volume 4: Detectors* (2013), ed. by T. Behnke et al., arXiv: 1306.6329 [physics.ins-det].

[6] L. Evans, S. Michizono, Linear Collider, *The International Linear Collider Machine Staging Report 2017* (2017), arXiv: 1711.00568 [physics.acc-ph].

[7] *A Multi-TeV Linear Collider Based on CLIC Technology: CLIC Conceptual Design Report* (2012), ed. by M. Aicheler et al., DOI: 10.5170/CERN-2012-007.

[8] P. Lebrun et al., *The CLIC Programme: Towards a Staged e+e- Linear Collider Exploring the Terascale: CLIC Conceptual Design Report* (2012), DOI: 10.5170/CERN-2012-005, arXiv: 1209.2543 [physics.ins-det].

[9] *Physics and Detectors at CLIC: CLIC Conceptual Design Report* (2012), ed. by L. Linssen et al., DOI: 10.5170/CERN-2012-003, arXiv: 1202.5940 [physics.ins-det].

[10] M. J. Boland et al., CLIC, CLICdp, *Updated baseline for a staged Compact Linear Collider* (2016), ed. by P. Lebrun et al., DOI: 10.5170/CERN-2016-004, arXiv: 1608.07537 [physics.acc-ph].

[11] *The Compact Linear Collider (CLIC) - Project Implementation Plan*, **4/2018** (2018), ed. by M. Aicheler et al., DOI: 10.23731/CYRM-2018-004, arXiv: 1903.08655 [physics.acc-ph].

[12] P. Bambade et al., *The International Linear Collider: A Global Project* (2019), arXiv: 1903.01629 [hep-ex].

[13] T. K. Charles et al., CLICdp, CLIC, *The Compact Linear Collider (CLIC) - 2018 Summary Report*, **2/2018** (2018), ed. by P. N. Burrows et al., DOI: 10.23731/CYRM-2018-002, arXiv: 1812.06018 [physics.acc-ph].

[14] A. Aryshev et al., ILC International Development Team, *The International Linear Collider: Report to Snowmass 2021* (2022), arXiv: 2203.07622 [physics.acc-ph].

[15] O. Brunner et al., *The CLIC project* (2022), arXiv: 2203.09186 [physics.acc-ph].

[16] The International Development Team, *The ILC – EPPSU submission*, 2025, arXiv: 2504.nnn [physics.acc-ph].

[17] CLIC Collaboration, *CLIC – EPPSU submission*, 2025, arXiv: 2504.nnn [physics.acc-ph].

[18] E. Adli et al., *CLIC Readiness Report* (2025), URL: https://edms.cern.ch/project/CERN-0000267313.

[19] LCVision Team, *The Linear Collider Facility (LCF) at CERN – EPPSU submission, abstract # 40*, URL: https://agenda.linearcollider.org/event/10624/.

[20] C. Vernieri et al., *Strategy for Understanding the Higgs Physics: The Cool Copper Collider*, JINST **18** (2023) P07053, DOI: 10.1088/1748-0221/18/07/P07053, arXiv: 2203.07646 [hep-ex].

[21] M. B. Andorf et al., *ESPPU INPUT: C^3 within the "Linear Collider Vision"* (2025), arXiv: 2503.20829 [physics.acc-ph].

[22] S. Belomestnykh et al., *HELEN: Traveling Wave SRF Linear Collider Higgs Factory*, JACoW **IPAC2023** (2023) MOPL098, DOI: 10.18429/JACoW-IPAC2023-MOPL098, arXiv: 2307.06248 [physics.acc-ph].

[23] S. Belomestnykh et al., *Superconducting radio frequency linear collider HELEN*, JINST **18** (2023) P09039, DOI: 10.1088/1748-0221/18/09/P09039.

[24] E. Adli et al., *HALHF: a hybrid, asymmetric, linear Higgs factory using plasma- and RF-based acceleration*, 2025, arXiv: 2503.19880 [physics.acc-ph], URL: http://arxiv.org/abs/2503.19880.

[25] B. Foster et al., *Proceedings of the Erice Workshop: A new baseline for the hybrid, asymmetric, linear Higgs factory HALHF*, 2025, arXiv: 2501.11072 [physics.acc-ph].

[26] B. Cros, P. Muggli, *ALEGRO input for the 2025 update of the European Strategy*, 2025, arXiv: 2504.nnn [physics.acc-ph].

[27] B. Cros, P. Muggli, ALEGRO, *ALEGRO input for the 2020 update of the European Strategy* (2019), arXiv: 1901.08436 [physics.acc-ph].

[28] *Report on the Advanced Linear Collider Study Group (ALEGRO) Workshop 2024*, 2024, arXiv: 2408.03968 [physics.acc-ph].

[29] S. Gessner, J. Osterhoff et al., *Design Initiative for a 10 TeV pCM Wakefield Collider*, 2025, DOI: 10.48550/ARXIV.2503.20214, URL: https://arxiv.org/abs/2503.20214.

[30] V. N. Litvinenko et al., *The ReLiC: Recycling Linear e^+e^- Collider* (2022), arXiv: 2203.06476 [hep-ex].

[31] T. Barklow et al., *XCC: an X-ray FEL-based $\gamma\gamma$ Compton collider Higgs factory*, Journal of Instrumentation **18** (2023) P07028, DOI: 10.1088/1748-0221/18/07/p07028.

[32] A. Aryshev et al., *The International Linear Collider: Report to Snowmass 2021*, 2023, arXiv: 2203.07622 [physics.acc-ph].

[33] G. Moortgat-Pick et al., *The Role of polarized positrons and electrons in revealing fundamental interactions at the linear collider*, Phys. Rept. **460** (2008) 131, DOI: 10.1016/j.physrep.2007.12.003, arXiv: hep-ph/0507011.

[34] T. Barklow et al., *ILC Operating Scenarios* (2015), arXiv: 1506.07830 [hep-ex].

[35] K. Fujii et al., *Physics Case for the 250 GeV Stage of the International Linear Collider* (2017), arXiv: 1710.07621 [hep-ex].

[36] M. Thomson, *Model-independent measurement of the $e^+e^- \to HZ$ cross section at a future e^+e^- linear collider using hadronic Z decays*, Eur. Phys. J. C **76** (2016) 72, DOI: 10.1140/epjc/s10052-016-3911-5, arXiv: 1509.02853 [hep-ex].

[37] A. Robson, P. Roloff, J. de Blas, *CLIC Higgs prospects with 100 Hz operation*, CLICdp-Note-2025-002, 2025, URL: http://cds.cern.ch/record/2927905.

[38] D. Ntounis, E. A. Nanni, C. Vernieri, *Luminosity and beam-induced background studies for the Cool Copper Collider*, Phys. Rev. Accel. Beams **27** (2024) 061001, DOI: 10.1103/PhysRevAccelBeams.27.061001, arXiv: 2403.07093 [physics.acc-ph].

[39] A. C. Abusleme Hoffman et al., *Detector Technologies for CLIC*, **1/2019** (2019), ed. by D. Dannheim et al., DOI: 10.23731/CYRM-2019-001, arXiv: 1905.02520 [physics.ins-det].

[40] H. Abramowicz et al., ILD Concept Group, *International Large Detector: Interim Design Report* (2020), arXiv: 2003.01116 [physics.ins-det].

[41] A. Robson et al. (Eds.), *ECFA Higgs/Electroweak/Top Factory Study*, CERN Yellow Report **CERN-2025-005** (2025), DOI: 10.23731/CYRM-2025-005.

[42] T. Suehara, T. Tanabe, *LCFIPlus: A Framework for Jet Analysis in Linear Collider Studies*, Nucl. Instrum. Meth. A **808** (2016) 109, DOI: 10.1016/j.nima.2015.11.054, arXiv: 1506.08371 [physics.ins-det].

[43] M. Meyer, *Machine Learning Flavour Tagging for Future Higgs Factories*, 2023, URL: https://agenda.infn.it/event/34841/contributions/207748/.

[44] U. Einhaus et al., *Implementation, performance and physics impact of particle identification at Higgs factories*, PoS **EPS-HEP2023** (2024) 598, DOI: 10.22323/1.449.0598, arXiv: 2311.09102 [hep-ex].

[45] P. Stylianou, G. Weiglein, *Constraints on the trilinear and quartic Higgs couplings from triple Higgs production at the LHC and beyond*, Eur. Phys. J. C **84** (2024) 366, DOI: 10.1140/epjc/s10052-024-12722-9, arXiv: 2312.04646 [hep-ph].

[46] J. Yan et al., *Measurement of the Higgs boson mass and $e^+e^- \to ZH$ cross section using $Z \to \mu^+\mu^-$ and $Z \to e^+e^-$ at the ILC*, Phys. Rev. D **94** (2016), [Erratum: Phys.Rev.D 103, 099903 (2021)] 113002, DOI: 10.1103/PhysRevD.94.113002, arXiv: 1604.07524 [hep-ex].

[47] H. Abramowicz et al., *Higgs physics at the CLIC electron–positron linear collider*, Eur. Phys. J. C **77** (2017) 475, DOI: 10.1140/epjc/s10052-017-4968-5, arXiv: 1608.07538 [hep-ex].

[48] J. de Blas et al., *Global SMEFT Fits at Future Colliders*, Snowmass 2021, 2022, arXiv: 2206.08326 [hep-ph].

[49] Y. Aoki, K. Fujii, J. Tian, *Study of the $h\gamma Z$ coupling at the ILC*, International Workshop on Future Linear Colliders, 2021, arXiv: 2105.06665 [hep-ex].

[50] Y. Aoki, K. Fujii, J. Tian, ILD concept group, *Study of $e^+e^- \to \gamma h$ at the ILC* (2022), arXiv: 2203.07202 [hep-ex].

[51] A. V. Gritsan et al., *Snowmass White Paper: Prospects of CP-violation measurements with the Higgs boson at future experiments* (2022), arXiv: 2205.07715 [hep-ex].

[52] D. Jeans, G. W. Wilson, *Measuring the CP state of tau lepton pairs from Higgs decay at the ILC*, Phys. Rev. D **98** (2018) 013007, DOI: 10.1103/PhysRevD.98.013007, arXiv: 1804.01241 [hep-ex].

[53] N. Vukasinovic et al., *Determination of the CPV Higgs mixing angle in ZZ-fusion at 1.4 TeV CLIC*, PoS **BPU11** (2023) 102, DOI: 10.22323/1.427.0102.

[54] R. M. Godbole et al., *Model-independent analysis of Higgs spin and CP properties in the process $e^+e^- \to t\bar{t}\Phi$*, Eur. Phys. J. C **71** (2011) 1681, DOI: 10.1140/epjc/s10052-011-1681-7, arXiv: 1103.5404 [hep-ph].

[55] A. V. Gritsan et al., *Snowmass White Paper: Prospects of CP-violation measurements with the Higgs boson at future experiments*, 2022, arXiv: 2205.07715 [hep-ex].

[56] A. Pich, P. Tuzon, *Yukawa Alignment in the Two-Higgs-Doublet Model*, Phys. Rev. D **80** (2009) 091702, DOI: 10.1103/PhysRevD.80.091702, arXiv: 0908.1554 [hep-ph].

[57] V. D. Barger, J. L. Hewett, R. J. N. Phillips, *New Constraints on the Charged Higgs Sector in Two Higgs Doublet Models*, Phys. Rev. **D41** (1990) 3421, DOI: 10.1103/PhysRevD.41.3421.

[58] Y. Grossman, *Phenomenology of models with more than two Higgs doublets*, Nucl. Phys. **B426** (1994) 355, DOI: 10.1016/0550-3213(94)90316-6, arXiv: hep-ph/9401311 [hep-ph].

[59] M. Aoki et al.,
Models of Yukawa interaction in the two Higgs doublet model, and their collider phenomenology,
Phys. Rev. **D80** (2009) 015017, DOI: 10.1103/PhysRevD.80.015017,
arXiv: 0902.4665 [hep-ph].

[60] H. Georgi, M. Machacek, *DOUBLY CHARGED HIGGS BOSONS*, Nucl. Phys. B **262** (1985) 463,
DOI: 10.1016/0550-3213(85)90325-6.

[61] M. S. Chanowitz, M. Golden, *Higgs Boson Triplets With M (W) = M (Z)* $\cos\theta\,\omega$,
Phys. Lett. B **165** (1985) 105, DOI: 10.1016/0370-2693(85)90700-2.

[62] A. Freitas et al.,
Theoretical uncertainties for electroweak and Higgs-boson precision measurements at FCC-ee
(2019), arXiv: 1906.05379 [hep-ph].

[63] J. Blümlein et al., *The* $O(\alpha^2)$ *initial state QED corrections to* $e^+e^- \to \gamma^*/Z_0^*$,
Nucl. Phys. B **956** (2020) 115055, DOI: 10.1016/j.nuclphysb.2020.115055,
arXiv: 2003.14289 [hep-ph].

[64] J. Ablinger et al.,
Subleading Logarithmic QED Initial State Corrections to $e^+e^- \to \gamma^*/Z^{0^*}$ *to* $O(\alpha^6 L^5)$,
Nucl. Phys. B **955** (2020) 115045, DOI: 10.1016/j.nuclphysb.2020.115045,
arXiv: 2004.04287 [hep-ph].

[65] J. Blümlein, A. De Freitas, K. Schönwald, *The QED initial state corrections to the forward-backward asymmetry of* $e^+e^- \to \gamma^*/Z^{0*}$ *to higher orders*, Phys. Lett. B **816** (2021) 136250,
DOI: 10.1016/j.physletb.2021.136250, arXiv: 2102.12237 [hep-ph].

[66] K. Fujii et al.,
The role of positron polarization for the inital 250 *GeV stage of the International Linear Collider*
(2018), arXiv: 1801.02840 [hep-ph].

[67] K. Yokoya, K. Kubo, T. Okugi, *Operation of ILC250 at the Z-pole* (2019),
arXiv: 1908.08212 [physics.acc-ph].

[68] G. Wilson, B. Madison, *Reimagining* e^+e^- *collider precision luminosity measurements*,
EPJ Web Conf. **315** (2024) 01024, DOI: 10.1051/epjconf/202431501024.

[69] B. Madison, G. W. Wilson,
Center-of-mass energy determination using $\mathrm{e}^+\mathrm{e}^- \to \mu^+\mu^-(\gamma)$ *events at future* $\mathrm{e}^+\mathrm{e}^-$ *colliders*,
Snowmass 2021, 2022, arXiv: 2209.03281 [hep-ex].

[70] G. W. Wilson,
Further investigation of dilepton-based center-of-mass energy measurements at e^+e^- *colliders*,
International Workshop on Future Linear Colliders, 2023, arXiv: 2308.10414 [hep-ex].

[71] M. Baak et al., *Working Group Report: Precision Study of Electroweak Interactions*,
Snowmass 2013: Snowmass on the Mississippi, 2013, arXiv: 1310.6708 [hep-ph].

[72] J. R. Christiansen, T. Sjöstrand, *Color reconnection at future* e^+ e^- *colliders*,
Eur. Phys. J. C **75** (2015) 441, DOI: 10.1140/epjc/s10052-015-3674-4,
arXiv: 1506.09085 [hep-ph].

[73] W. J. Stirling, *The Measurement of M(W) from the* W^+W^- *threshold cross-section at LEP-2*,
Nucl. Phys. B **456** (1995) 3, DOI: 10.1016/0550-3213(95)00509-8,
arXiv: hep-ph/9503320.

[74] A. Irles, R. Pöschl, F. Richard, *Experimental methods and prospects on the measurement of electroweak b and c-quark observables at the ILC operating at 250 GeV* (2023),
arXiv: 2306.11413 [hep-ex].

[75] A. Irles et al., *Probing gauge-Higgs unification models at the ILC with quark–antiquark forward–backward asymmetry at center-of-mass energies above the Z mass*,
Eur. Phys. J. C **84** (2024) 537, DOI: 10.1140/epjc/s10052-024-12918-z,
arXiv: 2403.09144 [hep-ph].

[76] Y. Hosotani, N. Yamatsu, *Gauge–Higgs grand unification*, Progress of Theoretical and Experimental Physics **2015** (2015) 111B01, DOI: 10.1093/ptep/ptv153, eprint: https://academic.oup.com/ptep/article-pdf/2015/11/111B01/8097507/ptv153.pdf.

[77] S. Funatsu et al., *Distinct signals of the gauge-Higgs unification in e^+e^- collider experiments*, Phys. Lett. B **775** (2017) 297, DOI: 10.1016/j.physletb.2017.10.068, arXiv: 1705.05282 [hep-ph].

[78] S. Funatsu et al., *Fermion pair production at e^-e^+ linear collider experiments in GUT inspired gauge-Higgs unification*, Phys. Rev. D **102** (2020) 015029, DOI: 10.1103/PhysRevD.102.015029, arXiv: 2006.02157 [hep-ph].

[79] S. Funatsu et al., *Single Higgs boson production at electron-positron colliders in gauge-Higgs unification*, Phys. Rev. D **107** (2023) 075030, DOI: 10.1103/PhysRevD.107.075030, arXiv: 2301.07833 [hep-ph].

[80] J. de Blas et al., *Focus topics for the ECFA study on Higgs / Top / EW factories* (2024), arXiv: 2401.07564 [hep-ph].

[81] D. Marzocca, M. Szewc, M. Tammaro, *Direct CKM determination from W decays at future lepton colliders*, JHEP **11** (2024) 017, DOI: 10.1007/JHEP11(2024)017, arXiv: 2405.08880 [hep-ph].

[82] H. Liang et al., *Measurement of CKM element $|V_{cb}|$ from W boson decays at the future Higgs factories*, JHEP **12** (2024) 071, DOI: 10.1007/JHEP12(2024)071, arXiv: 2406.01675 [hep-ph].

[83] V. A. Kuzmin, V. A. Rubakov, M. E. Shaposhnikov, *On the Anomalous Electroweak Baryon Number Nonconservation in the Early Universe*, Phys. Lett. B **155** (1985) 36, DOI: 10.1016/0370-2693(85)91028-7.

[84] A. G. Cohen, D. B. Kaplan, A. E. Nelson, *Progress in electroweak baryogenesis*, Ann. Rev. Nucl. Part. Sci. **43** (1993) 27, DOI: 10.1146/annurev.ns.43.120193.000331, arXiv: hep-ph/9302210.

[85] K. Radchenko, *in preparation*, PhD thesis, Hamburg: Hamburg U., 2025.

[86] G. Aad et al., ATLAS, *Combination of Searches for Higgs Boson Pair Production in pp Collisions at s=13 TeV with the ATLAS Detector*, Phys. Rev. Lett. **133** (2024) 101801, DOI: 10.1103/PhysRevLett.133.101801, arXiv: 2406.09971 [hep-ex].

[87] A. Tumasyan et al., CMS, *A portrait of the Higgs boson by the CMS experiment ten years after the discovery.* Nature **607** (2022), [Erratum: Nature 623, (2023)] 60, DOI: 10.1038/s41586-022-04892-x, arXiv: 2207.00043 [hep-ex].

[88] G. Aad et al., ATLAS, *Constraints on the Higgs boson self-coupling from single- and double-Higgs production with the ATLAS detector using pp collisions at s=13 TeV*, Phys. Lett. B **843** (2023) 137745, DOI: 10.1016/j.physletb.2023.137745, arXiv: 2211.01216 [hep-ex].

[89] The ATLAS and CMS Collaborations, *Highlights of the HL-LHC physics projections by ATLAS and CMS*, ATL-PHYS-PUB-2025-018, CMS-HIG-25-002 (2025).

[90] A. Djouadi et al., *Testing Higgs selfcouplings at e+ e- linear colliders*, Eur. Phys. J. C **10** (1999) 27, DOI: 10.1007/s100529900082, arXiv: hep-ph/9903229.

[91] T. Barklow et al., *Model-Independent Determination of the Triple Higgs Coupling at e+e- Colliders*, Phys. Rev. D **97** (2018) 053004, DOI: 10.1103/PhysRevD.97.053004, arXiv: 1708.09079 [hep-ph].

[92] J. List et al., *Higgs Self-coupling Strategy at Linear e+e- Colliders*, PoS **ICHEP2024** (2025) 079, DOI: 10.22323/1.476.0079, arXiv: 2411.01507 [hep-ex].

[93] K. Fujii et al., *Physics Case for the International Linear Collider* (2015), arXiv: 1506.05992 [hep-ex].

[94] P. Roloff et al., CLICdp, *Double Higgs boson production and Higgs self-coupling extraction at CLIC*, Eur. Phys. J. C **80** (2020) 1010, DOI: 10.1140/epjc/s10052-020-08567-7, arXiv: 1901.05897 [hep-ex].

[95] H. Abouabid et al., *Benchmarking di-Higgs production in various extended Higgs sector models*, JHEP **09** (2022) 011, DOI: 10.1007/JHEP09(2022)011, arXiv: 2112.12515 [hep-ph].

[96] H. Bahl, J. Braathen, G. Weiglein, *New Constraints on Extended Higgs Sectors from the Trilinear Higgs Coupling*, Phys. Rev. Lett. **129** (2022) 231802, DOI: 10.1103/PhysRevLett.129.231802, arXiv: 2202.03453 [hep-ph].

[97] S. Kanemura et al., *New physics effect on the Higgs selfcoupling*, Phys. Lett. B **558** (2003) 157, DOI: 10.1016/S0370-2693(03)00268-5, arXiv: hep-ph/0211308.

[98] S. Kanemura et al., *Higgs coupling constants as a probe of new physics*, Phys. Rev. D **70** (2004) 115002, DOI: 10.1103/PhysRevD.70.115002, arXiv: hep-ph/0408364.

[99] M. Aoki et al., *Radiative corrections to the Higgs boson couplings in the triplet model*, Phys. Rev. **D87** (2013) 015012, DOI: 10.1103/PhysRevD.87.015012, arXiv: 1211.6029 [hep-ph].

[100] S. Kanemura, M. Kikuchi, K. Yagyu, *Radiative corrections to the Higgs boson couplings in the model with an additional real singlet scalar field*, Nucl. Phys. **B907** (2016) 286, DOI: 10.1016/j.nuclphysb.2016.04.005, arXiv: 1511.06211 [hep-ph].

[101] S. Kanemura, M. Kikuchi, K. Yagyu, *Fingerprinting the extended Higgs sector using one-loop corrected Higgs boson couplings and future precision measurements*, Nucl. Phys. **B896** (2015) 80, DOI: 10.1016/j.nuclphysb.2015.04.015, arXiv: 1502.07716 [hep-ph].

[102] A. Arhrib et al., *Radiative corrections to the Triple Higgs Coupling in the Inert Higgs Doublet Model*, JHEP **12** (2015) 007, DOI: 10.1007/JHEP12(2015)007, arXiv: 1507.03630 [hep-ph].

[103] S. Kanemura, M. Kikuchi, K. Sakurai, *Testing the dark matter scenario in the inert doublet model by future precision measurements of the Higgs boson couplings*, Phys. Rev. **D94** (2016) 115011, DOI: 10.1103/PhysRevD.94.115011, arXiv: 1605.08520 [hep-ph].

[104] S. Kanemura, M. Kikuchi, K. Yagyu, *One-loop corrections to the Higgs self-couplings in the singlet extension*, Nucl. Phys. **B917** (2017) 154, DOI: 10.1016/j.nuclphysb.2017.02.004, arXiv: 1608.01582 [hep-ph].

[105] S.-P. He, S.-h. Zhu, *One-Loop Radiative Correction to the Triple Higgs Coupling in the Higgs Singlet Model*, Phys. Lett. **B764** (2017) 31, DOI: 10.1016/j.physletb.2016.11.007, arXiv: 1607.04497 [hep-ph].

[106] M. Krause et al., *Higgs-to-Higgs boson decays in a 2HDM at next-to-leading order*, Phys. Rev. D **95** (2017) 075019, DOI: 10.1103/PhysRevD.95.075019, arXiv: 1609.04185 [hep-ph].

[107] S. Kanemura et al., *Gauge invariant one-loop corrections to Higgs boson couplings in non-minimal Higgs models*, Phys. Rev. **D96** (2017) 035014, DOI: 10.1103/PhysRevD.96.035014, arXiv: 1705.05399 [hep-ph].

[108] S. Kanemura et al.,
H-COUP: a program for one-loop corrected Higgs boson couplings in non-minimal Higgs sectors,
Comput. Phys. Commun. **233** (2018) 134, DOI: 10.1016/j.cpc.2018.06.012,
arXiv: 1710.04603 [hep-ph].

[109] C.-W. Chiang, A.-L. Kuo, K. Yagyu,
One-loop renormalized Higgs boson vertices in the Georgi-Machacek model,
Phys. Rev. D **98** (2018) 013008, DOI: 10.1103/PhysRevD.98.013008,
arXiv: 1804.02633 [hep-ph].

[110] P. Basler, M. Mühlleitner, *BSMPT (Beyond the Standard Model Phase Transitions): A tool for the electroweak phase transition in extended Higgs sectors*, Comput. Phys. Commun. **237** (2019) 62,
DOI: 10.1016/j.cpc.2018.11.006, arXiv: 1803.02846 [hep-ph].

[111] E. Senaha, *Radiative Corrections to Triple Higgs Coupling and Electroweak Phase Transition: Beyond One-loop Analysis*, Phys. Rev. **D100** (2019) 055034, DOI: 10.1103/PhysRevD.100.055034,
arXiv: 1811.00336 [hep-ph].

[112] J. Braathen, S. Kanemura,
On two-loop corrections to the Higgs trilinear coupling in models with extended scalar sectors,
Phys. Lett. B **796** (2019) 38, DOI: 10.1016/j.physletb.2019.07.021,
arXiv: 1903.05417 [hep-ph].

[113] J. Braathen, S. Kanemura, *Leading two-loop corrections to the Higgs boson self-couplings in models with extended scalar sectors*, Eur. Phys. J. C **80** (2020) 227,
DOI: 10.1140/epjc/s10052-020-7723-2, arXiv: 1911.11507 [hep-ph].

[114] S. Kanemura et al., *H-COUP Version 2: a program for one-loop corrected Higgs boson decays in non-minimal Higgs sectors*, Comput. Phys. Commun. **257** (2020) 107512,
DOI: 10.1016/j.cpc.2020.107512, arXiv: 1910.12769 [hep-ph].

[115] P. Basler, M. Mühlleitner, J. Müller, *Electroweak Phase Transition in Non-Minimal Higgs Sectors*,
JHEP **05** (2020) 016, DOI: 10.1007/JHEP05(2020)016, arXiv: 1912.10477 [hep-ph].

[116] P. Basler, M. Mühlleitner, J. Müller, *BSMPT v2 a tool for the electroweak phase transition and the baryon asymmetry of the universe in extended Higgs Sectors*,
Comput. Phys. Commun. **269** (2021) 108124, DOI: 10.1016/j.cpc.2021.108124,
arXiv: 2007.01725 [hep-ph].

[117] J. Braathen, S. Kanemura, M. Shimoda,
Two-loop analysis of classically scale-invariant models with extended Higgs sectors,
JHEP **03** (2021) 297, DOI: 10.1007/JHEP03(2021)297, arXiv: 2011.07580 [hep-ph].

[118] H. Bahl et al., *Tripling down on the W boson mass*, Eur. Phys. J. C **82** (2022) 944,
DOI: 10.1140/epjc/s10052-022-10934-5, arXiv: 2207.04059 [hep-ph].

[119] H. Bahl et al.,
anyH3: precise predictions for the trilinear Higgs coupling in the Standard Model and beyond,
Eur. Phys. J. C **83** (2023), [Erratum: Eur.Phys.J.C 84, 498 (2024)] 1156,
DOI: 10.1140/epjc/s10052-023-12173-8, arXiv: 2305.03015 [hep-ph].

[120] M. Aiko et al., *H-COUP Version 3: A program for one-loop corrected decays of any Higgs bosons in non-minimal Higgs models*, Comput. Phys. Commun. **301** (2024) 109231,
DOI: 10.1016/j.cpc.2024.109231, arXiv: 2311.15892 [hep-ph].

[121] M. Aiko, J. Braathen, S. Kanemura,
Leading two-loop corrections to the Higgs di-photon decay in the Inert Doublet Model (2023),
arXiv: 2307.14976 [hep-ph].

[122] P. Basler et al., *BSMPT v3 A Tool for Phase Transitions and Primordial Gravitational Waves in Extended Higgs Sectors* (2024), arXiv: 2404.19037 [hep-ph].

[123] H. Bahl et al., *Generic two-loop results for trilinear and quartic scalar self-interactions* (2025), arXiv: 2503.15645 [hep-ph].

[124] C. Grojean, G. Servant, J. D. Wells, *First-order electroweak phase transition in the standard model with a low cutoff*, Phys. Rev. D **71** (2005) 036001, DOI: 10.1103/PhysRevD.71.036001, arXiv: hep-ph/0407019.

[125] S. Kanemura, Y. Okada, E. Senaha, *Electroweak baryogenesis and quantum corrections to the triple Higgs boson coupling*, Phys. Lett. B **606** (2005) 361, DOI: 10.1016/j.physletb.2004.12.004, arXiv: hep-ph/0411354.

[126] P. Basler, M. Mühlleitner, J. Wittbrodt, *The CP-Violating 2HDM in Light of a Strong First Order Electroweak Phase Transition and Implications for Higgs Pair Production*, JHEP **03** (2018) 061, DOI: 10.1007/JHEP03(2018)061, arXiv: 1711.04097 [hep-ph].

[127] T. Biekötter et al., *Fate of electroweak symmetry in the early Universe: Non-restoration and trapped vacua in the N2HDM*, JCAP **06** (2021) 018, DOI: 10.1088/1475-7516/2021/06/018, arXiv: 2103.12707 [hep-ph].

[128] T. Biekötter et al., *The trap in the early Universe: impact on the interplay between gravitational waves and LHC physics in the 2HDM*, JCAP **03** (2023) 031, DOI: 10.1088/1475-7516/2023/03/031, arXiv: 2208.14466 [hep-ph].

[129] W. Hollik, S. Penaranda, *Yukawa coupling quantum corrections to the selfcouplings of the lightest MSSM Higgs boson*, Eur. Phys. J. C **23** (2002) 163, DOI: 10.1007/s100520100862, arXiv: hep-ph/0108245.

[130] A. Dobado et al., *Selfinteractions of the lightest MSSM Higgs boson in the large pseudoscalar mass limit*, Phys. Rev. D **66** (2002) 095016, DOI: 10.1103/PhysRevD.66.095016, arXiv: hep-ph/0208014.

[131] M. Brucherseifer, R. Gavin, M. Spira, *Minimal supersymmetric Higgs boson self-couplings: Two-loop $O(\alpha_t\alpha_s)$ corrections*, Phys. Rev. D **90** (2014) 117701, DOI: 10.1103/PhysRevD.90.117701, arXiv: 1309.3140 [hep-ph].

[132] D. T. Nhung et al., *Higher Order Corrections to the Trilinear Higgs Self-Couplings in the Real NMSSM*, JHEP **11** (2013) 181, DOI: 10.1007/JHEP11(2013)181, arXiv: 1306.3926 [hep-ph].

[133] M. Mühlleitner, D. T. Nhung, H. Ziesche, *The order $\mathcal{O}\left(\alpha_t\alpha_s\right)$ corrections to the trilinear Higgs self-couplings in the complex NMSSM*, JHEP **12** (2015) 034, DOI: 10.1007/JHEP12(2015)034, arXiv: 1506.03321 [hep-ph].

[134] C. Borschensky et al., *The trilinear Higgs self-couplings at $\mathcal{O}(\alpha_t^2)$ in the CP-violating NMSSM*, Eur. Phys. J. C **83** (2023) 118, DOI: 10.1140/epjc/s10052-023-11215-5, arXiv: 2210.02104 [hep-ph].

[135] R. Grober, M. Muhlleitner, *Composite Higgs Boson Pair Production at the LHC*, JHEP **06** (2011) 020, DOI: 10.1007/JHEP06(2011)020, arXiv: 1012.1562 [hep-ph].

[136] M. Gillioz et al., *Higgs Low-Energy Theorem (and its corrections) in Composite Models*, JHEP **10** (2012) 004, DOI: 10.1007/JHEP10(2012)004, arXiv: 1206.7120 [hep-ph].

[137] R. Gröber, M. Mühlleitner, *Higgs Pair Production in Composite Higgs Models at the ILC*, 3rd Linear Collider Forum, DESY, Hamburg, 2013, p. 352.

[138] R. Grober, M. Muhlleitner, M. Spira, *Signs of Composite Higgs Pair Production at Next-to-Leading Order*, JHEP **06** (2016) 080, DOI: 10.1007/JHEP06(2016)080, arXiv: 1602.05851 [hep-ph].

[139] S. De Curtis et al., *Composite 2-Higgs doublet model: strong effects on Higgs pair production*, JHEP **06** (2024) 063, DOI: 10.1007/JHEP06(2024)063, arXiv: 2310.10471 [hep-ph].

[140] R. S. Gupta, H. Rzehak, J. D. Wells, *How well do we need to measure Higgs boson couplings?*, Phys. Rev. D **86** (2012) 095001, DOI: 10.1103/PhysRevD.86.095001, arXiv: 1206.3560 [hep-ph].

[141] R. S. Gupta, H. Rzehak, J. D. Wells, *How well do we need to measure the Higgs boson mass and self-coupling?*, Phys. Rev. D **88** (2013) 055024, DOI: 10.1103/PhysRevD.88.055024, arXiv: 1305.6397 [hep-ph].

[142] L. Di Luzio, R. Gröber, M. Spannowsky, *Maxi-sizing the trilinear Higgs self-coupling: how large could it be?*, Eur. Phys. J. C **77** (2017) 788, DOI: 10.1140/epjc/s10052-017-5361-0, arXiv: 1704.02311 [hep-ph].

[143] G. Durieux, M. McCullough, E. Salvioni, *Charting the Higgs self-coupling boundaries*, JHEP **12** (2022), [Erratum: JHEP 02, 165 (2023)] 148, DOI: 10.1007/JHEP12(2022)148, arXiv: 2209.00666 [hep-ph].

[144] G. Durieux, M. McCullough, E. Salvioni, *Gegenbauer's Twin*, JHEP **05** (2022) 140, DOI: 10.1007/JHEP05(2022)140, arXiv: 2202.01228 [hep-ph].

[145] H. Bahl et al., in preparation.

[146] G. Marchiori for the FCC collaboration, *Higgs physics opportunities at the Future Circular Collider (https://indico.cern.ch/event/1291157/contributions/5876729/)*, Talk given at ICHEP 2024, 2024, URL: https://indico.cern.ch/event/1291157/contributions/5876729/.

[147] N. G. Deshpande, E. Ma, *Pattern of Symmetry Breaking with Two Higgs Doublets*, Phys. Rev. D **18** (1978) 2574, DOI: 10.1103/PhysRevD.18.2574.

[148] R. Barbieri, L. J. Hall, V. S. Rychkov, *Improved naturalness with a heavy Higgs: An Alternative road to LHC physics*, Phys. Rev. D **74** (2006) 015007, DOI: 10.1103/PhysRevD.74.015007, arXiv: hep-ph/0603188.

[149] J. Braathen et al., *Probing the Inert Doublet Model via Vector-Boson Fusion at a Muon Collider* (2024), arXiv: 2411.13729 [hep-ph].

[150] A. David et al., LHC Higgs Cross Section Working Group, *LHC HXSWG interim recommendations to explore the coupling structure of a Higgs-like particle* (2012), arXiv: 1209.0040 [hep-ph].

[151] J. R. Andersen et al., LHC Higgs Cross Section Working Group, *Handbook of LHC Higgs Cross Sections: 3. Higgs Properties* (2013), ed. by S. Heinemeyer et al., DOI: 10.5170/CERN-2013-004, arXiv: 1307.1347 [hep-ph].

[152] F. Maltoni, D. Pagani, X. Zhao, *Constraining the Higgs self-couplings at e^+e^- colliders*, JHEP **07** (2018) 087, DOI: 10.1007/JHEP07(2018)087, arXiv: 1802.07616 [hep-ph].

[153] M. Chiesa et al., *Measuring the quartic Higgs self-coupling at a multi-TeV muon collider*, JHEP **09** (2020) 098, DOI: 10.1007/JHEP09(2020)098, arXiv: 2003.13628 [hep-ph].

[154] M. Gonzalez-Lopez, M. J. Herrero, P. Martinez-Suarez, *Testing anomalous $H-W$ couplings and Higgs self-couplings via double and triple Higgs production at e^+e^- colliders*, Eur. Phys. J. C **81** (2021) 260, DOI: 10.1140/epjc/s10052-021-09048-1, arXiv: 2011.13915 [hep-ph].

[155] A. Papaefstathiou, G. Tetlalmatzi-Xolocotzi, *Multi-Higgs boson production with anomalous interactions at current and future proton colliders*, JHEP **06** (2024) 124, DOI: 10.1007/JHEP06(2024)124, arXiv: 2312.13562 [hep-ph].

[156] A. D. Sakharov, *Violation of CP Invariance, C asymmetry, and baryon asymmetry of the universe*, Pisma Zh. Eksp. Teor. Fiz. **5** (1967) 32, DOI: 10.1070/PU1991v034n05ABEH002497.

[157] K. Enomoto, S. Kanemura, Y. Mura, *Electroweak baryogenesis in aligned two Higgs doublet models*, JHEP **01** (2022) 104, DOI: 10.1007/JHEP01(2022)104, arXiv: 2111.13079 [hep-ph].

[158] S. Kanemura, M. Tanaka, *Strongly first-order electroweak phase transition by relatively heavy additional Higgs bosons*, Phys. Rev. D **106** (2022) 035012, DOI: 10.1103/PhysRevD.106.035012, arXiv: 2201.04791 [hep-ph].

[159] E. Asakawa et al., *Higgs boson pair production in new physics models at hadron, lepton, and photon colliders*, Phys. Rev. D **82** (2010) 115002, DOI: 10.1103/PhysRevD.82.115002, arXiv: 1009.4670 [hep-ph].

[160] G. C. Dorsch, S. J. Huber, J. M. No, *A strong electroweak phase transition in the 2HDM after LHC8*, JHEP **10** (2013) 029, DOI: 10.1007/JHEP10(2013)029, arXiv: 1305.6610 [hep-ph].

[161] G. C. Dorsch et al., *Echoes of the Electroweak Phase Transition: Discovering a second Higgs doublet through $A_0 \to ZH_0$*, Phys. Rev. Lett. **113** (2014) 211802, DOI: 10.1103/PhysRevLett.113.211802, arXiv: 1405.5537 [hep-ph].

[162] G. C. Dorsch et al., *The Higgs Vacuum Uplifted: Revisiting the Electroweak Phase Transition with a Second Higgs Doublet*, JHEP **12** (2017) 086, DOI: 10.1007/JHEP12(2017)086, arXiv: 1705.09186 [hep-ph].

[163] P. Basler et al., *Strong First Order Electroweak Phase Transition in the CP-Conserving 2HDM Revisited*, JHEP **02** (2017) 121, DOI: 10.1007/JHEP02(2017)121, arXiv: 1612.04086 [hep-ph].

[164] T. Biekötter et al., *First shot of the smoking gun: probing the electroweak phase transition in the 2HDM with novel searches for $A \to ZH$ in $\ell^+\ell^- t\bar{t}$ and $\nu\nu b\bar{b}$ final states*, JHEP **01** (2024) 107, DOI: 10.1007/JHEP01(2024)107, arXiv: 2309.17431 [hep-ph].

[165] P. Basler et al., *Di-Higgs boson peaks and top valleys: Interference effects in Higgs sector extensions*, Phys. Rev. D **101** (2020) 015019, DOI: 10.1103/PhysRevD.101.015019, arXiv: 1909.09987 [hep-ph].

[166] Anisha et al., *Two Higgs doublets, effective interactions and a strong first-order electroweak phase transition*, JHEP **08** (2022) 091, DOI: 10.1007/JHEP08(2022)091, arXiv: 2204.06966 [hep-ph].

[167] Anisha et al., *Effective 2HDM Yukawa interactions and a strong first-order electroweak phase transition*, JHEP **02** (2024) 045, DOI: 10.1007/JHEP02(2024)045, arXiv: 2311.06353 [hep-ph].

[168] L. Biermann et al., *Double and triple Higgs boson production to probe the electroweak phase transition*, Phys. Rev. D **110** (2024) 095012, DOI: 10.1103/PhysRevD.110.095012, arXiv: 2408.08043 [hep-ph].

[169] M. Kakizaki, S. Kanemura, T. Matsui, *Gravitational waves as a probe of extended scalar sectors with the first order electroweak phase transition*, Phys. Rev. D **92** (2015) 115007, DOI: 10.1103/PhysRevD.92.115007, arXiv: 1509.08394 [hep-ph].

[170] K. Hashino et al., *Synergy between measurements of gravitational waves and the triple-Higgs coupling in probing the first-order electroweak phase transition*, Phys. Rev. D **94** (2016) 015005, DOI: 10.1103/PhysRevD.94.015005, arXiv: 1604.02069 [hep-ph].

[171] K. Hashino et al., *Selecting models of first-order phase transitions using the synergy between collider and gravitational-wave experiments*, Phys. Rev. D **99** (2019) 075011, DOI: 10.1103/PhysRevD.99.075011, arXiv: 1809.04994 [hep-ph].

[172] K. Hashino, S. Kanemura, T. Takahashi,
Primordial black holes as a probe of strongly first-order electroweak phase transition,
Phys. Lett. B **833** (2022) 137261, DOI: 10.1016/j.physletb.2022.137261,
arXiv: 2111.13099 [hep-ph].

[173] K. Hashino et al.,
Probing first-order electroweak phase transition via primordial black holes in the effective field theory,
Phys. Lett. B **838** (2023) 137688, DOI: 10.1016/j.physletb.2023.137688,
arXiv: 2211.16225 [hep-ph].

[174] R. R. Florentino, S. Kanemura, M. Tanaka,
Exploring loop-induced first-order electroweak phase transition in the Higgs effective field theory,
Phys. Lett. B **856** (2024) 138940, DOI: 10.1016/j.physletb.2024.138940,
arXiv: 2406.03957 [hep-ph].

[175] S. Kanemura, M. Tanaka, K.-P. Xie,
Primordial black holes from slow phase transitions: a model-building perspective,
JHEP **06** (2024) 036, DOI: 10.1007/JHEP06(2024)036, arXiv: 2404.00646 [hep-ph].

[176] P. M. Bredt et al., *NLO electroweak corrections to multi-boson processes at a muon collider*,
JHEP **12** (2022) 138, DOI: 10.1007/JHEP12(2022)138, arXiv: 2208.09438 [hep-ph].

[177] A. Denner, S. Rode,
Automated resummation of electroweak Sudakov logarithms in diboson production at future colliders,
Eur. Phys. J. C **84** (2024) 542, DOI: 10.1140/epjc/s10052-024-12879-3,
arXiv: 2402.10503 [hep-ph].

[178] Y. Ma, D. Pagani, M. Zaro,
EW corrections and Heavy Boson Radiation at a high-energy muon collider (2024),
arXiv: 2409.09129 [hep-ph].

[179] J. de Blas et al., CLIC, *The CLIC Potential for New Physics*, **3/2018** (2018),
DOI: 10.23731/CYRM-2018-003, arXiv: 1812.02093 [hep-ph].

[180] I. Marchesini,
Triple gauge couplings and polarization at the ILC and leakage in a highly granular calorimeter,
PhD thesis, Hamburg U., 2011,
URL: https://bib-pubdb1.desy.de/record/94888/files/main.pdf.

[181] A. Rosca, *Measurement of the charged triple gauge boson couplings at the ILC*,
Nucl. Part. Phys. Proc. **273-275** (2016), ed. by M. Aguilar-Benítez et al. 2226,
DOI: 10.1016/j.nuclphysbps.2015.09.362.

[182] R. Karl, *From the Machine-Detector Interface to Electroweak Precision Measurements at the ILC — Beam-Gas Background, Beam Polarization and Triple Gauge Couplings*,
PhD thesis, Hamburg: Hamburg U., 2019, DOI: 10.3204/PUBDB-2019-03013.

[183] T. Barklow, *private communication to J. List*, 2018.

[184] J. Beyer, *Achieving Electroweak Precision at Future Electron-Positron Colliders*,
PhD thesis, Hamburg: Hamburg U. (in preparation), 2022, DOI: 10.xxxx/PUBDB-2022-xxxxx.

[185] E. Boos et al., *Strongly interacting vector bosons at TeV e+ e- linear colliders*,
Phys. Rev. D **57** (1998) 1553, DOI: 10.1103/PhysRevD.57.1553, arXiv: hep-ph/9708310.

[186] E. Boos et al., *Strongly interacting vector bosons at TeV e+- e- linear colliders: Addendum*,
Phys. Rev. D **61** (2000) 077901, DOI: 10.1103/PhysRevD.61.077901,
arXiv: hep-ph/9908409.

[187] M. Beyer et al.,
Determination of New Electroweak Parameters at the ILC - Sensitivity to New Physics,
Eur. Phys. J. C **48** (2006) 353, DOI: 10.1140/epjc/s10052-006-0038-0,
arXiv: hep-ph/0604048.

[188] C. Fleper et al., *Scattering of W and Z Bosons at High-Energy Lepton Colliders*, Eur. Phys. J. C **77** (2017) 120, DOI: 10.1140/epjc/s10052-017-4656-5, arXiv: 1607.03030 [hep-ph].

[189] A. Alboteanu, W. Kilian, J. Reuter, *Resonances and Unitarity in Weak Boson Scattering at the LHC*, JHEP **11** (2008) 010, DOI: 10.1088/1126-6708/2008/11/010, arXiv: 0806.4145 [hep-ph].

[190] W. Kilian, T. Ohl, J. Reuter, *WHIZARD: Simulating Multi-Particle Processes at LHC and ILC*, Eur. Phys. J. C **71** (2011) 1742, DOI: 10.1140/epjc/s10052-011-1742-y, arXiv: 0708.4233 [hep-ph].

[191] W. Kilian et al., *High-Energy Vector Boson Scattering after the Higgs Discovery*, Phys. Rev. D **91** (2015) 096007, DOI: 10.1103/PhysRevD.91.096007, arXiv: 1408.6207 [hep-ph].

[192] W. Kilian et al., *Resonances at the LHC beyond the Higgs boson: The scalar/tensor case*, Phys. Rev. D **93** (2016) 036004, DOI: 10.1103/PhysRevD.93.036004, arXiv: 1511.00022 [hep-ph].

[193] A. H. Hoang, *What is the Top Quark Mass?*, Ann. Rev. Nucl. Part. Sci. **70** (2020) 225, DOI: 10.1146/annurev-nucl-101918-023530, arXiv: 2004.12915 [hep-ph].

[194] The ATLAS collaboration, *Climbing to the Top of the ATLAS 13 TeV data* (2024), arXiv: 2404.10674 [hep-ex].

[195] The CMS collaboration, *Review of top quark mass measurements in CMS* (2024), arXiv: 2403.01313 [hep-ex].

[196] P. Azzi et al., *Report from Working Group 1: Standard Model Physics at the HL-LHC and HE-LHC*, CERN Yellow Rep. Monogr. **7** (2019), ed. by A. Dainese et al. 1, DOI: 10.23731/CYRM-2019-007.1, arXiv: 1902.04070 [hep-ph].

[197] S. Gusken, J. H. Kuhn, P. M. Zerwas, *Threshold Behavior of Top Production in e^+e^- Annihilation*, Phys. Lett. B **155** (1985) 185, DOI: 10.1016/0370-2693(85)90983-9.

[198] V. S. Fadin, V. A. Khoze, *Threshold Behavior of Heavy Top Production in e+ e- Collisions*, JETP Lett. **46** (1987) 525.

[199] V. S. Fadin, V. A. Khoze, *Production of a pair of heavy quarks in e+ e- annihilation in the threshold region*, Sov. J. Nucl. Phys. **48** (1988) 309.

[200] M. J. Strassler, M. E. Peskin, *The Heavy top quark threshold: QCD and the Higgs*, Phys. Rev. D **43** (1991) 1500, DOI: 10.1103/PhysRevD.43.1500.

[201] R. J. Guth, J. H. Kuhn, *Top quark threshold and radiative corrections*, Nucl. Phys. B **368** (1992) 38, DOI: 10.1016/0550-3213(92)90196-I.

[202] F. Bach et al., *Fully-differential Top-Pair Production at a Lepton Collider: From Threshold to Continuum*, JHEP **03** (2018) 184, DOI: 10.1007/JHEP03(2018)184, arXiv: 1712.02220 [hep-ph].

[203] A. H. Hoang et al., *Top - anti-top pair production close to threshold: Synopsis of recent NNLO results*, Eur. Phys. J. direct **2** (2000) 3, DOI: 10.1007/s1010500c0003, arXiv: hep-ph/0001286.

[204] A. H. Hoang, M. Stahlhofen, *The Top-Antitop Threshold at the ILC: NNLL QCD Uncertainties*, JHEP **05** (2014) 121, DOI: 10.1007/JHEP05(2014)121, arXiv: 1309.6323 [hep-ph].

[205] M. Beneke et al., *Four-fermion production near the W pair production threshold*, Nucl. Phys. B **792** (2008) 89, DOI: 10.1016/j.nuclphysb.2007.09.030, arXiv: 0707.0773 [hep-ph].

[206] M. Beneke et al., *Next-to-Next-to-Next-to-Leading Order QCD Prediction for the Top Antitop S-Wave Pair Production Cross Section Near Threshold in e^+e^- Annihilation*, Phys. Rev. Lett. **115** (2015) 192001, DOI: 10.1103/PhysRevLett.115.192001, arXiv: 1506.06864 [hep-ph].

[207] M. Beneke et al., *Near-threshold production of heavy quarks with* QQbar_threshold, Comput. Phys. Commun. **209** (2016) 96, DOI: 10.1016/j.cpc.2016.07.026, arXiv: 1605.03010 [hep-ph].

[208] P. Marquard et al., *Quark Mass Relations to Four-Loop Order in Perturbative QCD*, Phys. Rev. Lett. **114** (2015) 142002, DOI: 10.1103/PhysRevLett.114.142002, arXiv: 1502.01030 [hep-ph].

[209] A. H. Hoang et al., *The MSR mass and the $\mathcal{O}\left(\Lambda_{\text{QCD}}\right)$ renormalon sum rule*, JHEP **04** (2018) 003, DOI: 10.1007/JHEP04(2018)003, arXiv: 1704.01580 [hep-ph].

[210] M. Martinez, R. Miquel, *Multiparameter fits to the t anti-t threshold observables at a future e+ e- linear collider*, Eur. Phys. J. C **27** (2003) 49, DOI: 10.1140/epjc/s2002-01094-1, arXiv: hep-ph/0207315.

[211] T. Horiguchi et al., *Study of top quark pair production near threshold at the ILC* (2013), arXiv: 1310.0563 [hep-ex].

[212] K. Seidel et al., *Top quark mass measurements at and above threshold at CLIC*, Eur. Phys. J. C **73** (2013) 2530, DOI: 10.1140/epjc/s10052-013-2530-7, arXiv: 1303.3758 [hep-ex].

[213] H. Abramowicz et al., CLICdp, *Top-Quark Physics at the CLIC Electron-Positron Linear Collider*, JHEP **11** (2019) 003, DOI: 10.1007/JHEP11(2019)003, arXiv: 1807.02441 [hep-ex].

[214] Z. Li et al., *Top quark mass measurements at the $t\bar{t}$ threshold with CEPC*, Eur. Phys. J. C **83** (2023), [Erratum: Eur.Phys.J.C 83, 501 (2023)] 269, DOI: 10.1140/epjc/s10052-023-11421-1, arXiv: 2207.12177 [hep-ex].

[215] M. Defranchis et al., *Prospects for the $\mathrm{t\bar{t}}$ threshold scan* (), arXiv: arXiv:2503.XXXX [hep-ex].

[216] S. Poss, A. Sailer, *Luminosity Spectrum Reconstruction at Linear Colliders*, Eur. Phys. J. C **74** (2014) 2833, DOI: 10.1140/epjc/s10052-014-2833-3, arXiv: 1309.0372 [physics.ins-det].

[217] M. Boronat et al., *Top quark mass measurement in radiative events at electron-positron colliders*, Phys. Lett. B **804** (2020) 135353, DOI: 10.1016/j.physletb.2020.135353, arXiv: 1912.01275 [hep-ph].

[218] D. B. Kaplan, *Flavor at SSC energies: A New mechanism for dynamically generated fermion masses*, Nucl. Phys. B **365** (1991) 259, DOI: 10.1016/S0550-3213(05)80021-5.

[219] M. Aaboud et al., ATLAS, *Observation of Higgs boson production in association with a top quark pair at the LHC with the ATLAS detector*, Phys. Lett. B **784** (2018) 173, DOI: 10.1016/j.physletb.2018.07.035, arXiv: 1806.00425 [hep-ex].

[220] A. M. Sirunyan et al., CMS, *Observation of $\mathrm{t\bar{t}}H$ production*, Phys. Rev. Lett. **120** (2018) 231801, DOI: 10.1103/PhysRevLett.120.231801, arXiv: 1804.02610 [hep-ex].

[221] M. Cepeda et al., *Report from Working Group 2: Higgs Physics at the HL-LHC and HE-LHC*, CERN Yellow Rep. Monogr. **7** (2019), ed. by A. Dainese et al. 221, DOI: 10.23731/CYRM-2019-007.221, arXiv: 1902.00134 [hep-ph].

[222] J. Ellis et al., *Top, Higgs, Diboson and Electroweak Fit to the Standard Model Effective Field Theory*, JHEP **04** (2021) 279, DOI: 10.1007/JHEP04(2021)279, arXiv: 2012.02779 [hep-ph].

[223] J. J. Ethier et al., SMEFiT, *Combined SMEFT interpretation of Higgs, diboson, and top quark data from the LHC*, JHEP **11** (2021) 089, DOI: 10.1007/JHEP11(2021)089, arXiv: 2105.00006 [hep-ph].

[224] G. Durieux et al., *Probing top-quark couplings indirectly at Higgs factories*, Chin. Phys. C **42** (2018) 123107, DOI: 10.1088/1674-1137/42/12/123107, arXiv: 1809.03520 [hep-ph].

[225] S. Boselli, R. Hunter, A. Mitov, *Prospects for the determination of the top-quark Yukawa coupling at future e^+e^- colliders*, J. Phys. G **46** (2019) 095005, DOI: 10.1088/1361-6471/ab2e5c, arXiv: 1805.12027 [hep-ph].

[226] S. Jung et al., *Higgs, top quark, and electroweak precision measurements at future e^+e^- colliders: A combined effective field theory analysis with renormalization mixing*, Phys. Rev. D **105** (2022) 016003, DOI: 10.1103/PhysRevD.105.016003, arXiv: 2006.14631 [hep-ph].

[227] R. Yonamine et al., *Measuring the top Yukawa coupling at the ILC at $\sqrt{s} = 500$ GeV*, Phys. Rev. D **84** (2011) 014033, DOI: 10.1103/PhysRevD.84.014033, arXiv: 1104.5132 [hep-ph].

[228] M. Vos et al., *Top physics at high-energy lepton colliders* (), arXiv: 1604.08122 [hep-ex].

[229] T. Price et al., *Full simulation study of the top Yukawa coupling at the ILC at $\sqrt{s}$ = 1 TeV*, Eur. Phys. J. C **75** (2015) 309, DOI: 10.1140/epjc/s10052-015-3532-4, arXiv: 1409.7157 [hep-ex].

[230] T. Han et al., *$e^+e^- \to t\bar{t}H$ with nonstandard Higgs boson couplings*, Phys. Rev. D **61** (2000) 015006, DOI: 10.1103/PhysRevD.61.015006, arXiv: hep-ph/9908236.

[231] C. F. Berger, M. Perelstein, F. Petriello, *Top quark properties in little Higgs models*, 2005 International Linear Collider Physics and Detector Workshop and 2nd ILC Accelerator Workshop, 2005, arXiv: hep-ph/0512053.

[232] A. Djouadi, G. Moreau, F. Richard, *Resolving the A(FB)**b puzzle in an extra dimensional model with an extended gauge structure*, Nucl.Phys. **B773** (2007) 43, DOI: 10.1016/j.nuclphysb.2007.03.019, arXiv: hep-ph/0610173 [hep-ph].

[233] C. Grojean, O. Matsedonskyi, G. Panico, *Light top partners and precision physics* (2013), arXiv: 1306.4655 [hep-ph].

[234] G. Durieux, O. Matsedonskyi, *The top-quark window on compositeness at future lepton colliders*, JHEP **01** (2019) 072, DOI: 10.1007/JHEP01(2019)072, arXiv: 1807.10273 [hep-ph].

[235] J. Yoon, M. E. Peskin, *Fermion Pair Production in SO(5) $\times$ U(1) Gauge-Higgs Unification Models* (2018), arXiv: 1811.07877 [hep-ph].

[236] M. S. Amjad et al., *A precise characterisation of the top quark electro-weak vertices at the ILC*, Eur. Phys. J. C **75** (2015) 512, DOI: 10.1140/epjc/s10052-015-3746-5, arXiv: 1505.06020 [hep-ex].

[237] G. Panico, A. Wulzer, private communication, Possible deviations of couplings in framework described in [233] ().

[238] M. S. Carena et al., *Light Kaluza Klein States in Randall-Sundrum Models with Custodial SU(2)*, Nucl.Phys. **B759** (2006) 202, DOI: 10.1016/j.nuclphysb.2006.10.012, arXiv: hep-ph/0607106 [hep-ph].

[239] A. Pomarol, J. Serra, *Top Quark Compositeness: Feasibility and Implications*, Phys.Rev. **D78** (2008) 074026, DOI: 10.1103/PhysRevD.78.074026, arXiv: 0806.3247 [hep-ph].

[240] Y. Cui, T. Gherghetta, J. Stokes, *Fermion Masses in Emergent Electroweak Symmetry Breaking*, JHEP **1012** (2010) 075, DOI: 10.1007/JHEP12(2010)075, arXiv: 1006.3322 [hep-ph].

[241] D. Barducci et al., *Top pair production at a future e^+e^- machine in a composite Higgs scenario* (2015), arXiv: 1504.05407 [hep-ph].

[242] F. Richard, *Present and future constraints on top EW couplings* (2014), arXiv: 1403.2893 [hep-ph].

[243] W. Bernreuther et al., *CP-violating top quark couplings at future linear e^+e^- colliders*, Eur. Phys. J. C **78** (2018) 155, DOI: 10.1140/epjc/s10052-018-5625-3, arXiv: 1710.06737 [hep-ex].

[244] G. Durieux et al., *Global and optimal probes for the top-quark effective field theory at future lepton colliders*, JHEP **10** (2018) 168, DOI: 10.1007/JHEP10(2018)168, arXiv: 1807.02121 [hep-ph].

[245] F. Cornet-Gomez et al., *Future collider constraints on top-quark operators* (2025), arXiv: 2503.11518 [hep-ph].

[246] F. Cornet-Gomez et al., *Future collider constraints on top-quark operators* (2025), arXiv: 2502.xxxxx [hep-ex].

[247] The CMS collaboration, *Probing effective field theory operators in the associated production of top quarks with a Z boson in multilepton final states at $\sqrt{s}$ = 13 TeV*, JHEP **12** (2021) 083, DOI: 10.1007/JHEP12(2021)083, arXiv: 2107.13896 [hep-ex].

[248] E. Celada et al., *Mapping the SMEFT at high-energy colliders: from LEP and the (HL-)LHC to the FCC-ee*, JHEP **09** (2024) 091, DOI: 10.1007/JHEP09(2024)091, arXiv: 2404.12809 [hep-ph].

[249] J. ter Hoeve et al., *Connecting Scales: RGE Effects in the SMEFT at the LHC and Future Colliders* (2025), arXiv: 2502.20453 [hep-ph].

[250] Y. Afik, J. R. M. de Nova, *Entanglement and quantum tomography with top quarks at the LHC*, Eur. Phys. J. Plus **136** (2021) 907, DOI: 10.1140/epjp/s13360-021-01902-1, arXiv: 2003.02280 [quant-ph].

[251] The ATLAS collaboration, *Observation of quantum entanglement with top quarks at the ATLAS detector*, Nature **633** (2024) 542, DOI: 10.1038/s41586-024-07824-z, arXiv: 2311.07288 [hep-ex].

[252] The CMS collaboration, *Observation of quantum entanglement in top quark pair production in proton–proton collisions at $\sqrt{s} = 13$ TeV*, Rept. Prog. Phys. **87** (2024) 117801, DOI: 10.1088/1361-6633/ad7e4d, arXiv: 2406.03976 [hep-ex].

[253] The CMS collaboration, *Measurements of polarization and spin correlation and observation of entanglement in top quark pairs using lepton+jets events from proton-proton collisions at s=13 TeV*, Phys. Rev. D **110** (2024) 112016, DOI: 10.1103/PhysRevD.110.112016, arXiv: 2409.11067 [hep-ex].

[254] A. J. Barr et al., *Quantum entanglement and Bell inequality violation at colliders*, Prog. Part. Nucl. Phys. **139** (2024) 104134, DOI: 10.1016/j.ppnp.2024.104134, arXiv: 2402.07972 [hep-ph].

[255] F. Maltoni et al., *Quantum tops at circular lepton colliders*, JHEP **09** (2024) 001, DOI: 10.1007/JHEP09(2024)001, arXiv: 2404.08049 [hep-ph].

[256] C. Altomonte et al., *Prospects for quantum process tomography at high energies* (2024), arXiv: 2412.01892 [hep-ph].

[257] C. Zhang, *Effective field theory approach to top-quark decay at next-to-leading order in QCD*, Phys. Rev. D **90** (2014) 014008, DOI: 10.1103/PhysRevD.90.014008, arXiv: 1404.1264 [hep-ph].

[258] C. Degrande et al., *Automatic computations at next-to-leading order in QCD for top-quark flavor-changing neutral processes*, Phys. Rev. D **91** (2015) 034024, DOI: 10.1103/PhysRevD.91.034024, arXiv: 1412.5594 [hep-ph].

[259] G. Durieux, F. Maltoni, C. Zhang, *Global approach to top-quark flavor-changing interactions*, Phys. Rev. D **91** (2015) 074017, DOI: 10.1103/PhysRevD.91.074017, arXiv: 1412.7166 [hep-ph].

[260] A. Cerri et al., *Report from Working Group 4: Opportunities in Flavour Physics at the HL-LHC and HE-LHC*, CERN Yellow Rep. Monogr. **7** (2019), ed. by A. Dainese et al. 867, DOI: 10.23731/CYRM-2019-007.867, arXiv: 1812.07638 [hep-ph].

[261] J. A. Aguilar-Saavedra, T. Riemann, *Probing top flavor changing neutral couplings at TESLA*, 2nd Workshop of the 2nd Joint ECFA / DESY Study on Physics and Detectors for a Linear Electron Positron Collider, 2001, p. 2428, arXiv: hep-ph/0102197.

[262] H. Khanpour et al., *Single top quark production as a probe of anomalous $tq\gamma$ and tqZ couplings at the FCC-ee*, Phys. Lett. B **775** (2017) 25, DOI: 10.1016/j.physletb.2017.10.047, arXiv: 1408.2090 [hep-ph].

[263] L. Shi, C. Zhang, *Probing the top quark flavor-changing couplings at CEPC*, Chin. Phys. C **43** (2019) 113104, DOI: 10.1088/1674-1137/43/11/113104, arXiv: 1906.04573 [hep-ph].

[264] F. Esser et al., *On the coupling of axion-like particles to the top quark*, JHEP **09** (2023) 063, DOI: 10.1007/JHEP09(2023)063, arXiv: 2303.17634 [hep-ph].

[265] S. Blasi et al., *Top-philic ALP phenomenology at the LHC: the elusive mass-window*, JHEP **06** (2024) 077, DOI: 10.1007/JHEP06(2024)077, arXiv: 2311.16048 [hep-ph].

[266] A. V. Phan, S. Westhoff, *Precise tests of the axion coupling to tops*, JHEP **05** (2024) 075, DOI: 10.1007/JHEP05(2024)075, arXiv: 2312.00872 [hep-ph].

[267] A. Anuar et al., *ALP-ine quests at the LHC: hunting axion-like particles via peaks and dips in $t\bar{t}$ production*, JHEP **12** (2024) 197, DOI: 10.1007/JHEP12(2024)197, arXiv: 2404.19014 [hep-ph].

[268] Y. Hosseini, M. Mohammadi Najafabadi, *Exploring axionlike particle couplings through single top tW-channel and top pair production at the LHC*, Phys. Rev. D **110** (2024) 055026, DOI: 10.1103/PhysRevD.110.055026, arXiv: 2408.11588 [hep-ph].

[269] J. Jaeckel, M. Jankowiak, M. Spannowsky, *LHC probes the hidden sector*, Phys. Dark Univ. **2** (2013) 111, DOI: 10.1016/j.dark.2013.06.001, arXiv: 1212.3620 [hep-ph].

[270] K. Mimasu, V. Sanz, *ALPs at Colliders*, JHEP **06** (2015) 173, DOI: 10.1007/JHEP06(2015)173, arXiv: 1409.4792 [hep-ph].

[271] J. Jaeckel, M. Spannowsky, *Probing MeV to 90 GeV axion-like particles with LEP and LHC*, Phys. Lett. B **753** (2016) 482, DOI: 10.1016/j.physletb.2015.12.037, arXiv: 1509.00476 [hep-ph].

[272] N. Steinberg, J. D. Wells, *Axion-Like Particles at the ILC Giga-Z*, JHEP **08** (2021) 120, DOI: 10.1007/JHEP08(2021)120, arXiv: 2101.00520 [hep-ph].

[273] G. Polesello, *Sensitivity of the FCC-ee to decay of an axion-like particle into two photons* (2025), arXiv: 2502.08411 [hep-ph].

[274] M. Bauer et al., *Axion-Like Particles at Future Colliders*, Eur. Phys. J. C **79** (2019) 74, DOI: 10.1140/epjc/s10052-019-6587-9, arXiv: 1808.10323 [hep-ph].

[275] S. C. İnan, A. V. Kisselev, *A search for axion-like particles in light-by-light scattering at the CLIC*, JHEP **06** (2020) 183, DOI: 10.1007/JHEP06(2020)183, arXiv: 2003.01978 [hep-ph].

[276] H.-Y. Zhang et al., *Searching for axionlike particles at future electron-positron colliders*, Phys. Rev. D **104** (2021) 096008, DOI: 10.1103/PhysRevD.104.096008, arXiv: 2103.05218 [hep-ph].

[277] C.-X. Yue et al., *Prospects for detecting axionlike particles via the decay $Z \to f\bar{f}$ at future Z factories*, Phys. Rev. D **105** (2022) 115027, DOI: 10.1103/PhysRevD.105.115027, arXiv: 2204.04702 [hep-ph].

[278] H. Wang et al., *Prospects for searching for axion-like particles at the CEPC*, J. Phys. G **49** (2022) 115002, DOI: 10.1088/1361-6471/ac8f61.

[279] C.-T. Lu, *Lighting electroweak-violating ALP-lepton interactions at e+e- and ep colliders*, Phys. Rev. D **108** (2023) 115029, DOI: 10.1103/PhysRevD.108.115029, arXiv: 2210.15648 [hep-ph].

[280] K. Cheung, C. J. Ouseph, *Axionlike particle search at Higgs factories*, Phys. Rev. D **108** (2023) 035003, DOI: 10.1103/PhysRevD.108.035003, arXiv: 2303.16514 [hep-ph].

[281] J. Bonilla et al., *One-loop corrections to ALP couplings*, JHEP **11** (2021) 168, DOI: 10.1007/JHEP11(2021)168, arXiv: 2107.11392 [hep-ph].

[282] M. B. Gavela et al., *Nonresonant Searches for Axionlike Particles at the LHC*, Phys. Rev. Lett. **124** (2020) 051802, DOI: 10.1103/PhysRevLett.124.051802, arXiv: 1905.12953 [hep-ph].

[283] C.-X. Yue, H.-Y. Zhang, H. Wang, *Production of axion-like particles via vector boson fusion at future electron-positron colliders*, Eur. Phys. J. C **82** (2022) 88, DOI: 10.1140/epjc/s10052-022-10007-7, arXiv: 2112.11604 [hep-ph].

[284] P. Rebello Teles et al., *Searches for axionlike particles via $\gamma\gamma$ fusion at future e+e- colliders*, Phys. Rev. D **109** (2024) 055003, DOI: 10.1103/PhysRevD.109.055003, arXiv: 2310.17270 [hep-ex].

[285] C.-X. Yue, H. Wang, Y.-Q. Wang, *Detecting the coupling of axion-like particles with fermions at the ILC*, Phys. Lett. B **848** (2024) 138368, DOI: 10.1016/j.physletb.2023.138368, arXiv: 2311.16768 [hep-ph].

[286] S. C. İnan, A. V. Kisselev, *Analysis of axion-like particles in a top-quark pair production at the CLIC* (2025), arXiv: 2501.15500 [hep-ph].

[287] M. Chala et al., *Running in the ALPs*, Eur. Phys. J. C **81** (2021) 181, DOI: 10.1140/epjc/s10052-021-08968-2, arXiv: 2012.09017 [hep-ph].

[288] A. M. Galda, M. Neubert, S. Renner, *ALP — SMEFT interference*, JHEP **06** (2021) 135, DOI: 10.1007/JHEP06(2021)135, arXiv: 2105.01078 [hep-ph].

[289] A. Biekötter et al., *A global analysis of axion-like particle interactions using SMEFT fits*, JHEP **09** (2023) 120, DOI: 10.1007/JHEP09(2023)120, arXiv: 2307.10372 [hep-ph].

[290] A. Canepa, *Searches for Supersymmetry at the Large Hadron Collider*, Rev. Phys. **4** (2019) 100033, DOI: 10.1016/j.revip.2019.100033.

[291] G. Aad et al., ATLAS, *The quest to discover supersymmetry at the ATLAS experiment* (2024), arXiv: 2403.02455 [hep-ex].

[292] H. Baer, V. Barger, M. Savoy, *Upper bounds on sparticle masses from naturalness or how to disprove weak scale supersymmetry*, Phys. Rev. D **93** (2016) 035016, DOI: 10.1103/PhysRevD.93.035016, arXiv: 1509.02929 [hep-ph].

[293] H. Baer et al., *Physics at a Higgsino Factory*, JHEP **06** (2014) 172, DOI: 10.1007/JHEP06(2014)172, arXiv: 1404.7510 [hep-ph].

[294] G. Aad et al., ATLAS, *Searches for electroweak production of supersymmetric particles with compressed mass spectra in $\sqrt{s}$ = 13 TeV pp collisions with the ATLAS detector*, Phys. Rev. D **101** (2020) 052005, DOI: 10.1103/PhysRevD.101.052005, arXiv: 1911.12606 [hep-ex].

[295] A. Tumasyan et al., CMS, *Search for supersymmetry in final states with two or three soft leptons and missing transverse momentum in proton-proton collisions at $\sqrt{s}$ = 13 TeV*, JHEP **04** (2022) 091, DOI: 10.1007/JHEP04(2022)091, arXiv: 2111.06296 [hep-ex].

[296] H. Baer et al., *The LHC higgsino discovery plane for present and future SUSY searches*, Phys. Lett. B **810** (2020) 135777, DOI: 10.1016/j.physletb.2020.135777, arXiv: 2007.09252 [hep-ph].

[297] H. Baer et al., *New angular and other cuts to improve the Higgsino signal at the LHC*, Phys. Rev. D **105** (2022) 095017, DOI: 10.1103/PhysRevD.105.095017, arXiv: 2109.14030 [hep-ph].

[298] H. Baer et al., *ILC as a natural SUSY discovery machine and precision microscope: From light Higgsinos to tests of unification*, Phys. Rev. D **101** (2020) 095026, DOI: 10.1103/PhysRevD.101.095026, arXiv: 1912.06643 [hep-ex].

[299] M. Berggren et al., *Tackling light higgsinos at the ILC*, Eur. Phys. J. C **73** (2013) 2660, DOI: 10.1140/epjc/s10052-013-2660-y, arXiv: 1307.3566 [hep-ph].

[300] H. Baer et al., *Naturalness and light higgsinos: A powerful reason to build the ILC*, PoS **ICHEP2016** (2016) 156, DOI: 10.22323/1.282.0156, arXiv: 1611.02846 [hep-ph].

[301] M. T. Núñez Pardo de Vera, M. Berggren, J. List, *Evaluating the ILC SUSY reach in the most challenging scenario: $\tilde{\tau}$ NLSP, low ΔM , lowest cross-section*, Snowmass 2021, 2022, arXiv: 2203.15729 [hep-ph].

[302] M. T. N. Pardo de Vera, M. Berggren, J. List, *Chargino production at the ILC*, International Workshop on Future Linear Colliders, 2020, arXiv: 2002.01239 [hep-ph].

[303] M. T. Núñez Pardo de Vera, M. Berggren, J. List, *$\widetilde{\tau}$ searches at the ILC*, International Workshop on Future Linear Colliders, 2021, arXiv: 2105.08616 [hep-ph].

[304] G. Aad et al., ATLAS, *Search for chargino–neutralino pair production in final states with three leptons and missing transverse momentum in $\sqrt{s} = 13$ TeV pp collisions with the ATLAS detector*, Eur. Phys. J. C **81** (2021) 1118, DOI: 10.1140/epjc/s10052-021-09749-7, arXiv: 2106.01676 [hep-ex].

[305] *Combined search for electroweak production of winos, binos, higgsinos, and sleptons in proton-proton collisions at sqrts = 13 TeV* (2023).

[306] N. Aghanim et al., Planck, *Planck 2018 results. VI. Cosmological parameters*, Astron. Astrophys. **641** (2020), [Erratum: Astron.Astrophys. 652, C4 (2021)] A6, DOI: 10.1051/0004-6361/201833910, arXiv: 1807.06209 [astro-ph.CO].

[307] J. Aalbers et al., LZ, *First Dark Matter Search Results from the LUX-ZEPLIN (LZ) Experiment*, Phys. Rev. Lett. **131** (2023) 041002, DOI: 10.1103/PhysRevLett.131.041002, arXiv: 2207.03764 [hep-ex].

[308] M. Chakraborti, S. Heinemeyer, I. Saha, *Consistent excesses in the search for $\tilde{\chi}_2^0\tilde{\chi}_1^\pm$ wino/bino vs. Higgsino dark matter*, Eur. Phys. J. C **84** (2024) 812, DOI: 10.1140/epjc/s10052-024-13180-z, arXiv: 2403.14759 [hep-ph].

[309] D. Agin et al., *Seeking a coherent explanation of LHC excesses for compressed spectra*, Eur. Phys. J. C **84** (2024) 1218, DOI: 10.1140/epjc/s10052-024-13594-9, arXiv: 2404.12423 [hep-ph].

[310] G. Aad et al., ATLAS, *Search for new phenomena in events with an energetic jet and missing transverse momentum in pp collisions at $\sqrt{s}$ =13 TeV with the ATLAS detector*, Phys. Rev. D **103** (2021) 112006, DOI: 10.1103/PhysRevD.103.112006, arXiv: 2102.10874 [hep-ex].

[311] A. Tumasyan et al., CMS, *Search for new particles in events with energetic jets and large missing transverse momentum in proton-proton collisions at $\sqrt{s}$ = 13 TeV*, JHEP **11** (2021) 153, DOI: 10.1007/JHEP11(2021)153, arXiv: 2107.13021 [hep-ex].

[312] M. Chakraborti, S. Heinemeyer, I. Saha, *Improved $(g-2)_\mu$ Measurements and Supersymmetry*, Eur. Phys. J. C **80** (2020) 984, DOI: 10.1140/epjc/s10052-020-08504-8, arXiv: 2006.15157 [hep-ph].

[313] A. Hayrapetyan et al., CMS, *Search for a standard model-like Higgs boson in the mass range between 70 and 110 GeV in the diphoton final state in proton-proton collisions at s=13TeV*, Phys. Lett. B **860** (2025) 139067, DOI: 10.1016/j.physletb.2024.139067, arXiv: 2405.18149 [hep-ex].

[314] G. Aad et al., ATLAS, *ATLAS searches for additional scalars and exotic Higgs boson decays with the LHC Run 2 dataset* (2024), arXiv: 2405.04914 [hep-ex].

[315] T. Biekötter, S. Heinemeyer, G. Weiglein, *95.4 GeV diphoton excess at ATLAS and CMS*, Phys. Rev. D **109** (2024) 035005, DOI: 10.1103/PhysRevD.109.035005, arXiv: 2306.03889 [hep-ph].

[316] R. Barate et al., LEP Working Group for Higgs boson searches, ALEPH, DELPHI, L3, OPAL, *Search for the standard model Higgs boson at LEP*, Phys. Lett. B **565** (2003) 61, DOI: 10.1016/S0370-2693(03)00614-2, arXiv: hep-ex/0306033.

[317] T. Biekötter, M. Chakraborti, S. Heinemeyer, *A 96 GeV Higgs boson in the N2HDM*, Eur. Phys. J. C **80** (2020) 2, DOI: 10.1140/epjc/s10052-019-7561-2, arXiv: 1903.11661 [hep-ph].

[318] T. Biekötter, M. O. Olea-Romacho, *Reconciling Higgs physics and pseudo-Nambu-Goldstone dark matter in the S2HDM using a genetic algorithm*, JHEP **10** (2021) 215, DOI: 10.1007/JHEP10(2021)215, arXiv: 2108.10864 [hep-ph].

[319] T. Biekötter, S. Heinemeyer, G. Weiglein, *The CMS di-photon excess at 95 GeV in view of the LHC Run 2 results*, Phys. Lett. B **846** (2023) 138217, DOI: 10.1016/j.physletb.2023.138217, arXiv: 2303.12018 [hep-ph].

[320] S. Heinemeyer et al., *Phenomenology of a 96 GeV Higgs boson in the 2HDM with an additional singlet*, Phys. Rev. D **106** (2022) 075003, DOI: 10.1103/PhysRevD.106.075003, arXiv: 2112.11958 [hep-ph].

[321] K. Mękała, J. Reuter, A. F. Żarnecki, *Heavy neutrinos at future linear e^+e^- colliders*, JHEP **06** (2022) 010, DOI: 10.1007/JHEP06(2022)010, arXiv: 2202.06703 [hep-ph].

[322] K. Mękała, J. Reuter, A. F. Żarnecki, *Optimal search reach for heavy neutral leptons at a muon collider*, Phys. Lett. B **841** (2023) 137945, DOI: 10.1016/j.physletb.2023.137945, arXiv: 2301.02602 [hep-ph].

[323] K. Mękała, J. Reuter, A. F. Żarnecki, *Discriminating Majorana and Dirac heavy neutrinos at lepton colliders*, JHEP **03** (2024) 075, DOI: 10.1007/JHEP03(2024)075, arXiv: 2312.05223 [hep-ph].

[324] A. Sirunyan et al., CMS, *Search for heavy neutral leptons in events with three charged leptons in proton-proton collisions at $\sqrt{s}$ = 13 TeV*, Phys. Rev. Lett. **120** (2018) 221801, DOI: 10.1103/PhysRevLett.120.221801, arXiv: 1802.02965 [hep-ex].

[325] S. Pascoli, R. Ruiz, C. Weiland, *Heavy neutrinos with dynamic jet vetoes: multilepton searches at $\sqrt{s} = 14$, 27, and 100 TeV*, JHEP **06** (2019) 049, DOI: 10.1007/JHEP06(2019)049, arXiv: 1812.08750 [hep-ph].

[326] J.-J. Blaising et al., CLICdp, *Physics performance for Dark Matter searches at $\sqrt{s}$ = 3 TeV at CLIC using mono-photons and polarised beams* (2021), arXiv: 2103.06006 [hep-ex].

[327] M. Habermehl, M. Berggren, J. List, *WIMP Dark Matter at the International Linear Collider*, Phys. Rev. D **101** (2020) 075053, DOI: 10.1103/PhysRevD.101.075053, arXiv: 2001.03011 [hep-ex].

[328] J. Kalinowski et al., *Sensitivity of future linear e^+e^- colliders to processes of dark matter production with light mediator exchange*, Eur. Phys. J. C **81** (2021) 955, DOI: 10.1140/epjc/s10052-021-09758-6, arXiv: 2107.11194 [hep-ph].

[329] M. Cirelli, A. Strumia, J. Zupan, *Dark Matter* (2024), arXiv: 2406.01705 [hep-ph].

[330] J. Hisano et al., *Non-perturbative effect on thermal relic abundance of dark matter*, Phys. Lett. B **646** (2007) 34, DOI: 10.1016/j.physletb.2007.01.012, arXiv: hep-ph/0610249.

[331] M. Cirelli, A. Strumia, M. Tamburini, *Cosmology and Astrophysics of Minimal Dark Matter*, Nucl. Phys. B **787** (2007) 152, DOI: 10.1016/j.nuclphysb.2007.07.023, arXiv: 0706.4071 [hep-ph].

[332] H. Baer et al., *Dark matter production in the early Universe: beyond the thermal WIMP paradigm*, Phys. Rept. **555** (2015) 1, DOI: 10.1016/j.physrep.2014.10.002, arXiv: 1407.0017 [hep-ph].

[333] K. Harigaya et al., *Indirect Probe of Electroweak-Interacting Particles at Future Lepton Colliders*, JHEP **09** (2015) 105, DOI: 10.1007/JHEP09(2015)105, arXiv: 1504.03402 [hep-ph].

[334] L. Di Luzio, R. Gröber, G. Panico, *Probing new electroweak states via precision measurements at the LHC and future colliders*, JHEP **01** (2019) 011, DOI: 10.1007/JHEP01(2019)011, arXiv: 1810.10993 [hep-ph].

[335] K. Kajantie et al., *Is there a hot electroweak phase transition at $m_H \gtrsim m_W$?*, Phys. Rev. Lett. **77** (1996) 2887, DOI: 10.1103/PhysRevLett.77.2887, arXiv: hep-ph/9605288.

[336] A. Alves et al., *Collider and Gravitational Wave Complementarity in Exploring the Singlet Extension of the Standard Model*, JHEP **04** (2019) 052, DOI: 10.1007/JHEP04(2019)052, arXiv: 1812.09333 [hep-ph].

[337] H.-L. Li, M. Ramsey-Musolf, S. Willocq, *Probing a scalar singlet-catalyzed electroweak phase transition with resonant di-Higgs boson production in the 4b channel*, Phys. Rev. D **100** (2019) 075035, DOI: 10.1103/PhysRevD.100.075035, arXiv: 1906.05289 [hep-ph].

[338] F. Arco, S. Heinemeyer, M. Mühlleitner, *Large One-Loop Effects of BSM Triple Higgs Couplings on Double Higgs Production at e^+e^- Colliders* (2025).

[339] F. Arco et al., *Sensitivity to Triple Higgs Couplings via Di-Higgs Production in the RxSM at the (HL-)LHC and future e^+e^- Colliders* (2025), arXiv: 2502.03878 [hep-ph].

[340] C. F. Dürig, *Measuring the Higgs Self-coupling at the International Linear Collider*, PhD thesis, Hamburg: Hamburg U., 2016, DOI: 10.3204/PUBDB-2016-04283.

[341] J. de Blas et al., *Higgs Boson Studies at Future Particle Colliders*, JHEP **01** (2020) 139, DOI: 10.1007/JHEP01(2020)139, arXiv: 1905.03764 [hep-ph].

[342] R. K. Ellis et al., *Physics Briefing Book: Input for the European Strategy for Particle Physics Update 2020* (2019), arXiv: 1910.11775 [hep-ex].

[343] T. Barklow et al., *Improved Formalism for Precision Higgs Coupling Fits*, Phys. Rev. D **97** (2018) 053003, DOI: 10.1103/PhysRevD.97.053003, arXiv: 1708.08912 [hep-ph].

[344] K. Fujii et al., LCC Physics Working Group, *Tests of the Standard Model at the International Linear Collider* (2019), arXiv: 1908.11299 [hep-ex].

[345] K. Asteriadis et al., *Impact of Next-to-Leading-Order Weak Standard-Model-Effective-Field-Theory Corrections in $e^+e^- \to ZH$*, Phys. Rev. Lett. **133** (2024) 231801, DOI: 10.1103/PhysRevLett.133.231801, arXiv: 2406.03557 [hep-ph].

[346] K. Asteriadis et al., *The $e^+e^- \to ZH$ Process in the SMEFT Beyond Leading Order* (2024), arXiv: 2409.11466 [hep-ph].

[347] B. Badelek et al., ECFA/DESY Photon Collider Working Group, *TESLA: The Superconducting electron positron linear collider with an integrated X-ray laser laboratory. Technical design report. Part 6. Appendices. Chapter 1. Photon collider at TESLA*, Int. J. Mod. Phys. A **19** (2004) 5097, DOI: 10.1142/S0217751X04020737, arXiv: hep-ex/0108012.

[348] I. Watanabe et al., *Gamma gamma collider as an option of JLC* (1998).

[349] I. F. Ginzburg et al., *Colliding gamma e and gamma gamma Beams Based on the Single Pass Accelerators (of Vlepp Type)*, Nucl. Instrum. Meth. **205** (1983) 47, DOI: 10.1016/0167-5087(83)90173-4.

[350] K. Yokoya, *Accelerator aspects of gamma gamma colliders*, Nucl. Instrum. Meth. A **455** (2000), ed. by T. Hirose, R. Hamatsu 25, DOI: 10.1016/S0168-9002(00)00687-2.

[351] E. Boos et al., *Gold plated processes at photon colliders*, Nucl. Instrum. Meth. A **472** (2001), ed. by R. D. Heuer, V. I. Telnov, N. J. Walker 100, DOI: 10.1016/S0168-9002(01)01168-8, arXiv: hep-ph/0103090.

[352] I. F. Ginzburg, I. P. Ivanov, *CP odd anomalous interactions of Higgs boson in its production at photon colliders*, Eur. Phys. J. C **22** (2001) 411, DOI: 10.1007/s100520100817, arXiv: hep-ph/0004069.

[353] M. Kramer et al., *Prospects of measuring the parity of Higgs particles*, Z. Phys. C **64** (1994) 21, DOI: 10.1007/BF01557231, arXiv: hep-ph/9404280.

[354] V. I. Telnov, *Prospects of high energy photon colliders*, Nucl. Part. Phys. Proc. **273-275** (2016), ed. by M. Aguilar-Benítez et al. 219, DOI: 10.1016/j.nuclphysbps.2015.09.029.

[355] M. M. Muhlleitner, *Higgs boson search at e+ e- and photon linear colliders*, Acta Phys. Polon. B **37** (2006), ed. by Z. Ajduk, M. Krawczyk, A. K. Wroblewski 1127, arXiv: hep-ph/0512232.

[356] M. M. Muhlleitner, P. M. Zerwas, *Elements of physics with a photon collider*, Acta Phys. Polon. B **37** (2006), ed. by Z. Ajduk, M. Krawczyk, A. K. Wroblewski 1021, arXiv: hep-ph/0511339.

[357] S. Kanemura, S. Moretti, K. Odagiri, *Heavy charged Higgs boson production at next generation e+- gamma colliders*, Eur. Phys. J. C **22** (2001) 401, DOI: 10.1007/s100520100828, arXiv: hep-ph/0104180.

[358] S. Moretti, S. Kanemura, *Heavy charged Higgs boson production at next generation gamma gamma colliders*, Eur. Phys. J. C **29** (2003) 19, DOI: 10.1140/epjc/s2003-01173-9, arXiv: hep-ph/0211055.

[359] T. Abe et al., *Linear Collider Physics Resource Book for Snowmass 2001 - Part 4: Theoretical, Accelerator, and Experimental Options* (2001), arXiv: hep-ex/0106058.

[360] A. Arbey et al., *Physics at the e+ e- Linear Collider*, Eur. Phys. J. C **75** (2015), ed. by G. Moortgat-Pick et al. 371, DOI: 10.1140/epjc/s10052-015-3511-9, arXiv: 1504.01726 [hep-ph].

[361] J. F. Gunion, P. C. Martin, *Prospects for and implications of measuring the Higgs to photon-photon branching ratio at the next linear e+ e- collider*, Phys. Rev. Lett. **78** (1997) 4541, DOI: 10.1103/PhysRevLett.78.4541, arXiv: hep-ph/9607360.

[362] G. V. Jikia, *Higgs boson pair production in high-energy photon-photon collisions*, Nucl. Phys. B **412** (1994) 57, DOI: 10.1016/0550-3213(94)90494-4.

[363] R. Belusevic, G. Jikia, *Higgs selfcoupling in gamma gamma collisions*, Phys. Rev. D **70** (2004) 073017, DOI: 10.1103/PhysRevD.70.073017, arXiv: hep-ph/0403303.

[364] T. Takahashi et al., *Simulation Study of gamma gamma —> hh in a Photon Collider*, International Linear Collider Workshop (LCWS08 and ILC08), 2009, arXiv: 0902.3377 [hep-ex].

[365] A. Bharucha et al., *Composite Higgs revealed in Higgs pair photo-production at future colliders*, JHEP **09** (2021) 069, DOI: 10.1007/JHEP09(2021)069, arXiv: 2012.09470 [hep-ph].

[366] M. Berger et al., *Di-Higgs production at a gamma-gamma collider*, 2025.

[367] I. Ginzburg, M. Krawczyk, *Testing Higgs Physics at the Photon Collider* (2013), arXiv: 1310.5881 [hep-ph].

[368] V. I. Telnov, *Gamma-gamma collider with $W_{\gamma\gamma} \leq$ 12 GeV based on the 17.5 GeV SC linac of the European XFEL*, JINST **15** (2020) P10028, DOI: 10.1088/1748-0221/15/10/P10028, arXiv: 2007.14003 [physics.acc-ph].

[369] K. I. Beloborodov et al., *Opportunities for studying C-even resonances at a 3–12 GeV photon collider*, Eur. Phys. J. C **83** (2023) 359, DOI: 10.1140/epjc/s10052-023-11533-8, arXiv: 2202.04468 [hep-ex].

[370] J. F. Gunion, T. Han, R. Sobey, *Measuring the coupling of a Higgs boson to ZZ at linear colliders*, Phys. Lett. B **429** (1998) 79, DOI: 10.1016/S0370-2693(98)00450-X, arXiv: hep-ph/9801317.

[371] B. Grzadkowski, J. F. Gunion, *Using back scattered laser beams to detect CP violation in the neutral Higgs sector*, Phys. Lett. B **294** (1992) 361, DOI: 10.1016/0370-2693(92)91534-G, arXiv: hep-ph/9206262.

[372] R. M. Godbole et al., *Probing CP-violating Higgs contributions in gamma gamma —> f anti-f through fermion polarization*, Phys. Rev. D **74** (2006), [Erratum: Phys.Rev.D 74, 119901 (2006)] 095006, DOI: 10.1103/PhysRevD.74.119901, arXiv: hep-ph/0609113.

[373] K. Fujii et al., LCC Physics Working Group, *Implications of the 750 GeV gamma-gamma Resonance as a Case Study for the International Linear Collider* (2016), arXiv: 1607.03829 [hep-ph].

[374] P. Aurenche et al., *Gamma gamma physics*, CERN Workshop on LEP2 Physics (followed by 2nd meeting, 15-16 Jun 1995 and 3rd meeting 2-3 Nov 1995), 1996, arXiv: hep-ph/9601317.

[375] A. Vogt, *Real photon structure at an e+ e- linear collider*, Nucl. Phys. B Proc. Suppl. **82** (2000), ed. by S. Soldner-Rembold 394, DOI: 10.1016/S0920-5632(00)00184-5, arXiv: hep-ph/9908315.

[376] I. F. Ginzburg et al., *The $W^{\pm}$ Boson Production on the Colliding e^+e^-, γe and $\gamma\gamma$ Beams*, Nucl. Phys. B **228** (1983), [Erratum: Nucl.Phys.B 243, 550–550 (1984)] 285, DOI: 10.1016/0550-3213(83)90325-5.

[377] J. Ellis et al., *Light-by-light scattering at future e^+e^- colliders*, Eur. Phys. J. C **82** (2022) 634, DOI: 10.1140/epjc/s10052-022-10565-w, arXiv: 2203.17111 [hep-ph].

[378] T. Kon, *Polarization effects in scalar lepton production at high-energy gamma gamma colliders*, Phys. Lett. B **316** (1993) 181, DOI: 10.1016/0370-2693(93)90677-A, arXiv: hep-ph/9307257.

[379] T. Kon, *Heavy selectron production with exotic signature in R-parity breaking SUSY models at e gamma colliders*, Nucl. Instrum. Meth. A **472** (2001), ed. by R. D. Heuer, V. I. Telnov, N. J. Walker 239, DOI: 10.1016/S0168-9002(01)01190-1.

[380] M. Alabau Pons et al., *Optimization of the e- e- option for the ILC*, Conf. Proc. C **060626** (2006), ed. by C. Prior 685, arXiv: physics/0609043.

[381] J. Cao, Y.-Q. Li, Y.-B. Liu, *Searching for the doubly charged scalars in the Georgi–Machacek model via $\gamma\gamma$ collisions at the ILC*, Int. J. Mod. Phys. A **33** (2018) 1841003, DOI: 10.1142/S0217751X18410038.

[382] Y. Yu, Y.-P. Bi, J.-F. Shen, *Associated production of the doubly-charged scalar pair with the Higgs boson in the Georgi–Machacek model at the ILC*, Phys. Lett. B **759** (2016) 513, DOI: 10.1016/j.physletb.2016.06.014.

[383] V. D. Barger et al., *Production of weak bosons and Higgs bosons in e- e- collisions*, Phys. Rev. D **50** (1994) 6704, DOI: 10.1103/PhysRevD.50.6704, arXiv: hep-ph/9404335.

[384] P. Minkowski, *'Central production' of scalars in e- e- collisions*, Int. J. Mod. Phys. A **13** (1998), ed. by C. A. Heusch 2255, DOI: 10.1142/S0217751X98001050.

[385] T.-K. Chen et al., *95 GeV Higgs boson in the Georgi-Machacek model*, Phys. Rev. D **109** (2024) 075043, DOI: 10.1103/PhysRevD.109.075043, arXiv: 2312.13239 [hep-ph].

[386] T. Asaka, T. Tsuyuki, *Seesaw mechanism at electron-electron colliders*, Phys. Rev. D **92** (2015) 094012, DOI: 10.1103/PhysRevD.92.094012, arXiv: 1508.04937 [hep-ph].

[387] S. Banerjee et al., *Prospects of Heavy Neutrino Searches at Future Lepton Colliders*, Phys. Rev. D **92** (2015) 075002, DOI: 10.1103/PhysRevD.92.075002, arXiv: 1503.05491 [hep-ph].

[388] C. Greub, P. Minkowski, *Heavy majorana neutrinos in e- e- collisions*, eConf **C960625** (1996), ed. by C. A. Heusch NEW149, DOI: 10.1142/S0217751X98001153, arXiv: hep-ph/9612340.

[389] D. R. Walz, J. Jurow, E. L. Garwin, *Water Cooled Beam Dumps and Collimators for the Stanford Linear Accelerator*, IEEE Trans. Nucl. Sci. **12** (1965) 867, DOI: 10.1109/TNS.1965.4323748.

[390] M. Wiseman et al., *High Power Electron Beam Dumps at CEBAF*, Conf. Proc. C **970512** (1997) 3761.

[391] P. Satyamurthy et al., *Design of an 18-MW vortex flow water beam dump for 500-GeV electrons/positrons of an international linear collider*, Nucl. Instrum. Meth. A **679** (2012) 67, DOI: 10.1016/j.nima.2012.01.075.

[392] C. Antel et al., *Feebly-interacting particles: FIPs 2022 Workshop Report*, Eur. Phys. J. C **83** (2023) 1122, DOI: 10.1140/epjc/s10052-023-12168-5, arXiv: 2305.01715 [hep-ph].

[393] Y. Sakaki, D. Ueda, *Searching for new light particles at the international linear collider main beam dump*, Phys. Rev. D **103** (2021) 035024, DOI: 10.1103/PhysRevD.103.035024, arXiv: 2009.13790 [hep-ph].

[394] O. Lantwin, *The BDF/SHiP experiment at the ECN3 high-intensity beam facility at the CERN SPS*, PoS **LHCP2024** (2025) 093, DOI: 10.22323/1.478.0093.

[395] K. Asai et al., *New physics searches at the ILC positron and electron beam dumps*, JHEP **09** (2021) 183, DOI: 10.1007/JHEP09(2021)183, arXiv: 2105.13768 [hep-ph].

[396] Z. Bai et al., *New physics searches with an optical dump at LUXE*, Phys. Rev. D **106** (2022) 115034, DOI: 10.1103/PhysRevD.106.115034, arXiv: 2107.13554 [hep-ph].

[397] I. Schulthess, F. Meloni, *New Physics Search with the Optical Dump Concept at Future Colliders* (2025), arXiv: 2503.20996 [hep-ph].

[398] M. M. Nojiri et al., *First evaluation of meson and τ lepton spectra and search for heavy neutral leptons at ILC beam dump*, JHEP **12** (2022) 145, DOI: 10.1007/JHEP12(2022)145, arXiv: 2206.13523 [hep-ph].

[399] K. Asai et al., *Sub-GeV dark matter search at ILC beam dumps*, JHEP **02** (2024) 129, DOI: 10.1007/JHEP02(2024)129, arXiv: 2301.03816 [hep-ph].

[400] D. L. Burke et al., *Positron production in multi - photon light by light scattering*, Phys. Rev. Lett. **79** (1997) 1626, DOI: 10.1103/PhysRevLett.79.1626.

[401] D. Reis, S. Meuren, *E-320 Progress in FY24 and Plans for FY25*, 2024 FACET-II PAC & User Meeting (SLAC, US), 2024, URL: https://indico.slac.stanford.edu/event/9280/contributions/10855/.

[402] H. Abramowicz et al., *Conceptual design report for the LUXE experiment*, Eur. Phys. J. ST **230** (2021) 2445, DOI: 10.1140/epjs/s11734-021-00249-z, arXiv: 2102.02032 [hep-ex].

[403] H. Abramowicz et al., LUXE, *Technical Design Report for the LUXE experiment*, Eur. Phys. J. ST **233** (2024) 1709, DOI: 10.1140/epjs/s11734-024-01164-9, arXiv: 2308.00515 [hep-ex].

[404] C. N. Danson et al., *Petawatt and Exawatt Class Lasers Worldwide*, High Power Laser Science and Engineering **7** (2019) e54, DOI: 10.1017/hpl.2019.36, (visited on 31/10/2023).

[405] T. G. Blackburn et al., *Reaching supercritical field strengths with intense lasers*, New J. Phys. **21** (2019) 053040, DOI: 10.1088/1367-2630/ab1e0d, arXiv: 1807.03730 [physics.plasm-ph].

[406] K. Qu, S. Meuren, N. J. Fisch, *Signature of Collective Plasma Effects in Beam-Driven QED Cascades*, Phys. Rev. Lett. **127** (2021) 095001, DOI: 10.1103/PhysRevLett.127.095001, arXiv: 2001.02590 [physics.plasm-ph].

[407] D. Lai, *Physics in Very Strong Magnetic Fields: Introduction and Overview*, Space Sci. Rev. **191** (2015) 13, DOI: 10.1007/s11214-015-0137-z, arXiv: 1411.7995 [astro-ph.HE].

[408] S. P. Kim, *Astrophysics in Strong Electromagnetic Fields and Laboratory Astrophysics*, 15th Marcel Grossmann Meeting on Recent Developments in Theoretical and Experimental General Relativity, Astrophysics, and Relativistic Field Theories, 2019, arXiv: 1905.13439 [gr-qc].

[409] D. Seipt, B. King, *Spin- and polarization-dependent locally-constant-field-approximation rates for nonlinear Compton and Breit-Wheeler processes*, Phys. Rev. A **102** (2020) 052805, DOI: 10.1103/PhysRevA.102.052805, arXiv: 2007.11837 [physics.plasm-ph].

[410] T. G. Blackburn, B. King, *Higher fidelity simulations of nonlinear Breit–Wheeler pair creation in intense laser pulses*, Eur. Phys. J. C **82** (2022) 44, DOI: 10.1140/epjc/s10052-021-09955-3, arXiv: 2108.10883 [hep-ph].

[411] D. Seipt, M. Samuelsson, T. Blackburn,
Nonlinear Breit–Wheeler pair production using polarized photons from inverse compton scattering,
Plasma Phys. Control. Fusion **67** (2025) 035002, DOI: 10.1088/1361-6587/adaa77,
arXiv: 2411.08559 [hep-ph].

[412] A. Fedotov et al., *Advances in QED with intense background fields*, Phys. Rept. **1010** (2023) 1,
DOI: 10.1016/j.physrep.2023.01.003, arXiv: 2203.00019 [hep-ph].

[413] K. Yokoya, P. Chen, *Beam-beam phenomena in linear colliders*,
Lect. Notes Phys. **400** (1992), ed. by M. Dienes, M. Month, S. Turner 415,
DOI: 10.1007/3-540-55250-2_37.

[414] K. Yokoya, *Beam-beam interaction in linear collider*,
AIP Conf. Proc. **592** (2001), ed. by S. I. Kurokawa et al. 185, DOI: 10.1063/1.1420416.

[415] D. Schulte, *High-energy beam-beam effects in CLIC* (1999).

[416] T. Barklow et al.,
Beam delivery and beamstrahlung considerations for ultra-high energy linear colliders,
JINST **18** (2023) P09022, DOI: 10.1088/1748-0221/18/09/P09022,
arXiv: 2305.00573 [physics.acc-ph].

[417] D. Schulte,
Study of Electromagnetic and Hadronic Background in the Interaction Region of the TESLA Collider,
PhD thesis, Hamburg U., 1997.

[418] P. Chen et al., *CAIN: Conglomerat d'ABEL et d'interactions nonlineaires*,
Nucl. Instrum. Meth. A **355** (1995) 107, DOI: 10.1016/0168-9002(94)01186-9.

[419] M. Filipovic et al., *Effect of transverse displacement of charged particle beams on quantum electrodynamic processes during their collision*, Kvantovaya Elektron. **51** (2021) 807,
DOI: 10.1070/QEL17606.

[420] V. Yakimenko et al., *Prospect of Studying Nonperturbative QED with Beam-Beam Collisions*,
Phys. Rev. Lett. **122** (2019) 190404, DOI: 10.1103/PhysRevLett.122.190404,
arXiv: 1807.09271 [physics.plasm-ph].

[421] G. Aad et al., ATLAS, *Observation of a new particle in the search for the Standard Model Higgs boson with the ATLAS detector at the LHC*, Phys. Lett. B **716** (2012) 1,
DOI: 10.1016/j.physletb.2012.08.020, arXiv: 1207.7214 [hep-ex].

[422] P. C. Bhat, CMS, *Observation of a Higgs-like Boson in CMS at the LHC*,
Nucl. Phys. B Proc. Suppl. **234** (2013), ed. by S. Narison 7,
DOI: 10.1016/j.nuclphysbps.2012.11.003.

[423] ICFA, *Preparation for the ILC Pre-Lab*, 2020, URL: https://icfa.hep.net/wp-content/uploads/ICFA_release_of_ILC_IDT_Proposal.pdf.

[424] KEK, the IDT, *Framework for the ILC Technology Network*, 2023,
URL: https://www2.kek.jp/kokusai/IDT/ITN_Framework20230602.pdf.

[425] G. Moortgat-Pick et al., *R&D for positron sources at high-energy lepton colliders*,
PoS **EPS-HEP2023** (2024) 626, DOI: 10.22323/1.449.0626.

[426] N. Walker, *The European XFEL Experience and Lessons Learned*,
International Workshop on Future Linear Colliders (LCWS2017), Strasbourg, France, 2017,
URL: https://agenda.linearcollider.org/event/7645/contributions/39682/attachments/32185/48802/LCWS17-NJW.pdf.

[427] D. Broemmelsiek et al., *Record High-Gradient SRF Beam Acceleration at Fermilab*,
New J. Phys. **20** (2018) 113018, DOI: 10.1088/1367-2630/aaec57.

[428] Y. Yamamoto et al., *Stable Beam Operation at 33 MV/m in STF-2 Cryomodules at KEK*,
20th Int. Conf. on RF Superconductivity SRF2019, JACoW Publishing, East LAnsing,, MI, USA, 2021,
p. 382, URL: https://jacow.org/srf2021/papers/tupfav003.pdf.

[429] S. Posen et al., *Ultralow Surface Resistance via Vacuum Heat Treatment of Superconducting Radio-Frequency Cavities*, Phys. Rev. Applied **13** (2020) 014024, DOI: 10.1103/PhysRevApplied.13.014024.

[430] W. Pan et al., *High Q and high gradient performance of the first medium-temperature baking 1.3 GHz cryomodule*, Phys. Rev. Accel. Beams **27** (9 2024) 092003, DOI: 10.1103/PhysRevAccelBeams.27.092003.

[431] A. Grassellino et al., *Accelerating fields up to 49 MV/m in TESLA-shape superconducting RF niobium cavities via 75C vacuum bake*, 2018, arXiv: 1806.09824 [physics.acc-ph].

[432] L. Steder et al., *Further improvement of medium temperature heat treated SRF cavities for high gradients*, 2024, arXiv: 2407.12570 [physics.acc-ph].

[433] M. Martinello et al., *Plasma Processing for In-Situ Field Emission Mitigation of Superconducting Radiofrequency (SRF) Cryomodules*, 2022, arXiv: 2203.12442 [physics.acc-ph].

[434] J. Branlard et al., *Four Years of Successful Operation of the European XFEL*, JACoW **SRF2021** (2022) MOOFAV06, DOI: 10.18429/JACoW-SRF2021-MOOFAV06.

[435] C. Schmidt et al., *Operational Experience with the European XFEL SRF Linac*, JACoW **SRF2023** (2023) MOIXA06, DOI: 10.18429/JACoW-SRF2023-MOIXA06.

[436] C. Gohil et al., *Luminosity performance of the Compact Linear Collider at 380 GeV with static and dynamic imperfections*, Phys. Rev. Accel. Beams **23** (2020) 101001, DOI: 10.1103/PhysRevAccelBeams.23.101001, arXiv: 2009.01184 [physics.acc-ph].

[437] O. Toshiyuki, *Present design of ILC BDS*, LCWS2024 (2024).

[438] R. Appleby et al., *Improved 2 mrad crossing angle layout for the International Linear Collider*, Proceedings of PAC 2007, THPMN077 (2007).

[439] R. B. Appleby et al., *The 2 mrad crossing angle scheme for the International Linear Collider*, Proceedings of EPAC 2008, MOPP005 (2008).

[440] ILC Collaboration, *ILC Baseline Conceptual Design Report, beam delivery section*, http://www.linearcollider.org/ (2006).

[441] G. Blair, *Beam Delivery System in ILC*, Proceedings of EPAC 2006, WEYPA01 (2006).

[442] ILC Collaboration, *ILC Baseline Reference Design Report, Accelerator*, ILC-REPORT-2207-001 http://ilcdoc.linearcollider.org/ **3** (2007).

[443] Y. Nosochkov et al., *14 mrad Extraction Line Optics for Push-Pull*, SLAC-PUB-12856 (2007).

[444] O. N. et al, *Technical Challenges for Head-On Collisions and Extraction at the ILC*, Proceedings of EPAC 2006 (2006).

[445] V. Cilento et al., *Dual beam delivery system serving two interaction regions for the Compact Linear Collider*, Phys. Rev. Accel. Beams **24** (2021).

[446] O. R. B. Garcia, *Beam dynamics in the final focus section of the future linear collider*, Ph.D. thesis, Orsay, LAL, 2015 - CERN-THESIS-2015-115 (2015).

[447] V. Telnov, *The lay-out of the photon collider at the international linear collider*, Pramana **69** (2007).

[448] V. Telnov, *Optimization of the beam crossing angle at the ILC for e^+e^- and $\gamma\gamma$ collisions*, J. Instrum. 13, P03020 **13** (2018).

[449] S. Bousson et al., *in European Strategy for Particle Physics - Accelerator R&D Roadmap*, ed. by N. Mounet, CERN Yellow Reports: Monographs, CERN-2022-001 (CERN, Geneva, 2022), DOI: 10.23731/CYRM-2022-001.

[450] S. Belomestnykh et al., *Key directions for research and development of superconducting radio frequency cavities*, 2022, arXiv: 2204.01178 [physics.acc-ph].

[451] S. Posen et al., *Nb_3Sn Superconducting Radiofrequency Cavities: a Maturing Technology for Particle Accelerators and Detectors*, 2022, arXiv: 2203.06752 [physics.acc-ph].

[452] A.-M. Valente-Feliciano et al., *Next-Generation Superconducting RF Technology based on Advanced Thin Film Technologies and Innovative Materials for Accelerator Enhanced Performance and Energy Reach*, 2022, arXiv: 2204.02536 [physics.acc-ph].

[453] H. Padamsee, J. Knobloch, T. Hays, *RF Superconductivity for Accelerators*, John Wiley & Sons, 1998.

[454] D. Bafia et al., *Gradients of 50 MV/m in TESLA shaped cavities via modified low temperature bake*, 19th Int. Conf. on RF Superconductivity SRF2019, JACoW Publishing, Dresden, Germany, 2019, p. 586, URL: http://dx.doi.org/10.18429/JACoW-SRF2019-TUP061.

[455] S. Belomestnykh et al., *Superconducting radio frequency linear collider HELEN*, Journal of Instrumentation **18** (2023) P09039, DOI: 10.1088/1748-0221/18/09/P09039.

[456] R. B. Neal, *Consideration of the use of feedback in a traveling wave superconducting accelerator*, tech. rep. SLAC-PUB-437, 1968.

[457] V. Yakovlev et al., *Progress towards development of a superconducting traveling wave accelerating structure*, Proceedings of 22nd Particle Accel. Conf. PAC2007, Albuquerque, NM, USA, 2007, p. 2182, URL: https://accelconf.web.cern.ch/p07/PAPERS/WEPMN066.PDF.

[458] S. Belomestnykh et al., *HELEN: Traveling wave SRF Linear Collider Higgs factory*, Proceedings of the 14th Intern. Particle Accel. Conf. IPAC2023, Venice, Italy, 2023, p. 788, DOI: 10.18429/JACoW-IPAC2023-MOPL098.

[459] V. Shemelin, H. Padamsee, V. Yakovlev, *Optimization of a Traveling Wave SRF Cavity for Upgrading the International Linear Collider*, JACoW **SRF2021** (2022) WEOCAV04, DOI: 10.18429/JACoW-SRF2021-WEOCAV04, arXiv: 2105.12276 [physics.acc-ph].

[460] F. Furuta et al., *Progress and challenges in traveling-wave (TW) SRF cavity*, Proceedings of the 32nd Linear Accel. Conf. LINAC2024, Chicago, IL, USA, 2024, p. 621, DOI: 10.18429/JACoW-LINAC2024-THAA009.

[461] S. Posen et al., *Advances in Nb_3Sn superconducting radiofrequency cavities towards first practical accelerator applications*, Supercond. Sci. Technol. **34** (2021) 025007, DOI: 10.1088/1361-6668/abc7f7.

[462] S. Posen, M. Liepe, D. L. Hall, *Proof-of-principle demonstration of Nb_3Sn superconducting radiofrequency cavities for high Q_0 applications*, Appl. Phys. Lett. **106** (2015) 082601, DOI: 10.1063/1.4913247.

[463] S. Posen, D. L. Hall, *Nb_3Sn superconducting radiofrequency cavities: fabrication, results, properties, and prospects*, Supercond. Sci. Technol. **30** (2017) 033004, DOI: 10.1088/1361-6668/30/3/033004.

[464] S. Posen et al., *Nb_3Sn superconducting radiofrequency cavities: a maturing technology for particle accelerators and detectors*, arXiv:2203.06752 [physics.acc-ph], 2022, arXiv: 2203.06752 [physics.acc-ph].

[465] A. Gurevich, *Enhancement of rf breakdown field of superconductors by multilayer coating*, Applied Physics Letters **88** (2006) 012511, DOI: 10.1063/1.2162264.

[466] A. Gurevich, *Maximum screening fields of superconducting multilayer structures*, AIP Advances **5** (2015) 017112, DOI: 10.1063/1.4905711.

[467] T. Kubo, *Multilayer coating for higher accelerating fields in superconducting radio-frequency cavities: a review of theoretical aspects*, Superconductor Science and Technology **30** (2016) 023001, DOI: 10.1088/1361-6668/30/2/023001.

[468] H. Ito et al., *Lower critical field measurement of NbN multilayer thin film superconductor at KEK*, 19th International Conference on RF Superconductivity (SRF 2019), 2019, p. 632, DOI: 10.18429/JACoW-SRF2019-TUP078, arXiv: 1907.03410 [physics.acc-ph].

[469] I. González Díaz-Palacio et al., *Thermal annealing of superconducting niobium titanium nitride thin films deposited by plasma-enhanced atomic layer deposition*, Journal of Applied Physics **134** (2023), DOI: 10.1063/5.0155557.

[470] M. Asaduzzaman et al., *Evidence for current suppression in superconductor–superconductor bilayers*, Superconductor Science and Technology **37** (2023) 025002, DOI: 10.1088/1361-6668/ad1462.

[471] C. Z. Antoine et al., *Optimization of tailored multilayer superconductors for RF application and protection against premature vortex penetration*, Superconductor Science and Technology **32** (2019) 085005, DOI: 10.1088/1361-6668/ab1bf1.

[472] C. Antoine et al., *Characterization of superconducting nanometric multilayer samples for superconducting rf applications: First evidence of magnetic screening effect*, Physical Review Special Topics—Accelerators and Beams **13** (2010) 121001, DOI: 10.1103/PhysRevSTAB.13.121001.

[473] D. Tikhonov et al., *Superconducting Thin Films Characterization at HZB with the Quadrupole Resonator*, Proceedings of 19th International Conference on RF Superconductivity (SRF 2019), 2019, p. 616, DOI: 10.18429/JACoW-SRF2019-TUP073.

[474] S. Keckert et al., *RF characterization of an SI-S'multilayer sample*, 19th International Conference on RF Superconductivity (SRF'19), Dresden, Germany, 30 June-05 July 2019, JACOW Publishing, Geneva, Switzerland, 2019, p. 800, DOI: 10.18429/JACoW-SRF2019-THFUA1.

[475] Y. Kalboussi et al., *Surface Engineering by ALD for Superconducting RF Cavities*, 21th International Conference on RF Superconductivity (SRF'23), Grand Rapids, MI, USA, 25-30 June 2023, JACOW Publishing, Geneva, Switzerland, 2023, p. 615, DOI: 10.18429/JACoW-SRF2023-WEIBA01.

[476] I. Syratchev, *High efficiency klystron technologies*, Workshop on efficient RF sources, 2022, URL: https://indico.cern.ch/event/1138197/contributions/4821294/.

[477] M. Breidenbach et al., *Sustainability Strategy for the Cool Copper Collider*, PRX Energy **2** (2023) 047001.

[478] E. A. Nanni et al., *Status and future plans for C^3 R&D*, JINST **18** (2023) P09040, DOI: 10.1088/1748-0221/18/09/P09040.

[479] M. Schneider et al., *High gradient C-band cryogenic copper silver structures*, APS April Meeting Abstracts, vol. 2024, 2024, T08.

[480] C. Liu et al., *High-Power Test of a C-band Linear Accelerating Structure with an RFSoC-based LLRF System* (2025), arXiv: 2502.10507 [physics.acc-ph].

[481] A. Dhar, *Vibration Analysis of Cryogenically Cooled Accelerating Structures*, tech. rep. SLAC-PUB-17776, SLAC National Accelerator Laboratory (SLAC), Menlo Park, CA (United States . . ., 2024.

[482] H. Xu et al., *DESIGN OF A TWO-CELL C-BAND ACCELERATOR CAVITY WITH HIGHER-ORDER MODE DAMPING* ().

[483] H. van der Graaf et al., *The alignment of the accelerator modules of the Cool Copper Collider C3 with the Rasnik 3-point alignment system*, EPJ Web of Conferences, vol. 315, EDP Sciences, 2024, p. 02018.

[484] C. Liu et al., *Next Generation LLRF Control Platform for Compact C-band Linear Accelerator*, EPJ Web of Conferences, vol. 315, EDP Sciences, 2024, p. 02008.

[485] S. Asai et al., *Pathways to Innovation and Discovery in Particle Physics - Particle Physics Project Prioritisation Panel Report*, 2024, URL: https://www.usparticlephysics.org/2023-p5-report/.

[486] B. Foster, R. D'Arcy, C. A. Lindstrøm, *A hybrid, asymmetric, linear Higgs factory based on plasma-wakefield and radio-frequency acceleration*, New J. Phys **25** (2023) 093037, DOI: DOI10.1088/1367-2630/acf395.

[487] G. J. Cao et al., *Positron acceleration in plasma wakefields*, Phys. Rev. Accel. Beams **27** (2024) 034801, DOI: 10.1103/PhysRevAccelBeams.27.034801.

[488] J. Farmer, A. Caldwell, A. Phukov, *Preliminary Investigation of a Higgs Factory based on Proton-Driven Plasma Wakefield Acceleration*, 2024, DOI: 10.48550/arXiv.2401.14765, arXiv: 2401.14765 [physics.acc-ph].

[489] A. Caldwell et al., *Proton-Driven Plasma Wakefield Acceleration for Future HEP Colliders* (2025), arXiv: 2503.21669 [physics.acc-ph].

[490] C. Jing, *Dielectric Wakefield Accelerators*, Reviews of Accelerator Science and Technology **09** (2016) 127, DOI: 10.1142/S1793626816300061.

[491] J. Power et al., *Beam Test Facilities for R&D in Accelerator Science and Technologies*, 2022, arXiv: 2203.11290 [physics.acc-ph].

[492] P. Muggli et al., *European facilities for advanced accelerators development*, Journal of Instrumentation **17** (2022) T05008, DOI: 10.1088/1748-0221/17/05/t05008.

[493] E. Gschwendtner et al., *The AWAKE Run 2 Programme and Beyond*, Symmetry **14** (2022) 1680, DOI: 10.3390/sym14081680.

[494] C. Joshi et al., *Plasma wakefield acceleration experiments at FACET II*, Plasma Physics and Controlled Fusion **60** (2018) 034001.

[495] C. Emma et al., *Experimental Generation of Extreme Electron Beams for Advanced Accelerator Applications*, Physical Review Letters **134** (2025), DOI: 10.1103/physrevlett.134.085001, URL: http://dx.doi.org/10.1103/PhysRevLett.134.085001.

[496] R. D'Arcy et al., *FLASHForward: plasma wakefield accelerator science for high-average-power applications*, Philosophical Transactions of the Royal Society A: Mathematical, Physical and Engineering Sciences **377** (2019) 20180392, DOI: 10.1098/rsta.2018.0392.

[497] A. Picksley et al., *Matched Guiding and Controlled Injection in Dark-Current-Free, 10-GeV-Class, Channel-Guided Laser-Plasma Accelerators*, Physical Review Letters **133** (2024), DOI: 10.1103/physrevlett.133.255001.

[498] R. Pompili et al., *Free-electron lasing with compact beam-driven plasma wakefield accelerator*, Nature **605** (2022) 659, DOI: 10.1038/s41586-022-04589-1.

[499] R. W. Assmann et al., *EuPRAXIA Conceptual Design Report*, The European Physical Journal Special Topics **229** (2020) 3675, DOI: 10.1140/epjst/e2020-000127-8.

[500] C. A. Lindstrøm et al., *SPARTA (ERC StG): Developing multistage plasma-based accelerators*, 2023, eprint: TheSpartaProjectWebPage, URL: https://www.mn.uio.no/fysikk/english/research/projects/staging-of-plasma-accelerators-for-timely-applications/.

[501] A. Grudiev, S. Calatroni, W. Wuensch, *New local field quantity describing the high gradient limit of accelerating structures*, Physical Review Special Topics - Accelerators and Beams **12** (2009) 102001, DOI: 10.1103/PhysRevSTAB.12.102001.

[502] C. Jing et al., *Argonne Flexible Linear Collider*, IPAC2013 (2013), URL: https://accelconf.web.cern.ch/ipac2013/papers/tupea088.pdf.

[503] W. Tan et al., *Demonstration of sub-*GV/m*accelerating field in a photoemission electron gun powered by nanosecond X-band radio-frequency pulses*, Physical Review Accelerators and Beams **25** (2022) 083402, DOI: 10.1103/PhysRevAccelBeams.25.083402.

[504] R. Hawkings, K. Monig, *Electroweak and CP violation physics at a linear collider Z factory*, Eur. Phys. J. direct **1** (1999) 8, DOI: 10.1007/s1010599c0008, arXiv: hep-ex/9910022.

[505] G. W. Wilson, *Updated Study of a Precision Measurement of the W Mass from a Threshold Scan Using Polarized e^- and e^+ at ILC*, International Workshop on Future Linear Colliders, 2016, arXiv: 1603.06016 [hep-ex].

[506] C. Rimbault et al., *GUINEA PIG++ : An Upgraded Version of the Linear Collider Beam Beam Interaction Simulation Code GUINEA PIG*, Conf. Proc. C **070625** (2007), ed. by C. Petit-Jean-Genaz 2728, DOI: 10.1109/PAC.2007.4440556.

[507] *Innovate for Sustainable Accelerating Systems" (iSAS)*, URL: https://isas.ijclab.in2p3.fr/.

[508] V. Litvinenko, *Energy Recovery (and particle recycling) in Linear Colliders*, URL: https://agenda.linearcollider.org/event/10134/contributions/54231/attachments/39542/62613/LCWS_Plenary_Litvinenko.pdf.

[509] V. Litvinenko, *Future e+e- colliders using recycling energy-recovery linacs*, URL: https://conference-indico.kek.jp/event/225/contributions/5545/attachments/3906/5350/THO03.pdf.

[510] H. Gerke, K. Steffen, *NOTE ON A 45-GeV - 100-GeV 'ELECTRON SWING' COLLIDING BEAM ACCELERATOR* (1979).

[511] V. N. Litvinenko, T. Roser, M. Chamizo-Llatas, *High-energy high-luminosity e^+e^- collider using energy-recovery linacs*, Phys. Lett. B **804** (2020) 135394, DOI: 10.1016/j.physletb.2020.135394, arXiv: 1909.04437 [physics.acc-ph].

[512] A. Grassellino et al., *Nitrogen and Argon Doping of Niobium for Superconducting Radio Frequency Cavities: A Pathway to Highly Efficient Accelerating Structures*, Supercond. Sci. Technol. **26** (2013) 102001, DOI: 10.1088/0953-2048/26/10/102001, arXiv: 1306.0288 [physics.acc-ph].

[513] V. Telnov, *A high-luminosity superconducting twin e+e- linear collider with energy recovery*, Journal of Instrumentation **16** (2021) P12025, DOI: 10.1088/1748-0221/16/12/P12025.

[514] K. Yokoya, *ILC Upgrade with Energy Recovery*, EPJ Web Conf. **315** (2024) 02016, DOI: 10.1051/epjconf/202431502016.

[515] T. Barklow et al., *XCC: An X-ray FEL-based $\gamma\gamma$ Compton Collider Higgs Factory*, JINST **18** (2023) P07028, DOI: 10.1088/1748-0221/18/07/P07028, arXiv: 2306.10057 [physics.acc-ph].

[516] T. Barklow et al., *XCC: An X-ray FEL-based $\gamma\gamma$ Collider Higgs Factory*, Snowmass 2021, 2022, arXiv: 2203.08484 [hep-ex].

[517] W. Bonivento et al., *Proposal to Search for Heavy Neutral Leptons at the SPS* (2013), arXiv: 1310.1762 [hep-ex].

[518] M. Anelli et al., SHiP, *A facility to Search for Hidden Particles (SHiP) at the CERN SPS* (2015), arXiv: 1504.04956 [physics.ins-det].

[519] H. Iwashita et al., *Energy-Resolved Soft-Error Rate Measurements for 1–800 MeV Neutrons by the Time-of-Flight Technique at LANSCE*, IEEE Transactions on Nuclear Science **67** (2020) 2363, DOI: 10.1109/TNS.2020.3025727, (visited on 14/01/2025).

[520] Y. Sakaki et al., *The potential of the ILC beam dump for high-intensity and large-area irradiation field with atmospheric-like neutrons and muons*, Nucl. Instrum. Meth. A **1050** (2023) 168144, DOI: 10.1016/j.nima.2023.168144, arXiv: 2210.08690 [physics.acc-ph].

[521] PRISMAP project, *Welcome to PRISMAP: Your European Provider for Medical Radionuclides and Beyond*, PRISMAP, 2021, URL: https://www.prismap.eu/ (visited on 17/01/2025).

[522] Y. Morikawa et al., *Potential of Multilateral Utilization of ILC*, Journal of the Particle Accelerator Society of Japan **15** (2018) 132, DOI: 10.50868/pasj.15.3_132.

[523] H. Vincke, C. Theis, *ActiWiz 3 – an overview of the latest developments and their application*, J. Phys. Conf. Ser. **1046** (2018) 012007, DOI: 10.1088/1742-6596/1046/1/012007.

[524] A. Ishikawa, Y. Sakaki, Y. Takubo, *Search for axion-like particles with electron and positron beams at the KEK linac*, PTEP **2022** (2022) 113B05, DOI: 10.1093/ptep/ptac129, arXiv: 2107.06431 [hep-ph].

[525] W. Scandale et al., *Observation of channeling for 6500 GeV/ c protons in the crystal assisted collimation setup for LHC*, Phys. Lett. B **758** (2016) 129, DOI: 10.1016/j.physletb.2016.05.004.

[526] E. Bagli et al., *Experimental evidence of independence of nuclear de-channeling length on the particle charge sign*, Eur. Phys. J. C **77** (2017) 71, DOI: 10.1140/epjc/s10052-017-4642-y, arXiv: 1606.08755 [physics.acc-ph].

[527] L. Bandiera et al., *Investigation on steering of ultrarelativistic $e^{\pm}$ beam through an axially oriented bent crystal*, Eur. Phys. J. C **81** (2021) 238, DOI: 10.1140/epjc/s10052-021-09021-y, arXiv: 2011.13283 [physics.acc-ph].

[528] Thales LAS France SAS, *Quark 200/350/500 Ultrafast Ti:Sa Laser Series*, 2020, URL: https://www.thalesgroup.com/sites/default/files/database/document/2020-01/07_Quark%20200_350_500_0.pdf (visited on 11/02/2025).

[529] D. N. Papadopoulos et al., *The Apollon 10 PW laser: experimental and theoretical investigation of the temporal characteristics*, High Power Laser Sci. Eng. **4** (2016) e34, DOI: 10.1017/hpl.2016.34.

[530] C. Radier et al., *10 PW Peak Power Femtosecond Laser Pulses at ELI-NP*, High Power Laser Science and Engineering **10** (2022) e21, DOI: 10.1017/hpl.2022.11, (visited on 15/03/2024).

[531] C. Joshi, T. C. Katsouleas, *Plasma accelerators at the energy frontier and on tabletops*, Phys. Today **56N6** (2003) 47, DOI: 10.1063/1.1595054.

[532] C. A. Lindstrøm, *Staging of plasma-wakefield accelerators*, Phys. Rev. Accel. Beams **24** (2021) 014801, DOI: 10.1103/PhysRevAccelBeams.24.014801, arXiv: 2007.05258 [physics.acc-ph].

[533] G. J. Cao et al., *Positron acceleration in plasma wakefields*, Phys. Rev. Accel. Beams **27** (2024) 034801, DOI: 10.1103/PhysRevAccelBeams.27.034801, arXiv: 2309.10495 [physics.acc-ph].

[534] M. Litos et al., *High-efficiency acceleration of an electron beam in a plasma wakefield accelerator*, Nature **515** (2014) 92, DOI: 10.1038/nature13882.

[535] The TESLA collaboration, *Conceptual Design of a 500 GeV e^+e^- Linear Collider Facility with Integrated X-ray Laser Facility*, DESY report 1997-048. ECFA 1997-182 (1997).

[536] M. Breidenbach et al., *Updating the SiD Detector concept* (2021), arXiv: 2110.09965 [physics.ins-det].

[537] G. Contin, *The MAPS-based vertex detector for the STAR experiment: Lessons learned and performance*, Nuclear Instruments and Methods in Physics Research Section A: Accelerators, Spectrometers, Detectors and Associated Equipment **831** (2016), Proceedings of the 10th International “Hiroshima” Symposium on the Development and Application of Semiconductor Tracking Detectors 7, DOI: 10.1016/j.nima.2016.04.109.

[538] B. Abelev et al., ALICE, *Technical Design Report for the Upgrade of the ALICE Inner Tracking System*, J. Phys. G **41** (2014) 087002, DOI: 10.1088/0954-3899/41/8/087002.

[539] A. Nomerotski et al., PLUME, *PLUME collaboration: Ultra-light ladders for linear collider vertex detector*, Nucl. Instrum. Meth. A **650** (2011), ed. by R. Horisberger, D. Kotlinski, A. Starodumov 208, DOI: 10.1016/j.nima.2010.12.083.

[540] R. Diener, LCTPC, *Development of a TPC for an ILC Detector*, Phys. Procedia **37** (2012), ed. by T. Liu 456, DOI: 10.1016/j.phpro.2012.02.393, arXiv: 1203.2074 [physics.ins-det].

[541] F. Sefkow et al., *Experimental Tests of Particle Flow Calorimetry*, Rev. Mod. Phys. **88** (2016) 015003, DOI: 10.1103/RevModPhys.88.015003, arXiv: 1507.05893 [physics.ins-det].

[542] G. Grenier, CALICE, *Technological Prototypes and Result Highlights of Highly Granular Calorimeters*, PoS **EPS-HEP2017** (2017), ed. by P. Checchia et al. 497, DOI: 10.22323/1.314.0497.

[543] F. Simon, CALICE, *Beam Test Results with Highly Granular Hadron Calorimeters for the ILC*, Conf. Proc. C **0908171** (2009), ed. by T. Behnke, J. Mnich 539, DOI: 10.3204/DESY-PROC-2010-04/P44, arXiv: 1002.1012 [physics.ins-det].

[544] G. Baulieu et al., *Construction and commissioning of a technological prototype of a high-granularity semi-digital hadronic calorimeter*, JINST **10** (2015) P10039, DOI: 10.1088/1748-0221/10/10/P10039, arXiv: 1506.05316 [physics.ins-det].

[545] D. R. Nygren, *Origin and development of the TPC idea*, Nuclear Instruments and Methods in Physics Research Section A: Accelerators, Spectrometers, Detectors and Associated Equipment **907** (2018) 22, DOI: 10.1016/j.nima.2018.07.015.

[546] J. Marx, *A Proposal for a General PEP Facility Based on the TPC* (1976).

[547] D. et al, Nuclear Instruments and Methods in Physics Research Section A: Accelerators, Spectrometers, Detectors and Associated Equipment **504** (2003) 48.

[548] H. Sadrozinski et al., *Sensors for ultra-fast silicon detectors*, Nucl. Instrum. Meth. A **765** (2014), ed. by Y. Unno et al. 7, DOI: 10.1016/j.nima.2014.05.006.

[549] I. Ravasenga, *Results of the new MAPS-based ALICE inner tracker operations in the LHC Run 3*, Nuclear Instruments and Methods in Physics Research Section A: Accelerators, Spectrometers, Detectors and Associated Equipment **1064** (2024) 169311, DOI: 10.1016/j.nima.2024.169311.

[550] G. Hallais et al., *Pixel device based on a quantum well: Preliminary results on gate dielectrics*, Nucl. Instrum. Meth. A **1047** (2023) 167906, DOI: 10.1016/j.nima.2022.167906.